



Cristallochimie du pyroxène dans les komatiites et basaltes lunaires

Sébastien Bouquain

► To cite this version:

Sébastien Bouquain. Cristallochimie du pyroxène dans les komatiites et basaltes lunaires. Géologie appliquée. Université Joseph-Fourier - Grenoble I, 2008. Français. <tel-00335493>

HAL Id: tel-00335493

<https://tel.archives-ouvertes.fr/tel-00335493>

Submitted on 29 Oct 2008

HAL is a multi-disciplinary open access archive for the deposit and dissemination of scientific research documents, whether they are published or not. The documents may come from teaching and research institutions in France or abroad, or from public or private research centers.

L'archive ouverte pluridisciplinaire **HAL**, est destinée au dépôt et à la diffusion de documents scientifiques de niveau recherche, publiés ou non, émanant des établissements d'enseignement et de recherche français ou étrangers, des laboratoires publics ou privés.



Université Joseph Fourier – GRENOBLE (France)
Centre de Recherches Pétrographiques et Géochimiques – NANCY (France)
Johannes Gutenberg-Universität – MAINZ (Deutschland)
Ecole Doctorale « Terre – Univers – Environnement » – Grenoble

--- PhD ---

Crystallochemistry of pyroxenes in komatiites and lunar basalts

Sébastien Bouquain

Members of the Jury :

<i>Rapporteurs :</i>	Dr. Michael Toplis Prof. Gerhard Wörner	DTP, Toulouse Geochemischen Institut, Göttingen
<i>Examinateurs :</i>	Dr. François Faure Dr. Jean-Emmanuel Martelat	CRPG, Nancy LGCA, Grenoble
<i>Directors :</i>	Prof. Nick Arndt Prof. Guy Libourel Prof. Stephen Foley	LGCA, Grenoble CRPG, Nancy Institut für Geowissenschaften, Mainz

Remerciements

Remerciements

Je remercie solennellement mes chefs : Nick Arndt à Grenoble, Guy Libourel à Nancy et Steve Foley à Mayence. Enfin surtout Nick, qui a commencé à me supporter il y a 5 ans en me montrant des komatiites dans un microscope. Après un stage d'initiation en maîtrise, puis un second stage de perfectionnement en Master, il a bien su continuer à éveiller ma curiosité sur ces objets fascinants, en me laissant une grande liberté pour mener ce projet à bien. Cette liberté conditionnelle a contribué à un résultat personnel plus que satisfaisant, en me permettant de conjuguer travaux manuels et intellectuels. Merci à Guy, François et Laurent au CRPG pour les discussions scientifiques et les conseils généreux.

Au final, cette thèse a été le paysage d'un bel épanouissement dans lequel une faune et une flore se sont cotoyées avec joie, bonne humeur ou simplement indifférence.

Un salut à la faune française : essentiellement buralistique et laboristique. Shaz, qui ne m'a toujours pas invité à bouffer (bravo !), et les autres coburo Marc et Vinçouille. La gnogna team au complet (Marion et Andrea), jamais avare en conseils et petits coups de main. Sans oublier l'aile sud et les Qpuqueurs de la belle époque. A Nancy, un coucou à Céline pour le coburotage. Sans oublier BTC pour l'accueil nancéen, et la vtt team du CRPG ! Antoine, garde ton accent c'est nickel, et bonne fin de thèse à toi.

La faune étrangère n'est pas en reste, et je ne remercierai jamais assez Anja pour son accueil incroyable à Mayence et son aide de tous les instants. Lina, bonne chance pour la suite que je te souhaite bien belle. Sebastian, merci pour l'appart à mon arrivée, et bonne continuation. Un salut à toute la fine équipe du labo : Matthias, Stephan, Tatjana, Stephie et tous les autres et leur petit thé après manger... Un bonjour également à Céline ma coloc d'un mois au Max Planck Institut.

Je remercie enfin tout ceux qui m'ont aidé d'une manière ou d'une autre : Eric Hellebrand à la SIMS au MPI, Pierre Baillot l'usineur fou du CRPG, Matthieu Corrazi et Manu Munoz à l'Eagle au LGCA, et Sophie Adeline à la sonde électronique à Nancy.

Table of Contents

Abstract	1
Résumé (in French)	2
Zusammenfassung (in German)	3
Introduction	4
Chapter 1: Komatiites	6
1.1. General	7
1.2. The formation of komatiite magma	9
1.3. The spinifex paradox	11
1.4. Model of crystallization of a thin differentiated komatiite lava flow	12
1.5. Thick differentiated komatiitic flows	14
Chapter 2: Pyroxenes	16
2.1. Introduction	17
2.2. Pyroxenes in komatiites	18
Chapter 3: Geology of studied flows	22
3.1. Introduction	23
3.2. The Alexo komatiite	23
3.3. The differentiated komatiitic basalt from Alexo	26
3.4. Fred's Flow	28
3.5. Komatiites from Barberton, South Africa	28
3.6. Pigeonite Basalts of Apollo 12 and Apollo 15	29

Chapter 4: Methodology (abstract)	32
Chapter 5: Detailed Petrography (abstract)	34
Chapter 6: Paper “Crystallization and origin of pyroxenes in komatiites and lunar basalts”; submitted to Contributions to Mineralogy and Petrology	38
Chapter 7: Paper “Experimental pyroxene spinifex”	82
Conclusions	108
Appendix	110
A. Chapitre 4: Méthodologie (in French)	112
4.1. Etude expérimentale	113
4.2. Les techniques de caractérisation	121
B. Chapitre 5 : Pétrographie détaillée (in French)	124
5.1. Rappel du contexte général	125
5.2. Coulée de basalte komatiitique d’Alexo	125
5.3. Coulée de komatiite d’Alexo	127
C. Tables	129
References	135

Abstract

Zoned pyroxene crystals with pigeonite cores and augite mantles crystallize in komatiites and lunar basalts. To understand the origin and conditions of crystallization of these unusual pyroxenes, a two-pronged approach was adopted, in part experimental and in part analytical. The experiments were conducted at the Centre de Recherches Pétrologiques et Géochimiques in Nancy in collaboration with François Faure, Laurent Tissandier and Guy Libourel. We adapted and improved the approach of Faure et al. (2006), to study selected compositions in the CMAS (Ca, Mg, Al, Si) system in which the pyroxenes protoenstatite, orthoenstatite, diopside and pigeonite crystallize under equilibrium conditions. These experiments allowed us to refine the pyroxene phase diagram. They also showed that it is possible to crystallize pyroxene with chemical compositions and textures similar to those observed in komatiites. As in the experiments of Faure et al (2006), a key condition is the presence of a thermal gradient. In particular, the zoned, acicular pigeonite-augite crystals characteristic of komatiites and lunar basalts were well reproduced. These results call into question the previous interpretations of experimental studies in which certain aspects of the compositions of these pyroxenes were attributed to crystallization of hydrous magmas.

The analytical study was undertaken on a series of samples of komatiites and lunar basalts. The komatiites were from the Archean (2.7 Ga) Abitibi greenstone belt in Canada. Emphasis was focused on three flows: a small differentiated komatiite flow and a thicker komatiitic basalt in the Alexo area, and Fred's Flow, a thick, differentiated komatiitic flow from Munro Township. The lunar basalts were selected from the NASA collection because they exhibit pyroxene crystals with pigeonite-augite zonation similar to that observed in the komatiites. For our study, they constitute an anhydrous reference because these rocks undoubtedly formed from anhydrous magma. Our results show that the textures and chemical compositions in the pyroxenes in the komatiites also reflect crystallization in the thermal gradient at the top of a lava flow. In addition, pyroxene crystallizes earlier than predicted on the basis of equilibrium experiments, an effect we attribute to Soret differentiation within the partially solidified lower portion of the crystal front. The results of this study, coupled with analytical modeling, and comparison with the geochemistry of komatiites from other regions, led to the conclusion that water is not necessary for the genesis of a komatiite.

Résumé

Des cristaux de pyroxène zonés, avec un cœur de pigeonite et une bordure d'augite, cristallisent dans les komatiites et les basaltes lunaires. Pour comprendre les conditions de cristallisation de ces pyroxènes singuliers, nous avons opté pour une double approche, expérimentale et analytique.

Des expériences de cristallisation du pyroxène ont été menées au Centre de Recherches Pétrologiques et Géochimiques à Nancy en collaboration avec François Faure, Guy Libourel et Laurent Tissandier. Nous avons repris l'approche de Faure et al. (2006), que nous avons développée et améliorée, en travaillant avec des compositions où le pyroxène (protoenstatite, orthoenstatite, pigeonite et diopside) cristallise. Ces expériences ont permis de mieux contraindre le diagramme de phases des pyroxènes dans le système CMAS. Elles ont également montré qu'il est possible de cristalliser des cristaux de pyroxène avec des compositions chimiques et des textures comparables à celles observées dans les komatiites, en présence d'un gradient thermique. En particulier, la zonation pigeonite-augite des cristaux dendritiques aciculaires est bien reproduite. Les expériences posent également la question de la présence métastable de l'olivine, qui cristallise dans des conditions de refroidissement moyennement rapide (jusqu'à 10°C/h) depuis un liquide avec la pigeonite au liquidus. Ces résultats remettent en question les interprétations de travaux expérimentaux antérieurs qui attribuaient les compositions des pyroxènes à de la cristallisation de magmas hydratés.

En parallèle, une étude analytique complète a été entreprise sur une série d'échantillons de komatiite archéenne et de basaltes lunaires. Les komatiites étudiées proviennent de la ceinture de roches vertes d'Abitibi, au Canada, et sont d'âge Archéen (2.7 Ga). L'accent s'est porté sur trois coulées : les deux coulées d'Alexo (une petite coulée différenciée de komatiite et une coulée épaisse de basalte komatiitique) et la coulée de Fred (une coulée très différenciée épaisse de komatiite). Les basaltes lunaires choisis pour cette étude parmi la collection de la NASA ont la particularité d'exhiber des cristaux de pyroxène avec une zonation pigeonite-augite similaire à celle observée dans les komatiites d'Abitibi. Pour notre étude, ils constituent un référentiel anhydre car ces roches se sont indubitablement formées à partir d'un magma dépourvu d'eau (Canup et Asphaug, 2001). Nos résultats montrent que les textures et compositions chimiques du pyroxène dans les komatiites reflètent la cristallisation dans un gradient thermique au sommet de la coulée. Nous attribuons la cristallisation précoce du pyroxène à une différenciation par effet Soret à l'avant du front de cristallisation du pyroxène. Les résultats de cette étude analytique couplés à un travail de modélisation, ainsi qu'une étude comparative de la géochimie de l'ensemble des komatiites mondialement recensées, arrivent à la conclusion que l'eau n'est pas nécessaire à la genèse d'une komatiite.

Zusammenfassung

Zonierte Pyroxen-Kristalle mit Pigeonite Kernen und Augite Mänteln kristallisieren in Komatiiten und lunaren Basalten. Um die Bedingungen für die Kristallisation dieser ungewöhnlichen Pyroxene zu verstehen, haben wir beschlossen, einen experimentalen und einen analytischen Ansatz zu verbinden.

Kristallisation-Experimente von Pyroxen wurden am "Centre de Recherches Pétrologiques et Géochimiques in Nancy durchgeführt, in Zusammenarbeit mit François Faure, Laurent Tissandier und Guy Libourel. Wir haben den Ansatz von Faure et al. (2006) weiterentwickelt und verbessert, indem wir mit Zusammensetzungen im CMAS (Ca, Mg, Al, Si)-System gearbeitet haben, in denen Pyroxene (Protoenstatite, Orthoenstatite, Diopsid und Pigeonite) kristallisiert. Diese Experimente erlauben uns das Pyroxen Phasendiagramm im CMAS System zu verfeinern. Sie zeigte auch, dass es möglich ist, Pyroxen zu kristallisieren, das eine chemische Zusammensetzung und Struktur vergleichbar mit Komatiiten hat. Wie in den Experimenten von Faure et al. (2006) ist eine zentrale Voraussetzung das Vorhandensein eines thermischen Gradienten. Vor allem die Zonierung von nadeligen Pigeonite-Augite Kristallen, charakteristisch für Komatiite und lunare Basalte, sind gut reproduziert worden. Diese Ergebnisse stellen vorherige Interpretationen von experimentellen Studien in Frage, in denen bestimmte Aspekte der Komposition dieser Pyroxene auf die Kristallisation von hydrierten Magmen zurückgeführt wurden.

Eine vollständige analytische Studie wurde gleichzeitig über eine Probenreihe von Komatiiten und lunaren Basalten ausgeführt. Die Komatiite kamen aus dem Abitibi greenstone belt in Kanada und stammen aus der Archeischen Epoche (2,7 Ga). Der Schwerpunkt wurde auf drei Flüsse gelegt: Ein kleiner differenzierter Komatiit-Fluss und ein dicker komatiischer Basalt-Fluss in der Gegend von Alexo, und Fred's Fluss, ein dicker, differenzierter Komatiit Fluss in Munro Township. Die lunaren Basalte wurden aus der Sammlung der NASA ausgewählt. Sie weisen Pyroxen-Kristalle mit Pigeonite-Augite Zonierung auf, die denen der Abitibi-Komatiite ähnlich sind. Für unsere Studie stellen sie die anhydrierte Referenz dar, weil dieses Gestein zweifellos aus wasserfreiem Magma gebildet wurde (Canup und Asphaug, 2001). Unsere Ergebnisse zeigen, dass die Textur und die chemische Zusammensetzung der Pyroxene in den Komatiiten die Konsequenz der unterschiedlichen Kristallisationbedingungen innerhalb desselben Flusses und zwischen verschiedenen Flüssen ist. Insbesondere beeinflusst der thermale Gradient an der Spitze des Lavaflusses die Kristallisation. Darüberhinaus kristallisiert Pyroxen früher als auf der Grundlage von Gleichgewicht-Experimenten vorhergesagt wurde. Dieser Effekt kann der Soret Differenzierung innerhalb der teilweise verfestigten unteren Zone der Kristallfront zugeschrieben werden. Die Ergebnisse dieser Studie, gepaart mit analytischer Modellierung und Vergleich mit der Geochimie der Komatiite aus anderen Regionen, führen zu dem Schluss, dass Wasser nicht notwendig für die Entstehung eines Komatiiten ist.

Introduction

Water is at the centre of global politics. Essential to life, water nourishes ecosystems; but where it is scarce it is also the source of conflicts. Water was essential for the appearance of life on Earth some 4 billion years ago, and plate tectonics is probably directly linked to the presence of oceans. Water plays a fundamental role in the planetary geodynamics of the planets.

The presence of water decreases the temperatures of melting in the mantle. If water were abundant in the mantle during the Archean (3.8-2.5 Ga), the temperatures at which magmas formed may have been lower than those commonly mentioned. One method to determine the presence of water in the mantle is to study the crystallization sequences and composition of minerals in rocks that crystallized from mantle-derived magmas. A key target for this type of study has been komatiites — ultramafic magmas which, because of their chemical similarity with mantle peridotite, have been used as probes to determine the composition and physical conditions in their mantle source.

This thesis project was conceived in part as a reaction to a series of papers by Parman et al. (1997, 2001, 2003) and McSween al. (2001) in which it is proposed that Archean ultramafic lavas (komatiites) and certain Martian magmas were hydrous. This idea, while not new (Allègre, 1982, Hart & Brooks, 1977), calls into question much of our understanding of geodynamics of the Archean Earth. A key argument of these authors is that the pyroxenes that crystallize in komatiites and in SNC-type Martian meteorites (Shergottites, Nakhrites, Chassignites) have particular geochemical and textural characteristics that can be attributed to the presence of water in these magmas.

The growth of spinifex, the texture emblematic of komatiite, has been used by de Wt et al. (1987), Grove et al. (1996) and Parman et al. (1997) as an argument in favour of the presence of water in the source of komatiites. However, Faure et al. (2006) subsequently conducted a series of experimental studies in which they were able to reproduce spinifex texture under anhydrous conditions similar to those that existed during the solidification of komatiite lavas.

McSween et al. (2001) based their arguments on a study of the geochemistry of light elements (Li, Be, B) in pyroxene in Martian basaltic shergottites. In a paper written by the same group comprising some of the authors of the hydrous komatiite paper, Dann et al. (2001) advocated the existence of hydrous magmatism on Mars on the basis of an experimental study of pyroxenes in the Shergotty meteorite. These authors found that the phase relations and compositions of pyroxenes in the meteorite were best approximated by crystallization under hydrous conditions and high pressure (56 MPa). These conclusions, which are quite similar to those reached by Parman et al. (1997), led us to undertake a detailed study of pyroxenes in mafic-ultramafic rocks from the early Earth (komatiites) and from the Moon, the latter representing an unequivocal example of anhydrous magma.

The overall goal of the thesis project was to obtain a better understanding of the mechanisms of formation of pyroxene in komatiites and the factors that control their compositions and textures. To this end, I used a dual approach, in part analytical and in part experimental. In the first approach, I analyzed in detail the pyroxenes from several Archean komatiites and from lunar basalts in order to help understand their compositional variations and to relate these compositions to the conditions under which they formed. In the experimental section, I applied the techniques developed by Faure et al. (2006) to the study of basaltic compositions in order to investigate in more detail how the conditions of crystallization affect the pyroxene compositions.

Introduction

In the first two chapters of the thesis, I describe the objects of study. The first chapter focuses on komatiites and provides a summary of current knowledge of these important rocks. The second chapter introduces the pyroxenes and describes how they occur in komatiites and lunar basalts. Then I outline the geology of all the flows and rocks that were studied (Chapter 3), before detailing the analytical and experimental methods (Chapter 4). The fifth chapter is a detailed petrographic description of the samples of komatiite and komatiitic basalt of Alexo. The sixth chapter is a paper submitted to Contributions to Mineralogy and Petrology in which my co-authors and I discuss in detail the analytical investigations of pyroxenes in komatiites and lunar basalts and develop a new explanation of their compositions. Finally, the seventh chapter consists of a second paper, yet to be submitted, in which the results of the experimental studies are presented and interpreted.



The spectacular spinifex texture of komatiites, photographed on an outcrop.

Chapter 1: Komatiites

1.1. General	7
1.2. The formation of komatiite magma.....	9
1.2.1. Physical properties.....	9
1.2.2. Origin of komatiite magma.....	10
1.2.3. Eruption	11
1.3. The spinifex paradox	11
1.4. Model of crystallization of a thin differentiated komatiite lava flow	12
1.5. Thick differentiated komatiitic flows	14

1.1. General

The year 1969 saw two major scientific advances: Man walked on the Moon, and Viljoen and Viljoen (1969) described a new class of ultrabasic volcanic rocks - the komatiites. These rocks are found primarily in the greenstone belts in the oldest cratons. They are mainly Archaean in age, but some Proterozoic and Cretaceous examples are known, the latter from Gorgona Island off the coast of Colombia (Arndt & Nisbet, 1982). A fundamental characteristic of the komatiites is their MgO content, which is defined as being higher than 18%. To be more precise it is appropriate, in definition of a komatiite, to include concept of spinifex texture. The term spinifex was used by Australian prospectors to describe texture distinctive of these rocks which were used to them as a guide in their prospecting for gold and nickel deposits (Naldrett & Gasparrini, 1971). The term stems from the similarity between the texture in the komatiites and that of a variety of spiky grass. Spinifex texture is characterized by the presence of large skeletal or dendritic crystals of olivine or pyroxene, oriented randomly or parallel to one another, in a matrix of fine skeletal clinopyroxene grains and devitrified glass. One speaks of komatiitic basalt when a rock contains between 8% and 18% MgO and contains petrologic, textural and geochemical characteristics similar to those of komatiites.

Most komatiites are extrusive and erupt as lava flows, but high-level sills are also known (Arndt et al., 2004). The most distinctive form of komatiite flow is differentiated into two or more layers, but according to Dann (2000) 75% of Barberton komatiite flows (South Africa) were massive sheet flows and only 25% of the komatiite flows were spinifex-textured. "The thicknesses of layered komatiite flows vary greatly", said Arndt et al. (2008) in their recent book. Miniature (50cm thick) flows are reported in several areas, some being fully differentiated with an upper spinifex and a lower cumulate layer. At the opposite, we know several 100m thick and more, for example in the Abitibi greenstone belt. These thicker flows are invariably differentiated.

Pyke et al. (1973) defined a typical section of a layered komatiite flow. This standard description and those of many others authors (Arndt, 1986, Barnes et al., 1973, Donaldson, 1982, Nisbet et al., 1977, Renner, 1989) were summarized by Arndt et al. (2008) (Fig. 1.1): A typical differentiated spinifex-textured flow contains, from top to base, a chilled margin and aphanitic flow top (A1), a spinifex layer (A2-A3), a thin layer of foliated skeletal olivines (B1), an olivine cumulate layer (B2-B3-B4), and a lower chilled margin.

- Flow Top (A1) The upper chilled margin ranges in thickness from 5 cm to 1.5 m and is composed of very fine-grained lava cut by close-spaced (1-3 cm) polyhedral joints. The lava between the joints contains randomly oriented, elongate skeletal and polyhedral olivine phenocrysts set in a fine-grained or glassy groundmass.
- Spinifex (A2-A3) At the top of the spinifex layer the olivine grains are a few millimeters long and 0.5 mm thick. Deeper in the flow, they become progressively larger and grade into spectacular composite blades up to 1 metre long. The habit and orientation also changes. In random spinifex, olivine forms simple, randomly oriented, skeletal tablets (Figure 2.2.a). In platy spinifex (Figure 2.2.b) the olivine blades are oriented parallel to one another within book-like crystals. The matrix between olivine grains normally is composed of clinopyroxene, glass and minor oxides except for some slowly cooled samples in thick flows where plagioclase found. The habit of pyroxene ranges from parallel needles with cores of pigeonite or enstatite and mantles of augite to very fine, complex skeletal grains of irregular pyroxene-plagioclase

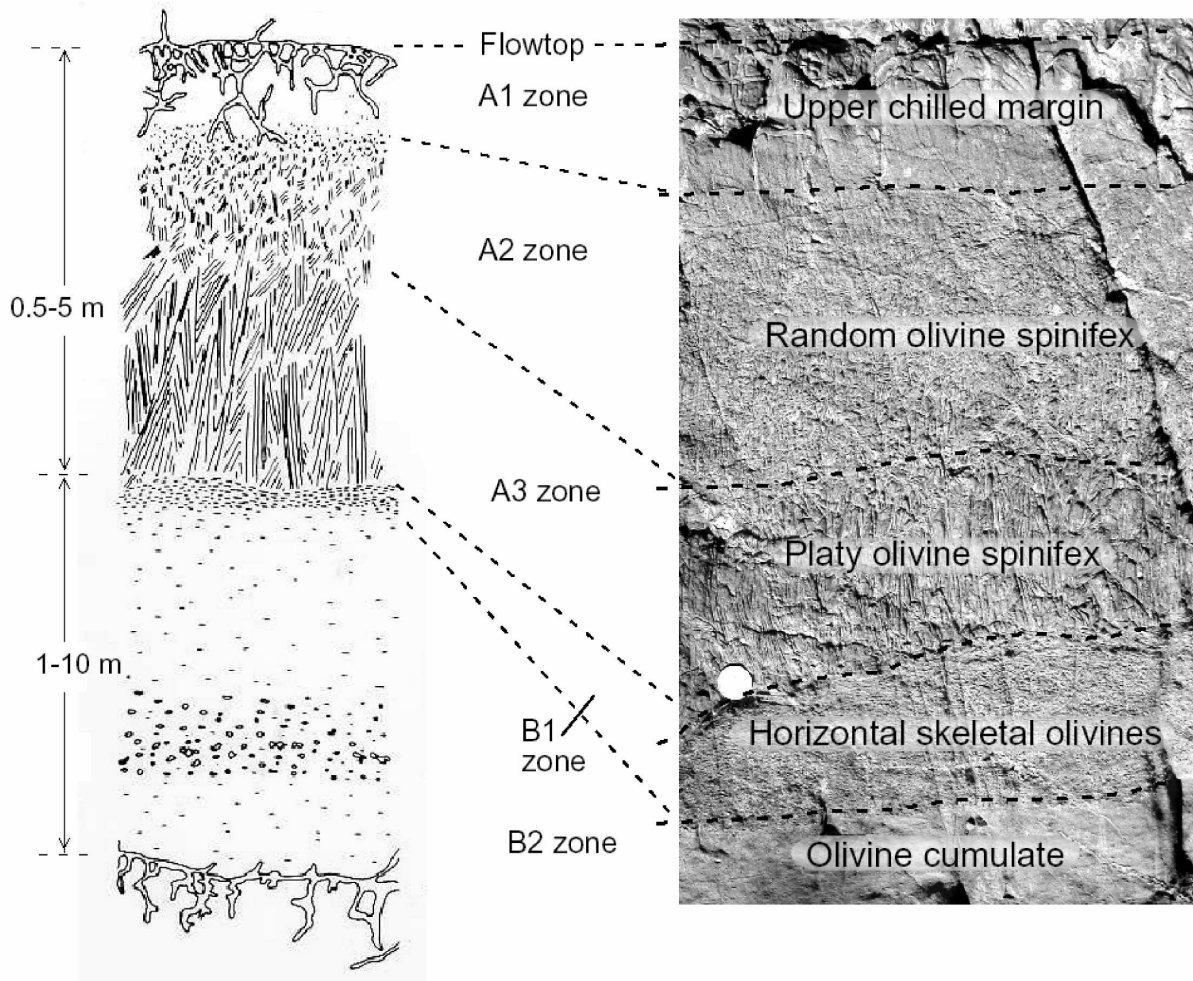


Fig. 1.1. Schematic section of a komatiite flow and associated outcrop photograph (Arndt et al. 2008, d'après Pyke et al. 1973, modifié). Upper part (A) is made of two zones: the flow top (A1) and the spinifex layers (A2-A3). Lower part (B) is a succession of cumulates and a lower chill zone.

- intergrowths. Chromite occurs as inclusions in olivine and as skeletal grains that apparently grew outwards from the margins of olivine plates.
- The B1 Layer is composed of small (1-3 mm) elongate hopper olivine phenocrysts orientated parallel to the flow margins within a pyroxene-glass matrix.
- The cumulate layer (B2-B4) is divided into four subunits; B1 to B4. The B2 and B4 layers consist of (70-95%) equant to tabular, polyhedral to granular olivine grains in a pyroxene-glass matrix. The intervening B3 or "knobby peridotite" layer is distinguished by the presence of "knobs", or patches, 1 cm across, of pyroxene-glass matrix material.
- Textures in the basalt chill zones resemble those of the overlying cumulates. They consist of polyhedral olivine grains in a finer-grained pyroxene-glass groundmass but the olivine grains are far smaller (0.1-0.3 mm) and far less abundant (typically 5-20%).

The mineral assemblage characteristic of komatiites is olivine + chromite + clinopyroxene + (plagioclase - very rare) + glass. Some flows also crystallized orthopyroxene and/or

pigeonite. Pigeonite crystallized in three flows from the Abitibi greenstone belt, those that form the subject of this thesis. Proportions of magmatic minerals vary significantly within each flow because of differentiation that accompanied or followed eruption. The differentiation mechanisms are still poorly constrained and the study of pyroxene in this thesis aims to obtain a better understanding of this process.

1.2. The formation of komatiite magma

To understand the formation of komatiite magma, we have to mention the physical properties and the origin of the magma that influenced eruption.

1.2.1. Physical properties

Komatiite magma has a main feature: its very high MgO content. Komatiites formed from liquids with about 30% MgO and more. In comparison, liquids that form mid-oceanic ridge basalts (MORB) contain about 10% MgO. Most authors agree that komatiites are produced by partial melting of mantle peridotite. Under normal conditions, the product of melting of the mantle is a basaltic melt. Ultramafic melts instead of basaltic melts can be produced by three ways:

- A high degree of partial melting of the mantle (30-50%), which leads to the fusion of MgO-rich minerals such as olivine and orthopyroxene, in addition to clinopyroxene and garnet, which melt at lower degrees of melting.
- Partial melting at high pressure, which destabilizes olivine with respect to the other minerals (pyroxene, garnet) and produces a magma that is richer in olivine and thus more magnesian than a magma produced at low pressure.
- Melting of a depleted source — one from which basaltic magma has yet been extracted, leaving only olivine and orthopyroxene. A melt from such a source produces a more magnesian magma than that from more primitive source at an equivalent degree of melting.

Other features of komatiite magma are the low SiO₂, Al₂O₃ and alkalis contents. “Viljoen and Viljoen (1969) and Nesbitt (1971) realized that the unusually high temperatures and very low viscosities of komatiite would strongly influence the way these magmas erupted and crystallized” said Arndt et al. (2008). They pointed out the importance of a high temperature of the magma, that will influence eruption mechanisms. The eruption temperature of a komatiite magma can be estimated from liquidus temperature. This liquidus temperature was determined in experimental studies, and summarized by the following relationship:

$$T_{\text{liq}} = \text{MgO}_{\text{liq}} \times 20 + 1000 \quad (\text{Nisbet, 1982})$$

Thus a liquid with 30% MgO may erupt at a given temperature of 1600°C. As shown in Figure 1.2, this implicates a large temperature interval between the liquidus and the solidus (temperature where the rock is fully solidified), and a large temperature of crystallization of olivine. The second silicate phase to crystallize is pyroxene at about 1200°C and then plagioclase join the assemblage. For a given komatiite magma, the liquidus temperature calculated above may change because of the presence of a significant amount of water. There are many evidences that support a submarine eruption of most komatiites. With a several

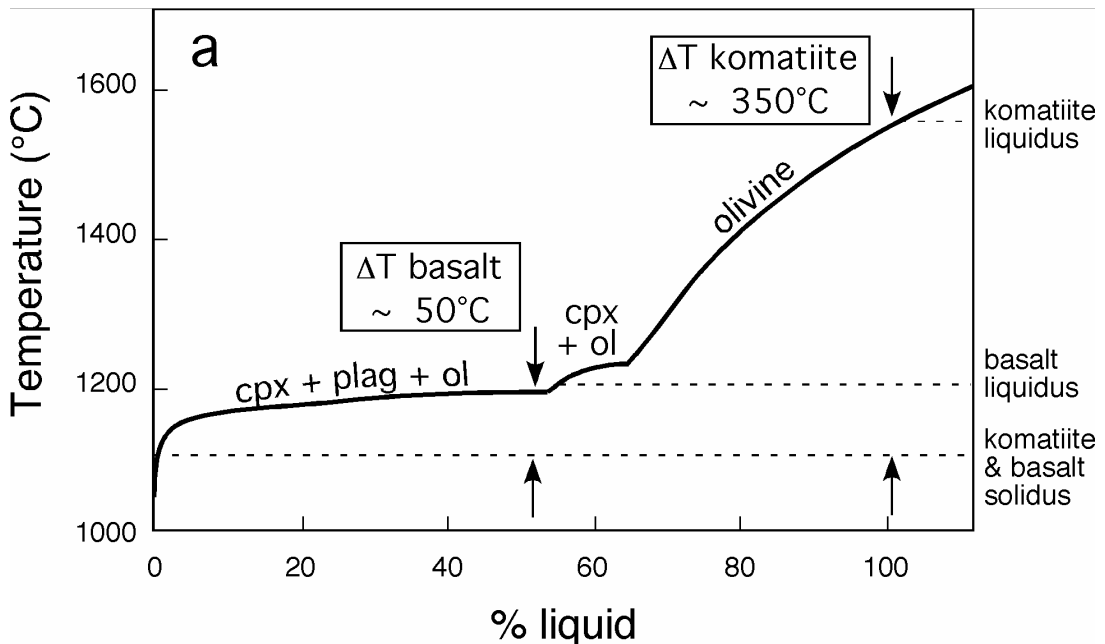


Fig. 1.2. Simplified 1-atm phase relations of komatiite containing about 30% MgO (Arndt et al., 2008, from Arndt (1976), Kinzler & Grove (1985) and Parman et al. (1997)) contrasting the large temperature interval between liquidus and solidus with the much smaller interval in basalt.

hundreds of meters depth of water on their head, the komatiite liquids could have retained a small quantity of water. 0.5wt% H₂O will decrease the “dry” liquidus by about 50°C. Other physical characteristics of komatiite magma are their very low viscosity (Huppert & Sparks, 1985) and a relatively high density. The density of a komatiite magma with 30% MgO is about 2738 kg.m⁻³, according to Bottinga & Weill (1970) method (Arndt et al., 2008), and will increase during crystallization.

1.2.2. Origin of komatiite magma

“High temperature is the defining feature of the komatiite source”, conclude Arndt et al. (2008). According to Arndt (2003), the most plausible explanation to explain the origin of most komatiites is the melting of an anhydrous and exceptionally hot source. In this model, komatiite is the product of a high-degree melting at great depth of a mantle plume. This hypothesis is disputed by Grove and co-workers (Grove et al., 1997, Grove et al., 1999, Parman et al., 1997) who propose that komatiites result instead from melting of a colder, but hydrated source. To support their hydrous model, these authors use the composition of augite and absence of pigeonite in komatiites from Barberton, South Africa, and their experiments of dynamic crystallization. According to these experiments, the spinifex-textured komatiite forms through crystallization in the presence of water.

High density of the komatiitic magma is another key characteristic: such magma would rise up from its source only through a less dense material. Even if density increases with depth, the partial melt produced at pressures about 8GPa (the pressure at a depth of 240km) has the same density as solid mantle minerals (Arndt et al., 2008). However, the plume ascent driven by mantle convection could allow the melt to rise up. Barberton-type Al-depleted komatiites form under these conditions, where majorite garnet is the residual phase. Munro-type Al-undepleted komatiites form at shallower levels in a mantle plume, from a trace-element-depleted source where earlier melts formed (Arndt et al., 2008). When approaching the surface, the melt can pass indifferently through a low-density continental crust ($\rho=2.7$) or an oceanic crust ($\rho=3.0$).

Arndt et al. (2008) give a good summary: “We have no real idea of the exact nature of a komatiite source but a mantle plume probably fits the bill. This could have been the type of plume believed (by most authors) to be feeding Hawaii and other chains of oceanic islands — a cylinder of hot, buoyant material rising from far deeper in the mantle — or it could have been a “starting mantle plume” — a huge, roughly mushroom-shaped structure that probably rose from the core-mantle boundary”.

1.2.3. Eruption

The mechanisms of eruption of komatiites are poorly understood, and many uncertainties persist. Being very low-viscosity lavas, komatiites can erupt easily over broad surfaces. These eruptions are probably fed by lava fountains that passed through fissures. It is difficult to estimate the power of the lava fountains because the low viscosity of the magma would be more or less counterbalanced by its high density ($\rho=2.74$; Arndt et al. (2008)). In the Barberton greenstone belt, Dann (2000) reports massive komatiites that extend laterally up to 11km. Some authors predict that komatiite flows may have been hundreds of kilom (Huppert & Sparks, 1985, Williams et al., 2000). Field studies do not bring more answers, mainly because of limits of outcrops and deformation of most greenstone belts.

Komatiite magma is easy to contaminate during its ascension. The high temperature of the komatiitic magma makes it “fragile”; i.e. the magma rapidly loses heat to its surroundings, which causes it to partially crystallize, or it can assimilate the wall rocks and thus become contaminated.

In the same way, the gas content of the lava (and thus the efficiency of degassing) is strongly debated (Arndt et al., 1998, Grove et al., 1999).

1.3. The spinifex paradox

Within a komatiite flow, the rate of cooling is controlled by the thermal conduction through the solidified crust (Donaldson, 1982). Even in a relatively thin, 2-meter flow, the cooling rate does not exceed 3°C per hour and would be less than 1°C/h in the middle of a thick (tens of meters) flow. Thus, spinifex texture, which commonly occurs 1-2 meters beneath the flow top, should have formed at low cooling rates, at most 3°C/h according to Donaldson (1982). However, during the experimental studies of Donaldson (1982) and others (Faure et al., 2003) the distinctive dendritic morphologies of olivine crystals in spinifex crystals were reproduced only at cooling rates higher than 30°C/h. In other words, magma in the interior of a komatiite flow cannot have cooled fast enough to explain spinifex-textured crystals, if the interpretation of the experimental data is correct. Several possible solutions to what has become known as the “spinifex paradox” (Faure, 2001, Faure et al., 2006) have been advanced:

- Hydrothermal cooling: seawater circulation inside a network of fractures in the solidified crust increased the rate of cooling (Shore & Fowler, 1999). This mechanism can not explain the growth of spinifex minerals deep in a flow.
- The rate of heat loss is increased by thermal radiation along large spinifex olivine crystals, which is 3 to 5 times greater than by conduction alone (Shore & Fowler, 1999). However, the efficiency of this mechanism decreases in cooler, less magnesian liquids, such as in komatiitic basalts where we find spinifex-textured pyroxenes.
- Crystallization of a hydrous magma: (Grove et al., 1997, Grove et al., 1999) use the spinifex paradox as an argument for the presence of water (3 to 6% H₂O) in the komatiites. According to them, the presence of water in a silicate liquid decreases the

rate of crystal nucleation and increases the rate of diffusion, which results in rapid growth of large, skeletal crystals. Moreover, degassing during the ascent of a hydrous

- Komatiitic magma produces a supercooled liquid. Spinifex texture then results from the rapid growth of crystals in a hydrous and/or supercooled komatiitic liquid.
- During crystallization, the spinifex crystals expulse some chemical components – those that do not enter in their network –, in particular around the tips. Thus this residual liquid forms a layer below the crystallization front. The tips of spinifex crystals grow in a liquid depleted in the chemical components necessary for their growth. Faure (2001) suggested that to pierce this depleted layer, the crystals develop fine needles with a skeletal morphology.
- The presence of a thermal gradient in the upper part of the flow influences the crystal morphology. In a series of experiments in which synthetic komatiites were cooled slowly (between 2 and 10 °C/h) in the presence of a thermal gradient (typically 20°C/cm), Faure et al. (2006) produced olivine crystals showing the same types of morphologies than those obtained during fast cooling and those in natural komatiites.

1.4. Model of crystallization of a thin differentiated komatiite lava flow

The most recent model of crystallization (Faure, 2001) is presented below. This model follows the broad outline of the model proposed by Pyke et al. (1973), while being freed from the problematic presence of low cooling rates in the middle of the flow. The model explains: 1) the formation of the lower cumulate layer, 2) the presence of the B1 layer, 3) the formation of the different types of spinifex layers.

For better understanding of the model, we introduce the concept of “cold front”. Intuitively, the flow interior is the hottest part of the flow and the last to cool. The flow top cools the quickest because it is in contact with air or water. Cooling rates at the base are lower because of the insulating properties of the underlying rock. During the cooling of a flow, the isotherms move from top towards the middle of the flow, a process referred to as the “propagation of the cold front”. Calculations based on the rate of heat transfer by conduction through the upper crust of the flow show that this cold front propagates more and more slowly towards the middle of the flow and that the shallowest isotherms propagate the most rapidly, whatever the depth. Crystallization follows the descent of the cold front and proceeds progressively from the top towards the interior of the flow. At the same time phenocrysts introduced in incoming lava or nucleated homogeneously settle towards the base of the flow to form the cumulate layer.

The crystallization of a flow of komatiite is divided into five stages: (Fig. 1.3)

Stage 1:

Eruption of the komatiitic magma. Both the roof and base of the flow are chilled through contact with the air, water or floor rock and this leads to formation of the upper and lower chill zones. These borders contain a small amount (<5 to 20%) of euhedral phenocrysts of olivine which reflect the presence of crystals that probably formed either during ascent of the magma or following its eruption. As soon as the flow is in place, the olivine crystals start to settle to the floor of the flow.

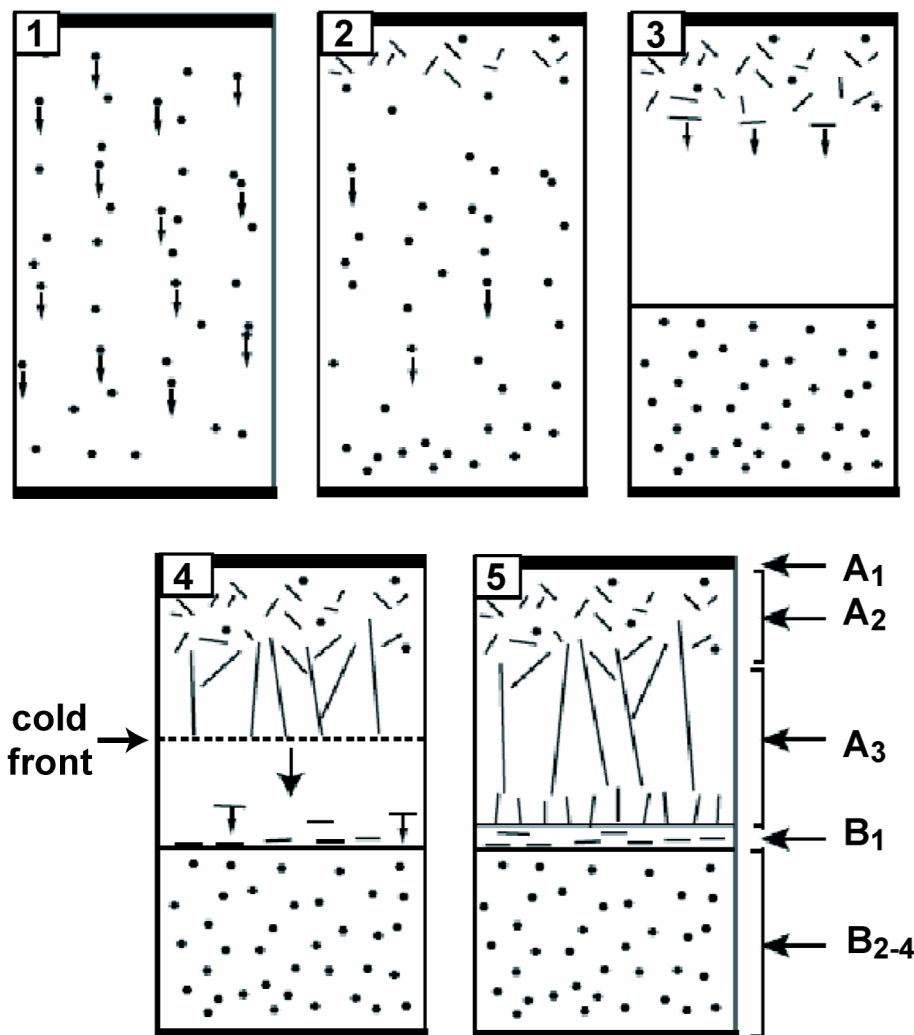


Fig. 1.3. Model of crystallization of a layered spinifex-textured komatiite flow (from Faure, 2001).

Stage 2:

The euhedral crystals continue to settle and accumulate to form the cumulate layer. At the top of the flow, rapid cooling causes the crystallization of dendritic crystals of olivine, to form the random spinifex (A2) layer. Nucleation of these crystals is homogeneous and the orientation of nuclei and subsequent crystals is random. The flow interior remains totally liquid and very hot, while the higher part of the flow (under the chill zone) is cooler and contains crystals.

Stage 3:

Crystallization and sedimentation of small dendritic olivine crystals, which settle to form the B1 layer. According to Faure (2001), there is a small lapse of time during which 1) the cooling rate is sufficient to form dendrites and 2) the cold front progresses slowly enough so that the formed crystals can fall by gravity.

Stage 4:

Growth of dendritic crystals in a constrained manner, parallel to the thermal gradient, and downwards towards the interior of the flow, to form the platy spinifex (A3) layer. The

preferred orientation perpendicular to the flow top results because only crystals that are oriented in the right direction continue to grow: misoriented crystals grow only until they collide with a downward growing crystal.

Stage 5:

End of the crystallization of the spinifex layer. The olivine megacrysts grow until they reach the B1 layer. An inversion of the thermal gradient may cause the crystallization of spinifex-textured olivine from the roof of B1 towards the top of the flow.

This model of crystallization is strictly valid only for traditional komatiitic flows where all layers are present (Fig. 2). The final structure of a flow, as well as the proportions of minerals, are controlled by:

- (1) The environment and mechanism of eruption, which influence the thickness and internal structure of the flow.
- (2) The composition of the komatiitic magma, which influences the viscosity of the lava and the sequence of crystallization: a highly magnesian magma will be likely more to form a well differentiated flow.
- (3) The history of eruption: as the flow progresses from its site of eruption it cools and grows phenocrysts that influence the physical properties of the lava. Distal flows are charged with olivine phenocrysts and are poorly differentiated.

1.5. Thick differentiated komatiitic flows

The description above applies mainly to relatively thin (<10m) flows of ultramafic composition. Also present in most greenstone belts are far thicker flows, up to 120m or more, which are strongly differentiated into lower ultramafic cumulates and upper mafic gabbroic or spinifex textured layers. The type example of this type of flow is Fred's Flow in Munro Township (Arndt, 1977). Compared with the thinner ultramafic flows the thicker flows are characterized by:

- A much thicker spinifex textured zone. In Fred's Flow a 1m thick layer of olivine spinifex is underlain by up to 3m of pyroxene spinifex. Thick pyroxene spinifex layers are also present in the Boston Creek flow (Stone et al., 1987) and in flows from the Nondweni belt (Wilson et al., 2003). If the spinifex texture formed by the mechanism proposed above, this implies a thermal gradient persisted across a particularly thick zone of partially crystallized lava.
- Below the crystal front, convective efficiently mixes liquid rejected by the downward-growing crystals with unfractionated liquid in the interior of the flow. The spinifex crystals therefore grow downward into more fertile liquid.
- Meanwhile, in the lower part of the flow, euhedral olivine crystals leak out of the convecting liquid to form the cumulate zone.
- In the upper part of the cumulate zone, layers of olivine and pyroxene cumulate alternate. This requires that convection ceased so that the two types of mineral could accumulate.
- A thick layer of gabbro intervenes between the spinifex and cumulate layers. This layer crystallized at the end of the solidification process and represents residual liquid of near eutectic composition.

Chapter 2. Pyroxenes

2.1. Introduction	17
2.2. Pyroxene in komatiites	18

2.1. Introduction

Pyroxene (“stranger to fire” from the Greek *pyros* - fire and *xenos* – stranger) is a ubiquitous mineral in igneous and metamorphic rocks. It is part of the inosilicate group, as reflected in the organization of its silica tetrahedra $[\text{SiO}_4]^{4-}$ in chains. In the pyroxene structure, each chain has a periodicity of two tetrahedra. The general formula is $\text{XY}(\text{SiO}_3)^2$ where X is a large cation (Na^+ , Ca^+ , Li^+ , Mg^{2+} , Fe^{2+} , Mn^{2+}) and Y a cation of average size (Mg^{2+} , Fe^{2+} , Mn^{2+} , Fe^{3+} , Al^{3+} , Cr^{3+} , Ti^{4+}). Because of this flexible structure, pyroxene is capable of accepting most of the major elements present in the magmatic liquids. Pyroxene normally crystallizes in the monoclinic system (clinopyroxene), and less commonly in the orthorhombic system (orthopyroxene).

The principal clinopyroxene species (and those that interest us the most) are defined by three cations: Mg^{2+} , Ca^+ et Fe^{2+} . The pure end-members contain only a single cation:

- enstatite (En): $\text{Mg}_2(\text{SiO}_3)_2$
- wollastonite (Wo): $\text{Ca}_2(\text{SiO}_3)_2$
- ferrosilite (Fs): $\text{Fe}_2(\text{SiO}_3)_2$

The pure end-members do not exist in nature, but synthesized minerals of approach these compositions.

In nature, all common pyroxenes plot in the quadrilateral “pyroxene quadrilateral” which has the following end-members: $\text{Mg}_2(\text{SiO}_3)_2$ - $\text{CaMg}(\text{SiO}_3)_2$ - $\text{CaFe}(\text{SiO}_3)_2$ - $\text{Fe}_2(\text{SiO}_3)_2$ or enstatite (En) - diopside (Di) - hedenbergite (Hd) - ferrosilite (Fs) (Fig. 2.1). The pyroxenes in the upper part of the quadrilateral pyroxene are known as calcic or Ca-rich pyroxenes. Their space group is C_2/c . Augite, the most common pyroxene in igneous rocks, has the composition $(\text{Ca}, \text{Na})(\text{Mg}, \text{Fe}, \text{Al})[(\text{Si}, \text{Al})\text{O}_3]_2$. It contains 20-45 mol% wollastonite and accepts aluminium and sodium in its network. In lower part of the quadrilateral, one finds pigeonite, whose formula is $(\text{Mg}, \text{Fe}, \text{Ca})_2(\text{SiO}_3)_2$, as well as clinoenstatite ($\text{Mg}_2(\text{SiO}_3)_2$) and the clinoferrosilite ($\text{Fe}_2(\text{SiO}_3)_2$). Pigeonite contains 5 to 20% wollastonite and is distinguished from augite by its space group of P_{21}/c . There is a miscibility gap between these two species, and many pyroxenes that are reported to contain 15-25% wollastonite most probably are mixtures.

Orthorhombic pyroxenes have two space groups: Pbca and Pbcn . The latter is only stable at very high temperature and its Wo content does not exceed 2%. For the Pbca form, the Wo content varies between 1.5 and 5%. The orthorhombic pyroxenes, whose general formula is $(\text{Mg}, \text{Fe})(\text{SiO}_3)_2$, form a solid solution between the end-members enstatite (MgSiO_3) and ferrosilite (FeSiO_3). Enstatite is not found of high temperature in nature. The minerals of this series are (from the most to least magnesian): protoenstatite, orthoenstatite (previously called hypersthene) and bronzite. The official nomenclature of pyroxenes (Morimoto et al., 1988) recommends the terms enstatite and ferrosilite for all pyroxenes that crystallize in the orthorhombic system, the limit between the two being equidistant from the two pure end-members. There is a link between the two crystal systems because pigeonite and the orthopyroxene are not polymorphs; their compositions are different. During the crystallization of mafic magmas, the stable form at high temperature is pigeonite, while the orthopyroxene crystallizes at lower temperatures. Thus there is a temperature inversion between these two forms. In slowly cooled rocks, pigeonite inverts; i.e. calcic pyroxene exsolves along (001) planes at high temperature and along (100) planes at low temperature. Most volcanic rocks cool sufficient quickly to keep pigeonite in a metastable state.

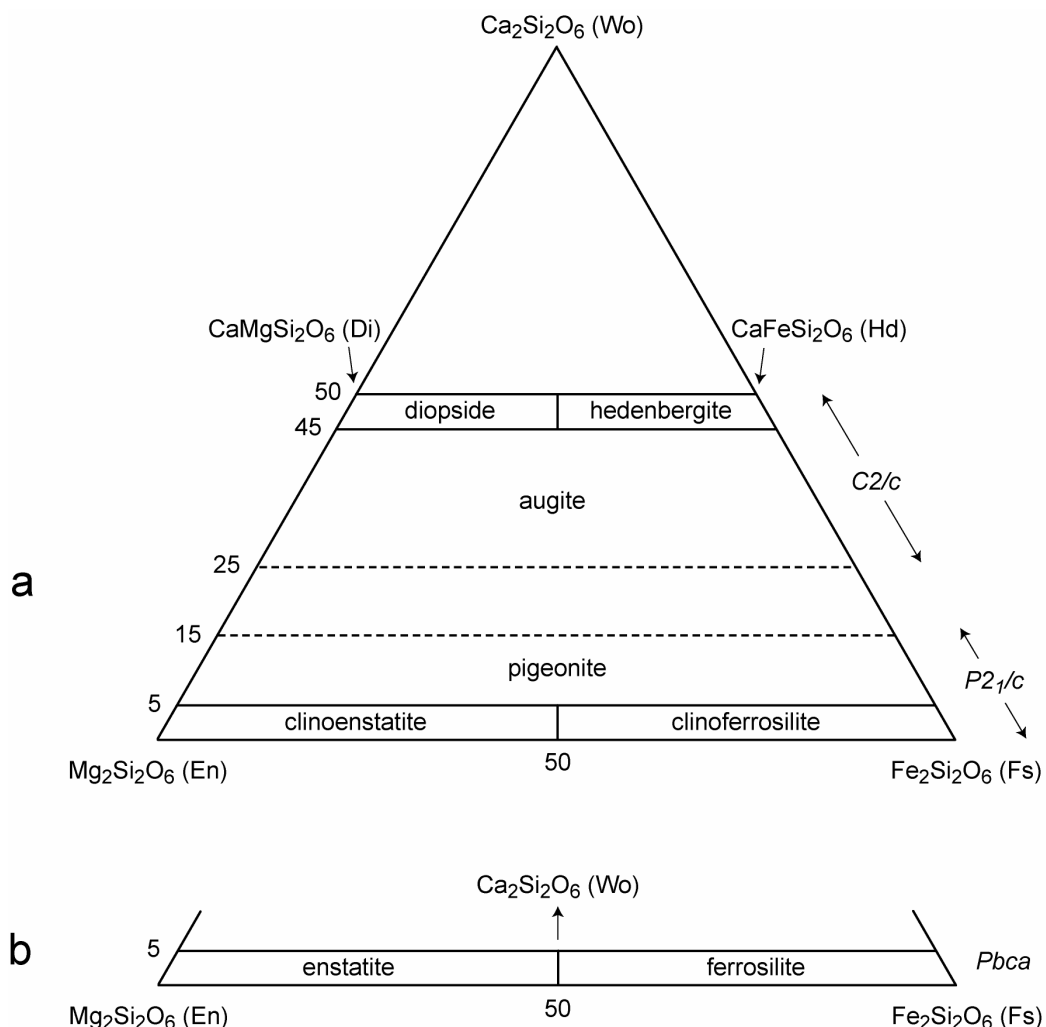


Fig. 2.1. (a) Ternary diagram enstatite (En) – wollastonite (Wo) – ferrosilite (Fs). En, Fs, diopside (Di) and hedenbergite (Hd) end members form the pyroxene quadrilateral. The composition fields of naturally occurring components are presented and the space groups of pyroxenes as well.

(b) Diagram similar to (a), showing composition fields of orthopyroxenes.

Low-Ca pyroxenes have been the subject of many studies in past decades. In particular, experimental studies have provided a better understanding of the mechanisms of interaction between different types of pyroxene and the relationships between their compositions and crystallization conditions. The experimental studies have focused on simplified systems such as CMAS (Calcium-Magnesium-Aluminium-Silica), which is an acceptable analogue for the study of mafic and ultramafic rocks. This subject is treated in detail in Chapter 7.

2.2. Pyroxene in komatiites

We saw in the previous section that three types of pyroxene crystallize in komatiites: orthopyroxene, a low calcium clinopyroxene (pigeonite) and a high-Ca clinopyroxene (usually augite). The most common type is augite which occurs as small acicular grains between olivine crystals in komatiites and intergrows with plagioclase in komatiitic basalts. Here we place the emphasis on more spectacular type of pyroxene that crystallizes in some differentiated komatiite and komatiitic basaltic flows. In these units, the large acicular pyroxene crystals that are the subject of this thesis are found in two different settings: (1) as large crystals oriented perpendicular to the flow top in the “string-beef” pyroxene spinifex

layers of differentiated komatiitic basaltic flows (Arndt & Fleet, 1979, Barnes, 1983, Campbell & Arndt, 1982, Kinzler & Grove, 1985), and (2) in “cells” between large olivine blades in the lower parts of the olivine spinifex layers of some komatiite flows.

The pyroxene crystals in both setting are similar. Large, acicular crystals (0.5mm wide and up to 4 cm long) with a pigeonite core and an augite margin lie in a matrix of small stubby prismatic augites that commonly are intergrown with plagioclase. The dimensions of the cells between olivine spinifex crystals of the komatiite flow from Alexo vary from about 1 to about 10 cm (Fig. 2.2b). The pyroxene needles are parallel to one another and are oriented perpendicular the flow top in the thick differentiated komatiitic basalt flows (Fig. 2.3b) or perpendicular to the olivine plates in the olivine spinifex layer. When studied in thin section, the pyroxene needles prove to be parts of large complex dendritic crystals that consist of one or more rows of parallel needles. These needles are elongate along their c axes as a result of preferential growth on the {110} and {010} crystal faces. Many needles have a hollow pigeonite core surrounded by an augite margin. In the best-developed examples, a thin veneer of augite lines the hollow core.

The two different settings represent contrasting conditions of crystallization. In the thick differentiated flows, the pyroxene needles grew downwards from the upper crust of the flow within a thermal gradient between the cold surface and the hot interior. Since the layers of pyroxene spinifex are located below several meters of low-conductivity solid lava of the flow top, the cooling rate was low, probably less than 0.5-1°C/h (Donaldson, 1982, Faure, 2001). On the other hand, the thermal gradient across the crust may have been high, between 20 and 100°C/cm (the manner in which the gradient develops and evolves is discussed in a later section). The formation of these pyroxene crystals is readily explained in a model of crystal growth in a thermal gradient, as proposed by Faure et al. (2006) and described in Chapter 6. In contrast, during the growth of the similar-looking acicular pyroxene crystals in the cells between spinifex olivine plates, a thermal gradient related to the cold surface of the flow will be poorly developed and its direction will not the highly variable orientation of the pyroxene needles. To explain these crystals requires the development of another model, as described in Chapter 6.

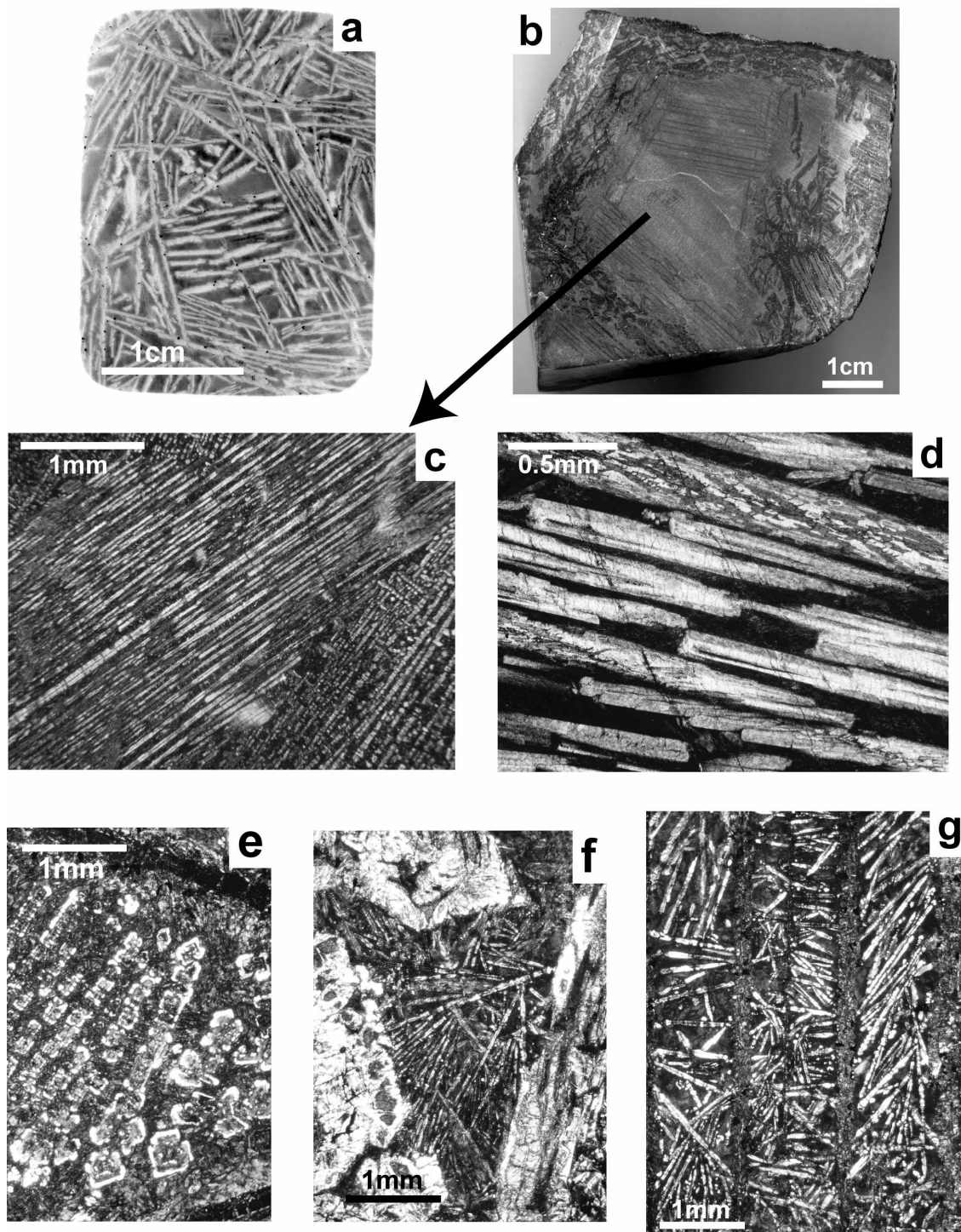


Fig. 2.2. Textures of komatiites from the Alexo area. (a) A scanned thin section of a random olivine spinifex-textured lava (sample M662). Olivine crystals (in white) are randomly oriented and lie in a fine-grained matrix. (b) Polished slab of coarse platy olivine spinifex textured lava, sample Ax105. Large complex dendritic grains of olivine (black, serpentinized) enclose a cell within which large pyroxene needles have grown. (c) Thin section showing thin needles of complex zoned pyroxene crystals in sample Ax105 (cross-polarized light). (d) Thin section showing in greater detail the zoned pyroxene megacrysts from Ax106. White pigeonite cores are mantled by grey-coloured augite margins. (e) Zoned pyroxene grains cut perpendicular to the c-axis, from within an olivine cell in olivine spinifex textured lava, sample M626. Augite rims (in white) are well preserved; pigeonite cores have altered to chlorite. (f, g) Small skeletal augites between olivine grains, sample M626. Olivine appears in white in Figure f, and dark grey in Figure g.

Chapter 3. Geology of studied flows

3.1. Introduction	23
3.2. The Alexo komatiite.....	23
3.3. The differentiated komatiitic basalt from Alexo	26
3.4. Fred's Flow	28
3.5. Komatiites from Barberton, South Africa.....	29
3.6. Pigeonite Basalts of Apollo 12 and Apollo 15	29

3.1. Introduction

The thesis focuses on two lava flows, one composed of komatiite and the second of komatiitic basalt. Both are in the Alexo area, which is located in Dundonald Township, 50km east of Timmins, Ontario, in the Abitibi Greenstone Belt (Figs. 3.1 and 3.2). The Abitibi Greenstone Belt is part of the Superior Province and is bordered in the northwest by the Kapuskasing gneiss belt and in southeast by the Grenville Province. In the Alexo area, various types of volcanic rock occur: komatiitic and basaltic sheet flows, andesitic pillow lavas, as well as a large mafic-ultramafic intrusion called the Dundonald sill. The degree of regional metamorphism is prehnite-pumpellyite facies. Dupré et al. (1984) determined the age of the komatiite flow of Alexo using the Pb-Pb and Sm-Nd methods at 2.690 ± 0.015 and 2.760 ± 0.097 Ga, respectively. This age has been confirmed by the U-Pb zircon dating of Barrie et al. (1999) who obtained 2.717 ± 0.001 Ga on a felsic flow from Dundonald Township. More information on local geology of the Alexo area can be obtained from Naldrett and Mason (1968) and Barnes (1983). Reference is also made to Fred's Flow, another thick, layered komatiitic basaltic flow in Munro Township, which is located about 50 km east of Alexo.

3.2. The Alexo komatiite

The Alexo komatiite flow was previously studied by Barnes (1983), Arndt (1986) and Lahaye and Arndt (1996). As shown in Figure 3.2, this flow is approximately 16m thick and rests on the komatiitic basalt flow described in the following section. From flow-top to base, it comprises a 2m thick ultramafic breccia, an 8m thick spinifex layer and a 6m thick cumulate layer.

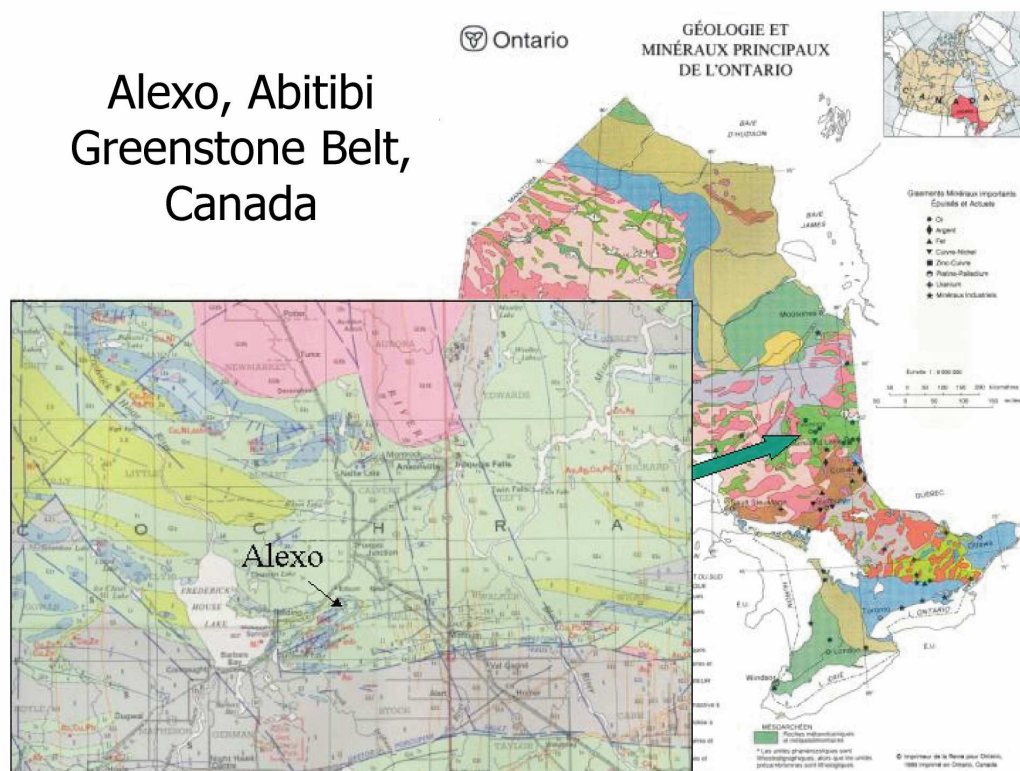


Fig. 3.1. General map of the Abitibi Greenstone Belt, Canada showing the Alexo area.

Figure 3.3 shows the principal textural variations within the flow. The mineralogical variations are described below.

- The *flow top breccia* (about 1m thick) is a hyaloclastite that consists of angular or rounded lithic fragments of maximum size 1cm surrounded by a chlorite-rich matrix. Some fragments are microporphyrlic with 1-3% of (serpentinized) olivine phenocrysts; others have microspinifex textures or are composed of hydrated glass. Olivine microlites in the fragments are approximately 50 mm long and show a preferential orientation. Some fragments contain small amygdales (1-2%). All primary minerals are altered to chlorite, magnetite, serpentine and tremolite.

- Beneath the breccia one finds a thin layer (2-5cm) called the *chilled margin*. This is a porphyritic rock with variable texture. Some parts are made up of small (0.1 to 0.4 mm) euhedral phenocrysts of fresh olivine in a fine-grained or completely vitreous matrix. The interiors of the olivine grains have a homogeneous very magnesian composition ($\text{Fo}_{94.1}$, Arndt (1986)) and they are surrounded by a fine, strongly zoned margin (to Fo_{88}). According to Arndt (1986) these olivine profiles show that the olivine phenocrysts cooled slowly at equilibrium with the initial komatiite liquid, then underwent a late episode of fast cooling in the chilled margin. Other parts consist of very small (<0.1 mm) skeletal olivine crystals (hopper crystals in the terminology of Donalson (1982)) in a vitreous matrix. These crystals are strongly zoned but have cores of composition similar to that of the euhedral phenocrysts. Arndt (1986) observed that the composition of the vitreous matrix is the same as that of the whole rock and concluded that the matrix is representative of the initial magmatic liquid. This liquid was highly ultramafic and contained about 28% MgO . Rare (2-3%) chlorite- and serpentine-filled amygdales are present in some parts of the chilled margin.

- *Random spinifex* forms the upper part of the spinifex layer. This rock contains stubby skeletal olivine crystals averaging about 2mm which are randomly oriented in a matrix of small skeletal pyroxenes, skeletal chromites and devitrified glass (Fig 2.2a). The olivines have cores of $\text{Fo}_{93.5}$ but are strongly zoned, with margins of Fo_{87} . Rare amygdales are present in

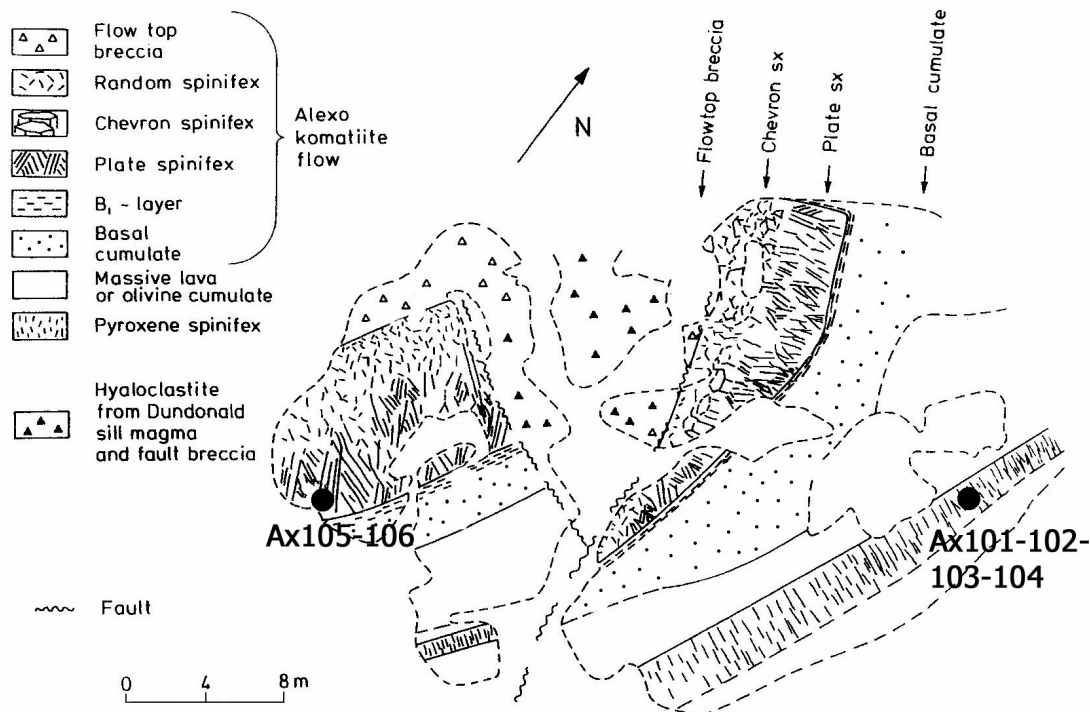


Fig. 3.2. Field map of Alexo area (from Arndt, 1986, modified).

this zone as well.

- *Chevron spinifex* is the name proposed by Arndt (1986) for the peculiar texture of this type of spinifex which occurs in some parts of the flow. Examination of the olivine grains in this textures reveals that each crystal consists of a complex network, several centimeters in length, of segments with a chevron shape. The zonation of olivine crystals is comparable with that observed in the overlying random spinifex zone.

• The *platy olivine spinifex* layer located in the interior of the flow is similar at the A3 layer that one finds in many komatiite flows. The olivine crystals can be enormous: they vary in length from a few centimeters to as much a 50 cm. They have a platy morphology; i.e. each crystal is less than a centimeter thick but tens of centimeters wide and long. The olivines are less rich in forsterite than in the higher zones. The compositions of the cores of the skeletal crystals vary between Fo₉₁ at the top and Fo₈₉ at the base of the layer. Arndt (1986) reports a significant variation of the proportion of olivine within this layer. Within the platy spinifex layer, the proportion decreases from the top to the middle, then increases towards the base. The amount of pyroxene varies inversely to that of olivine. Moreover, plagioclase is present as a phase intergrown with augite in the matrix of spinifex lavas with the lowest olivine contents.

Two types of pyroxene are found in this layer: pigeonite forms the cores of complex acicular crystals and augite forms the margins. One also finds crystals of augite alone, with smaller size but comparable morphology (Fig. 2.2b-g). Textures of pyroxene were previously discussed in Chapter 2. All the spinifex-textured rocks are partially altered but one finds well-preserved pyroxene crystals throughout the zone.

- The *B1 layer* is a thin (2-5 cm) layer that marks the abrupt transition between the spinifex horizons and the cumulate layer. This layer is primarily made of complex elongate and tabular skeletal olivine grains whose size varies between 1mm and 1cm. These grains

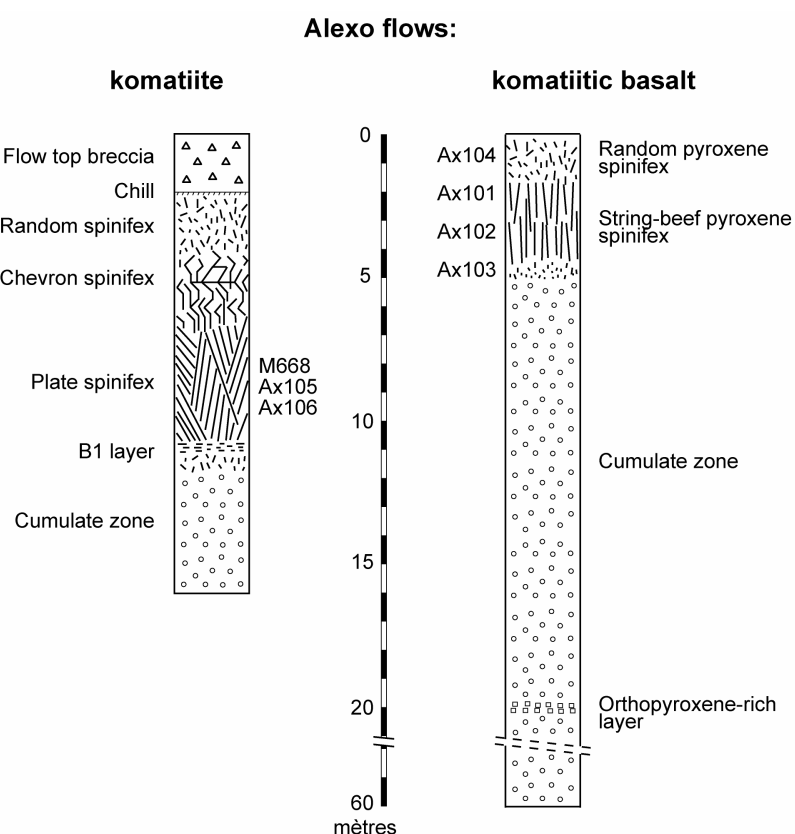


Fig. 3.3. Sections through the Alexo flows, showing sample locations and textural variations (after Arndt, 1986 and Barnes, 1983).

have a preferential orientation parallel to the strike of the flow and thus perpendicular to olivine megacrystals of the horizon located just above. This orientation attenuates towards the base of the layer before disappearing completely in the underlying B layer where the olivine grains are equant and euhedral. The olivine grains of the B1 layer have cores of $\text{Fo}_{93.8}$ and are zoned continuously to margins of Fo_{88} . The degree of alteration of the olivine of the cumulate horizon is variable. In some samples all grains are replaced by serpentine; in others up to 50% remains fresh.

3.3. The differentiated komatiitic basalt from Alexo

The komatiitic basalt of Alexo was the object of several studies (Arndt & Fleet, 1979, Barnes, 1983, Campbell & Arndt, 1982). Barnes (1983) estimated the thickness of this flow at approximately 60m (Fig. 3.3). According to these authors, the top of the flow consists of a rock containing millimeter length skeletal olivine grains in a matrix of smaller spherolitic and dendritic clinopyroxene grains and altered glass. Below this rock, one finds a pyroxene spinifex layer with a thickness of approximately 2m. In the upper random pyroxene spinifex part of this layer, the crystals of clinopyroxene do not have a preferential orientation; in the lower part one finds “stringbeef spinifex” in which the pyroxene crystals are oriented perpendicular to the strike of the flow. The pyroxene crystals are zoned with cores of pigeonite and margins of augite and are needle-shaped (Fig. 3.4.a-b). Textures of pyroxene in this layer were previously discussed in Chapter 2. Plagioclase is also present in the form of subhedral laths spherulites, and these crystals lie in a matrix of devitrified glass.

Under the spinifex layer, one finds up to 55m of massive olivine cumulate. Barnes (1983) reports the presence of patches of komatiite in which the olivine has a skeletal morphology. Elsewhere in the layer, the olivine is tabular, solid and euhedral. A thin layer (30cm) rich in orthopyroxene cuts the massive komatiite a level approximately 20m beneath the top of the flow. The orthopyroxene has a stubby platy morphology and contains abundant clinopyroxene inclusions along (010) planes. The matrix consists of acicular augites in devitrified glass (Arndt & Fleet, 1979).

The locations of samples taken in this study are indicated on Figures 3.2 and 3.3.

Samples Ax101 to Ax104 come from the komatiitic basalt flow. Ax104, located at the top of flow, consists of acicular pyroxene crystals. Ax101 and Ax102 come from the upper and middle parts of the pyroxene spinifex layer and Ax103 is located at the base of the spinifex layer.

Samples Ax105-106 are from the platy olivine spinifex layer of the Alexo komatiite, at the same place as the M668 sample described by Arndt (1986). In these samples, large spinifex olivine crystals delimit volumes of pyroxene-rich lava with widths of several centimeters (see Chapter 2).

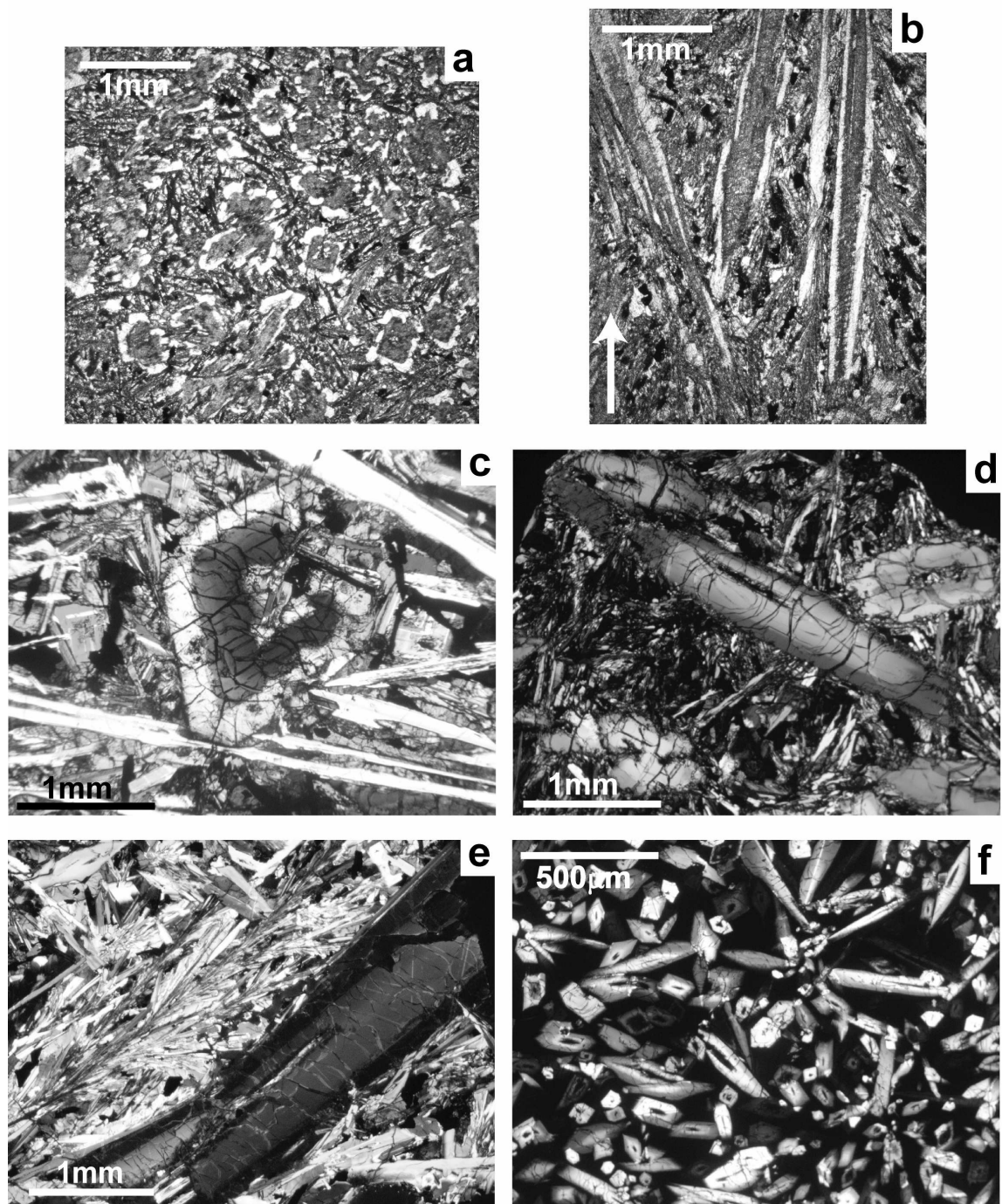


Fig. 3.4. Photomicrographs of representative thin sections, showing zoned pyroxene with pigeonite cores and augite rims. (a) Pyroxene spinifex lava (sample Ax101) from upper part of the komatiitic basalt flow of Alexo; the section is cut perpendicular to the flow and perpendicular to the c-axes of the pyroxenes. (b) Same sample, cut parallel to the c-axes. The direction to the flow top is indicated by the white arrow. (c) Lunar basalt, sample 12021,136. This sample contains a zoned pyroxene with a dark grey pigeonite core and a pale grey augite mantle. Plagioclase laths (white) are intergrown with augite (grey) in the matrix. (d) Zoned pyroxene with hollow shapes in a matrix of augite+plagioclase+oxides (lunar sample 12052,336). (e) Coarse phenocrysts of pyroxene (light grey pigeonite and dark grey augite) embedded in a fine-grained groundmass of intergrown pyroxene and plagioclase (plumose structure), opaque phases and glass (lunar sample 12052,336). (f) Small phenocrysts of zoned pyroxene in a silica glass, lunar sample 15597,75.

3.4. Fred's Flow

This flow was studied in detail by Arndt (1977) and Arndt & Fleet (1979). It is located in Munro Township in Ontario, approximately 70km east of Alexo and close to Pyke Hill where Abitibi komatiites were first described in detail by Pyke et al. (1973) and then studied by Arndt et al. (1977) and Arndt (1977). Fred's Flow is the type example of a thick differentiated mafic-ultramafic komatiitic flow. It is exceptionally thick (approximately 120m) and is strongly differentiated into a complexly zoned flow top, an interior gabbro and lower ultramafic cumulate. Its extrusive origin was recognized by Arndt (1977). Fred's Flow is made up of 5 units:

- a metre-thick flow-top breccia
- a 15m thick spinifex layer comprising an upper olivine spinifex zone underlain by a lower pyroxene spinifex zone
- a 40m thick gabbroic unit
- a 50m thick layer of pyroxene and olivine cumulates
- an olivine-poor marginal zone.

The extreme differentiation of this flow is reflected by the variation of MgO contents shown in Fig. 3.5. The parental komatiitic liquid is estimated to have contained 20% MgO, whereas the gabbro contains only 6% MgO and the olivine cumulate contains 45% MgO (Arndt, 1977). A recent petrographic study by Siegle (pers. comm.) shows that the spinifex layer comprises, from top to bottom: (1) a succession of layers of random and platy olivine spinifex (2) a layer of stringbeef pyroxene spinifex texture like that of the Alexo komatiitic basalt. Fred's Flow has chemical characteristics intermediate between those of the komatiites and komatiitic basalts (Arndt & Nesbitt, 1984). These authors reported series of observations that support magma mixing. For example, the presence of augite phenocrysts in the flow top breccia cannot be explained by a normal single komatiite magma crystallization. Instead, Arndt & Nesbitt (1984) proposed that the lava that initially erupted in Fred's Flow was a mixture between two liquids, one with a komatiitic composition, and another with basaltic composition. This idea of magma mixing was also suggested by Kinzler & Grove (1985), who explained the presence of the orthopyroxene cumulate by mixing between a low density evolved liquid in the lower part of the flow.

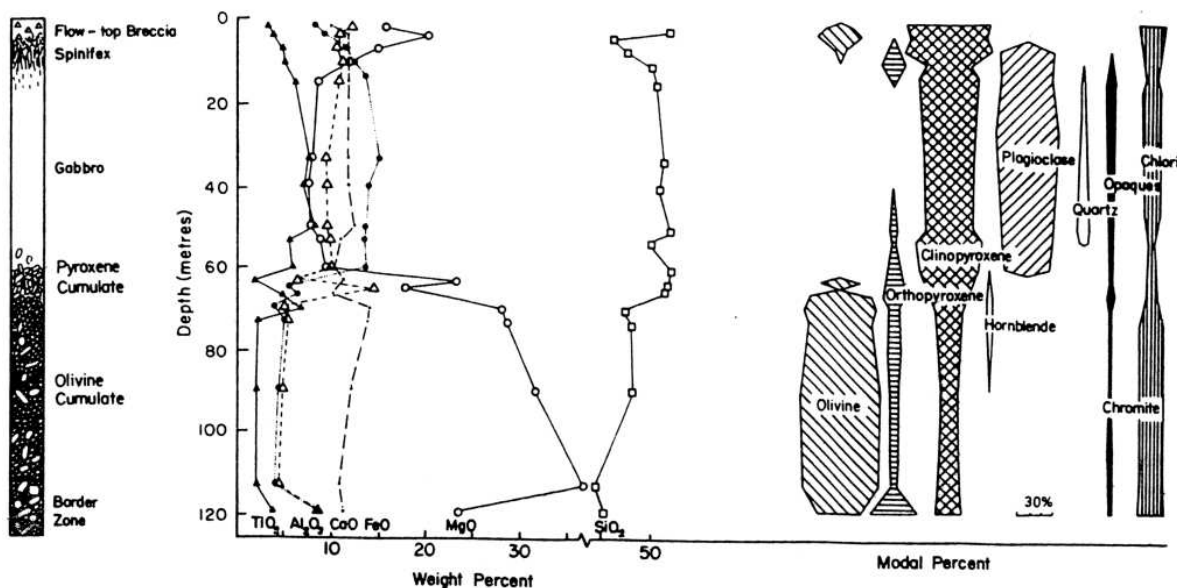


Fig. 3.5. Rock types, chemical and mineralogical variation in Fred's Flow (from Arndt, 1977).

In the flow top breccia and spinifex zones, augite (and chromite spinel) is the only non-altered mineral. Olivine altered to serpentine, chlorite, quartz or carbonate; pigeonite to chlorite; and plagioclase to albite or saussurite (Arndt, 1977). In gabbroic unit, clinopyroxene and orthopyroxene remain fresh, except at the base of the gabbro zone where patches of chlorite replace orthopyroxene. In cumulate zones, all orthopyroxene altered to chlorite. Olivine is still fresh in both zones.

In this thesis, Fred's Flow is used as a reference for the modeling of the solidification of a thick layered flow.

3.5. Komatiites from Barberton, South Africa

The name “komatiite” was proposed by the Viljoen brothers for their discovery of a new kind of ultrabasic rock, in reference to the Komati River which flows through the Barberton Greenstone Belt where the rocks were first found (Viljoen & Viljoen, 1969). These komatiites constitute the oldest komatiites known (the oldest komatiites in this region are at least 3.55 Ga old (Byerly et al., 1996) and they have an unusual chemical composition being characterized by relatively low $\text{CaO}/\text{Al}_2\text{O}_3$ ratio. The region is subdivided into several Formations. The Komati Formation is the lower stratigraphic unit and was recently mapped in detail by Dann (2000). In this formation, most komatiites are thick sheet flows and spinifex-textured flows are less abundant. According to Arndt et al. (2008), “komatiitic basalts, identified by their pyroxene spinifex texture, olivine-pyroxene-rich mineralogy and less magnesian chemical compositions, alternate with komatiites and tholeiitic basalts in the upper part of the Komati Formation”. Their state of preservation is much worse than that of the Abitibi komatiites, because their metamorphic grade is greenschist to amphibolite facies. In most samples all magmatic minerals have been replaced by secondary minerals and the textures are partially obliterated by recrystallization. In some samples, however, relatively unaltered pyroxenes are preserved and olivine cores are still fresh enough to be analyzed. Textures are well preserved and the proportion of magmatic minerals can be estimated.

The group led by Tim Grove of MIT have studied the Barberton komatiites over the past ten last years and have developed a model in which the magmas were emplaced as sills deep within a basaltic lava pile. On the basis of a series of petrologic and geochemical arguments (Grove et al., 1997, Grove et al., 1994, Grove et al., 1996, Grove et al., 1999, Parman et al., 1997, Parman et al., 2001, Parman et al., 2004, Parman et al., 2003), these authors proposed that the komatiites of Barberton were formed from a relatively cool hydrated magma that formed through melting in a subduction zone.

In chapter 6, we question whether pyroxenes in Barberton komatiites can be used to infer a hydrous setting of Barberton ultramafic melts.

3.6. Pigeonite Basalts of Apollo 12 and Apollo 15

The success of the Apollo missions made it possible to study lunar basalts for the first time. The samples brought back to Earth were subjected to intensive investigations in the 1970's and 1980's (BVSP, 1981, Papike et al., 1976), but few studies have been carried out using modern analytical techniques.

The basalts sampled by the missions Apollo 12 and 15 show similar mineralogical characteristics to komatiitic basalts. The basalts of Apollo 12 are divided into four rock series each characterized by one of the following index minerals: olivine, pigeonite, ilmenite and feldspar (BVSP, 1981). In olivine and pigeonite mare basalts, pyroxene has a skeletal morphology, and is often zoned from a pigeonite core to an augite margin (Fig. 3.4.c-f). These two characteristics are similar so those we observed in pyroxenes of the komatiites of Alexo

and Fred flows. The two magmatic series are thought to be co-magmatic and related by the fractionation of olivine (Papike et al., 1976).

The pigeonite basalts of Apollo 15 are similar with those of Apollo 12, and like them are related by olivine fractionation. Apollo 12 and Apollo 15 pigeonite mare basalts have MgO content from 7 to 20wt% with an average value of 11wt%. Pyroxene is the main silicate phase, followed by plagioclase. The sequence of crystallization may be comparable to that of komatiitic basalts (BVSP, 1981). According to Kushiro & Haramura (1971), the pyroxenes of Apollo 12 pigeonite basalts formed in the same way as that proposed for some komatiites, namely by rapid and metastable crystallization of a superheated liquid.

To study lunar pigeonite basalts is interesting, because these rocks form the unique totally fresh mafic rocks where pigeonite-augite zoning is present. In spite of their very old age, about 4 Ga (Canup & Asphaug, 2001), pigeonite has an exceptionally good state of preservation, due to very low temperatures and anhydrous conditions reigning at lunar surface.

Chapter 4. Methodology

The methods used in the experimental and analytical parts of the project are given in Appendix A (in French).

In the first part, the experimental procedures are described in detail. I explain why the CMAS system was used and show how I resolved some experimental problems encountered during the preparation of the starting material. A phase diagram for the pyroxenes is proposed, using both our isothermal experimental data and those compiled by Longhi & Boudreau (1980).

The isothermal experiments employed conventional techniques using a 1atm vertical quenching furnace. A second series of experiments were conducted in the thermal gradient in the upper part of the furnace, using the procedure developed by Faure et al. (2006).

In the second part, I list the procedures used during the in-situ analyses of pyroxene. Major elements were measured with the electron microprobe in Nancy and Mainz and trace elements were measured with the ion probe in Mainz. Bulk rock trace element data were obtained with ICPMS in Grenoble and bulk rock major element data were acquired with ICPAES in Nancy. For each instrument, the operating conditions and estimates of precision and accuracy are provided.



IMS-3f microprobe – Max Planck Institute for Chemistry, Mainz



Vertical furnace – CRPG, Nancy

Chapter 5. Petrography

The petrographic features of Alexo samples are summarized in Table 5.1 and illustrated in Fig. 5.1, 5.2 and 5.3. Brief account of the petrography is given in the paper submitted to Contribution to Mineralogy and Petrology (Chapter 6) and more detailed descriptions are given in French in Appendix B.

Table 5.1. Main petrographic features of Alexo samples that contain pyroxene

# éch.		Minerals	Ø (mm)	Size (mm) : max / avg	Vol. %	Features
Alexo komatiitic basalt	Ax104	pigeonite + augite		- / 5	40	Large zoned crystals
		pigeonite + augite		20 / -	30	Acicular zoned crystals with hollow core
		plagioclase oxides	ground- mass	3 / - - / -	25 5	Intergrown with augite. Rims of crystals are altered to a secondary mineral
	Ax101	pigeonite + augite	0,2-1	45 / 25	40	Acicular zoned and twinned megacrysts
	Ax102	augite	groundmass	2 / -	30	Plumose crystals with nucleation sites in the groundmass or on megacrysts
		plagioclase oxides		0,4 / - - / -	25 5	Intergrown with augite
		pigeonite + augite	0,3-1	40 / 20	20	Acicular zoned megacrysts – Pigeonite is altered to chlorite
	Ax103	augite	groundmass	1 / -	40	Plumose crystals with nucleation sites in the groundmass or on megacrysts
		plagioclase oxides		- / -	10	Intergrown with augite
		secondary minerals		- / -	5	Fine-grained phyllosilicates, quartz
Alexo komatiite	Ax105	pigeonite + augite	max 1	- / -	20	Acicular zoned crystals – Pigeonite is altered to chlorite
		augite	groundmass	- / -	40	Plumose texture
		plagioclase oxides		- / -	35	Intergrown with augite
	Ax106	olivine	0,1-0,2	50 / 30	15	Platy olivine + dendritic crystals
		pigeonite + augite	0,1-0,2	30 / -	60	Dendritic zoned and twinned crystals + zoned needles
		pyroxene + plagioclase chromite	ground- mass	1 / - 1 / -	25	Intergrown crystals with plumose texture Dendritic crystals – nucleation near olivine
		olivine	0,1-0,2	8 / 4	5	Dendritic crystals
		pigeonite + augite	0,1-0,4	>30 / -	70	Dendritic zoned and twinned crystals + zoned needles
		pyroxene + plagioclase chromite	ground- mass	0,4 / - 0,8 / -	25	Intergrown crystals with plumose texture Dendritic crystals – nucleation near olivine

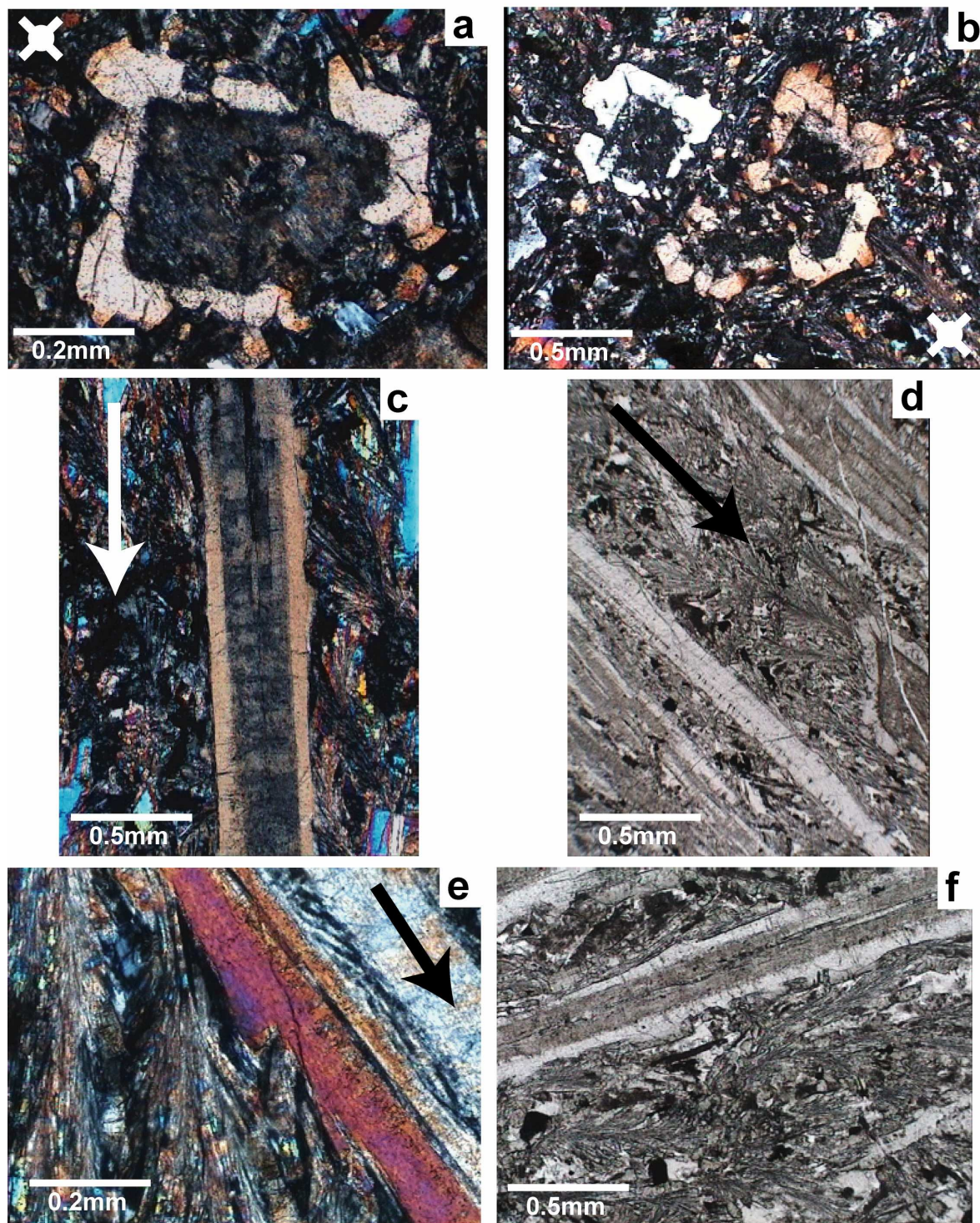


Fig. 5.1. Photomicrographs of representative thin sections of the upper part of Alexo komatiitic basalt (samples Ax101-102). (a-b) Basal sections (cut perpendicular to the flow top) of acicular zoned crystals of pyroxene (polarized light); augite rim is fresh but pigeonite core altered to chlorite. (c) Twinning in a zoned crystal; the arrow shows the bottom of the flow. (d) Zoned pyroxene megacrysts and plumose clinopyroxene in the groundmass. (e) Nucleation of plumose clinopyroxene on a pyroxene megacryst. (f) Nucleation of plumose clinopyroxene in the groundmass.

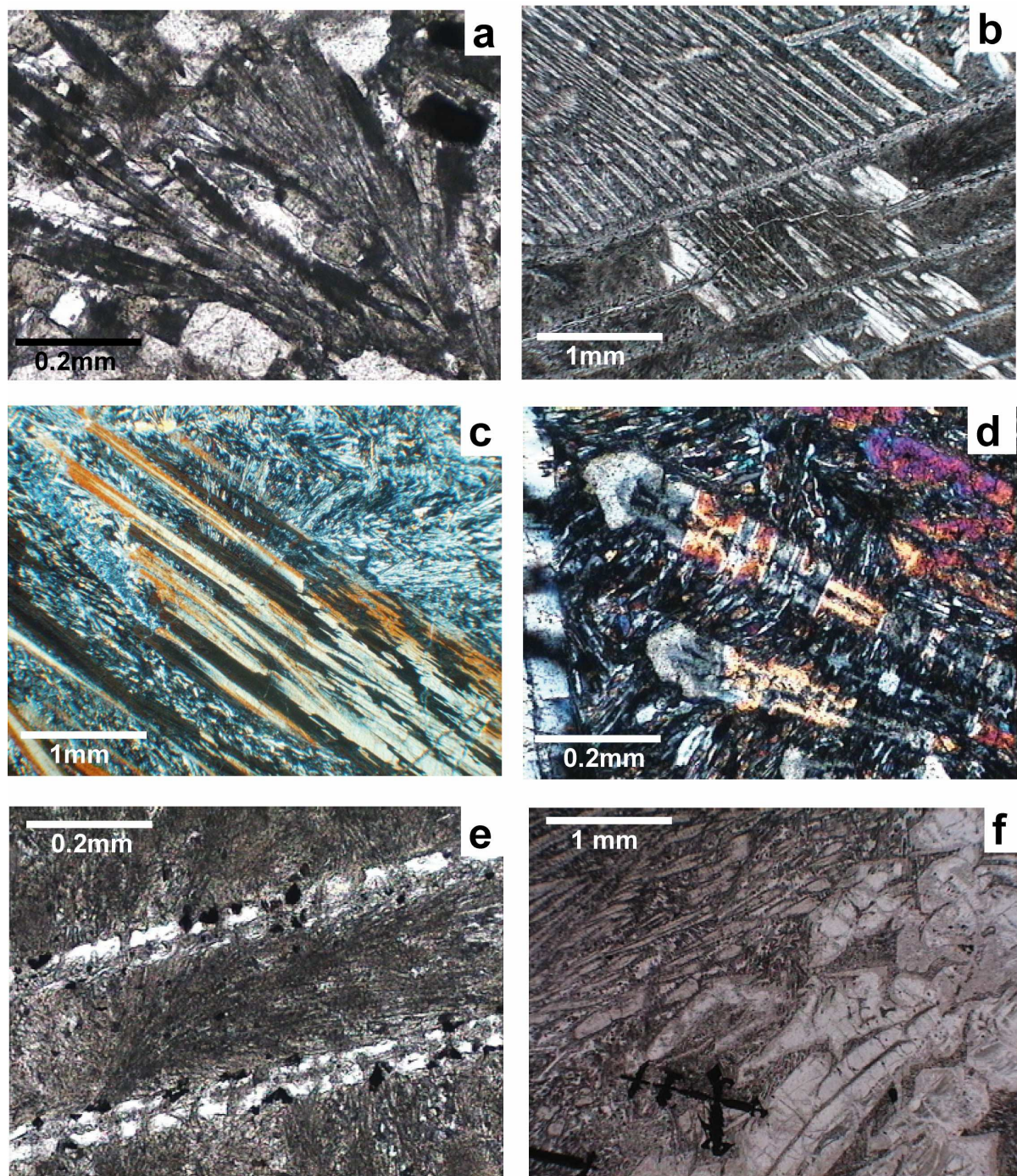


Fig. 5.2. Photomicrographs of thin sections of Alexo komatiitic basalt (sample Ax102) and A3-layer of Alexo komatiite (sample Ax105). (a) Intergrowth of clinopyroxene and plagioclase in the groundmass, Ax102. (b) Acicular zoned crystals of pyroxene perpendicular to parallel plates of olivine, Ax105. (c) Complex zoned crystal of pyroxene: acicular dendrites show parallel alignment (pigeonite in white, augite in orange, sample Ax105). (d) Hollow dendrites of small zoned crystals of pyroxene. (e) Plumose clinopyroxene growing between two plates of spinifex olivine. Chromite crystallizes near the olivine. (f) Massive dendritic olivine (on the right) surrounded by acicular crystals of pyroxene and cruciform chromite (sample Ax105).

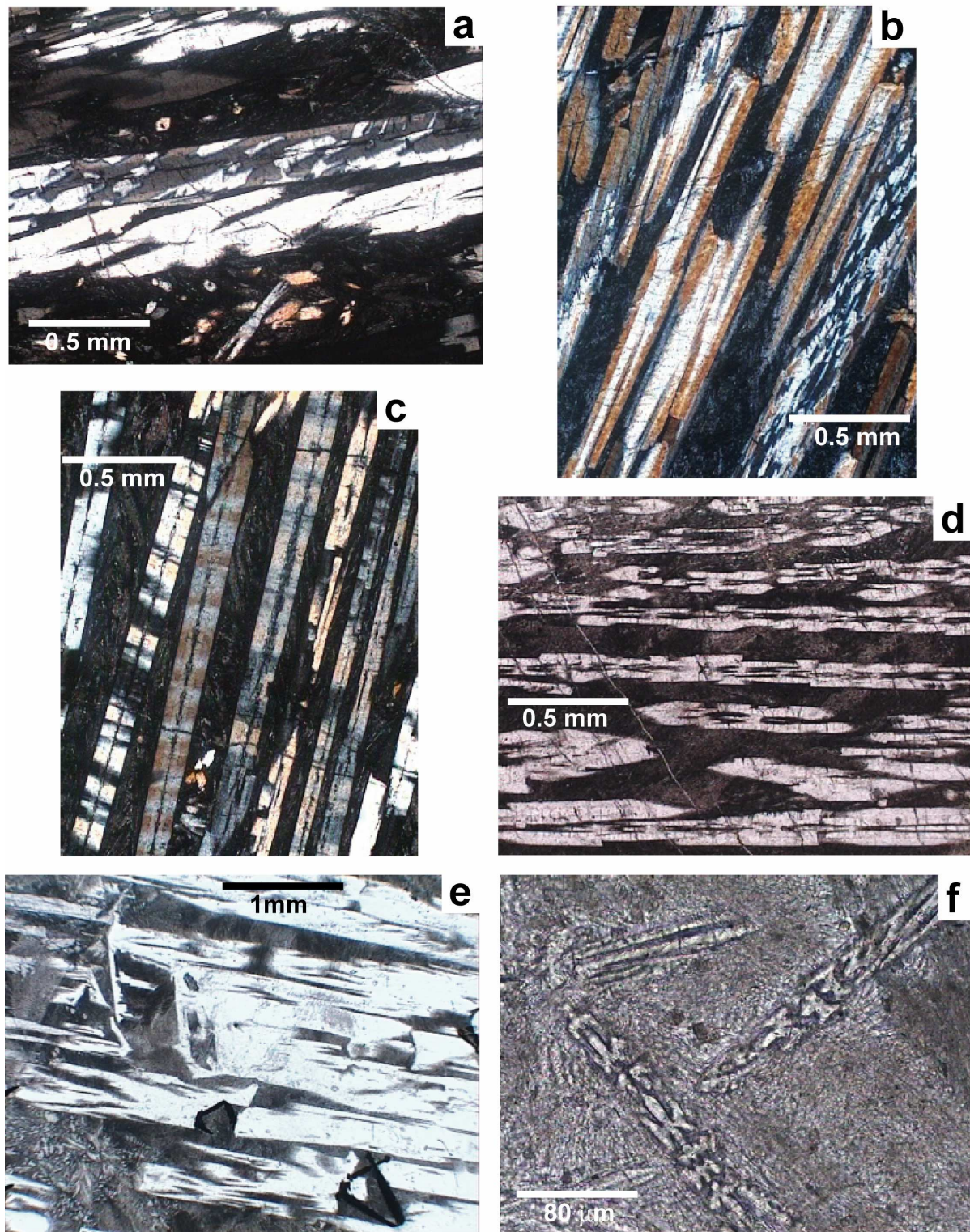


Fig. 5.3. Photomicrographs of thin sections of Alexo komatiite (sample Ax106) (a,b) “Screw” structure of acicular zoned pyroxene. (c) Twinning of acicular pyroxene. (d) Dendritic clinopyroxene showing a “step” structure. (e) Complex dendritic crystals of olivine and cruciform chromites. (f) Small dendritic crystals of clinopyroxene in the groundmass.

Chapter 6:

Crystalllochemistry and origin of pyroxenes in komatiites and lunar basalts

S. Bouquain¹, N.T. Arndt¹, E. Hellebrand² and F. Faure³

¹LGCA, CNRS UMR 5025, Université J. Fourier, BP53, 38041 Grenoble Cedex, France

²Department of Geology and Geophysics, University of Hawaii, 1680 East-West Road, Honolulu, Hawaii 96822, USA

³Nancy Université, CNRS/INSU, CRPG, 15 rue Notre Dame des Pauvres, 54501 Vandoeuvre-les-Nancy, France

Corresponding author:

sebastien.bouquain@ujf-grenoble.fr; Tel: +33476514063; Fax: +33476514058

Keywords: pyroxene; pigeonite; komatiite; lunar basalt; spinifex

Submitted to Contribution to Mineralogy and Petrology

Abstract

Pyroxenes in spinifex-textured komatiites and some lunar basalts commonly are zoned with cores of pigeonite and rims of augite. Concentrations of incompatible trace elements are low in pigeonite and jump to higher values in the augite mantles. In lunar pyroxenes, B, Li and Be retain magmatic profiles like the rare earth elements (REE) but in komatiites the pattern is disrupted by alteration. Crystallization paths are very different in different parts of two komatiitic flows in Alexo, Canada. In the flow top, the sequence is olivine followed by augite; deeper in the flow it is olivine-pigeonite-augite. Pigeonite crystallization is enhanced in spinifex lavas, perhaps as a result of constrained growth and Soret differentiation. Augites in Al-undepleted Archean komatiites in Canada and Zimbabwe have high moderate to high Wo contents but their Mg# ($Mg/(Mg+Fe)$) are lower than in augites in Barberton komatiites. Rather than attributing the high Wo and Mg# to crystallization from hydrous magma, we relate the higher Mg# of the Barberton augites to the unusually high CaO/Al_2O_3 of these Al-depleted komatiites.

1. Introduction

Three types of pyroxene occur in komatiites. The most common is augite, which is found in almost every komatiite as the main component of pyroxene spinifex textures, as fine acicular grains in the matrix, or as cumulus grains in differentiated flows. It also coexists with plagioclase in komatiitic basalts (Arndt 1977; Arndt and Fleet 1979; Fleet and MacRae 1975; Pyke et al. 1973). Pigeonite has a more restricted occurrence, but in well-preserved samples it is commonly present in the interiors of zoned pigeonite-augite needles in pyroxene spinifex textures, or, more rarely at the borders of augite crystals (Shimizu et al. 2005). Orthopyroxene is rare, being restricted to the cumulate layers of some differentiated flows, or, in exceptional cases, to the interiors of zoned needles in spinifex textures (Bickle et al. 1993). It also is a major phase, together with augite, in unusual silica-rich komatiites from South Africa (Wilson 2003).

The general characteristics of pyroxene in komatiites have been documented by Fleet (1975) and Arndt and Fleet (1979). Campbell and Arndt (1982) noted a discrepancy between sequence of crystallization of Ca-pyroxenes in komatiitic lavas, as inferred from variations in whole-rock compositions, and the 1-atmosphere phase relations of representative samples. They attributed this difference to the accumulation of pyroxene during the growth of spinifex texture. Kinzler and Grove (1985) then undertook a detailed experimental study that established the phase relations and crystallization sequences of samples with compositions representing those of parental magmas of a thick layered komatiite flow. To explain the compositions of pyroxenes in these lavas, they called on departures from equilibrium trends in the rapidly-cooled upper part of the flow, combined with the effects of magma mixing or contamination.

Up to this time, komatiites had been interpreted as lava flows and the pyroxenes had been thought to crystallize at low pressures under near-surface conditions. An alternative interpretation was given in a series of papers by Parman, Grove, de Wit and co-authors (Grove et al. 1997; Grove et al. 1999; Parman et al. 1997) who suggested that komatiites from the Barberton greenstone belt in South Africa crystallized from hydrous magma that had intruded as sills at a depth of around 6 km in the volcanic lava pile. One of the main lines of evidence in support of this hypothesis was the composition of the augite in Barberton

komatiites. Parman et al. (1997) undertook experiments at 0.1 MPa on anhydrous samples and at 2 MPa on water-saturated samples, and they found that compositions of the augite in the komatiites most closely matched that of the pyroxene that crystallized in the hydrous experiments. The key parameter is the Wo content of the augite, which is high in both the pyroxene from the hydrous experiments and in the analyses of natural augite in the Barberton komatiites. Both types of pyroxene plot separately from the pyroxene that crystallized in the anhydrous experiments, which have lower Wo contents. The high Wo contents of Barberton augites is consistent with crystallization at relatively low temperatures from hydrous komatiite, and this relationship led to subsequent models in which Barberton komatiites were proposed to have formed in a subduction environment (Grove and Parman 2004; Parman et al. 2001; Parman et al. 2004).

Although an intrusive origin of the Barberton komatiites has subsequently been called into question by the detailed mapping of Dann (2000; 2001), the high Wo contents of the augites have not been explained. In this paper, we compare their compositions with those of pyroxenes in other komatiite flows. Most of the data come from the study of two well-preserved flows from the Alexo area in the Abitibi Belt in Canada, and we augment these data with information from other Archean and Proterozoic flows. We also report major and trace element data from pyroxenes in lunar basalts.

Drawing on the results of an experimental study of pyroxene crystallization reported in a companion paper (Bouquain *et al.*, in prep), we then show that the specific compositions of the Barberton pyroxenes are related in part to the unusual composition of the Barberton lavas and in part to their conditions of emplacement. We go on to discuss in more detail the factors that control the crystallochemistry, and the major and trace element compositions, of pyroxene in komatiites and other highly magnesian rocks.

2. Geological Background

In this paper, we present new electron and ion microprobe analyses of pyroxenes in Archean komatiites and lunar basalts. The Archean rocks are the main focus of the paper, for the reasons discussed above. The lunar rocks contain pyroxenes that have morphologies and compositions similar in many ways to those in komatiites. They are included as a reference because these samples are not subjected to the alteration and metamorphism that complicates study of the Archean samples, and because they crystallized from a magma that was undoubtedly anhydrous.

The Archean komatiites are from Alexo, in the Abitibi Greenstone Belt, about 50 km to the east of Timmins in northern Ontario, Canada. These rocks form part of the Stauton-Roquemaure Group, a sequence of mainly tholeiitic basalts and sedimentary units intruded by large mafic-ultramafic sills. The sequence has been dated using the U-Pb zircon method at 2719-2710 Ma (Ayer *et al.* 2002). The rocks have been subjected to prehnite-pumpellyite facies metamorphism (Jolly 1982) and now dip steeply to the northwest. More complete descriptions of the geological setting are found in Naldrett and Mason (1968), Barnes (1983) and Ayer *et al.* (2002).

Two flows in the Alexo area have been closely studied by Barnes (1983), Arndt (1986) and Lahaye *et al.* (1996) (Fig. 1). The first is a 16-m thick komatiite flow, comprising a hyaloclastite flow-top breccia, a thin chilled margin, an olivine spinifex layer, and a lower olivine cumulate layer (B zone). The olivine spinifex layer contains an upper unit of random olivine spinifex, an intervening zone of chevron spinifex and a lower layer of coarse platy spinifex. The second flow has a less magnesian komatiitic basaltic composition and is made up of a thin (4m) upper pyroxene spinifex layer overlying a much thicker (50m) unit

composed mainly of olivine cumulate with a thin interlayer of orthopyroxene cumulate. The uppermost part of this unit may have been removed by erosion during emplacement of the overlying komatiite (Dupré et al. 1984).

As in most komatiites, olivine is the liquidus phase, followed by chromite, and pyroxene crystallizes at lower temperatures. The textures and morphology of the olivine and chromite have been described in the publications cited above and here the emphasis is on the pyroxene, which occurs in several different situations.

In the olivine spinifex textured upper part of the komatiite flow, augite forms small skeletal crystals embedded in a (now altered) glassy matrix between randomly oriented olivine blades. In the extremely coarse platy olivine spinifex textured lava just above the olivine cumulate, large complex olivine plates, up to 70 cm long, enclose polyhedral “cells” in which trapped liquid has crystallized to an assemblage of large pigeonite-augite needles, smaller augite grains, and interstitial plagioclase (Fig. 2). Chromite occurs as skeletal, millimetre-sized crystals mainly at the margins of olivine blades. The smaller cells contain randomly oriented augite grains in a glassy matrix, just as in samples from higher in the flow. In the larger cells, the pyroxene needles are oriented parallel to one another and are distinctly zoned with pigeonite cores and augite margins. The largest pyroxene needles are 3cm long and about 0.2 mm wide.

The uppermost part of the spinifex zone of the komatiitic basalt flow contains randomly orientated zoned pigeonite-augite crystals with subhedral outlines, commonly 2mm in width. These zoned crystals coexist with smaller grains of augite and laths of plagioclase. In the centre of the pyroxene spinifex zone, large acicular crystals of zoned pyroxene, commonly 0.5mm in width and at least 3mm in length, are oriented perpendicular to the flow top. A second generation of pyroxene (augite) is intergrown with plagioclase, commonly with a plumose structure. In the lower part of the spinifex zone, pyroxene is less abundant and occurs as randomly oriented prismatic grains intergrown with small laths of plagioclase.

The morphology of the large zoned pyroxene needles, supported by analytical data presented later in the paper, indicate that hollow, elongate grains of pigeonite crystallized first and that augite grew later, both on the outer margin and in the hollow centres of the crystals (Arndt and Fleet 1979). The pyroxene needles are organized into colonies of individuals, oriented roughly parallel to one another in near-perfect optical continuity.

Most of the magmatic minerals in the spinifex lavas are partially to completely replaced by secondary minerals (Lahaye and Arndt 1996). The exceptions are chromite and augite, which are rarely altered. Olivine is partially replaced by serpentine or chlorite depending on the position in the flow. In most samples, pigeonite is replaced by chlorite but in samples from the cells between olivine plates in the olivine spinifex zone, a large proportion of the pigeonite is preserved. These rocks provided the samples that we analysed in detail in this study. More specifically, we analysed two samples that contain abundant fresh pigeonite in the cores of zoned crystals from the lower part of the spinifex layer in the komatiite flow (M668-Ax105-106) and four samples with rare relicts of pigeonite from the upper spinifex zone of the komatiitic basalt (Ax101-104). Sample locations are shown in Fig. 1.

For the study we analysed in detail, using electron and ion microprobe, the best-preserved pigeonite-augite needles from the cells in the coarse olivine spinifex lava from the komatiite flow (samples Ax105-106). We supplemented this information with analyses of pyroxenes in other parts of both komatiitic flows and from komatiitic rocks from other regions.

The lunar basalts analyzed in this study are from the Apollo 12 and Apollo 15 missions. Four samples of pigeonite-bearing basalts were chosen in the NASA collection, all of which contain extremely fresh crystals of zoned pyroxene. The Apollo pigeonite basalts have radiometric ages of 3260 Ma (Apollo 12) and 3340 My (Apollo 15) (BVSP 1981). In three

samples (12021, 15495 and 15597), pigeonite is the first silicate to crystallize. Sample 12052 has olivine on the liquidus and contains about 4% of olivine in mode (Papike et al. 1976). The Apollo 12 pigeonite basalts are slightly vesicular and highly porphyritic, characterized by large, zoned phenocrysts of pyroxene. Pyroxene occurs as subhedral lathlike grains with fractured cores of pigeonite mantled by augite that is zoned to pyroxferroite (Papike et al. 1976). These authors noted little chemical evidence for near-surface fractionation and concluded that Apollo 12 pigeonite basalts probably represent samples from a single, relatively thin cooling unit. Samples 12021 and 12052 contain pyroxenes with similar chemical compositions, the former being the coarsest sample of the Apollo 12 pigeonite basalt suite. Papike et al. (1976) estimated cooling rates between 1 and 5°C/hr. Bence et al. (1970) determined the major and minor element compositions of the bulk rocks and Shearer et al. (1989) analysed the rare earths and several other trace elements.

The Apollo 15 pigeonite basalts are strongly porphyritic lavas characterized by composite pyroxene phenocrysts with pigeonite cores and augite mantles (Papike et al. 1976). Sample 15495 consists of coarse phenocrysts of pyroxene (with pigeonite cores and augite rims, up to 2.5cm long) embedded in a fine-grained groundmass of pyroxene, plagioclase, opaque phases and glass. On basis of comparisons between phenocryst morphologies and results from dynamic cooling experiments, Lofgren et al. (1975) estimated a cooling rate of 1-5°C/hr and concluded that this rock crystallized in a two-meter-thick flow extruded without phenocrysts. The pigeonite basalt 15597 is a well-known sample that has been the subject of several studies (Grove and Bence 1977; Grove and Raudsepp 1978; Lofgren et al. 1975; Weigand and Hollister 1973). It is a fine-grained pigeonite basalt, displaying small phenocrysts of zoned pyroxene, without preferential orientation, in a groundmass of silica-rich glass. According to Lofgren et al. (1975), this sample has the most rapidly cooled groundmass of the Apollo 15 basalts. This rock experienced a complex cooling history: an initial period of slow initial cooling rate was followed by a rapid cooling. On basis of minor element contents, Grove and Bence (1977) proposed that the pyroxene cores of 15597 crystallized under sub-equilibrium conditions near the lunar surface.

In our study, we performed two or more detailed profiles in zoned pyroxenes in each sample using the electron probe, focusing on sample 15597 but including some analyses of sample 12052. We also determined trace element (REE, K, Sr, Y, Zr) and light element (Li, Be, B) contents using the ion microprobe.

3. Analytical methods

The beam size of the electron microprobe is sufficiently small that the size of the crystals is not restrictive and we were able to obtain several high precision core-to-rim profiles for zoned pigeonite-augite crystals. In most cases the profiles were oriented roughly perpendicular to c axis and the distance between analyses was 10 microns. Representative data are given in Table 1. The beam of the ion probe is far larger (12 µm), and we were able to analyse at most six analyses on a same profile. Cases where the electron beam penetrated into the material underlying the crystal we detected using stoichiometry and were discarded. Alteration was identified using the Ba/K ratio, which is abnormally high or low in regions where the pyroxene is partially replaced by secondary phases. Comparison of regions with different Ba/K ratios allowed us to investigate the influence of alteration on trace elements patterns.

Pyroxenes were analysed *in-situ* for major elements at the University of Mainz and at the University of Nancy. In Mainz, we worked on a five-spectrometer JEOL JXA 8900RL electron probe microanalyser (EPMA) using an acceleration potential of 20 kV, a beam

current of 20 nA and a spot size of 2 μm . Counting time was 30 s for major elements and 60 s for minor elements. In Nancy, we used a CAMECA SX100 electron probe, with an acceleration potential of 15 kV, a beam current of 10 nA and a spot size of 2 μm .

Trace elements (selected REE as well as Li, Be, B Sr, Y, and Zr) were analyzed using secondary ion mass spectrometry on an upgraded Cameca IMS-3f in Mainz. Spots were selected for ion microprobe analysis after detailed petrographic and electron microprobe study. Negative oxygen ions were used as primary ions, (accelerating potential of 12.5 kV and 4 nA beam current). The spot size for these operating conditions was \sim 12 μm . Positive secondary ions were extracted using an accelerating potential of 4.5 kV with a 25 eV energy window, a high-energy offset of -80 V, and fully open entrance and exit slits.

Detailed explanations of the procedure can be found in (Hellebrand et al. 2002). The differences between both analytical methods are listed below. 1) Each measurement consisted of a six-cycle routine, where in each cycle the species ^{16}O , ^{23}Na , ^{30}Si , ^{39}K , ^{40}Ca , ^{88}Sr , ^{89}Y , ^{90}Zr , ^{138}Ba , ^{139}La , ^{140}Ce , ^{141}Pr , ^{146}Nd , ^{147}Sm , ^{153}Eu , ^{157}Gd , ^{163}Dy , ^{167}Er , ^{174}Yb , ^7Li , ^9Be and ^{11}B were analysed in this order. In each cycle, La, Sm and Be were measured for 60 seconds, Ce, Pr, Nd and Eu for 40 s, Gd, Er, Yb and B for 30 s, Ba and Dy for 20s, Sr and Zr for 15 s, Y for 8 s, K and Li for 5 s and the other elements for 1 s. 2) In order to minimize surface B contamination, thin sections were cleaned using ultrasonic baths of alcohol and ultra pure water during 10 minutes, and rinsed in B-free distilled water. Then they were promptly gold-coated. All the samples were analyzed in a continuous session, with a standard measurement twice a week (showing no critical variations). The standard was komatiite glass GOR-132-G (Jochum et al. 2000). 3) We used an additional procedure to combat B contamination, on basis of the method Herd *et al.* (2004). A 20nA beam current was applied during 5 minutes on the selected area, burning the area before starting the measurement. We used this additional method on sample #Ax101.

4. Results

4.1. Komatiites

Representative major and trace element data of pyroxenes in komatiites are presented in Table 1. In a diagram of Mg# vs Wo content (Fig. 4), the zoned pyroxene grains from the Alexo komatiite flow plot in three broad fields: the pigeonite cores, the augite mantles and mixtures between both pyroxenes. The smaller grains from the matrix have lower Mg# and mid- to low-Wo content and plot to the right of the other pyroxenes. In pigeonite, Mg# ranges from 0.86 to 0.77 and Wo contents from 6 to 21, with an average at about Mg#=0.84, Wo=10. Some of the pigeonite analyses with the highest Wo contents in Fig. 4a are mixed signals from juxtaposed pigeonite and augite, due to beam depth of the electron probe. In augite, Mg# ranges from 0.82 to 0.63 and Wo contents from 26 to 42. Figures 4b and c show profiles in two individual zoned pyroxene grains. The profile in Fig 4b shows almost no variation of Mg# and Wo in the pigeonite core and a slight increase of Wo content as Mg# decreases from the inner to outer part of the augite rim. Variations in augite compositions are almost identical in both sides of the crystal. In the profile in Fig 4c, the pigeonite composition varies from low Wo-low Mg# to medium Wo-medium Mg#. In the same crystal, the augite displays no variation in Wo content as Mg# decreases from inner to outer margin. Mg# decreases gradually except in both last points where Mg# drops more abruptly. Also plotted is an analysis of orthopyroxene from the orthopyroxene-rich layer in the Alexo komatiitic basalt flow. This orthopyroxene is highly magnesian, displaying an Mg# of 0.88.

4.2. Lunar pyroxenes

We analyzed in detail three grains from sample 12052, five grains from sample 15597, one grain from sample 15495, and several isolated grains. As seen in the Mg# vs Wo diagrams (Fig 5), lunar pyroxenes are more Fe-rich than those in Alexo komatiites and their maximum Mg# are no greater than 0.74. Due to different cooling histories, the zoning patterns of pyroxene grains are slightly different from one sample to another. Pyroxene grains from 12052 show the strongest Ca-Mg-Fe zoning with a trend of Ca enrichment and Mg depletion from pigeonite to augite, and a trend of Fe enrichment and Ca depletion to pyroxferroite (Fig. 5.a-d). The first pyroxene to nucleate (“inner pigeonite”) has a composition of Wo₉En₆₃Fs₂₈, and is zoned to Wo₂₀En₅₃Fs₂₇ (“outer pigeonite”). Pigeonite is rimmed by augite of average composition Wo₃₆En₄₁Fs₂₃, which is sometimes zoned to pyroxferroite (Fig. 5.b). The two profiles of Fig. 5c,d do not show a normal trend from augite to pyroxferroite. These crystals do not have sharp borders and their edges are crenulated, reflecting rapid growth of the late-stage pyroxene. This may be the cause for both abnormal profiles. Pyroxene from 15597 has a very Ca-poor, Mg-rich core and a Ca-rich rim (Fig. 5. a,e-h), similar to the compositions obtained in the similar samples by Weigand and Hollister (1973). Both cores and rims display extreme chemical zoning. The inner pigeonite has the extreme composition of Wo₅En₇₀Fs₂₅, and falls within the range of orthopyroxene. However, Brown and Wechsler (1973) identified the mineral as pigeonite using single-crystal X-ray studies. Outwards from the core, the composition changes first to outer pigeonite (average Wo_xEn_yFs_z) then to Ca-rich pyroxene (“inner augite”), and finally to a very Mg-poor ferroaugite (“outer augite”). The ferroaugite has about the same Wo content as “inner augite”, except for one grain (Fig. 5. e).

Weigand and Hollister (1973) report a composition of ~Wo₁₅En₅₂Fs₃₃ for outer pigeonite and ~Wo₃₀En₄₀Fs₃₀ for inner augite. We obtained slightly higher Wo contents: ~Wo₂₂En₄₈Fs₃₀ for outer pigeonite and ~Wo₃₈En₃₂Fs₃₀ for inner augite. The intermediate composition measured in one grain (Fig. 5g) may be due to sector zoning of pigeonite, particularly in hollow crystals, as reported by Weigand and Hollister (1973). Intermediate compositions in two other grains (Fig. 5e,h) may be mixtures of pigeonite and augite. A pyroxene grain from sample 15495 shows a large compositional gap between its pigeonite core, which has an average composition of Wo₆En₆₇Fs₂₇, and its augite rim, which has the composition Wo₂₈En₂₂Fs₅₀.

We did not analyze pigeonite in sample 12021, focusing our analysis on the augite rim. Thus we only observed a trend of Fe enrichment and slight Ca depletion from “inner augite” to “outer augite”.

5. Zoning profiles

5.1. In komatiites

The profile across a pyroxene grain in sample Ax106 (Fig. 6) shows pronounced core-to-rim zoning: a core of highly magnesian pigeonite is surrounded by a mantle of Ca-rich augite. At the contact between core and mantle, the Ca (or Wo) content increases and Mg content decreases, in both cases abruptly. In contrast, Mg# and Cr contents decrease continuously from the centre of the pigeonite core to the outer rim of the augite margin, from 1.5% to a few ppm in the case of Cr, with no discontinuities at the pigeonite-augite contact. Al₂O₃ and TiO₂ contents are relatively flat in the pigeonite core (Al₂O₃ varies only from 3.5 to 2.5% and TiO₂ from 1.3 to 1%) but increase steadily in the augite mantle, from 3.5 to 10.5 wt% for Al₂O₃ and from 0.1 to 0.8 wt% for TiO₂. The analysis in the middle of the crystal has a composition intermediate between that of pigeonite and augite: this analysis probably sampled a mixture

between a thin lamella of augite (seen clearly in the back-scattered electron image; Fig. 6) and the surrounding pigeonite. The augite could be part of an inner veneer of augite that lined the interior of an initially hollow pigeonite grain. The most primitive pigeonite in this profile is located on both sides of this point where CaO values are lowest and Cr₂O₃ highest.

In Fig. 6 we plot the concentrations of three representative rare earth elements, La, Sm and Yb, and the light elements Li, Be and B. The analyses were made along the same profile as for the major elements. Rare earth element contents vary as predicted by Rayleigh fractionation: the core of pigeonite (points from #2 to 5) is less enriched in REE than the augite rim (points #1 and 6). Concentrations of Yb are higher than those of Sm and La because of the higher compatibility of heavy rare earth elements in pyroxene.

Figure 7 shows representative mantle-normalized trace-element patterns of two augites and three pigeonites in sample Ax105 of the Alexo komatiite. These patterns include commonly analyzed rare earth elements (La, Ce, Pr, Nd, Sm, Eu, Gd, Dy, Er, Yb) and some other incompatible elements; Sr, Zr and Y. The patterns for augite show moderate depletion in light rare earth elements (LREE) and a flat slope for the heavy rare earth elements (HREE). In pigeonite, the concentrations of trace elements are far lower and the patterns are almost linear from La to Yb. Negative Sr anomalies are present in augite but not in pigeonite.

The profiles of light elements in Fig. 6 do not show any evidence of differential partitioning between pigeonite and augite. The Li profile is nearly flat, and that of Be shows only a slight increase towards the rims of the pyroxene grain (points #1, 2 and 6). These patterns are very different from those measured in pyroxene in the lunar basalts (described below), which raises the possibility that these elements were mobile during the alteration that affected the komatiites.

5.2. In lunar basalts

Figure 8 shows profiles across a pyroxene grain in the lunar pigeonite basalt sample #12052; the major and trace element data are presented in Table 1. The large variations of Mg# and Wo content of this grain are shown in Fig. 5b. The point at 150 µm is the first pyroxene to nucleate, and that at 340 µm on the right side is the last. From 150 µm to 230 µm, within the pigeonite core, CaO increases dramatically, MgO decreases slightly and the concentrations of other elements remain essentially constant. Between 230 µm and 240 µm, in the augite margin, the trends are repeated: CaO increases and MgO decreases and the other elements remain constant but at a higher level than in the pigeonite. The exception is Al₂O₃, which increases progressively from interior to exterior of the augite mantle. From 300 µm to 340 µm, in the pyroxferroite outer margin, the concentration of every element is lower, except for FeO which climbs to 42wt% and Ca which first increases and then decreases in the outer rim.

Variations in Sm and Yb contents distinguish clearly the low-Ca pigeonite core and the augite rim. The trace element contents in the pigeonite core are much lower than in the augite mantle due to a combination of normal fractionation effects and different partition coefficients for pigeonite and augite. As for the pyroxene in the Alexo komatiite, the HREE (represented by Yb) are more compatible than LREE (as represented by La), in both pigeonite and augite.

The profiles for Li, Be and B show strong evidence of contrasting partitioning behaviour for each of the three elements and for both pyroxenes. Boron contents are low in the pigeonite core and augite mantle whereas Li and Be behave like the REE. The concentrations of the latter two elements are far higher in augite than in pigeonite and the concentrations increase progressively and strongly toward the margins.

6. Modelling of compositional variations

Figure 9 shows the results of our modelling of the variations of the CaO and Cr contents of zoned pyroxenes in komatiites; and Fig. 10 shows the modelled variations of two rare earth elements. To realize these models, we first assumed that the magma that crystallized the pyroxenes had the composition of sample M668, the coarse olivine spinifex lava sampled at the same location as sample Ax106 and analyzed by Arndt (1986) (Table 2). We assumed that crystallization started with olivine (and minor chromite), then continued with pigeonite alone, then augite alone, and finally augite and plagioclase. We used two approaches to estimate the proportions of each phase. First we used the modal proportions, as measured by quantitative analysis of the images of thin sections and polished slabs. This approach provided relatively imprecise data because of the large and irregular size of the olivine crystals: the best estimate is that 30 to 50% olivine crystallized before pigeonite appeared. From analysis of images of zoned pyroxene needles, we estimated that ~20% of pigeonite crystallized before augite started to crystallize.

The second approach was to model incremental batch fractionation. We used Mg-Fe distribution coefficients between the olivine or pyroxene and liquid, and the measured compositions of these minerals, to estimate the composition of the liquid at the first appearance of each new mineral. Arndt (1986) reported that the most forsterite-rich olivine in the flow has the composition $Fo_{94.1}$ and that this mineral is in equilibrium with a liquid containing 28% MgO — that of the chilled margin of the flow, if a Mg-Fe distribution coefficient ($(MgO/FeO)_{liq}/(MgO/FeO)_{ol}$) of 0.33 is used and if Fe^{3+} is assumed to represent 10% of the total iron. A similar approach can be adopted for pigeonite and augite. The most magnesian pigeonite that we measured has an Mg# of 0.86. Adopting a distribution coefficient of 0.30 and assuming again that Fe^{3+} constitutes 10% of the total iron, we calculated that this mineral would be in equilibrium with a liquid with an MgO/FeO of 0.967. We then calculated how MgO/FeO changes during fractional crystallization of olivine in a liquid with the composition of sample M668. To do this we used MINSUB, a simple program in which small increments (1-2%) of olivine are sequentially subtracted from the liquid until a target composition is reached. (Commonly used programs like MELTS do not reproduce the correct compositions for pigeonite and augite). After each step, a new equilibrium olivine composition is calculated and this composition is then subtracted from the liquid. Using this approach, we estimated that 38% olivine had crystallized at the onset of pigeonite crystallization.

The next step was to estimate the MgO/FeO of the liquid at the onset of augite crystallization, using 0.82 as the Mg# of the most magnesian augite and 0.30 for the MgO-FeO distribution coefficient. The variation of MgO/FeO induced by pigeonite fractionation was calculated using MINSUB and from this we estimated that 54% of the liquid had solidified at the onset of augite crystallization. Finally, we estimated that 80% of the liquid had solidified when plagioclase first started to crystallize. In summary, the crystallization sequence is: olivine (+ minor chromite) – 0 to 38%; pigeonite – 38 to 54%; augite – 54 to 80%.

Using the results of MINSUB modelling for the major elements and Shaw's (1970) equations for the trace elements, we calculated how the liquid composition changed during the course of crystallization. Finally, we used measured CaO contents in the pyroxenes in combination with Mg# derived from the modelling and the concentrations of Gd and Yb calculated using partition coefficients to obtain the compositions of pigeonite and augite plotted in Figs. 9 and 10. The validity of the last part of the exercise clearly depends strongly on the choice of partition coefficients. In our modelling we initially used the data of Hart and Dunn (1993), then we changed the values iteratively until we obtained a good fit between

measured and calculated values. The final choice of partition coefficients is listed in Table 3, and compared with other selected partition coefficients. Those of Hart and Dunn (1993) and Sobolov (1996) were obtained from experimentally produced clinopyroxene and those of Schwandt and McKay (1998) from low-calcium pyroxene. Our estimations fall well in the range of these literature data. Our values of partitioning between pigeonite and liquid are higher than those of Schwandt and McKay (1998) but in the same order (except for the very low value of La). Our partition coefficients between augite and liquid fall in the low range of available data for basaltic liquids but are very similar to those of Sobolev (1986). Our coefficient of Sr is slightly lower and is probably wrong, due to high mobility of this element.

In Fig. 9, the modelled Cr contents in augite are slightly higher than the measured values. This difference might be explained by co-crystallization of Cr-Fe-oxides, which were not included in our calculations. Otherwise the agreement is reasonable, which gave us confidence to use the results to model the evolution of liquid compositions during olivine and pyroxene crystallization. The REE contents of liquids in equilibrium with both pyroxenes are plotted in Fig. 7. These were calculated using representative compositions of the pigeonite and augite in sample Ax105 and the partition coefficients listed in Table 3. Both calculated liquids have almost flat patterns, with small Sr negative anomalies. The pattern of liquid in equilibrium with augite is flatter and at higher concentrations, reflecting the crystallization of this mineral from a more evolved melt. Also shown in Fig. 7 is the composition of the olivine-poor portion of sample M668, prepared by cutting away all the large olivine crystals and leaving only the pyroxene-rich matrix in the cells between the olivine crystals (see Figure 2b). The composition of this material is very similar to that of the liquid in equilibrium with pigeonite.

We note in Fig. 8 that the Be and Li profiles (flat profiles in pigeonite, increase in augite margins) resemble the magmatic profiles of the REE. Li is a small univalent cation known to diffuse rapidly in geological systems (Hofmann 1980) and it could be questioned whether the profile is not due to diffusion, especially since the lunar rocks are more than 4Ga old (Canup and Asphaug 2001). On the other hand, very low temperature at the lunar surface would have decreased the diffusion rate, perhaps allowing pigeonite to retain Li in its crystal structure. Li is moderately incompatible in pyroxene (Herd et al. 2004) and during crystallization it should behave like a REE, showing enrichment at pyroxene rim. Seitz et al. (2006) measured a Li concentration of 6.4ppm in a low-Ti mare basalt. Using the partition coefficient for pyroxene of 0.2 that Herd et al. (2004) obtained experimentally on a Martian basalt composition, and the average value of 1.6ppm that we measured in pigeonite cores from our Apollo 12 and 15 samples, we obtain a value of 8ppm Li for the equilibrium melt, similar to that of the low-Ti mare basalt. The Li enrichment in augite margins reflects both Li enrichment in the melt and higher partition coefficient of Ca-rich pyroxene. The same should apply for Be. Thus Be and Li profiles are interpreted as reflecting crystallization only.

7. Phase relations

In Fig. 11, we plot in the olivine-clinopyroxene-quartz pseudo-ternary diagram, the bulk compositions of komatiitic rocks from Alexo and from Fred's Flow, a thick layered unit in Munro Township described by Arndt (1976) and Kinzler and Grove (1985). Only samples from the upper to middle parts of the flows — the chilled margins, spinifex lavas and gabbros — are included, and cumulates from the lower parts of the flows are excluded. We selected the best-preserved samples and excluded samples that showed petrographic evidence of strong alteration. The data include analyses from Arndt (1986), Arndt and Nesbitt (1982) and Barnes (1983) and new analyses from this study. With the exception of three pyroxene

spinifex samples analyzed by Barnes (1983), which plot very close to the composition of augite, all the other analyses plot in the primary phase field of olivine. These samples include not only olivine-bearing rocks such as the olivine-phyric chilled margins and spinifex lavas, but also many pyroxene-spinifex lavas that are devoid of modal olivine. The problem posed by the absence of olivine in komatiites that plot in the olivine field was raised long ago by Arndt and Fleet (1979) and Campbell and Arndt (1982). The presence of cumulus pyroxene, as proposed by Barnes (1983), is only a partial answer, as discussed later in this paper.

We also plot our analyses of pigeonite and augite and one analysis of orthopyroxene (from Arndt and Fleet, 1979). The dashed lines from olivine to the reaction points are the compositional boundaries that determine whether augite (above), pigeonite (in the middle) or orthopyroxene (below) is the first pyroxene to crystallize.

All samples of olivine spinifex lava plot in the olivine liquidus field, and most are in the field of liquids that crystallize augite as the first pyroxene. Pyroxene spinifex lavas also plot in the olivine field but closer to the Cpx apex, near the Ol-Cpx join. The three samples lying within the liquidus field of Ca-rich pyroxene come from the upper part of the Alexo komatitic basalt flow: they probably represent parts of the flow that had accumulated clinopyroxene during the growth of spinifex texture (Barnes 1983).

Compositions P and E are liquid compositions that we calculated on basis of modal mineral proportions estimated using quantitative analysis of the images of thin sections and polished slabs of Alexo rocks (see Table 2). Composition P is our estimate of the liquid that crystallized to form the coarse olivine spinifex lava near the base of the spinifex layer, sampled as M668, Ax105 and Ax106. These samples contain about 30% olivine and the bulk composition of the weighted average of modal minerals contains about 24% MgO, very similar to that in the bulk analysis of sample M668 (Table 2). Composition E is based on the modal mineralogy of pyroxene spinifex lavas such as sample Ax102. It contains 20% pigeonite, 45% augite, 15% plagioclase and 0% olivine and its bulk composition contains 13.5% MgO.

Under equilibrium conditions, liquid with composition P should crystallize olivine until it arrives at the cotectic. Then olivine and augite crystallize together until the reaction point is reached, at which point pigeonite starts to crystallize. Although the sequence olivine-to-augite is seen in the olivine spinifex lavas in the upper part of the two flows, in many of the pyroxene spinifex samples pigeonite, and not augite, is the first pyroxene to appear.

The compositions of pyroxene spinifex lavas plot in a position in the phase diagram that is aberrant for two reasons: first they plot within the primary phase field of olivine but do not contain this mineral; second, from the phase diagram, they should crystallize augite before pigeonite whereas the opposite is indicated by the petrological observations described earlier in the paper. Yet another puzzling feature of the mineralogy of these layered flows emerges from a comparison of the crystallization sequence in the upper part of the flow with that in the lower cumulates (Fig. 1). In rapidly cooled samples from the uppermost part the sequence is:

olivine (+minor chromite) → augite → glass.

In more slowly cooled samples deeper in the spinifex layer it is

olivine (+chromite) → pigeonite → augite → augite + plagioclase (+Fe-Ti oxides).

In the lower cumulates it is

olivine (+chromite) → orthopyroxene ± augite → augite + plagioclase (+Fe-Ti oxides).

Possible explanations for these differences include the following:

(1) All the samples have undergone low-grade metamorphism and their compositions may have been affected by the circulation of hydrous or carbonate-bearing fluids (Barnes 1983; Lahaye and Arndt 1996). Although we excluded the obviously altered samples, it remains possible that the compositions of even the freshest samples are not pristine. However, to

change the composition of a sample from the field in which augite is the first pyroxene to one in which pigeonite crystallizes first requires large-scale element mobility. For example, to move our composition P into the field that crystallizes pigeonite before augite requires either the loss of an enormous amount of Ca or the addition of 7-8% SiO₂. There is no evidence of changes of this magnitude: indeed, Table 2 shows a good correspondence between the analysed whole-rock composition and the composition constructed from the weighted mean compositions of the magmatic minerals. The single sample of pyroxene spinifex lava that plots in the “pigeonite-first” field (sample P9-172 from (Arndt and Nisbet 1982)) has an abnormally high SiO₂ content that is probably due to alteration. This sample from Fred’s Flow in fact has a composition not far from that of Composition B of Kinzler and Grove (1985), a composition that did indeed crystallize pigeonite before augite in their experimental study. As can be seen from the diagram, this composition is far richer in SiO₂ than any of the fresher samples from the Alexo komatiitic flows.

(2) Another possibility is that the rocks in the olivine field do not represent liquids but instead contain a significant component of cumulus pyroxene, as suggested by Campbell and Arndt (1982), Barnes (1983) and Kinzler and Grove (1985). However, inspection of Fig. 11 shows that if the plotted spinifex lavas did contain a significant amount of either pigeonite or augite, their liquid compositions would have plotted even deeper in the olivine field, and farther from compositions that crystallize pigeonite.

(3) A third explanation is the presence of a non-negligible amount of water in the komatiitic liquid. Even a small amount of water may have an influence on the pyroxene phase relations. If the initial liquid contained 0.2% H₂O {McDonough, 1995 #999, the evolved liquid that crystallized pigeonite would contain about 0.5% H₂O. Parman et al. (1997) showed in their experiments that the presence of H₂O lowers the appearance temperature of both augite and pigeonite, but that this effect is more pronounced for pigeonite. In other words, augite crystallization is favoured, the opposite to what is required.

(4) Yet another possibility is that the equilibrium phase relations, as determined by Kinzler and Grove, are not appropriate for the conditions under which the spinifex lavas crystallized. In the course of their study, Kinzler and Grove (1985) established that under conditions of rapid cooling, pigeonite crystallization is suppressed more than that of augite, such that their Composition B crystallized augite as the first pyroxene. This might explain the contrasting crystallization sequences in the upper part of the flows, but, as explained in point (1), the composition B probably is not representative of liquids in either komatiitic flow. In order that liquids with compositions like P or E — those that represent the least altered komatiites — crystallize pigeonite before augite, the phase boundaries must have been shifted dramatically. The position of the olivine-pigeonite boundary must have moved away from the quartz apex and towards olivine, such that all the samples in which pigeonite crystallized first plot in an expanded primary phase volume of pigeonite. This explanation is improbable because it requires that the crystallization of pigeonite is enhanced under conditions of rapid cooling. This is unlikely because pigeonite is a mineral that nucleates with difficulty, compared to augite and olivine {Kinzler, 1985 #136}.

(5) To move chemical composition toward pigeonite field, Si must be added and/or Ca removed. As we previously said, only one sample displays abnormally Si enrichment and this enrichment is probably related to alteration. Therefore global SiO₂ enrichment of the flow seems unrealistic. Local increase of SiO₂ may, however, be possible. Dynamic crystallization experiments show that a chemical boundary layer forms at the liquid-olivine crystal interface during rapid crystal growth (Faure and Schiano 2005; Lofgren and Donaldson 1975). This layer results from the chemical gradient that develops when crystal growth is more rapid than the diffusion of elements in the liquid. Elements like Si or Ca, whose concentrations are lower in olivine than in the liquid, become enriched in the boundary layer. Experiment results show

that the boundary layer is best developed at the olivine dendrite tips (Faure et al. 2006) where SiO₂ and CaO contents can increase by 1-2 wt.% and 3-4 wt.% respectively. Simple enrichment of SiO₂ and CaO will not lead to pigeonite crystallization because the liquid in the boundary layer has an olivine-depleted composition which lies along an olivine control line in Fig and far from the pigeonite field. However diffusion out of the boundary layer will change its composition. Ca diffuses rapidly and Si slowly (Liang et al. 1996) and as a result, the composition of the boundary layer will shift towards the pigeonite field.

(6) A final possibility is that internal processes that acted during the solidification of the lava flow differentiated the komatiitic liquid. Faure et al. (2006) showed that the thermal gradient in the crust of a komatiite flow is a key element in the formation of spinifex texture, influencing both the morphologies of olivine and pyroxene and their sequence of crystallization. The thermal gradient may also have caused chemical diffusion which could have led to contrasting compositions at the hot and cold portions of the mush zone in the lower part of the crust (Fig. 12).

When a temperature gradient is applied to a liquid, it produces not only a heat flux but also gives rise to diffusion of the constituent components. This differentiation, known as the Soret effect, results in separation of the components along a concentration gradient parallel to the temperature gradient (Latypov 2003; Soret 1879; Walker et al. 1981). The consequence is the formation of two liquids of contrasting compositions: the liquid at the hot end is relatively enriched in Si, Na and K, and that at the cold end is enriched in Mg, Fe, Al and Ca.

In the lower portion of the crust of a lava flow (Fig. 12), the Soret effect will be established in the temperature gradient between the solidified upper margin and the hot interior of the flow. During the crystallization of platy olivine or “string-beef” pyroxene spinifex, the orientation of crystals is parallel to the flow contact and this geometry facilitates thermal diffusion in the volumes of liquid interstitial to the crystals, as shown in Fig. 12. During the cooling of a komatiite flow such as Fred’s Flow, the composition of the liquid in the interior of the flow changes progressively as a result of crystallization of olivine in the lower cumulate part of the flow. The lava temperature (or the liquidus of the magma) can be estimated with the simple relation:

$$T_{\text{liquidus}} = 1000^{\circ}\text{C} + 20 \times \text{MgO} \quad (\text{Nisbet 1982})$$

which imposes a thermal gradient G across the crust from hot interior at T_{liquidus} to cold surface at T_{surface} (=0):

$$G \left(^{\circ}\text{C/cm} \right) = (T_{\text{liquidus}} - T_{\text{surface}}) / H$$

where H=crust thickness in cm. The thickness of mush zone, taken here as that part of the crust where the proportion of liquid exceeds 50%, is defined by the 1200°C isotherm, which is the temperature of crystallization of pigeonite under equilibrium conditions. There is therefore a temperature difference T across the mush zone of thickness L. The time taken for the growing crystal front to pass from the initiation of crystallization to the 1200°C limit is given by the equation:

$$t_1 = (T_{\text{liquidus}} - 1200) / c$$

where c = cooling rate.

We present here some calculations to test if a thermal gradient is maintained for a time sufficient for Soret diffusion to operate. During the cooling of Fred’s Flow, pigeonite started to crystallize when the crust was about 4 m thick. At this stage we estimate that the MgO

content of the interior liquid was about 13.5wt% and its temperature was 1270°C. The thermal gradient across the 4 m crust, from 1270°C in the interior to 0°C at the surface, is 3.2°C/cm. The thickness of the mush zone is then 22cm, from a “cold” end at 1200°C to a “hot” end at 1270°C, and the temperature difference is 70°C.

Soret differentiation in a liquid can be calculated from the following equation (Lesher and Walker 1991):

$$X_{\text{cold}} - X_{\text{hot}} = X_i(1-X_i) \Delta T \sigma$$

where X_{cold} and X_{hot} are the weight proportions of the oxides at the cold and hot ends, ΔT is the temperature difference and σ is the Soret coefficient. The time for the system to reach Soret steady state is given by:

$$t = 3L^2/\pi^2 D \quad (\text{Latypov 2003; Schott 1983})$$

where L is the thickness of the liquid layer and D is the chemical diffusion coefficient in the liquid. Both relations are linked by:

$$\sigma = S_T (1 - e^{-t/\theta}) \quad (\text{Schott 1983})$$

where $\theta = L^2/\pi^2 D$.

Soret coefficients were taken from Lesher and Walker (1991). A critical parameter is the water content of the magma. When coefficients for anhydrous liquids are used (5.10^{-7} (LaTourrette et al. 1996)), the calculated time for the system to reach Soret steady state is several years and thus far longer than the cooling time of a komatiite flow (Donaldson, 1982). Latypov (2003) in his modelling of the solidification of mafic intrusions used much lower diffusion coefficients of 10^{-4} to 10^{-5} cm²/s, but these were for H₂O-saturated melts. Several authors (McDonough and Danyushevsky 1995; Shimizu et al. 2001) have measured small but not insignificant water contents of 0.3 wt% in melt inclusions in komatiites. Moreover recent studies show that because of kinetic effect, degassing is not complete at the time of eruption but continues during flowage of the lava (Moune et al. 2007; Polacci et al. 2006). When a diffusion coefficient of 5.10^{-5} cm²/s is used, our estimate of a coefficient appropriate for a water-poor magma, the system reaches steady state in only 34 days. The results of our calculations are shown in Figure 13a.

Turner et al. (1986) calculated the rate of cooling of komatiite flows using both conductive and convective models and they predicted very low cooling rates of less than 0.1°C per hour for a liquid beneath a 4 m thick solid crust — the position where pyroxene spinifex forms in Fred’s Flow. At these cooling rates the magma would take several months to cool from 1270°C to 1200°C the temperature difference between hot and cold ends of the mush zone. Thus there is enough time for Soret effect to become established in this zone.

We propose that the acicular pigeonite-augite megacrysts in spinifex-textured lavas might have grown under these conditions. If Soret differentiation had acted as we suggest, the tips of the spinifex crystals could have grown at the crystallization front in liquid with high Si/Mg that stabilized pigeonite. This effect is illustrated in Fig. 13a, which shows the crystallization path of coarse pyroxene spinifex lavas at a time when the flow crust is 4 metres thick. Liquid of composition X, produced by olivine fractionation from the parental komatiite, could have differentiated through the Soret effect into a hot liquid enriched in Si, Na and K at the base of the mush zone, and a cold liquid enriched in Mg, Fe, Al and Ca at the top of the zone. Crystallization at the hot crystal front results in the growth of the pigeonite cores while

crystallization from interstitial liquid at shallower levels in the crust results in the growth of the augite margins.

Figure 13b is a schematic view of what occurs in random olivine spinifex lavas higher in the Alexo komatiite flow, where the crust is thinner and pigeonite is absent. During crystallization of these lavas, the cooling rate was far higher than deeper in the flow, a factor that, according to Faure et al. (2006) leads to random nucleation of olivine crystals and an absence of aligned crystal growth. A combination of olivine removal (step #1) and supercooling produces a liquid composition in the augite phase volume, allowing augite to crystallize as small acicular crystals between the olivine megacrysts (step #2). The cooling rate is high, plagioclase does not nucleate and the residual liquid is transformed into glass.

Figure 13c shows the crystallization history for rocks in the lower cumulus part of a layered komatiitic basaltic flow such as Fred's Flow. In the interior of this 120m thick unit, the cooling rate is low, and under these conditions, pigeonite does not crystallize (Kinzler and Grove 1985). The crystallization sequence, as inferred from changes in cumulate mineralogy, is olivine followed by clinopyroxene with or without orthopyroxene and finally plagioclase \pm clinopyroxene \pm orthopyroxene. This sequence is explained in Fig. 13c. Olivine-clinopyroxene cumulates are not common in Fred's Flow and it is possible that the clinopyroxene removal of step #2 took place either through crystallization in the spinifex layers or crystallization within the cumulus pile. Circulation of melt through the cooler, deeper parts of the cumulate pile would crystallize clinopyroxene interstitially and the signature of clinopyroxene subtraction would be imparted to the melt in the interior of the flow once the interstitial liquid exited the cumulus pile. Orthopyroxene-clinopyroxene cumulates formed once the liquid composition reached the triple reaction point, and the plagioclase-pyroxene cumulates formed when the composition reached the plagioclase reaction curve (not in the plane of the diagram).

The composite pigeonite-augite megacrysts that are present in the platy olivine (A3) zones present a special problem. One possibility is that pigeonite growth in these cells is related to the formation of a boundary layer at the liquid-olivine crystal interface during growth of olivine spinifex crystals, as explained above. Another possibility is development of Soret diffusion at a much smaller scale. Composite pigeonite-augite megacrysts grew in polyhedral cells between large plates of olivine (Figs. 2, 14): they appear to have nucleated on the olivine crystals and then they grew inwards towards the centre of the cell. Under such conditions, we cannot count on the thermal gradient between the flow interior and surface to produce Soret differentiation. Instead we speculate that a local thermal gradient may have been set up between olivine crystals and the liquid interior of the cells. Shore and Fowler (1999) have argued that at the high temperatures of komatiite crystallization, radiative heat transfer along big platy olivine crystals is efficient and contributes considerably to the cooling of the flow. At the same time, latent heat of crystallization will increase the temperature in the interior of the cells. The consequence is the development of local thermal gradients from relatively cool olivine crystals to relatively hot cell interiors. Although the scale of these gradients is much smaller than that across the mush zone of the flow, they would be long-lived and might, over a distance of a few millimetres, produce the Soret differentiation necessary to stabilize pigeonite. A combination of both processes — the boundary layer effect and Soret differentiation — could explain the abnormal crystallization of pigeonite in the coarse platy spinifex zone.

8. Comparison with Barberton pyroxenes

In the Wo vs Mg# diagram (Fig. 15), we compare the compositions of pyroxenes from the Alexo komatiite flow with pyroxene data from Barberton komatiites, previously studied by Parman et al. (1997; 2003). It is immediately apparent that the distinguishing feature of the Barberton pyroxenes is not so much their unusually high Wo content but their high Mg#. The range of Wo in the cores of Barberton pyroxenes is from about 26 to 42 (Parman et al. 1997; Parman et al. 2003), the same as the range from 26 to 42 in Alexo pyroxenes, but the minimum Mg# of the Barberton pyroxenes corresponds to the maximum Mg# of Alexo pyroxenes. In Fig. 16, data from komatiites from Zimbabwe (Nisbet et al. 1987; Shimizu et al. 2005) and Gilmour Island (Arndt 1982) show generally lower Mg# and Wo than the Alexo and Barberton komatiites. There are, however, several examples of pyroxenes in komatiite flows whose Wo and Mg# are as high, or higher, than those of Barberton. Data for Gorgona komatiites (Echeverria and Aitken 1986) show highest Wo contents of pyroxene in komatiites reported in the literature, but they have relatively low Mg# (0.72-0.74). Pyroxene from the spinifex layer of the Boston Creek unit (Stone et al. 1987) contains Wo contents of 46-47 (higher than Barberton) and Mg# in the range 0.66-0.80. Pyroxenes in the cumulate layer of the same unit show even more extreme values, with Wo contents ranging from 45 to 48 and Mg# from 0.58 to 0.86. Similarly, intercumulus clinopyroxene in Fred's Flow also has high Wo and high Mg#.

The Wo vs Al₂O₃ and Al₂O₃ vs TiO₂ diagrams (Fig. 17) show Al₂O₃ and TiO₂ variations in pyroxene for three different komatiites: Alexo (this study), Barberton (Parman et al. 1997; 2003) and Gilmour (unpublished data). Alexo pyroxenes display a trend from moderate Al₂O₃ (2.0 wt %) and low TiO₂ (0.04 wt %), to high Al₂O₃ (10.9 wt %) and high TiO₂ (1.0 wt %). Data for Gilmour pyroxenes show almost no variation of Al₂O₃ contents while their TiO₂ vary from 0.17 to 0.85 wt% and they plot in a field intermediate between those of Barberton and Alexo. Barberton pyroxenes have far lower contents of the two elements: Al₂O₃ values are between 0.2 and 2.3 wt% and TiO₂ values between 0.02 and 0.3 wt%. The only pigeonite composition reported from Barberton (in a komatiitic basalt analyzed by Parman et al., 1997) has an Al₂O₃ value of 0.8wt% whereas the lowest value for pyroxene in the Alexo komatiite is 2.0 wt%.

Explanations for high Wo and Mg# of Barberton

According to Parman et al. (1997; 2003), the unusual high Mg# and high Wo contents of augites in Barberton komatiites are explained by the presence of water in the melt. As explained in the introduction, they based this explanation on the results of their experiments conducted with and without water, using starting compositions like those of Barberton komatiites. They found that the compositions of Barberton pyroxenes were similar to those in the hydrous experiments and they attributed the high Wo contents to crystallization at low temperature in hydrous magmas.

As pointed out above, the main difference between pyroxenes from Barberton komatiite and Alexo komatiite is Mg#, not Wo content (see Fig. 15). We emphasize that crystallization from hydrous magma is not a likely explanation because all the examples listed above are lava flows, even Barberton (Dann 2001) and under low-pressure extrusive conditions water would have escaped from the magma. Several processes may explain, or at least contribute to, these differences. First, careful reading of the supporting material of Parman et al. (2003) indicates that only one of the pyroxenes analyzed in their study was in a spinifex-textured komatiite; the others were in olivine cumulates. It may be significant that the augites with the highest Wo contents reported in Fig. 16 are also from olivine cumulates, some from the lower

portion of Fred's Flow, others from the Boston Creek unit. It is possible that the composition of the augite changed during slow cooling of the interior of these units, perhaps through interaction with Fo-rich olivine, resulting in higher Mg# than pyroxenes from the upper portions. Another possible influence is change in the pyroxene composition during metamorphism. The Barberton komatiites are metamorphosed to upper greenschist or lower amphibolite facies, and preservation of primary phases is far less complete than in the more weakly metamorphosed komatiites from the Abitibi belt and other locations reported in Fig. 16. Inspection of the photos and descriptions in Parman et al. (1997; 2003) show that the analysed pyroxenes are small remnants preserved in largely altered grains, and the possibility that the pyroxene composition changed during metamorphism cannot be ruled out.

The most likely explanation, however, for the unusual composition of Barberton pyroxenes is the unusual composition of the komatiites themselves. Viljoen and Viljoen (1969), in their initial definition of the rock type, emphasized that these komatiites have high CaO/Al₂O₃ ratios due to relatively low Al₂O₃ contents. Experiments carried out in anhydrous conditions using synthetic komatiite compositions with variable CaO/Al₂O₃ (Arndt 1976) show that pyroxene crystallizes at higher temperatures in liquids with high CaO/Al₂O₃, like those of Barberton komatiites, than in liquids with lower CaO/Al₂O₃, like those of Abitibi komatiites (Figs 18 and 19). In these experiments, the Mg# of the pyroxene are anomalously high because of Fe loss to the platinum wire on which the sample was suspended, but despite this complication, the relationship between CaO/Al₂O₃ and Mg# remains valid: pyroxene that crystallizes from a melt with high CaO/Al₂O₃ has high Mg# because it crystallizes early when the melt still has a relatively magnesian composition. We propose, therefore, that the high Wo contents and high Mg# do not record the presence of water in hypabyssal komatiites but are mainly a reflection of the unusual composition of Barberton komatiites.

Conclusions

1. Zoned pyroxene with pigeonite cores and augite rims crystallize in komatiites and lunar basalts. Mg# and Cr are good indicators of the evolution of the liquid that crystallized the pyroxenes and these can be used to model the changes in trace element contents such as the REE and light elements (Li, Be and B).
2. In the well-preserved lunar pyroxenes, the light elements behave like the REE and are present in higher concentrations in augite than in pigeonite; in pyroxene in the komatiites the light element contents are similar in the two pyroxenes and appear to have been changed during alteration.
3. Pyroxene crystallized under contrasting compositions at different parts of the komatiite flows: from very rapid cooling in the flow top, to constrained growth in a thermal gradient in the pyroxene spinifex layer, to slow cooling in the lower cumulates. The type of pyroxenes and the crystallization sequence reflects the conditions of crystallization. Pigeonite is absent in olivine spinifex lava from the rapidly cooled flow top but its crystallization is enhanced in pyroxene spinifex lavas. Here constrained growth in the thermal gradient appears to have caused pigeonite to crystallize earlier than at equilibrium conditions leading to the crystallization sequence olivine-pigeonite-augite.
4. Augites in komatiite flows from various locations have Wo contents as high as those from Barberton komatiites but their Mg# are lower. The differences are unlikely to be due to high water contents but are ascribed to: (1) metamorphism, which may have influenced the compositions of Barberton pyroxenes, (2) interaction between pyroxene

and olivine in cumulate samples, and, most importantly, (3) the unusual, high CaO/Al₂O₃ contents of Barberton komatiites.

References

- Arndt NT (1976) Melting relations of ultramafic lavas (komatiites) at 1 atm and high pressure. Carnegie Institution Washington, Yearbook 75:555-562
- Arndt NT (1977) Thick, layered peridotite-gabbro lava flows in Munro Township, Ontario. Can. J. Earth Sci. 14:2620-2637
- Arndt NT (1982) Proterozoic spinifex-textured basalts of Gilmour Island, Hudson Bay. Geol. Surv. Can. Paper 83-1A:137-142
- Arndt NT (1986) Differentiation of komatiite flows. J. Petrol. 27:279-301
- Arndt NT, Fleet ME (1979) Stable and metastable pyroxene crystallization in layered komatiite flows. Am. Mineralogist 64:856-864
- Arndt NT, Nesbitt RW (1982) Geochemistry of Munro Township basalts. In: Arndt NT, Nisbet EG (eds) Komatiites, vol. George Allen and Unwin, London, pp 309-330
- Arndt NT, Nisbet EG (1982) Komatiites, vol. George Allen & Unwin, London, p 526
- Ayer JA, Y. A, Corfu F, Kamo SL, Ketchum J, Kwok K, Trowell N (2002) Evolution of the southern Abitibi greenstone belt based on U-Pb geochronology: autochthonous volcanic construction followed by plutonism, regional deformation and sedimentation. Precamb. Res. 115:63-95
- Barnes S-J (1983) A comparative study of olivine and clinopyroxene spinifex flows from Alexo, Abitibi greenstone belt, Canada. Contrib. Mineral. Petrol. 83:293-308
- Bence AE, Papike JJ, Prewitt CT (1970) Apollo 12 clinopyroxenes: Chemical trends. Earth and Planetary Science Letters 8(6):393-399
- Bickle MJ, Arndt NT, Nisbet EG, Orpen JL, Martin A, Keays RR, Renner R (1993) Geochemistry of the igneous rocks of the Belingwe greenstone belt: alteration, contamination and petrogenesis. In: Bickle MJ, Nisbet EG (eds) The geology of the Belingwe Greenstone Belt, Zimbabwe, vol. Balkema, Rotterdam, pp 175-214
- Brown GE, Wechsler BA (1973) Crystallography of pigeonites from basaltic vitrophyre 15597. Proceedings of the 4th Lunar Science Conference. 1(Supplement 4, Geochimica et Cosmochimica Acta):887-900
- BVSP BVSP (1981) Basaltic Volcanism on the Terrestrial Planets, vol. Pergamon Press, New York, p 1286
- Campbell IH, Arndt NT (1982) Pyroxene accumulation in spinifex-textured rocks. Geological Magazine 119:605-610
- Canup RM, Asphaug E (2001) Origin of the Moon in a giant impact near the end of the Earth's formation. Nature 412(6848):708-712
- Dann JC (2000) The Komati Formation, Barberton Greenstone Belt, South Africa, part I: new map and magmatic architecture. S. Afr. J. Earth Sci. 6:681-730
- Dann JC (2001) Vesicular komatiites, 3.5-Ga Komati Formation, Barberton Greenstone Belt, South Africa: inflation of submarine lavas and origin of spinifex zones. Bull. Volcanol. 63:462-481
- Dupré B, Chauvel C, Arndt NT (1984) Pb and Nd isotopic study of two Archean komatiitic flows from Alexo, Ontario. Geochim. Cosmochim. Acta 48:1965-1972
- Echeverria LM, Aitken B (1986) Pyroclastic rocks: another manifestation of ultramafic volcanism of Gorgona Island, Colombia. Contrib. Mineral. Petrol. 92:428-436
- Faure F, Arndt N, Libourel GUY (2006) Formation of Spinifex Texture in Komatiites: an Experimental Study. J. Petrology 47(8):1591-1610

- Faure F, Schiano P (2005) Experimental investigation of equilibration conditions during forsterite growth and melt inclusion formation. *Earth and Planetary Science Letters* 236(3-4):882-898
- Fleet ME, MacRae ND (1975) A spinifex rock from Munro Township, Ontario. *J. Can. Earth Sci.* 12:928-939
- Grove TL, Bence AE (1977) Experimental study of pyroxene-liquid interaction in quartz-normative basalt 15597. *Proceedings of the 8th Lunar and Planetary Science Conference*:1549-1579
- Grove TL, de Wit MJ, Dann J (1997) Komatiites from the Komati Type Section, Barberton, South Africa. In: de Wit MJ, Ashwal LD (eds) *Greenstone Belts*, vol. Oxford Science Publications, Oxford, pp 422-437
- Grove TL, Parman S (2004) Thermal evolution of the Earth as recorded by komatiites. *Earth Planet. Sci. Lett.* 219:173-187
- Grove TL, Parman SW, Dann JC (1999) Conditions of magma generation for Archean komatiites from the Barberton Mountainland, South Africa. In: Fei Y, Bertka CM, Mysen BO (eds) *Mantle petrology: field observations and high-pressure experimentation*, vol. The Geochemical Society, Houston, pp 155-167
- Grove TL, Raudsepp M (1978) Effects of kinetics on the crystallization of quartz-normative basalt 15597: An experimental study. *Proceedings of the 9th Lunar and Planetary Science Conference*:585-599
- Hart SR, Dunn T (1993) Experimental Cpx Melt Partitioning of 24 Trace-Elements. *Contributions to Mineralogy and Petrology* 113(1):1-8
- Hellebrand E, Snow JE, Hoppe P, Hofmann AW (2002) Garnet-field Melting and Late-stage Refertilization in 'Residual' Abyssal Peridotites from the Central Indian Ridge. *J. Petrology* 43(12):2305-2338
- Herd CDK, Treiman AH, McKay GA, Shearer CK (2004) The behavior of Li and B during planetary basalt crystallization. *American Mineralogist* 89(5-6):832-840
- Hofmann AW (1980) Diffusion in natural silicate melts: a critical review. In: Hargraves RB (ed) *Physics of Magmatic Processes*, vol. Princeton University Press, Princeton, pp 385-418
- Jochum KP, Dingwell DB, Rocholl A, Stoll B, Hofmann A, Becker S, Besmehn A, Besesette D, Dietze H-J, Dulski P, Erzinger J, Hellebrand E, Hoppe P, Horn I, Janssens K, Jenner G, Klein M, McDonough WM, Maetz M, Mezger K, Münker C, Nikogosian IK, Pickhart C, Raczek I, Rhede D, Seufert HM, Simakin SG, Sobolev AV, Spettel B, Straub S, Vincze L, Wallianos A, Weckwerth G, Weyer S, Wolf D, Zimmer M (2000) The Preparation and Preliminary Characterisation of Eight Geological MPI-DING Reference Glasses for In-Situ Microanalysis. *Geostandards Newsletter* 24:87-133
- Jolly WT (1982) Progressive metamorphism of komatiites and related Archaean lavas of the Abitibi area, Canada. In: Arndt NT, Nisbet EG (eds) *Komatiites*, vol. George Allen and Unwin, London, pp 245-266
- Kinzler RJ, Grove TL (1985) Crystallization and differentiation of Archean komatiite lavas from northeast Ontario: Phase equilibrium and kinetic studies. *Am. Mineralogist* 70:40-51
- Lahaye Y, Arndt NT (1996) Alteration of a komatiitic flow: Alexo, Ontario, Canada. *J. Petrol.* 37:1261-1284
- LaTourrette T, Wasserburg GJ, Fahey AJ (1996) Self diffusion of Mg, Ca, Ba, Nd, Yb, Ti, Zr, and U in haplobasaltic melt. *Geochimica Et Cosmochimica Acta* 60(8):1329-1340
- Latypov RM (2003) The Origin of Marginal Compositional Reversals in Basic-Ultrabasic Sills and Layered Intrusions by Soret Fractionation. *J. Petrology* 44(9):1579-1618

- Lesher CE, Walker D (1991) Thermal diffusion in petrology. In: Ganguly J (ed) Diffusion, atomic ordering, and mass transport; selected topics in geochemistry, vol. Springer, New York, NY, pp 396-451
- Liang Y, Richter FM, Watson EB (1996) Diffusion in silicate melts: II. Multicomponent diffusion in CaO---Al₂O₃---SiO₂ at 1500[degree sign]C and 1 GPa. *Geochimica et Cosmochimica Acta* 60(24):5021-5035
- Lofgren GE, Donaldson CH (1975) Curved branching crystals and differentiation in comb-layered rocks. *Contrib. Mineral. Petrol.* 274:243-273
- Lofgren GE, Donaldson CH, Usselman TM (1975) Geology, petrology, and crystallization of Apollo 15 quartz-normative basalts. *Proceedings of Lunar Science Conference* 6:79-99
- McDonough WF, Danyushevsky LV (1995) Water and sulfur contents of melt inclusions from Archean komatiites. *EOS* 76:266
- Moune S, Faure F, Gauthier P-J, Sims KWW (2007) Pele's hairs and tears: Natural probe of volcanic plume. *Journal of Volcanology and Geothermal Research* 164(4):244-253
- Naldrett AJ, Mason GD (1968) Contrasting Archean ultramafic igneous bodies in Dundonald and Clerque Townships, Ontario. *J. Can. Earth Sci.* 5:111-143
- Nisbet EG (1982) The tectonic setting and petrogenesis of komatiites. In: Arndt NT, Nisbet EG (eds) *Komatiites*, vol. George Allen and Unwin, London, pp 501-520
- Nisbet EG, Arndt NT, Bickle MJ, Cameron WE, Chauvel C, Cheadle M, Hegner E, Kyser TK, Martin A, Renner R, Roedder E (1987) Uniquely fresh 2.7 Ga komatiites from the Belingwe greenstone belt, Zimbabwe. *Geology* 15:1147-1150
- Papike JJ, Hodges FN, Bence AE, Cameron M, Rhodes JM (1976) Mare Basalts - Crystal-Chemistry, Mineralogy, and Petrology. *Reviews of Geophysics* 14(4):475-540
- Parman S, Dann J, Grove TL, de Wit MJ (1997) Emplacement conditions of komatiite magmas from the 3.49 Ga Komati Formation, Barberton Greenstone Belt, South Africa. *Earth Planet. Sci. Lett.* 150:303-323
- Parman S, Grove TL, Dann J (2001) The production of Barberton komatiites in an Archean subduction zone. *Geophys. Res. Lett.* 28:2513-2516
- Parman S, Grove TL, Dann J, de Wit MJ (2004) A subduction origin for komatiites and cratonic lithospheric mantle. *South African J. Geol.* 107:107-118
- Parman SW, Shimizu N, Grove TL (2003) Constraints on the pre-metamorphic trace element composition of Barberton komatiites from ion probe analyses of preserved clinopyroxene. *Contrib. Mineral. Petrol.* 144:383-396
- Polacci M, Corsaro RA, Andronico D (2006) Coupled textural and compositional characterization of basaltic scoria: Insights into the transition from Strombolian to fire fountain activity at Mount Etna, Italy. *Geology* 34(3):201-204
- Pyke DR, Naldrett AJ, Eckstrand OR (1973) Archean ultramafic flows in Munro Township, Ontario. *Geol. Soc. Amer., Bull.* 84:955-978
- Schott J (1983) Thermal diffusion and magmatic differentiation: a new look at an old problem. *Bulletin of Mineralogy* 106:247-262
- Schwandt CS, McKay GA (1998) Rare earth element partition coefficients from enstatite/melt synthesis experiments. *Geochimica et Cosmochimica Acta* 62:2845-2848
- Seitz H-M, Brey GP, Weyer S, Durali S, Ott U, Munker C, Mezger K (2006) Lithium isotope compositions of Martian and lunar reservoirs. *Earth and Planetary Science Letters* 245(1-2):6-18
- Shearer CK, Papike JJ, Simon SB, Shimizu N (1989) An Ion Microprobe Study of the Intra-Crystalline Behavior of Ree and Selected Trace-Elements in Pyroxene from Mare Basalts with Different Cooling and Crystallization Histories. *Geochimica Et Cosmochimica Acta* 53(5):1041-1054

- Shimizu K, Nakamura E, Maruyama S (2005) The geochemistry of ultramafic to mafic volcanics from the Belingwe Greenstone Belt, Zimbabwe: Magmatism in an Archean continental large igneous province. *J. Petrol.* 46(11):2367-2394
- Shimizu KT, Komiya S, Maruyama S, Hirose K (2001) Water content of melt inclusion in Cr-spinel of 2.7 Ga komatiite from Belingwe Greenstone Belt, Zimbabwe. *Earth Planet. Sci. Lett.* 18:750
- Shore M, Fowler AD (1999) The origin of spinifex texture in komatiites. *Nature* 397(6721):691-694
- Sobolev AV, Migdisov, A.A. and Portnyagin, M.V. (1996) Incompatible element partitioning between clinopyroxene and basalt liquid revealed by the study of melt inclusions in minerals from Troodos lavas, Cyprus. *Petrology* 4(3):307-317
- Soret C (1879) Concentrations différentes d'une dissolution dont deux parties sont à des températures différentes. *Arch. Sci. Phys. Nat.* 2:48-31
- Stone WE, Jensen LS, Church WR (1987) Petrography and geochemistry of an unusual Fe-rich basaltic komatiite from Boston Township, northeastern Ontario. *Can. J. Earth Sci.* 24:2537-2550
- Turner JS, Huppert HE, Sparks RSJ (1986) Komatiites II: Experimental and theoretical investigations of post-emplacement cooling and crystallization. *J. Petrol.* 27:397-437
- Viljoen MJ, Viljoen RP (1969) The geology and geochemistry of the lower ultramafic unit of the Onverwacht Group and a proposed new class of igneous rocks. *Geol. Soc. S. Africa, Spec. Publ.* 21:55-85
- Walker D, Lesher CE, Hays JF (1981) Soret separation of lunar liquid. *Proceedings of the 12th Lunar and Planetary Science Conference* 12B:991-999
- Weigand PW, Hollister LS (1973) Basaltic vitrophyre 15597: An undifferentiated melt sample. *Earth and Planetary Science Letters* 19(1):61-74
- Wilson AH (2003) A new class of silica enriched, highly depleted komatiites in the southern Kaapvaal Craton, South Africa. *Precambrian Research* 127:125-141

List of Figures

- Fig. 1. Sections through the Alexo flows, showing sample locations and textural variations (after Arndt 1986 and Barnes 1983)
- Fig. 2. Textures of komatiites from the Alexo area. (a) A scanned thin section of a random olivine spinifex-textured lava (sample M662). Olivine crystals (in white) are randomly oriented and lie in a fine-grained matrix. (b) Polished slab of coarse platy olivine spinifex textured lava, sample Ax105. Large complex dendritic grains of olivine (black, serpentinized) enclose a cell within which large pyroxene needles have grown. (c) Thin section showing thin needles of complex zoned pyroxene crystals in sample Ax105 (cross-polarized light). (d) Thin section showing in greater detail the zoned pyroxene megacrysts from Ax106. White pigeonite cores are mantled by grey-coloured augite margins. (e) Zoned pyroxene grains cut perpendicular to the c-axis, from within an olivine cell in olivine spinifex textured lava, sample M626. Augite rims (in white) are well preserved; pigeonite cores have altered to chlorite. (f, g) Small skeletal augites between olivine grains, sample M626. Olivine appears in white in figure f, and dark grey in Figure g
- Fig. 3. Photomicrographs of representative thin sections, showing zoned pyroxene with pigeonite cores and augite rims. (a) Pyroxene spinifex lava (sample Ax101) from upper part of the komatiitic basalt flow of Alexo; the section is cut perpendicular to

the flow and perpendicular to the c-axes of the pyroxenes. (b) Same sample, cut parallel to the c-axes. The direction to the flow top is indicated by the white arrow. (c) Lunar basalt, sample 12021,136. This sample contains a zoned pyroxene with a dark grey pigeonite core and a pale grey augite mantle. Plagioclase laths (white) are intergrown with augite (grey) in the matrix. (d) Zoned pyroxene with hollow shapes in a matrix of augite+plagioclase+oxides (lunar sample 12052,336). (e) Coarse phenocrysts of pyroxene (light grey pigeonite and dark grey augite) embedded in a fine-grained groundmass of intergrown pyroxene and plagioclase (plumose structure), opaque phases and glass (lunar sample 12052,336). (f) Small phenocrysts of zoned pyroxene in a silica glass, lunar sample 15597,75

- Fig. 4. (a) Mg# vs Wo content of pyroxenes from Alexo komatiites (b,c) Representative profiles of zoned pyroxenes in plate olivine spinifex lavas from the Alexo komatiite flow. The distance between points is 15 μm for the profile on the left and 20 μm for the profile on the right
- Fig. 5. (a) Mg# vs Wo content of pyroxenes from lunar pigeonite basalts. (b to j) Representative profiles of zoned pyroxenes. The distance between points is 10 μm for all profiles, except profiles g and h where it is 5 μm . All profiles are rim-core-rim except for profiles d, g and j which are core-to-rim
- Fig. 6. Komatiite sample Ax106: profiles across a pyroxene grain in plate olivine spinifex unit showing zoning in major and minor element concentrations, plus three representative rare earth elements (La, Sm, Yb) and the light lithophile elements Li, Be, B. Variations are discussed in the text. The picture is a back-scattered electron (BSE) image acquired with an electron microprobe in Nancy
- Fig. 7. Mantle-normalized trace elements showing representative analyses of the pigeonite core and augite rim compositions of pyroxene in olivine spinifex unit of the Alexo komatiite flow, sample AX105. Also shown are calculated compositions of liquids in equilibrium with these pyroxenes and the bulk rock composition of sample Ax105
- Fig. 8. Profiles across a pyroxene grain in lunar basalt 12052. Variations are discussed in the text. The picture is a BSE image. For a more comprehensive view, FeO data were intentionally hidden on the right of the bottom profile. Values of FeO are linear and climb to 42wt%. Data can be found in Table 1
- Fig. 9. Variations of CaO (a) and chromium (b) in zoned pyroxenes from komatiites. These data can be modelled in terms of crystallization of olivine (from 0 to 38%), pigeonite (from 38 to 54%) and augite (from 54%). Olivine crystallization is not shown here. Partition coefficients are given in Table 3
- Fig. 10. The behaviour of REE can be modelled as Rayleigh fractionation trends (black lines). Partition coefficients for Gd and Yb were adjusted with a graphical approach. Partition coefficients are given in Table 3. Pyroxene data were acquired by ion microprobe on a single spinifex crystal from sample Ax106
- Fig. 11. Bulk compositions of spinifex rocks from the Alexo komatiite and komatiitic basalt and from Fred's Flow, plotted in the olivine-clinopyroxene-quartz pseudo-ternary diagram. Also shown are our analyses of pigeonite and augite from spinifex part of Alexo komatiite. Orthopyroxene was measured in the cumulate layer of the Alexo komatiitic basalt (data from Arndt & Fleet, 1979). The dashed lines from olivine to the pigeonite reaction boundary delineate the field of liquids in which pigeonite is the first pyroxene to crystallize. Above the upper dashed line, augite will crystallize first; below the lower dashed line, orthopyroxene will be first. One-atmosphere liquidus phase relations are shown from Kinzler & Grove (1985)
- Fig. 12. Role of the Soret effect in crystallizing pyroxene megacrysts in pyroxene spinifex-textured lavas. The schematic view on the right shows a typical komatiitic

flow being cooled, with an upper spinifex-textured rock separated to a molten interior by the crystallization front, and a basal cumulate. The sketch on the left is a detail of the crystallization front, where a Soret effect is present

Fig. 13. Proposed crystallization history for pyroxene spinifex-textured komatiite. 'P' is a possible composition of the komatiitic parental melt. Grey fields represent the compositions of pigeonite and augite data. Dashed lines correspond to the two- or three-step fractionation paths, as discussed in the text

Fig. 14. Schematic view of crystallization processes within a cell between olivine plates in coarse platy olivine spinifex-textured lava. Heat is efficiently evacuated along the platy olivine crystals and latent heat is released by crystallization. Pigeonite nucleates on relatively cold olivine crystals, then grows towards the hot interior of cells. Augite develops as rims on pigeonite, and crystallization ends with the growth of augite and plagioclase between the larger pyroxene crystals

Fig. 15. Mg# vs Wo contents of clinopyroxene from Alexo (this study) and Barberton (Parman et al., 1997 and 2003). Circles are clinopyroxene in Alexo komatiite (pigeonites cores in black, augite rims as white circles and mixtures of both pyroxenes in grey)

Fig. 16. Mg# vs Wo contents of clinopyroxene in komatiites from various studies and locations worldwide. The light grey field represents analyses of this study (Alexo), dark grey fields are from Parman et al. (1997, 2003) papers. Solid lines define fields of pigeonite and augite from Belingwe komatiites and komatiitic basalts of Shimizu et al. (2005). High Wo content of clinopyroxene is not a particularity of Barberton komatiite: clinopyroxene in these rocks only have higher Mg# than pyroxene in other komatiites

Fig. 17. Wo content vs Al_2O_3 and Al_2O_3 vs TiO_2 plots of pyroxenes in komatiites from Alexo, Barberton (Parman et al. 1997, 2003) and Gilmour Island (unpublished data). Barberton clinopyroxenes have lower Al (and Ti) contents due to lower Al (and Ti) contents of the liquid

Fig. 18. Compositions of glasses produced by melting natural (FC-1; SA3091 and FSX) and synthetic (SKIE) komatiite samples at 1atm (from Arndt 1977 and unpublished data). Clinopyroxene crystallizes at higher temperatures in starting compositions with high $\text{CaO}/\text{Al}_2\text{O}_3$ ratios

Fig. 19. Diagram showing the crystallization sequences of a series of experimental charges whose compositions are those of komatiitic basalts with differing $\text{CaO}/\text{Al}_2\text{O}_3$. The temperature of the first crystallization of augite increases with increasing $\text{CaO}/\text{Al}_2\text{O}_3$. Data from Arndt (1977, unpublished)

Table headings

Table 1: Major and trace element data

Table 2: Major element data used for modelling of pyroxene-bearing spinifex-textured komatiitic rocks

Table 3: Partition coefficients used during the modelling of the REE behaviour in komatiites

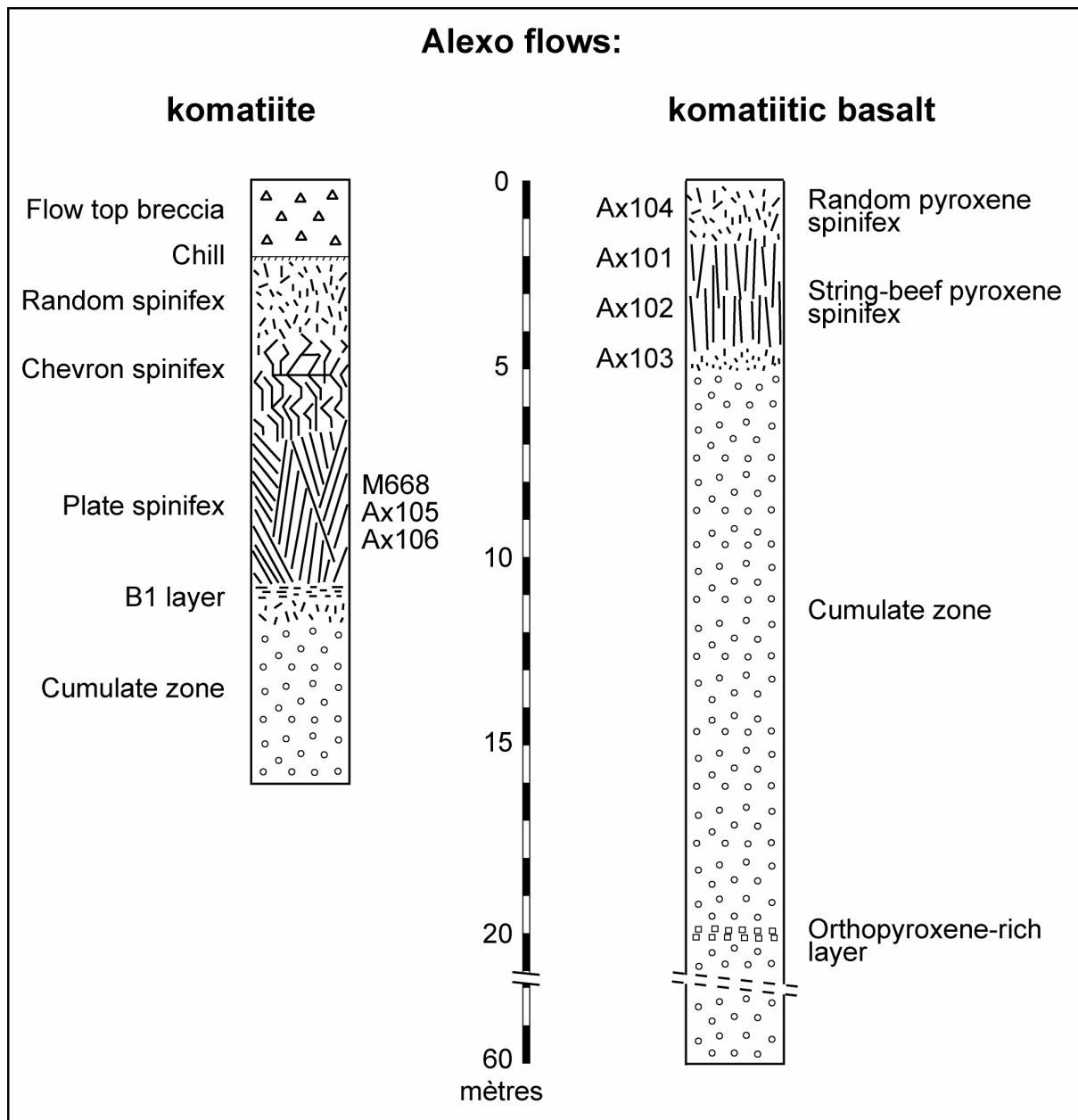


Fig. 1. Sections through the Alexo flows, showing sample locations and textural variations (after Arndt 1986 and Barnes 1983)

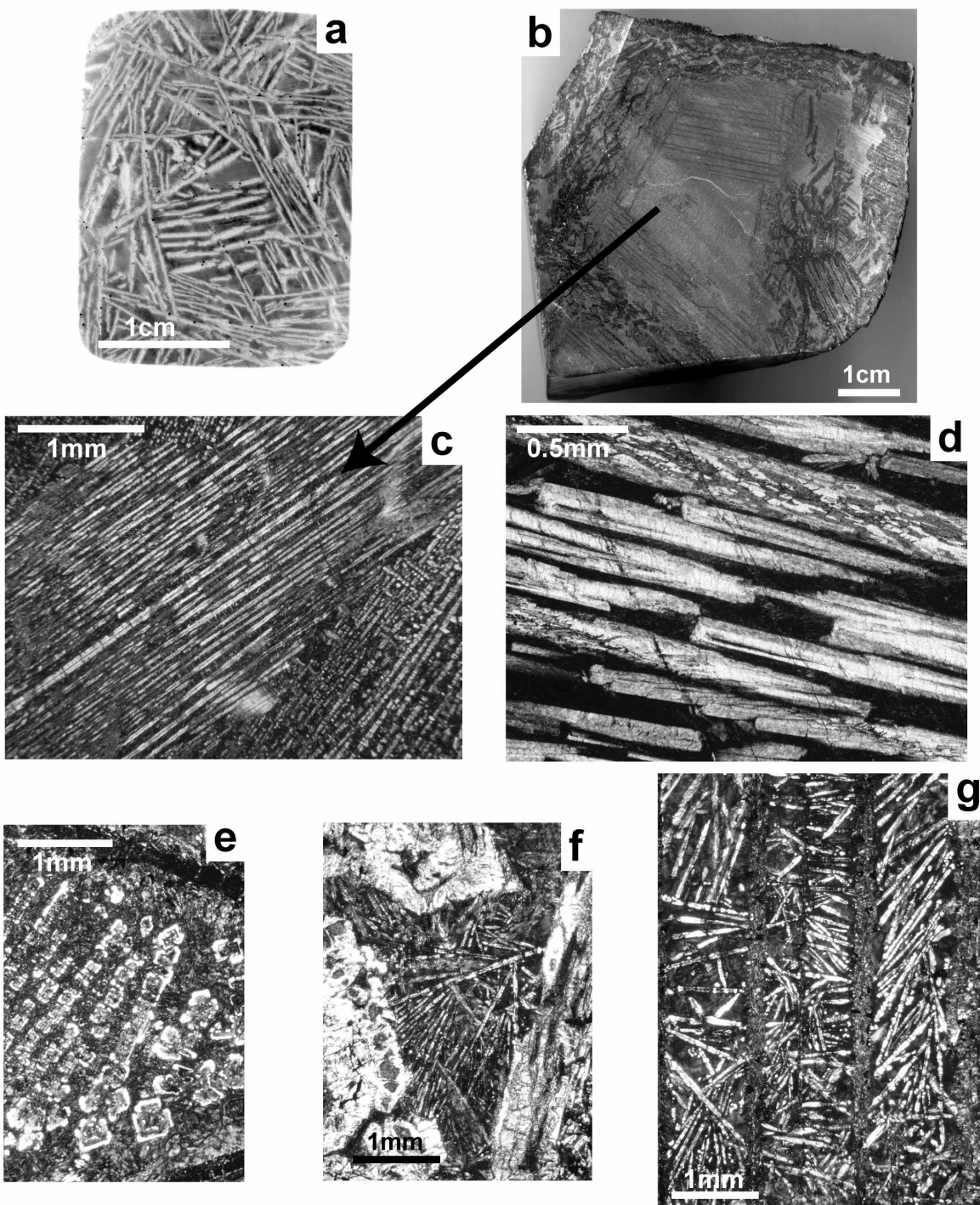


Fig. 2. Textures of komatiites from the Alexo area. (a) A scanned thin section of a random olivine spinifex-textured lava (sample M662). Olivine crystals (in white) are randomly oriented and lie in a fine-grained matrix. (b) Polished slab of coarse platy olivine spinifex textured lava, sample Ax105. Large complex dendritic grains of olivine (black, serpentinized) enclose a cell within which large pyroxene needles have grown. (c) Thin section showing thin needles of complex zoned pyroxene crystals in sample Ax105 (cross-polarized light). (d) Thin section showing in greater detail the zoned pyroxene megacrysts from Ax106. White pigeonite cores are mantled by grey-coloured augite margins. (e) Zoned pyroxene grains cut perpendicular to the c-axis, from within an olivine cell in olivine spinifex textured lava, sample M626. Augite rims (in white) are well preserved; pigeonite cores have altered to chlorite. (f, g) Small skeletal augites between olivine grains, sample M626. Olivine appears in white in figure f, and dark grey in Figure g

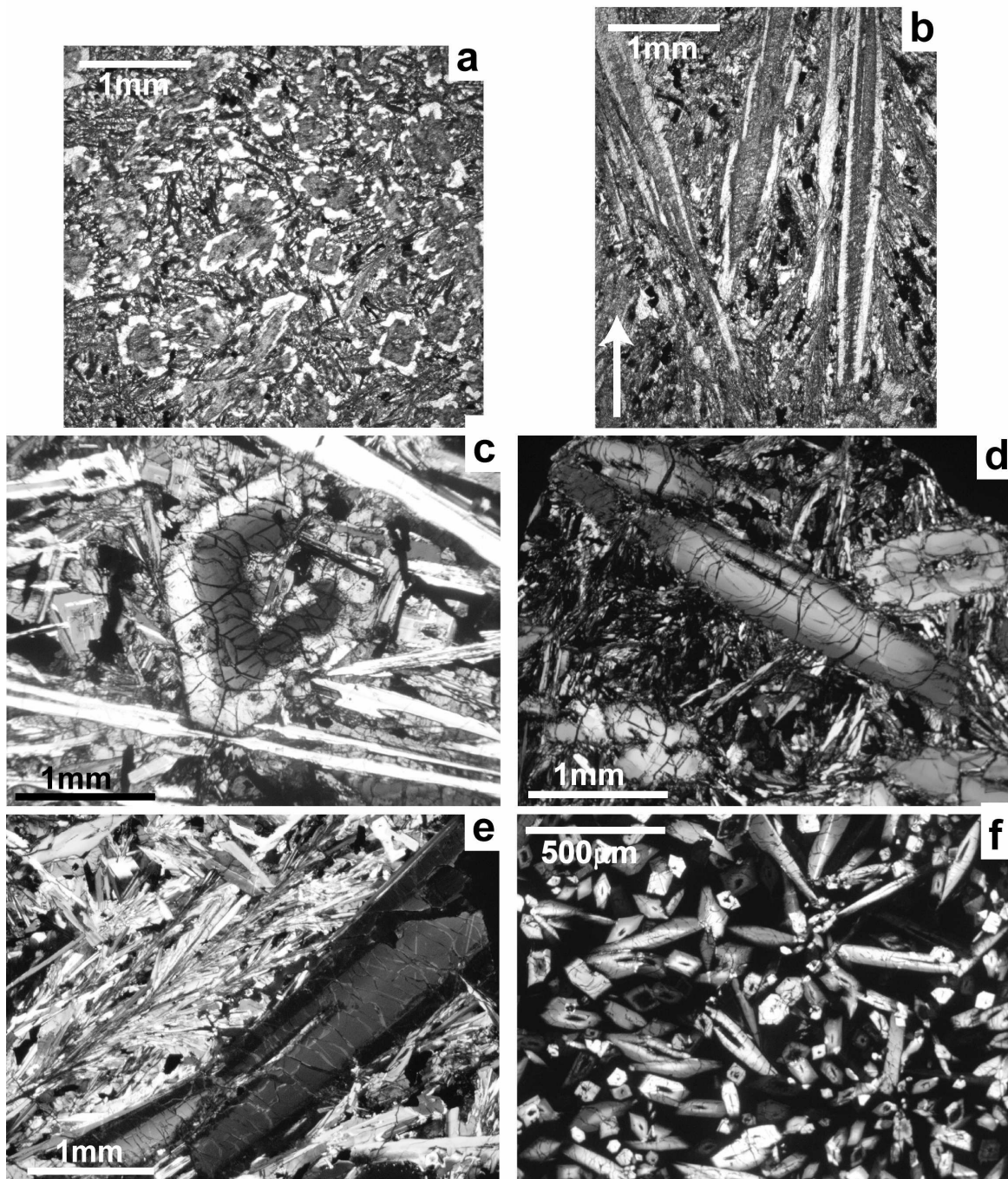


Fig. 3. Photomicrographs of representative thin sections, showing zoned pyroxene with pigeonite cores and augite rims. (a) Pyroxene spinifex lava (sample Ax101) from upper part of the komatiitic basalt flow of Alexo.; the section is cut perpendicular to the flow and perpendicular to the c-axes of the pyroxenes. (b) Same sample, cut parallel to the c-axes. The direction to the flow top is indicated by the white arrow. (c) Lunar basalt, sample 12021,136. This sample contains a zoned pyroxene with a dark grey pigeonite core and a pale grey augite mantle. Plagioclase laths (white) are intergrown with augite (grey) in the matrix. (d) Zoned pyroxene with hollow shapes in a matrix of augite+plagioclase+oxides (lunar sample 12052,336). (e) Coarse phenocrysts of pyroxene (light grey pigeonite and dark grey augite) embedded in a fine-grained groundmass of intergrown pyroxene and plagioclase (plumose structure), opaque phases and glass (lunar sample 12052,336). (f) Small phenocrysts of zoned pyroxene in a silica glass, lunar sample 15597,75

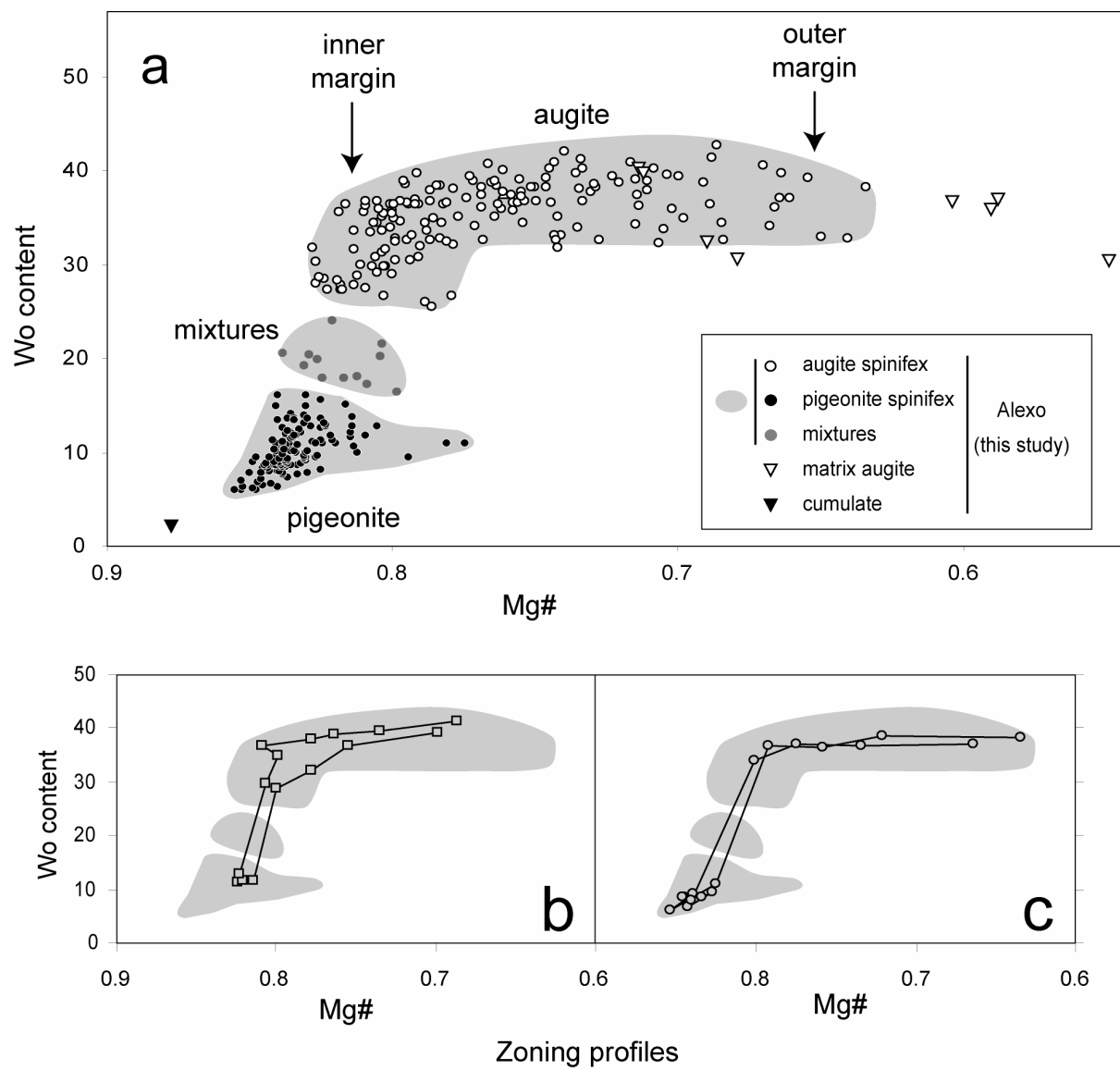


Fig. 4. (a) Mg# vs Wo content of pyroxenes from Alexo komatiites (b,c) Representative profiles of zoned pyroxenes in plate olivine spinifex lavas from the Alexo komatiite flow. The distance between points is 15 m for the profile on the left and 20 m for the profile on the right

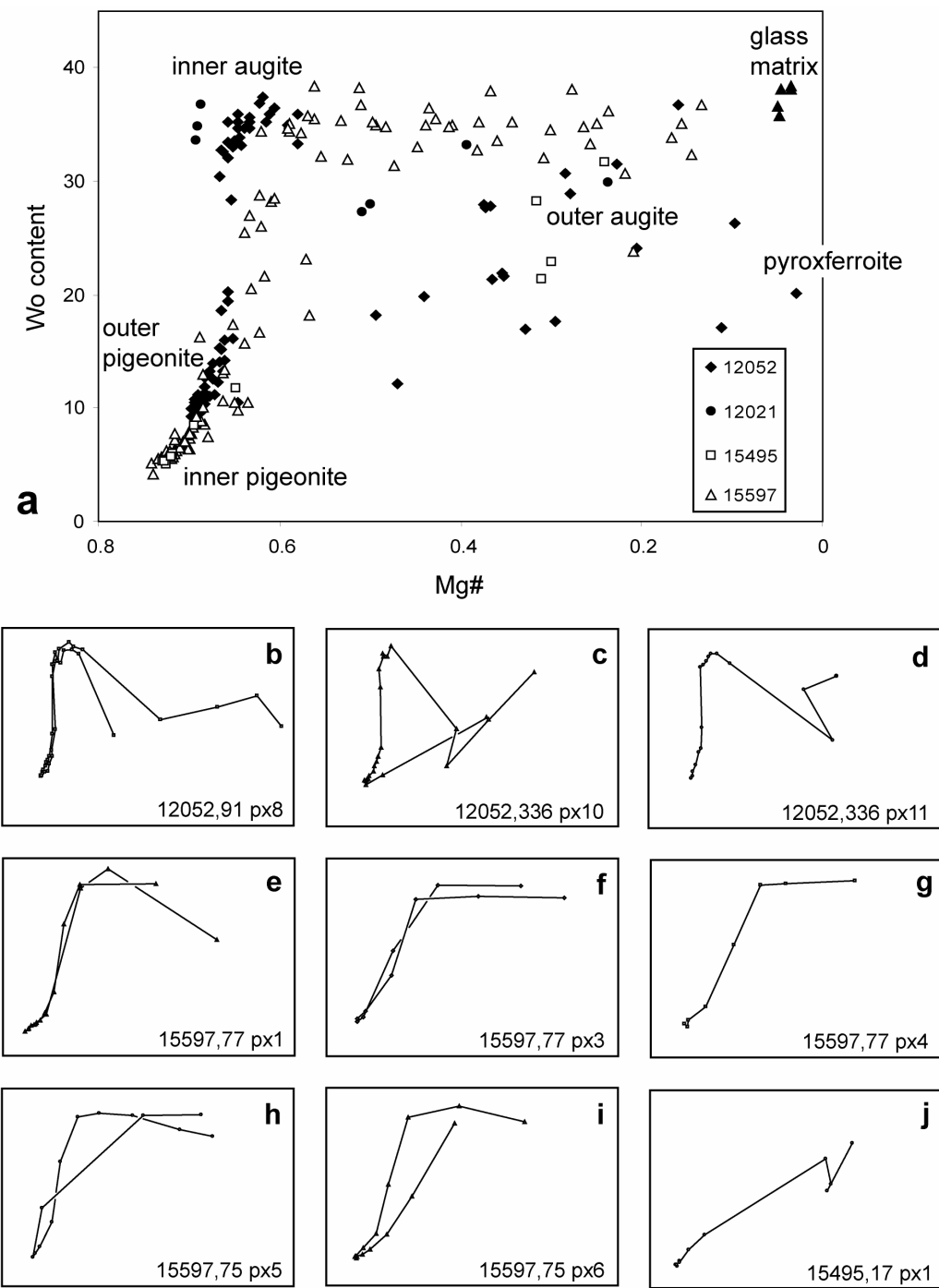


Fig. 5. (a) Mg# vs Wo content of pyroxenes from lunar pigeonite basalts. (b to j) Representative profiles of zoned pyroxenes. The distance between points is 10 m for all profiles, except profiles g and h where it is 5 m. All profiles are rim-core-rim except for profiles d, g and j which are core-to-rim

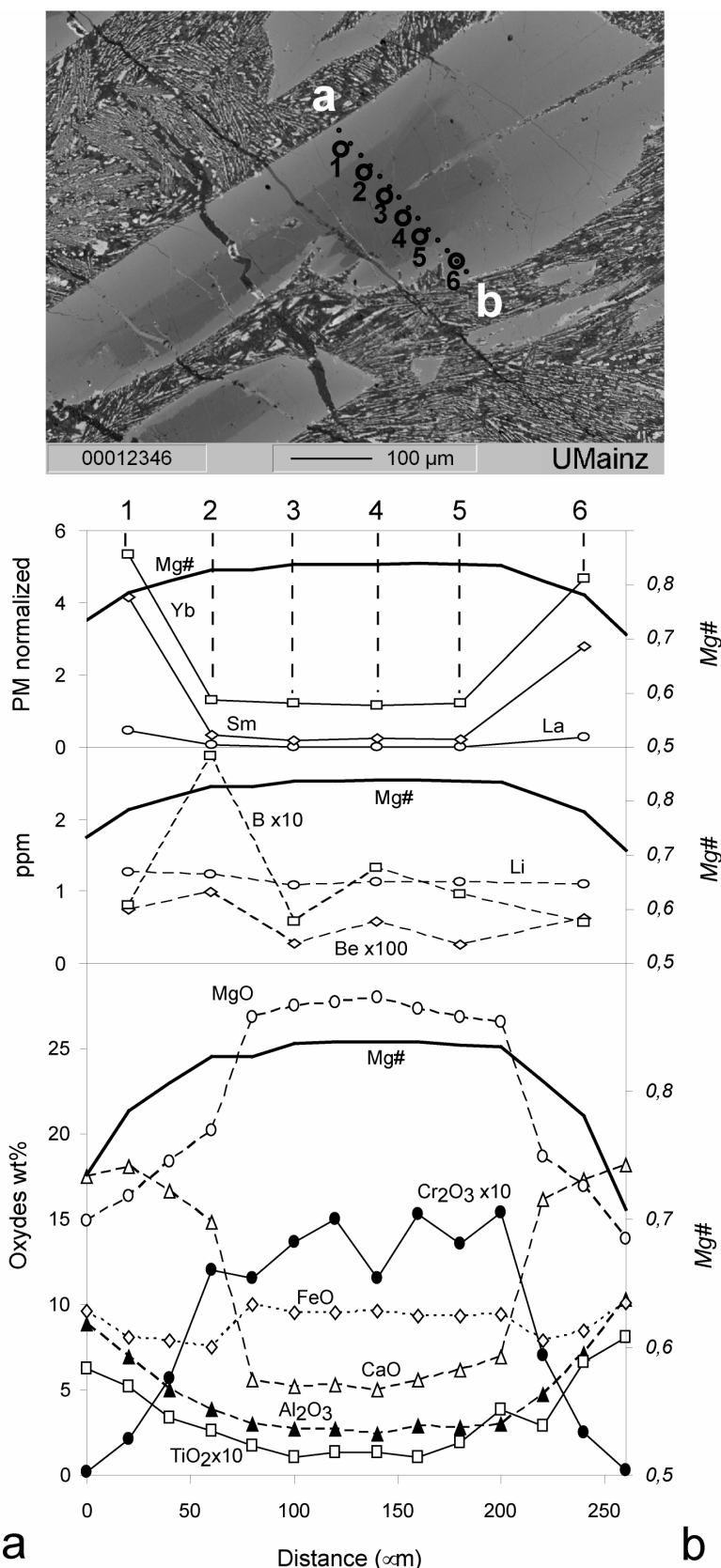


Fig. 6. Komatiite sample Ax106: profiles across a pyroxene grain in plate olivine spinifex unit showing zoning in major and minor element concentrations, plus three representative rare earth elements (La, Sm, Yb) and the light lithophile elements Li, Be, B. Variations are discussed in the text. The picture is a back-scattered electron (BSE) image acquired with an electron microprobe in Nancy

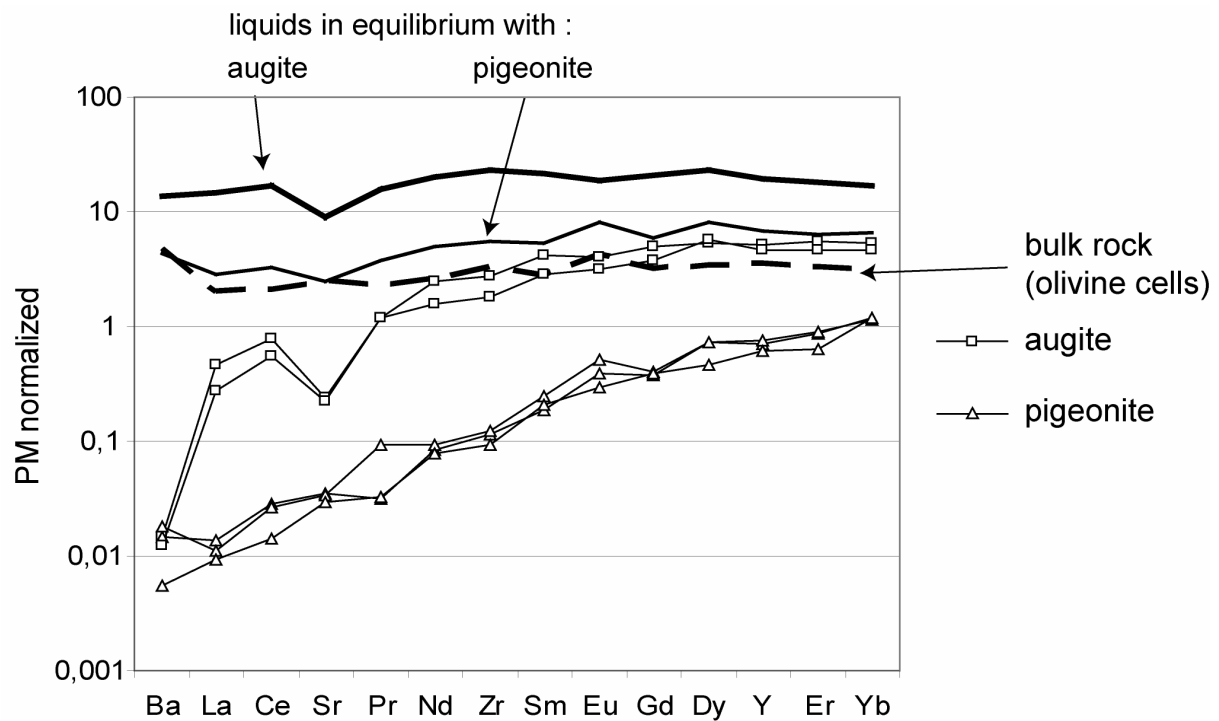


Fig. 7. Mantle-normalized trace elements showing representative analyses of the pigeonite core and augite rim compositions of pyroxene in olivine spinifex unit of the Alexo komatiite flow, sample AX105. Also shown are calculated compositions of liquids in equilibrium with these pyroxenes and the bulk rock composition of sample Ax105

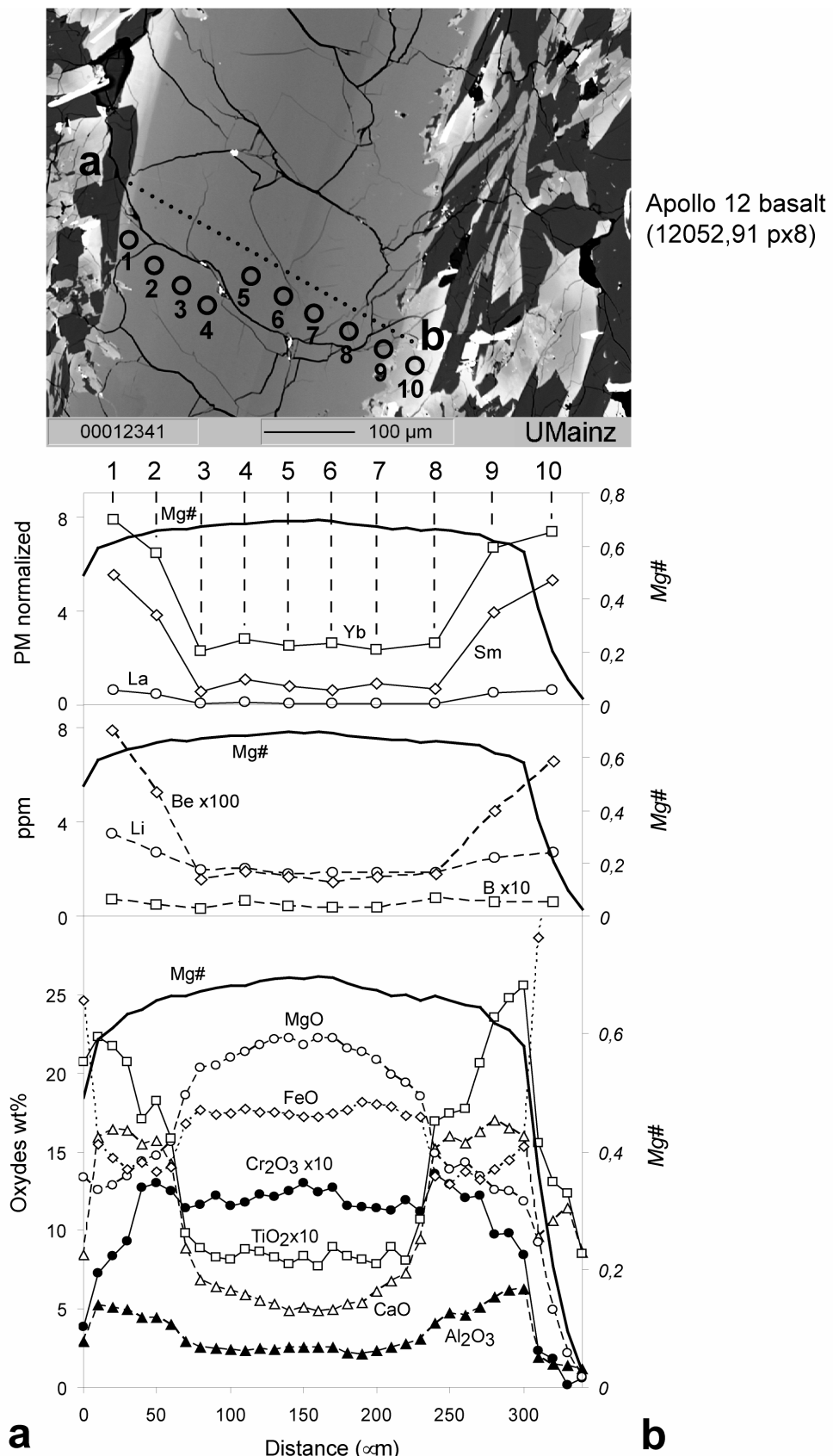


Fig. 8. Profiles across a pyroxene grain in lunar basalt 12052. Variations are discussed in the text. The picture is a BSE image. For a more comprehensive view, FeO data were intentionally hidden on the right of the bottom profile. Values of FeO are linear and climb to 42wt%. Data can be found in Table 1

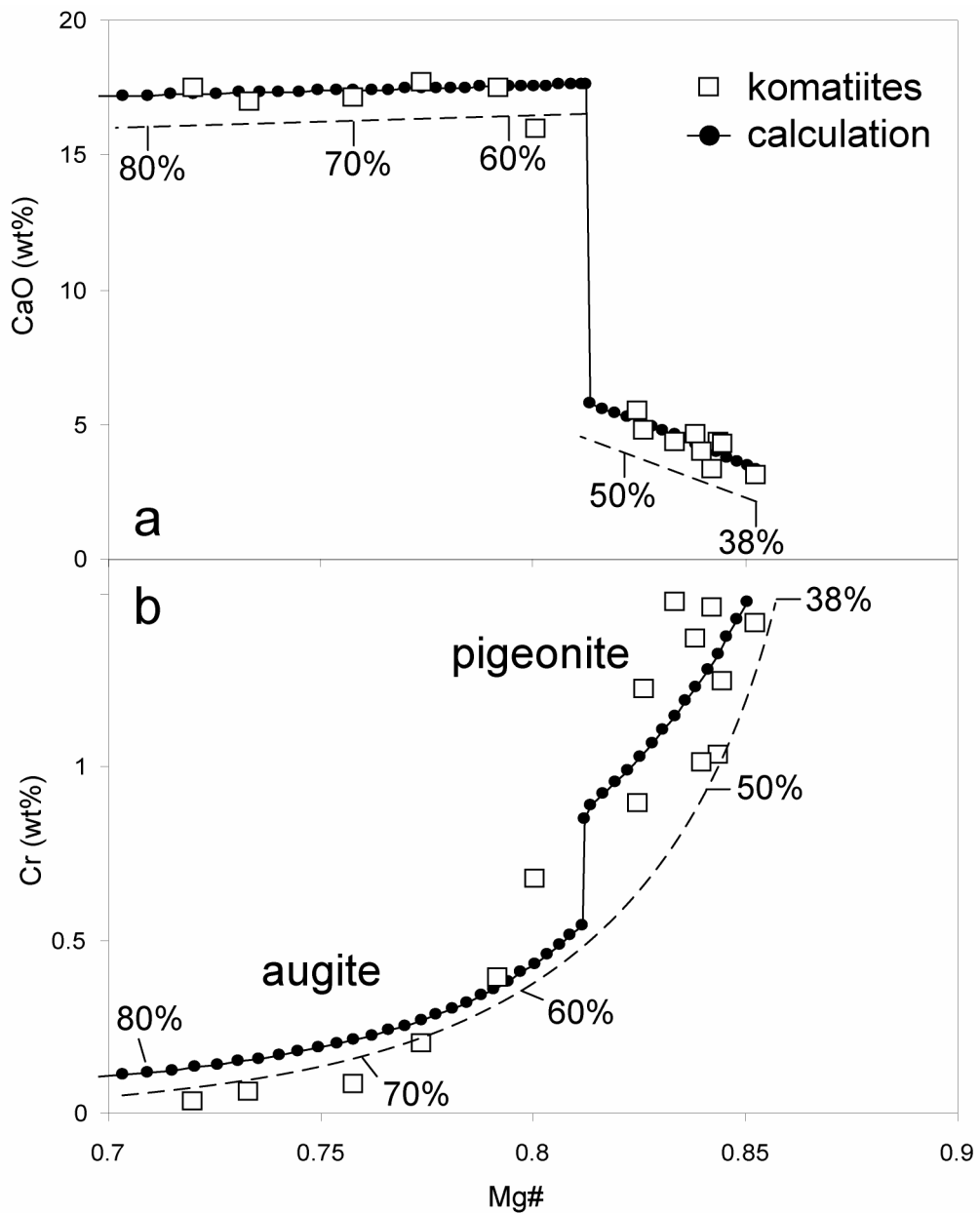


Fig. 9. Variations of CaO (a) and chromium (b) in zoned pyroxenes from komatiites. These data can be modelled in terms of crystallization of olivine (from 0 to 38%), pigeonite (from 38 to 54%) and augite (from 54%). Olivine crystallization is not shown here. Partition coefficients are given in Table 3

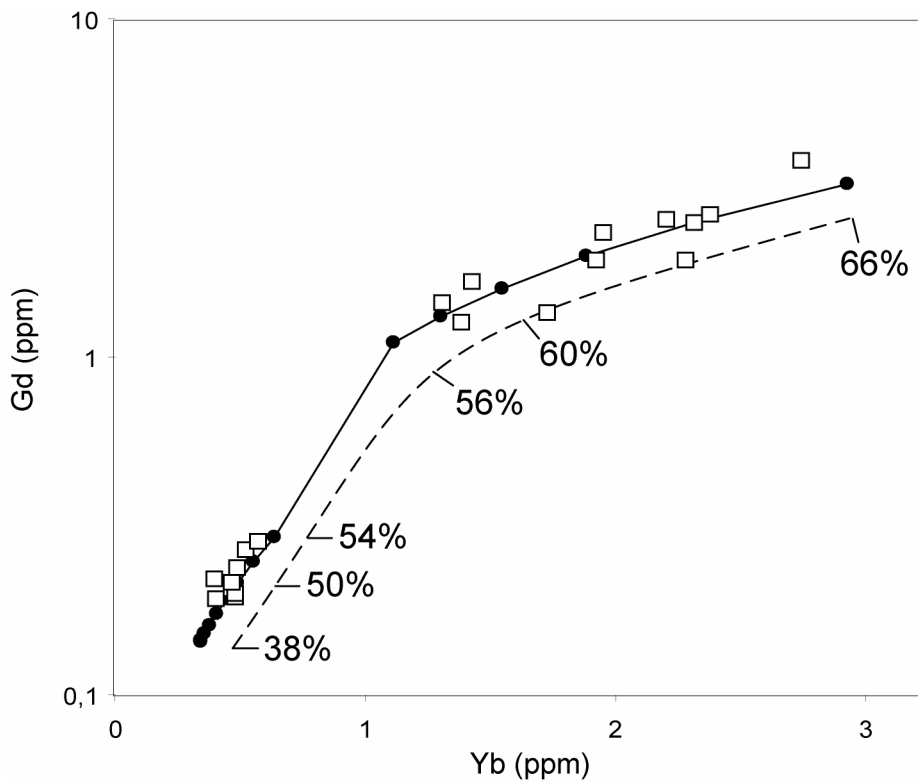


Fig. 10. The behaviour of REE can be modelled as Rayleigh fractionation trends (black lines). Partition coefficients for Gd and Yb were adjusted with a graphical approach. Partition coefficients are given in Table 3. Pyroxene data were acquired by ion microprobe on a single spinifex crystal from sample Ax106

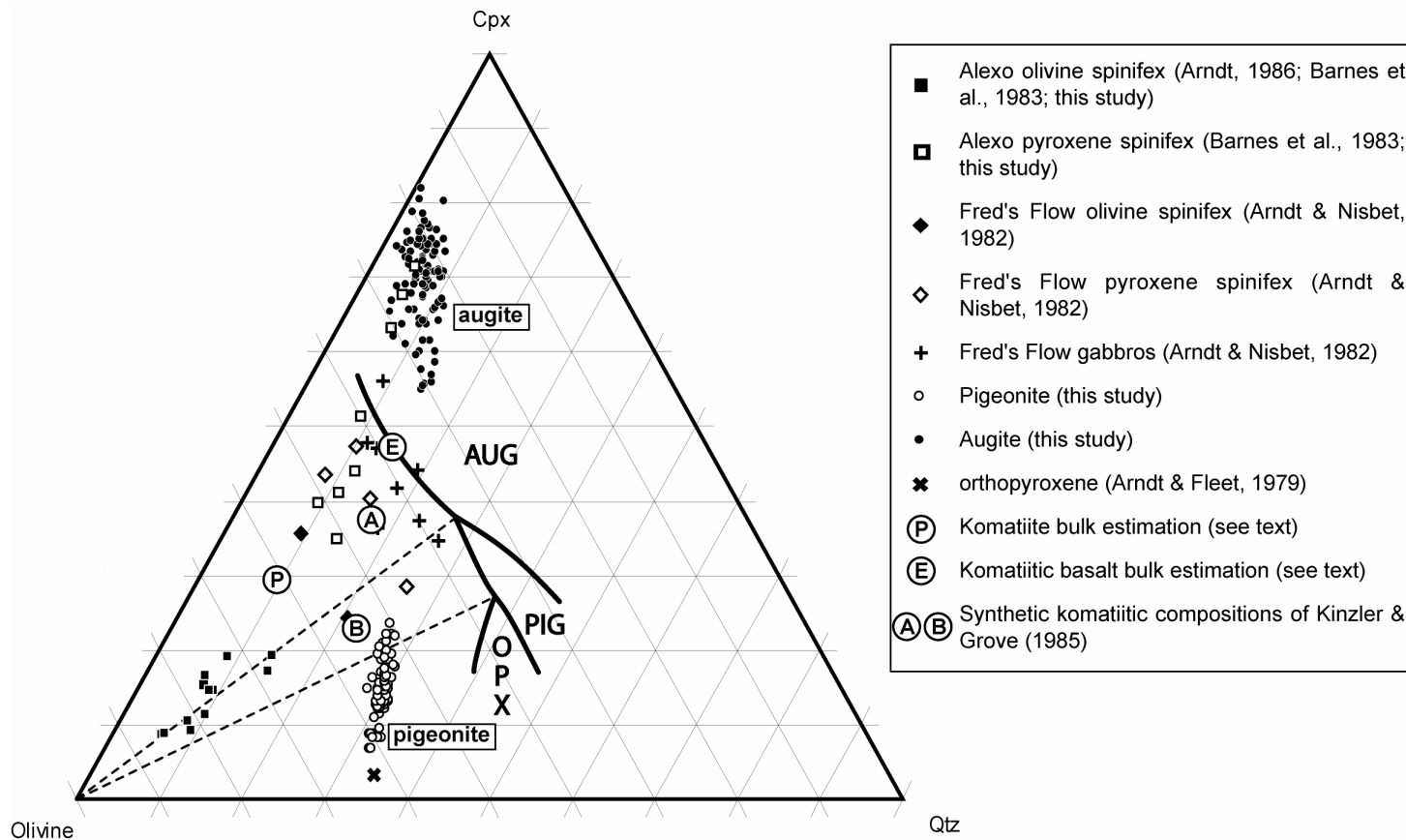


Fig. 11. Bulk compositions of spinifex rocks from the Alexo komatiite and komatiitic basalt and from Fred's Flow, plotted in the olivine-clinopyroxene-quartz pseudo-ternary diagram. Also shown are our analyses of pigeonite and augite from spinifex part of Alexo komatiite. Orthopyroxene was measured in the cumulate layer of the Alexo komatiitic basalt (data from Arndt & Fleet, 1979). The dashed lines from olivine to the pigeonite reaction boundary delineate the field of liquids in which pigeonite is the first pyroxene to crystallize. Above the upper dashed line, augite will crystallize first; below the lower dashed line, orthopyroxene will be first. One-atmosphere liquidus phase relations are shown from Kinzler & Grove (1985)

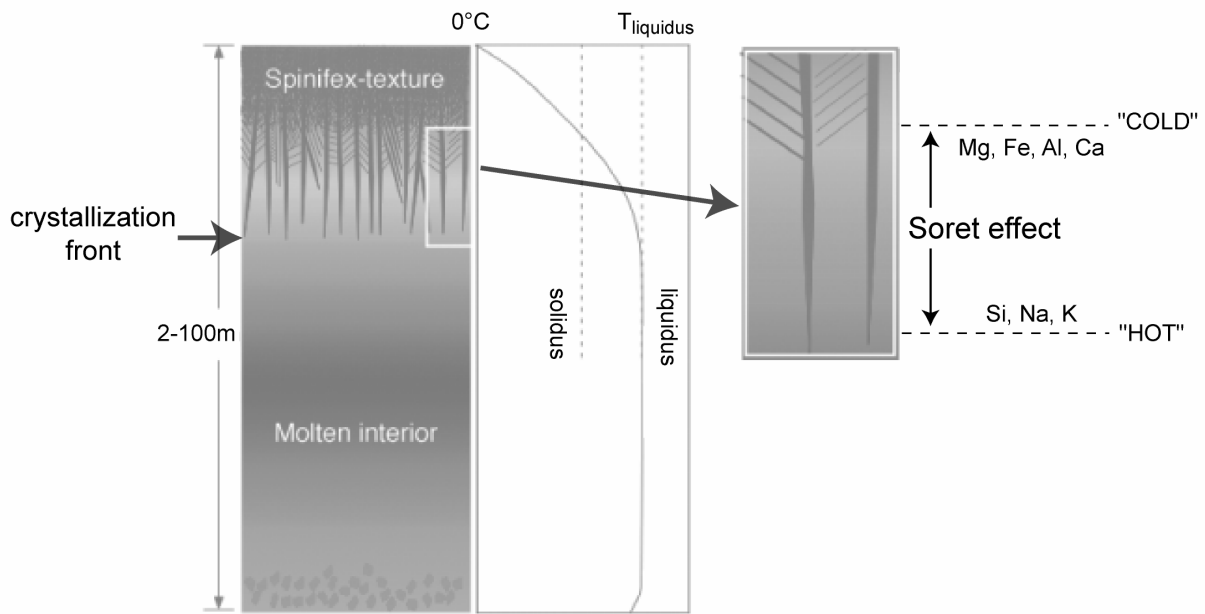


Fig. 12. Role of the Soret effect in crystallizing pyroxene megacrysts in pyroxene spinifex-textured lavas. The schematic view on the right shows a typical komatiitic flow being cooled, with an upper spinifex-textured rock separated to a molten interior by the crystallization front, and a basal cumulate. The sketch on the left is a detail of the crystallization front, where a Soret effect is present

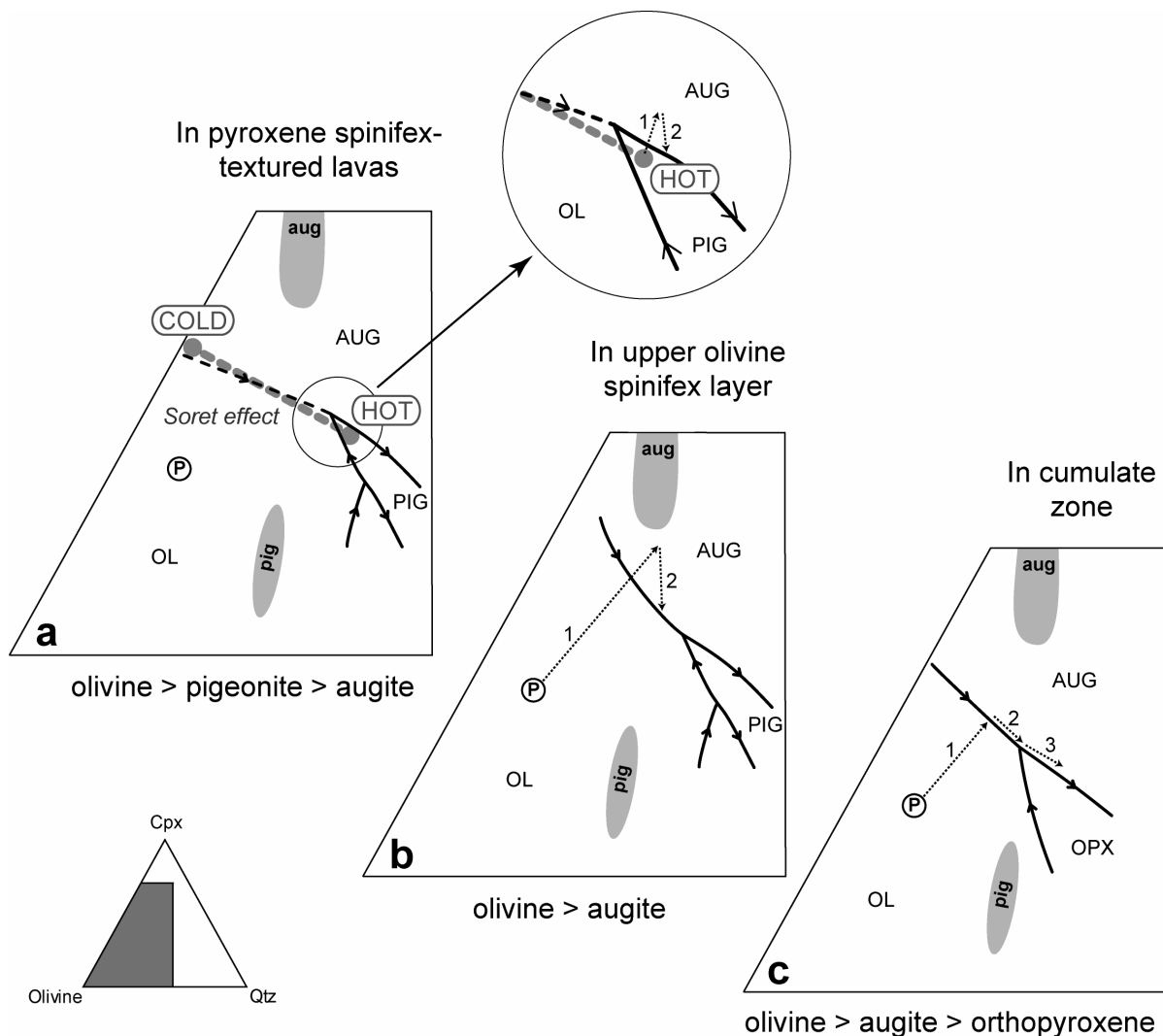


Fig. 13. Proposed crystallization history for pyroxene spinifex-textured komatiite. 'P' is a possible composition of the komatiitic parental melt. Grey fields represent the compositions of pigeonite and augite data. Dashed lines correspond to the two- or three-step fractionation paths, as discussed in the text.

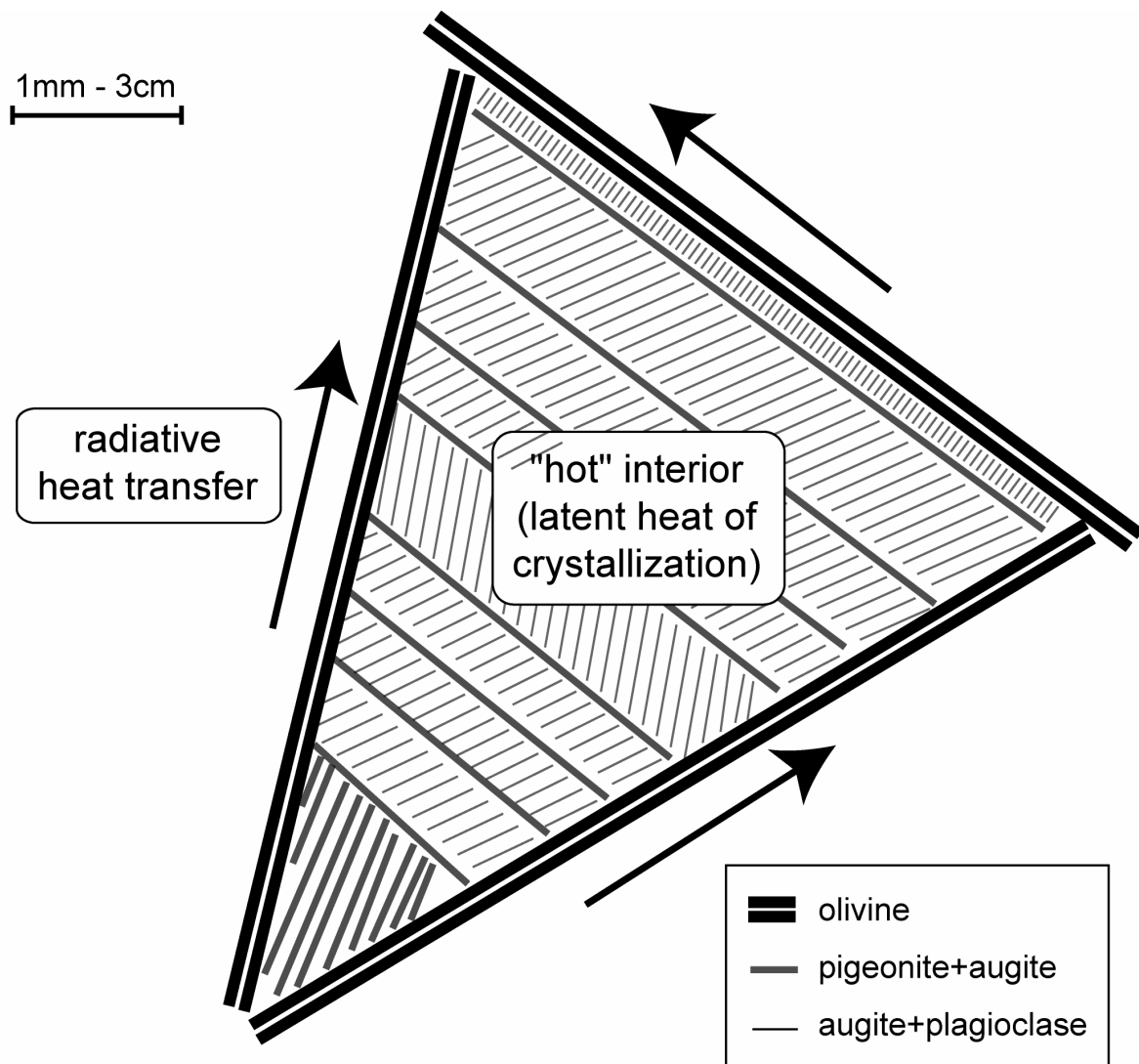


Fig. 14. Schematic view of crystallization processes within a cell between olivine plates in coarse platy olivine spinifex-textured lava. Heat is efficiently evacuated along the platy olivine crystals and latent heat is released by crystallization. Pigeonite nucleates on relatively cold olivine crystals, then grows towards the hot interior of cells. Augite develops as rims on pigeonite, and crystallization ends with the growth of augite and plagioclase between the larger pyroxene crystals

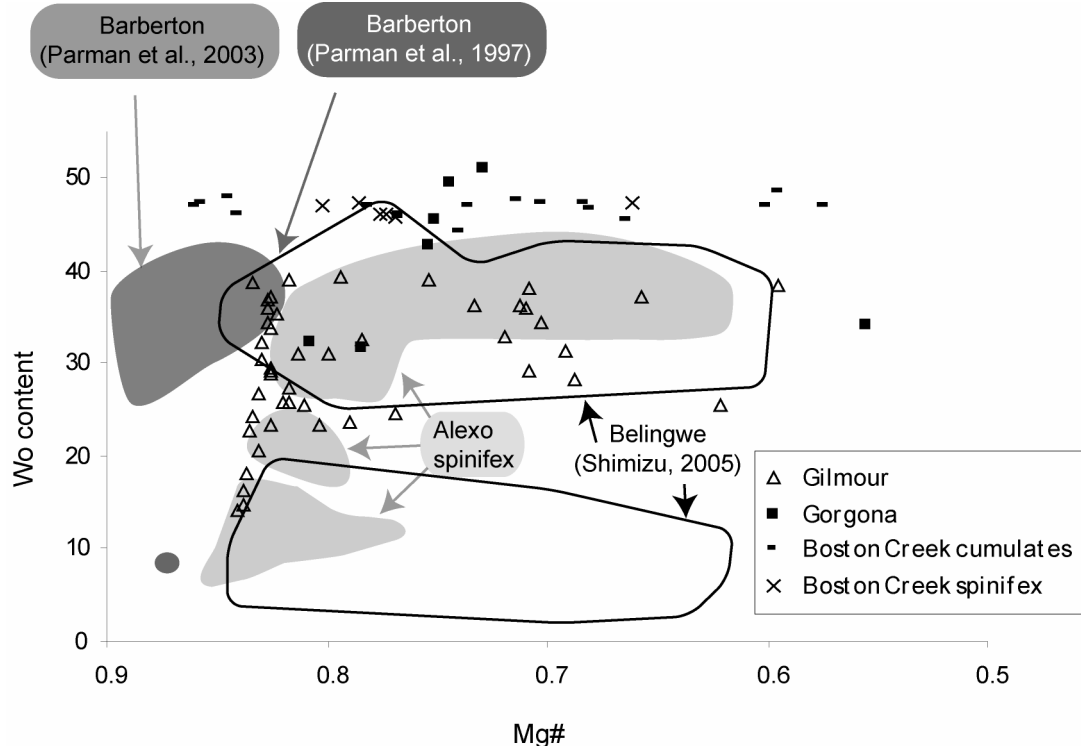


Fig. 15. Mg# vs Wo contents of clinopyroxene from Alexo (this study) and Barberton (Parman et al., 1997 and 2003). Circles are clinopyroxene in Alexo komatiite (pigeonites cores in black, augite rims as white circles and mixtures of both pyroxenes in grey)

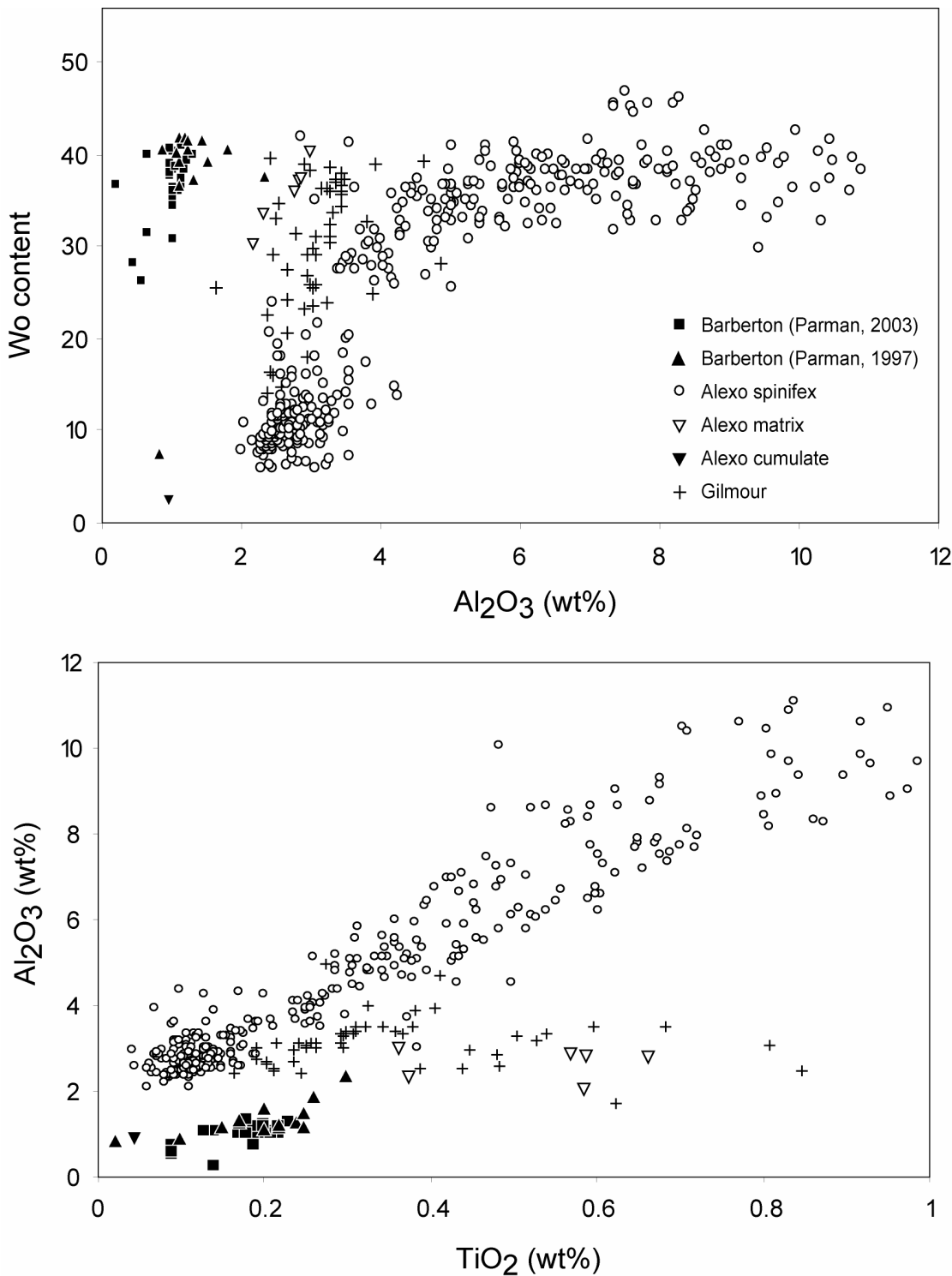


Fig. 16. Mg# vs Wo contents of clinopyroxene in komatiites from various studies and locations worldwide. The light grey field represents analyses of this study (Alexo), dark grey fields are from Parman et al. (1997, 2003) papers. Solid lines define fields of pigeonite and augite from Belingwe komatiites and komatiitic basalts of Shimizu et al. (2005). High Wo content of clinopyroxene is not a particularity of Barberton komatiite: clinopyroxene in these rocks only have higher Mg# than pyroxene in other komatiites

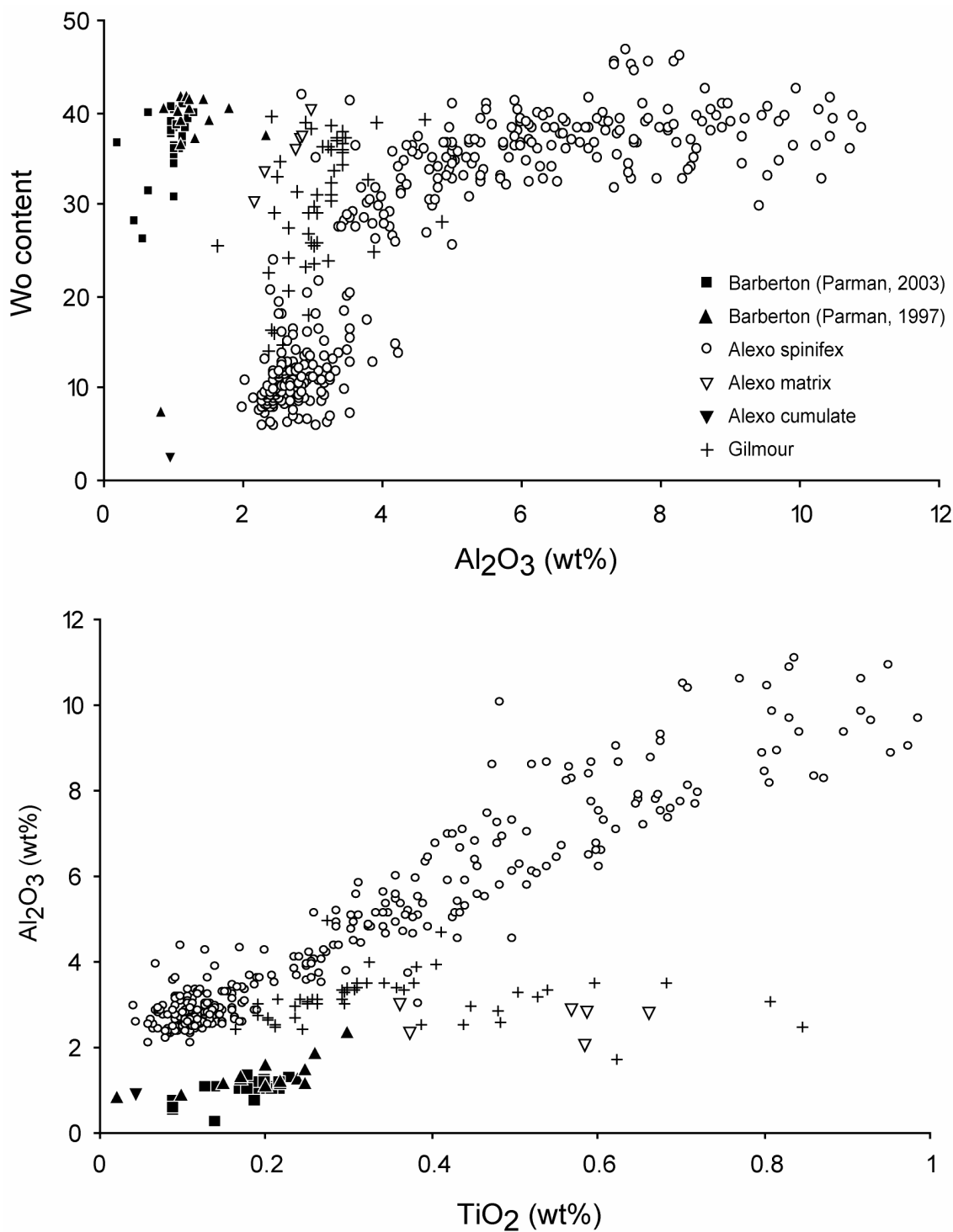


Fig. 17. Wo content vs Al_2O_3 and Al_2O_3 vs TiO_2 plots of pyroxenes in komatiites from Alexo, Barberton (Parman et al. 1997, 2003) and Gilmour Island (unpublished data). Barberton clinopyroxenes have lower Al (and Ti) contents due to lower Al (and Ti) contents of the liquid

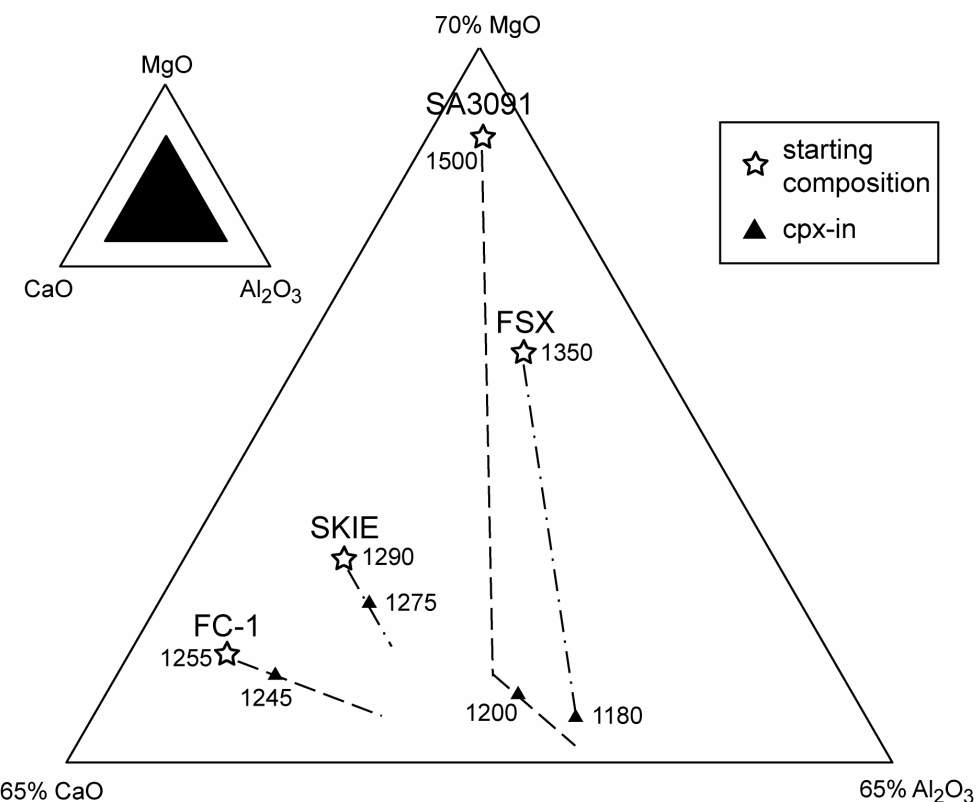


Fig. 18. Compositions of glasses produced by melting natural (FC-1; SA3091 and FSX) and synthetic (SKIE) komatiite samples at 1atm (from Arndt 1977 and unpublished data). Clinopyroxene crystallizes at higher temperatures in starting compositions with high CaO/Al₂O₃ ratios

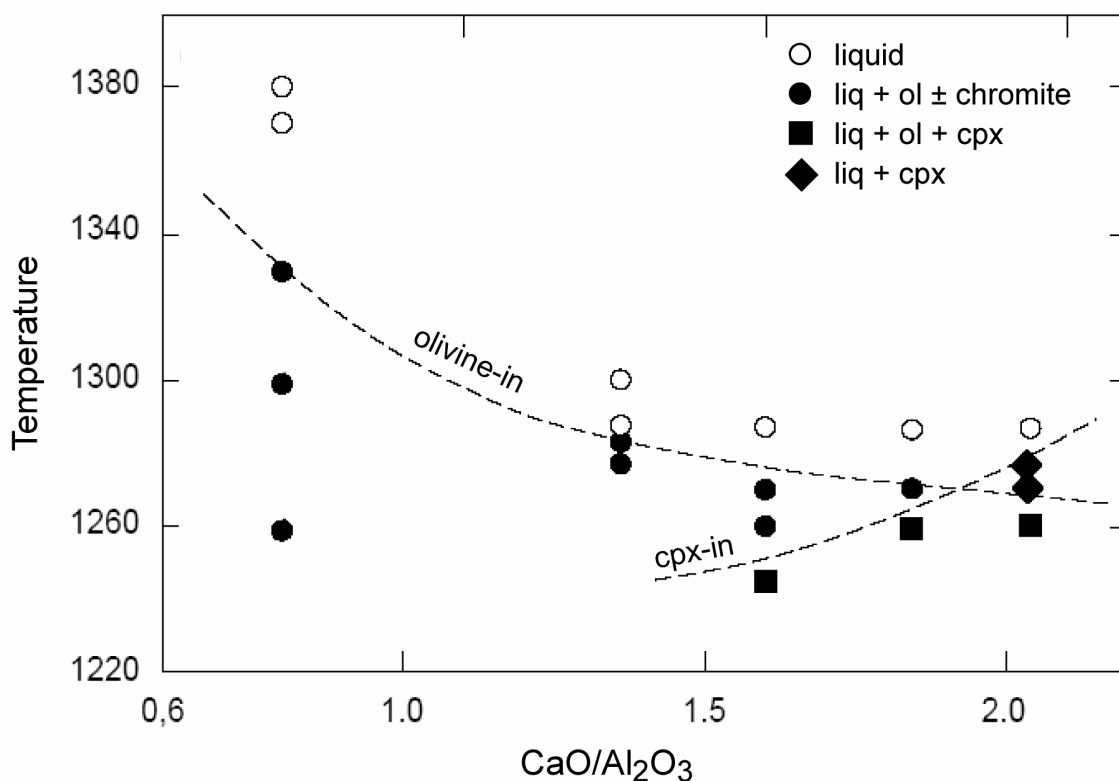


Fig. 19. Diagram showing the crystallization sequences of a series of experimental charges whose compositions are those of komatiitic basalts with differing CaO/Al₂O₃. The temperature of the first crystallization of augite increases with increasing CaO/Al₂O₃. Data from Arndt (1977, unpublished)

Table 1. Major and trace element data

	Ax106 px4		Ax106 px2		12052,91 px8			
mineral	augite	pigeonite	augite	pigeonite	inner pigeonite	outer pigeonite	inner augite	outer augite
link	point #1 in Fig. 6	point #3 in Fig. 6			point #5 in Fig. 8	point #8 in Fig. 8	point #9 in Fig. 8	point #10 in Fig. 8
SiO ₂	48,99	53,80	49,71	52,86	51,54	49,35	47,85	47,97
Al ₂ O ₃	6,93	2,71	5,44	2,89	2,54	4,08	5,71	1,48
TiO ₂	0,52	0,10	0,31	0,14	0,79	1,69	2,35	1,31
Cr ₂ O ₃	0,21	1,37	0,19	1,59	1,25	1,36	0,97	0,19
FeO	8,03	9,52	9,19	9,57	17,33	13,42	13,87	34,04
MnO	0,20	0,26	0,22	0,30	0,31	0,25	0,24	0,49
MgO	16,36	27,54	18,39	26,70	22,25	14,88	12,59	4,91
CaO	18,08	5,20	15,70	6,32	4,89	15,20	16,97	10,59
Na ₂ O	0,13	0,04	0,11	0,08	0,01	0,01	0,10	0,06
K ₂ O	0,00	0,01	0,00	0,01	0,00	0,01	0,01	0,02
Total	99,46	100,55	99,32	100,57	100,91	100,24	100,67	101,05
Mg#	0,78	0,84	0,78	0,83	0,70	0,66	0,62	0,20
En	48,31	75,20	52,79	72,92	62,69	44,63	38,65	15,53
Wo	38,38	10,21	32,40	12,41	9,91	32,78	37,46	24,07
Fs	13,31	14,59	14,80	14,67	27,40	22,59	23,89	60,40
Li	1,27	1,08	0,92	1,01	1,78	1,83	2,49	2,67
Be	0,008	0,003	0,004	0,003	0,02	0,02	0,04	0,07
B	0,08	0,06	0,11	0,04	0,04	0,07	0,06	0,06
Ba	0,09	0,09	0,29	0,02	0,01	0,06	0,03	0,04
Sr	4,29	0,63	2,91	0,50	1,06	0,68	7,05	8,85
Zr	26,98	1,10	12,41	1,03	5,00	4,55	23,27	30,29
Y	20,37	2,77	18,74	2,93	7,40	6,98	22,98	26,85
La	0,28	0,01	0,18	0,01	0,04	0,02	0,33	0,39
Ce	1,27	0,04	0,79	0,04	0,23	0,14	1,55	2,04
Pr	0,29	0,01	0,22	0,02	0,04	0,05	0,44	0,51
Nd	2,90	0,10	1,95	0,08	0,41	0,35	3,01	3,22
Sm	1,60	0,07	1,15	0,09	0,31	0,28	1,52	2,06
Eu	0,59	0,06	0,47	0,02	0,03	0,01	0,16	0,16
Gd	2,55	0,19	1,95	0,22	0,58	0,57	2,66	2,99
Dy	3,40	0,47	3,26	0,54	1,30	1,12	4,14	4,87
Er	2,31	0,37	2,12	0,40	0,89	0,75	2,61	2,91
Yb	2,21	0,50	2,29	0,48	1,03	1,07	2,76	3,03

Note

Oxides in wt%; trace elements in ppm

Table 2. Major element data used for modelling of pyroxene-bearing spinifex-textured komatiitic rocks

	M668	P	E
SiO ₂	45.80	46.32	48.90
TiO ₂	0.44	0.31	0.37
Al ₂ O ₃	8.60	6.63	10.55
Fe ₂ O ₃	12.70	13.30	12.90
MnO	0.16	-	-
MgO	23.50	23.92	13.49
CaO	7.80	8.88	12.81
Na ₂ O	0.09	0.39	0.63
K ₂ O	0.04	-	-
Cr	2790	2640	3440
<i>Modal estimations</i>			
olivine	0.30	0	
pigeonite	0.10	0.20	
augite	0.30	0.45	
plagioclase	0.05	0.15	
glass	0.20	0.15	
oxide	0.05	0.05	

Notes

1. Analyses recalculated to 100% on volatile-free basis
2. Total iron as Fe₂O₃
3. Oxides in wt%; Cr in ppm

Table 3. Partition coefficients used during the modelling of the REE behaviour in komatiites

	this paper	Hart & Dunn, 1993	Sobolev, 1996	Schwandt & McKay, 1998	
	pigeonite	augite	cpx	cpx	low-Ca pyroxene
Fe-Mg _{pyroxene-liq}	0,3	0,3	-	-	-
Cr	4,5	7	3,8	-	-
La	0,004	0,025	0,054	0,032	0,00045
Ce	0,007	0,04	0,086	0,057	0,0011
Sr	0,013	0,03	0,128	0,082	
Nd	0,019	0,10	0,187	0,129	0,0039
Zr	0,02	0,10	0,123	0,046	
Sm	0,04	0,16	0,291	0,211	0,0110
Eu	0,06	0,19	0,300		0,0039
Gd	0,08	0,21			
Dy	0,09	0,24	0,442	0,256	0,045
Y	0,11	0,25	0,467	0,245	
Er	0,15	0,28	0,387	0,259	0,084
Yb	0,21	0,30	0,430	0,214	0,097

Chapter 7:
**An experimental study of pyroxene crystallization during rapid
cooling in a thermal gradient; applications to komatiites**

S. Bouquain¹, N.T. Arndt¹, F. Faure² and G. Libourel²

¹LGCA, CNRS UMR 5025, Université J. Fourier, BP53, 38041 Grenoble Cedex, France

²Nancy Université, CNRS/INSU, CRPG, 15 rue Notre Dame des Pauvres, 54501 Vandoeuvre-les-Nancy, France

Corresponding author:

sebastien.bouquain@ujf-grenoble.fr; Tel: +33476514063; Fax: +33476514058

Keywords: pyroxene; pigeonite; komatiite; spinifex; thermal gradient

Abstract

To investigate the crystallization of pyroxene in spinifex-textured komatiites and in chondrites we undertook a series of experiments in which compositions in the CMAS system were cooling rapidly in a thermal gradient. Cooling rates were generally between 5 to 10°C/h but some runs were made at 100-200°C/h; thermal gradients were between 10 and 20°C/cm. These conditions reproduced those at various levels in the crust of komatiitic lava flow. The starting composition was chosen to have pigeonite on the liquidus and a majority of the experiments crystallized zoned pigeonite-diopside crystals like those in komatiite lavas. A conspicuous aspect of the experimental results was their lack of reproducibility. Some experiments crystallized forsterite whereas others that were run under similar conditions crystallized two pyroxenes and no forsterite; some experiments were totally glassy but others totally crystallized to pyroxene. The degree of supercooling at the onset of pyroxene crystallization was variable, from less than 25°C to more than 100°C. We attribute these results to the difficulty of nucleation of pyroxene. In some cases forsterite crystallized metastably and modified the liquid composition to inhibit pyroxene crystallization; in others no nucleation took place until a large degree of supercooling was achieved, then pyroxene crystallized rapidly. Pigeonite crystallized under a wide range of conditions, at cooling rates from 3 to 100°C/h. The notion that this mineral only forms at low cooling rates is not correct.

1. Introduction

Pyroxenes in spinifex-textured komatiites display unusual textures and compositional variations that are probably related to the unusual conditions in which they crystallized. In the internal zones of spinifex layers in thick komatiitic basaltic flows, two pyroxenes commonly are present. Where best developed, pyroxene spinifex texture consists of zoned needles with pigeonite cores and augite margins, commonly organized in clusters that are oriented approximately perpendicular to the flow contacts. Analysis of the compositions of these pyroxenes and of the rocks in which are found has revealed some puzzling features. In many samples pyroxene, usually pigeonite, can be inferred to be the liquidus phase on the basis of textural data, yet when the phase relations of compositions like those of the samples are investigated, it is found that only olivine should have crystallized under equilibrium conditions. The problem has been addressed from a mineralogical and chemical point of view in a companion paper (Bouquain et al. 2008). Here we present the results of a parallel experimental study.

Faure et al. (2006) conducted a series of experiments in which they investigated the origin of spinifex textures. They addressed what has been called the spinifex paradox: the skeletal or dendritic habits of olivine crystals in spinifex textures resemble those in experimental charges that crystallized at high cooling rates (50-100°C/h), but these textures are found deep in the interior of lava flows at depths where the cooling rate, limited by conduction through the flow top, must have been low (<1 to 5°C/h). A novel aspect of Faure et al.'s experiments is that they were conducted within the thermal gradient in the upper part of the 1-atm furnace, reproducing the gradient that exists in the upper parts of a lava flow. These experiments produced textures that closely resembled those in olivine spinifex-textured komatiites.

In this paper we present the results of experiments that build on Faure et al.'s work. The major difference is in the composition of the experimental charges: whereas Faure et al. worked on an analogue in the CMAS system of the ultramafic composition of komatiites, we

worked on a less magnesian composition, one chosen so that pigeonite was the liquidus phase. With this choice we developed an experimental program designed to help understand the phase relations and habits of pyroxenes that crystallized under conditions like those in komatiitic lava flows and in chondrites.

2. Experimental procedures

The experiments described in this paper were conducted in the experimental petrology laboratory of Centre de Recherches Pétrographiques et Géochimiques in Nancy using the method developed by Faure et al. (2006). The starting composition in the CMAS (CaO-MgO-Al₂O₃-SiO₂) system was chosen so as to have pigeonite the liquidus and thus to be comparable to the komatiitic liquids that crystallize pyroxene spinifex textures. The starting material was prepared from pure oxides which were fused in platinum crucibles for 8h at 1550°C, a temperature well above the liquidus. The quenched material was then ground to a fine powder in an agate mortar.

For the isothermal crystallization experiments, the powder was mixed with a small amount of polyvinyl alcohol to produce a charge that could be suspended on a platinum wire (Donaldson et al. 1975). The charge was held at constant temperature for several hours in a 1-atm vertical quenching furnace, and quenched in water at the end of the experiment.

For the dynamic crystallization experiments, the powder was packed tightly into a graphite tube (length 5.5-6.5cm, diameter 4mm) that was placed in a GERO HTRV 70-250 vertical quenching furnace. Depending on the location of the tube above the hot spot of the furnace, the temperature gradient across the experimental charge varied from 8 to 40°C/cm. The temperature inside the furnace was measured by PtRh6-PtRh30 thermocouples that had been calibrated by melting gold and palladium wires. Throughout the course of the experiment, a stream of argon maintained a reducing atmosphere, preventing the oxidation of the graphite tubes. In the standard procedure, called procedure 1 (Fig. 1), each experiment began with a stage at which the entire charge was held for one to five hours at a temperature of 1413°C (1505°C at the bottom of the charge), about 27-119°C above the equilibrium liquidus temperature (see Table 1). During this phase, air trapped in the powder escaped, and as the charge compacted during melting, its length decreased from 5-6cm to 2.5-4.5 cm. The charge was then cooled at a constant rate which varied from 3, 5, 10, 100 to 200°C/h depending on the experiment. The temperature gradients across the experimental charge are around 20°C/cm and match those calculated in the upper part of a komatiitic flow.

The intent of this procedure was to progressively crystallize the charge, downwards from the cooler top to the warmer base, thus simulating progressive solidification in the upper crust of a lava flow. As described by Faure et al (2006), this procedure provides important information about the kinetics of crystallization under conditions that reproduce those in natural lavas.

During the experiments labelled CPX15-26, a modified procedure, called procedure 2 (Fig. 1), was used: the experimental charges were first heated to a higher temperature of 1470°C (1555°C at the bottom of the charge), 84-169°C above the liquidus, for two hours, then the temperature was rapidly lowered to bring the top of the capsule (the cool end) to a temperature about 12°C above the liquidus for one hour. The period of high-temperature fusion resulted in optimal homogenization of the charge and the elimination of any relict solid phases. In the other experiments (those labelled CPX04; CPX06-14), the charges were held at a constant temperature 119°C above the liquidus for one or several hours. We also performed two experiments with two other similar procedures (procedures 3 and 4, Fig. 1), in order to

undoubtedly crystallize pyroxene. In procedure 3, the experimental charge was first heated to a high temperature (1525°C at the bottom of the charge) for one hour, then the temperature was rapidly lowered to bring the bottom of the capsule to a temperature about that of the liquidus. The charge was then cooled at a constant rate of 3°C/h. In the procedure 4, the first heat temperature was very low: 1401°C at the bottom of the charge, at the hot end. The temperature before the cooling step was also very low: 1325°C at the bottom of the charge.

At the end of each experiment, the charge was quenched in distilled water. The tube and its experimental charge were then cut along the long axis, imbedded of resin, polished, and then analyzed using an electron microprobe (Cameca SX100 at the University Henri Poincaré, Nancy) and a microfluorescence spectrometer (Eagle III at the University of Grenoble). An attempt was made to terminate each experiment at a temperature calculated to quench to glass an interval of uncrystallized liquid in the lower (hotter) end of the charge: in practice this proved to be very difficult, as described in the following section.

Figure 2 illustrates a typical experimental charge. The lower third consists mostly of translucent glass which became fractured during quenching. Elongate crystals of pyroxene become increasingly abundant toward the top of the charge and the upper portion is totally crystallized to pigeonite, augite and a silica phase, probably tridymite. The temperatures of initial crystallization of each of these phases can be determined with precision by measuring the position in charge, which was previously calibrated for temperature (Faure et al. 2006). During the experiment CPX15 (Fig. 2), a bubble formed at the bottom of the load because of incomplete outgassing of powder during the initial phase of high-temperature fusion. This happened during several experiments, but does not significantly affect their interpretation (this problem was not encountered during the experiments of Faure et al. (2006) who worked on a less viscous komatiitic composition). In the case of CPX15, the experiment was not terminated soon enough to preserve crystal-free glass below the crystallization front. The temperature of the first appearance of pigeonite is therefore a minimum temperature and the estimated degree of nominal undercooling is a maximum value.

The results of the isothermal crystallization experiments are summarized in Table 1 and those of the dynamic cooling experiments are given in Table 2.

Experimental problems

Many experiments did not work as intended, with variable consequences.

- 1) The early experiments were carried out in thin graphite tubes that partially disintegrated in the course of the run. In some cases multiple fine, delicate forsterite crystals penetrated the walls of the capsule and grew outwards to form remarkable porcupine-like structures. Although no detailed information about the crystallization sequence is provided by such experiments, they indicate that forsterite nucleated and grew rapidly at relatively high temperatures, as in the case of experiment CPX06 in which forsterite grew in part of the tube that was at a temperature of 1406°C at the time of quenching.
- 2) In several experiments, empty segments of varying size (5-30mm long) were distributed throughout in the capsule, most commonly near the base or in the middle. We interpret these empty segments as air bubbles that were trapped in the liquid phase during initial melting at high temperatures. Because of the small size of the capsules and the relatively high viscosity of the molten starting material, air trapped in the powder could not always be evacuated. When the air bubble is located at the bottom of the capsule, it has little effect on the course of the experiment. In some experiments, small volumes of melt (a few cubic millimeters) were isolated at the bottom of the capsule, or at the top. The products of crystallization of these melts can be very different from those in the main volume of melt. For example, we observed anorthite and spinel in experiment CPX11, and very Ca-rich

diopside in experiment CPX07.

- 3) It was very difficult to stop the experiments before the crystallization front had reached the base of the capsule. Some experiments were almost entirely glassy or contained only isolated forsterite crystals, and two notable exceptions contained crystal-free glass in the lower portion, but most were entirely crystallized. As discussed below, we infer that the once pyroxene nucleates, it grows rapidly to fill most, or all, of the capsule.
- 4) The experiments were not reproducible. The phases that crystallized, and the order in which they appeared, was not systematic but varied from one experiment to another, even when the experimental conditions were similar or identical. For example, experiments CPX14 and CPX15 were conducted at identical cooling rates ($10^{\circ}\text{C}/\text{h}$) and in the same thermal gradient ($20^{\circ}\text{C}/\text{cm}$). The temperatures at capsule ends at the time of quenching were similar: 1336°C and 1352°C at the hot end and 1272°C and 1278°C at the cool end. Yet despite these similar conditions, forsterite is present in experiment CPX14 (as isolated hopper crystals) but is absent in experiment CPX15. In addition, the morphologies of pyroxene are very different in the two experiments, as described in the section presenting the results of the dynamic cooling experiments.

3. Experimental results

3.1. Isothermal crystallization experiments

The isothermal crystallization experiments were employed to determine the liquidus phase relations of the starting material. The material used in the dynamic cooling experiments (Table 1) was chosen to have pigeonite in the liquidus and appropriately only this mineral crystallized in experiment SB613, which was conducted at 1385°C . The crystals are rounded, with sizes ranging from 5 to $30\ \mu\text{m}$. The calcium content of this pigeonite is very low, around 3.1wt% CaO. The nucleation was heterogeneous and took place on the platinum wire, on the walls of the charge, on a platinum bead that became detached during the preparation of the experiment, and on an air bubble. In an experiment conducted at 1388°C , the entire charge (SB623) is glassy. The temperature liquidus is therefore $1386 \pm 1^{\circ}\text{C}$. Only pigeonite crystallizes at temperatures down to 1359°C , and its Ca content increases gradually from 3.1% to 6.0 wt% (SB625). At 1354°C , diopside appears as abundant, rounded, very small crystals, each a few microns across. The rate of nucleation of diopside was evidently higher than that of pigeonite. A silica mineral, probably tridymite, joined the assemblage to 1348°C (SB618). When it first appears, this mineral has an elongate anhedral habit but at lower temperature it forms euhedral laths that are highly elongated along the c axis. The solidus temperature was not determined because there was still a fraction of the liquid at 1277°C (SB630).

We also performed six other series of isothermal crystallization experiments, each with a different starting material composition (Fig. 3). The results are shown in Fig. 4. This phase diagram represents the 5% An plane in the forsterite-diopside-anorthite-silica system, which is part of the CMAS system. The size of the pigeonite field decreases with increasing anorthite component and disappears completely at moderate Al_2O_3 contents (Longhi and Boudreau 1980).

3.2. Dynamic crystallization experiments

Major results of dynamic crystallization experiments are summarized in Figure 7. Associated data are in Table 2. Nomenclature is from Donaldson (1976) and Faure et al (2003).

Forsterite: In many of the dynamic crystallization experiments, we observed forsterite in addition to one or two pyroxenes. Forsterite crystallized in approximately one third of the experiments, an unexpected result because this mineral did not crystallize in any of isothermal crystallization experiments. In some experiments it coexists with tridymite and is evidently not an equilibrium phase in the starting material. Forsterite was the only crystalline phase in four experimental runs (Table 2), all conducted at a moderate cooling rate of 5°C/h. In experiments with higher cooling rates (100-200°C/h) forsterite did not appear. In most experiments, the forsterite crystals have euhedral, or elongate platy, or dendritic habits (Fig. 5). In the runs labelled CPX03 and CPX04, conducted with a low thermal gradient (10°C/cm), a few euhedral forsterite crystals with well-developed faces were observed at the base of the capsule (Fig. 5f). These experiments were quenched at about 1380°C. The crystals contain about 0.7 wt% CaO, and residual glass has a forsterite-depleted composition, with lower SiO₂ and higher CaO, compared to the starting material.

In the two other experiments (CPX02 and CPX06), forsterite displays dendritic morphologies. The CPX02 experimental charge contains two parts: the 12mm-long lower part contains mm-sized elongate platy crystals with fine dendrite tips (Fig. 5b), and the 10mm-long upper part displays fine dendritic crystals (Fig. 5a). The latter nucleated on the capsule border, and are 100-300µm long. The residual glass is strongly zoned around the forsterite crystals. CPX06 was not a successful run because the graphite capsule partially disintegrated but in this experiment olivine grew at a very high temperature (1406°C).

In experiments in which olivine coexists with pyroxene, the forsterite habit is generally similar to that in pyroxene-free runs, but in some case the borders of the crystals are rounded and embayed. Experiment CPX09 (Fig. 8) contains good examples of the variety of textures deployed by this mineral. In the lower part of the capsule, forsterite has a hopper or platy habit (Fig. 6c) whereas at the top of the capsule, it forms crystals with a complex, irregular, elongate morphology. Pigeonite and diopside grow around forsterite crystals (Fig. 6a, b). Some of the forsterite crystals are rounded and embayed, particularly where they are surrounded by smaller pigeonite and diopside crystals (Fig. 6a, b).

The forsterite crystals have high CaO contents, up to 0.5% in solid crystals and more in fine dendrites. We were not able to measure CaO contents in fine dendrites because of their extreme thinness, but BSE images (Fig. 5e) show enrichment in this heavy component in dendrites. The glass immediately surrounding the fine dendrites is strongly depleted in the forsterite component, with low SiO₂ and high CaO compared to starting material. A strong chemical gradient is present around dendritic crystals.

Pyroxene crystallized over a large range of temperatures, from 1365°C to 1102°C. In these experiments, cooling rates were between 3 and 100°/h and the temperature gradient was 20°C/cm. One or two pyroxenes, pigeonite and diopside, crystallized in about two thirds of the experiments. The two pyroxenes coexist in all experiments except for CPX08, the unsuccessful experiment with porcupine-like forsterite, where only diopside crystallized. Pigeonite and diopside were present over the entire temperature range but diopside appears in only one experiment at a temperature over 1336°C. Isolated crystals of pigeonite were observed in only one run, CPX 15; in all others this mineral occurs as the cores of zoned crystals with diopside margins.

Pyroxene usually crystallizes as acicular, zoned crystals, each with a core of pigeonite and a border of augite (e.g. Fig 6e, f). In experiment CPX09, the larger zoned crystals have a "plumose" morphology (Fig. 6c) while the smaller diopside crystals have a more euhedral, prismatic or chain-like morphology (Fig. 6b). In other experiments such as CPX19 and CPX22, pyroxene forms complex or cross-shaped dendrites (Fig 6d). In the two experiments

conducted under similar conditions but with contrasting results, the pyroxene morphologies were very different. As mentioned above, forsterite crystallized as isolated hopper crystals in experiment CPX14, but was absent in experiment CPX15. In experiment CPX14, skeletal prismatic to highly dendritic grains of pyroxene crystallized between larger forsterite grains, like those illustrated in Figures 6b and c. In experiment CPX15, pyroxene crystals fill the entire charge, mainly as elongated needles oriented parallel to one another and approximately parallel to the walls of the capsule. As illustrated in Figure 2, in the lower, hotter, part of the capsule, pigeonite occurs alone as acicular, dendritic crystals; in the upper, cooler part, diopside and pigeonite crystallized as a dense mat of fine, zoned, dendritic crystals. In the uppermost part, tridymite appears in the matrix (Fig. 2).

In experiment CPX22, pigeonite and diopside crystallize as zoned cross-shaped dendrites. These are found in the lower part of the capsule, at a temperature of 1365°C, 9°C above diopside liquidus temperature as determined in isothermal experiments.

Representative pyroxene compositions are given in Table 3. The CaO content of pigeonite varies from 3.9% in the core of a grain that crystallized at the highest temperature, to an apparent 9% in a grain in one of the lowest-temperature runs. The high value could be a bad analysis resulting from a mixed signal between the pigeonite core and the diopside border of a fine zoned crystal.

Most diopside grains have CaO contents between 13% and 20%. In the run CPX08, where diopside formed complex dendritic crystals, the cores are unusually calcic (25%) and the borders are rich in Al (2%).

Other minerals. Silica phase (probably tridymite) is present in about one-third of experimental charges, irrespective of the presence of forsterite. Other crystalline phases include Ca-rich pyroxene (CPX07), anorthite (CPX11) and spinel (CPX11). In all three cases, these minerals crystallized in small volumes of liquid, commonly isolated from the main mass of the charge and they are not representative of the normal crystallization sequence.

4. Discussion

Perhaps the most significant aspect of the results is their unpredictability. Although other experiments have explored the crystallization of Ca-poor pyroxene under conditions of rapid cooling (Kinzler and Grove 1985; Parman et al. 1997), none has coupled this with the presence of a thermal gradient. Under such conditions the kinetics of nucleation and crystallization come into play and strongly influence the sequence and extent of crystallization, or, under some circumstances, the very presence or absence of certain phases.

The problem of the presence of forsterite

A significant result of our study is the observation that forsterite crystallized in about a third of the experiments conducted in a thermal gradient but was absent in the equilibrium experiments. Even in the thermal-gradient experiments, the phase crystallized in a rather unpredictable manner. Consider, for example the following experiments which were carried out at similar cooling rates, thermal gradients and quenching temperatures. In one run, CPX14, forsterite is present, but in another, CPX15, the entire charge crystallized to a dense intergrowth of pigeonite and diopside. Another example is CPX04, which crystallized forsterite, and CPX 10, which was entirely glassy even though it was quenched at far lower temperature.

Another important aspect is the morphologies of the forsterite crystals, which were very

different in different experiments (Fig. 5). Faure et al. (2003) had shown that the presence of a thermal gradient leads to the crystallization of grains with skeletal or dendritic morphologies even at relatively low cooling rates. In run CPX04 the crystals were euhedral, which is consistent with the low cooling rate of this experiment (Faure et al. 2003), but the non-skeletal morphology suggests that the significant thermal gradient $10.7^{\circ}\text{C}/\text{cm}$ had no effect on the growth of forsterite. This observation is inconsistent with the results of Faure et al. (2006) who showed that the action of the thermal gradient on the morphology of forsterite (growth constraint) started for low gradients ($> 5^{\circ}\text{C}/\text{cm}$). However, the experiments of Faure et al. were conducted with compositions in which forsterite was the liquidus phase under equilibrium conditions. This was not the case with our experiments. A contrasting result was given by experiment CPX09 which was also conducted at a low cooling rate ($10^{\circ}\text{C}/\text{cm}$), but which shows the presence of forsterite with a distinctive skeletal or dendritic morphologies consistent with rapid growth (Fig. 5c, and Fig. 6b). The forsterite crystals in this charge do not show a pronounced preferential orientation, but many are aligned in the direction of the temperature gradient. This observation is consistent with constrained growth of forsterite under conditions in which the influence of the thermal gradient counterbalances the low cooling rate.

In another type of texture, dendritic forsterite crystals are randomly oriented in a glassy matrix (Fig. 5a, b). These crystals appeared in a charge (CPX02) that was not quenched in water but was rapidly cooled in air. The random orientation suggests heterogeneous nucleation and the dendritic morphology suggests rapid crystal growth. Furthermore, the presence of dendritic overgrowths on large euhedral crystals indicates that this charge had a dual thermal history: the euhedral crystals probably grew during initial slow cooling when the influence of the thermal gradient was minimal, then the dendritic crystals grew rapidly while the charge cooled quickly in air.

Some logic can be introduced to the interpretation of these observations if we consider more carefully the conditions in which individual experiments were conducted. Euhedral forsterite grows when the cooling rate is relatively low; when the thermal gradient is also low, the crystals are euhedral and solid or mildly skeletal; when the gradient is higher, they develop highly skeletal to dendritic morphologies (Table 1).

Several authors (Baker and Grove 1985; Kirkpatrick 1983) have experimentally demonstrated the crystallization of metastable forsterite in compositions with pyroxene on the liquidus. This crystallization results from the difficulty of nucleation of pyroxene, which allows metastable olivine to appear in its place. The seemingly haphazard appearance of forsterite may be related to differences in experimental conditions – not those during the course of the main experiment but those during initial heating on the charge above its liquidus. For example, the charge in run CPX14, which crystallized abundant forsterite, was heated at a temperature only moderately above the liquidus ($\text{DT} = 119^{\circ}\text{C}$) while that of run CPX15, which crystallized abundant pyroxene and no olivine, was heated at a higher temperature ($\text{DT} = 169^{\circ}\text{C}$). Although the nucleation of forsterite is known to be less sensitive than other minerals to the degree of superheating (Lofgren 1983), the effect is not entirely negligible (Donaldson 1979). When the degree of superheating is only moderate, forsterite nucleates and crystallizes in the field of metastable forsterite, but when the superheating is more pronounced, the charge passes entirely through this field and starts to crystallize only in the pyroxene field.

Crystallization of pigeonite and zoned pyroxene crystals with various morphologies

The influence of experimental conditions is also seen in the morphology and crystallization sequence of the pyroxenes. Notable aspects of the crystallization of pyroxene are as follows: (1) pyroxene is difficult to nucleate, as shown by the large degree of supercooling measured at the crystallization front, (2) once nucleated, it grows very rapidly; (3) pigeonite crystallizes at high cooling rates, (4) a wide variety of morphologies are developed by the pyroxene, (5) the presence of the thermal gradient leads to parallel orientation of pyroxene crystals.

(1) In those experiments where pyroxene (diopside and pigeonite) crystallized, the two phases routinely showed a significant delay in the nucleation, as illustrated in Figures 7 and 9. The delay was smallest in charge CPX15 (Fig. 2), which shows large acicular crystals of pigeonite at the bottom of the capsule, as well as zoned acicular crystals with pigeonite cores and diopside mantle in the centre of the capsule. All crystals are oriented roughly parallel to one another and parallel to the walls of the capsule; i.e. perpendicular to the thermal gradient. In this charge, the temperature at the appearance of pigeonite is 1352°C and the degree of supercooling ($-\Delta T$) is estimated as 34°C. However, this is a maximum value because pigeonite fills the entire charge and persists to the base of the capsule. Diopside appears along the borders of pigeonite crystals at 1336°C, giving a $-\Delta T$ of 18°C.

In other charges the apparent delay ranged from 21 to 109°C. A delay in the nucleation of pyroxene is well documented in the literature: this mineral, pigeonite especially, nucleates less readily than olivine, but more easily than plagioclase (Kinzler and Grove 1985; Lofgren 1983). These authors have shown, for example, that under conditions of rapid cooling (but in the absence of a thermal gradient), the temperature of appearance of augite and pigeonite is suppressed when the cooling rate exceeded 10°C/h. Kinzler and Grove (1985) found that at a cooling rate of 50°C/h, the nucleation of augite was delayed by 100°C and that of pigeonite by 250°C. Faure et al. (2006) observed a similar effect in the presence of a thermal gradient. In experiments conducted at a cooling rate of 5°C/h, the diopside liquidus was suppressed by about 46°C. A significant difference is that although the suppression of the forsterite liquidus was very small in normal dynamic crystallization experiments, Faure et al. monitored a ~50° suppression in the thermal-gradient experiments.

Charges CPX19 and 26 show almost simultaneous appearance of pigeonite and diopside, at 1320°C and 1317°C, respectively. The nucleation delay of pigeonite is 32°C greater than that of diopside, with a mean value of 67°C for pigeonite, compared to 35°C for diopside. These values are consistent with the rapid cooling (100°C/h) of these charges. In the run CPX10, which was cooled at 200°C/h, pyroxene did not crystallize, despite a large $-\Delta T$ of 117°C. The charges CPX01, CPX05 and CPX14 do not permit meaningful estimate of the delay in the nucleation of pyroxene, because the crystals reached the bottom of the capsule. In charge CPX09, the nucleation delay of zoned pyroxene crystals is high ($-\Delta T_{\text{pig}} = 109^\circ\text{C}$ and $-\Delta T_{\text{aug}} = 77^\circ\text{C}$). This charge was cooled to 10°C/h, the same as for CPX15. We attribute the sharp difference in the degree of supersaturation to the crystallization of metastable forsterite in CPX09, which has changed the composition of the fluid, promoting the crystallization of pyroxene. The difference in experimental procedure of the two experiments may also contribute to the different crystallization behaviour. Experiment CPX14 was pre-heated at a lower temperature and this may have promoted the nucleation of metastable olivine on relict nuclei that survived the pre-heating (Lofgren 1983). The presence of small nuclei of pyroxene, particularly in the early experiments that were conducted using procedure 1, greatly complicate the interpretation and become a key factor controlling the onset of crystallization.

(2) The capacity of pyroxene to grow rapidly once it nucleated is illustrated by the image of the experimental charge CPX15, shown as Figure 2. Pyroxene fills the whole capsule, from the cool top, which was quenched at 1278°C, to the hot base quenched at 1352°C. In this

charge pyroxene crystallized at temperatures far higher than those in experiment CPX10, which was entirely glassy even though it was quenched at a lower temperatures of 1269 to 1307°C. Pyroxene is absent at the hot end (1298°C) in experiment CPX09, where only olivine has crystallized. The differences in the phase assemblages can in part be attributed to the experimental conditions. The cooling rate in experiment CPX10, which produced an entirely glassy charge, was 200°C/h and this rapid rate no doubt prevented nucleation. For experiment CPX15, in which the charge shows long acicular crystals of pyroxene, procedure 2 was used and it is possible that the initial period of high-temperature heating destroyed the relict structures in the liquid that in other experiments facilitated the nucleation of olivine, as discussed by Lofgren (1983). It appears that during experiment CPX15 no olivine crystallized at high temperatures and once pyroxene nucleated it grew rapidly to fill the entire capsule. In experiment CPX09, conducted using procedure 1, pyroxene also nucleated and it crystallized throughout the upper two-thirds of the capsule. However, in this case it did not penetrate into the lower portion of the capsule, presumably because the composition of the liquid had been modified by the growth of the large olivine crystals.

Finally, the charge CPX22 poses a problem because it contains complex zoned pigeonite-diopside crystals that apparently grew at a temperature of 1365°C. Thus, if the delay in the nucleation temperature of pigeonite is the same as in other experiments, at 21°C, then diopside appeared 9°C above the equilibrium liquidus temperature. Local variations of chemical compositions may explain this phenomenon.

(3) Another aspect that needs to be emphasized is the presence of pigeonite even in rapidly cooled runs. For example, zoned crystals with pigeonite cores are present in experiments CPX19 and 26, both of which were cooled at 100°C/h. The idea that pigeonite only forms at slow cooling rates less than 10°C per hour (Kinzler and Grove 1985; Parman et al. 1997) is clearly not valid.

(4) Pyroxene develops a variety of morphologies that differ from one charge to another (Fig. 6). In experiments CPX01, 05, 15, 26 we see acicular crystals, in CPX09 pyroxene develops plumose texture, in CPX09 chain-like or finely dendritic, and in CPX14, 19 and 22 it forms larger, complex dendrites. All these morphologies are classically attributed to rapid growth (Donaldson 1982). We interpret them as reflecting the degree of delay in the nucleation of pyroxene. The more delicate, dendritic habits form preferentially when both the cooling rate and the delay in nucleation are high. The charge CPX09 shows an almost spherolitic texture symptomatic of the highest supercooling rate of all the charges.

(5) In five experiments in which both the cooling rate and the thermal gradient were moderate pyroxene crystallizes as needles of variable thickness that are oriented close to parallel to one another and parallel to the capsule walls. Some of these are zoned with pigeonite cores but others contain only one phase. The charge most representative of this phenomenon is CPX15 (Fig. 6, f) where pyroxene crystals develop from the top to the base of the capsule. This texture is similar to that observed by Faure et al. (Faure et al. 2006) for forsterite in their experiments on komatiitic compositions. We interpret this texture as reflecting constrained growth of pyroxene crystals under the influence of the dominant thermal gradient. When the thermal gradient is moderate, about 20°C/cm and the cooling rate is 10°C/h, relatively large well-oriented crystals result. When the cooling rate is higher, at 100°C/h as in run CPX26, finer dendritic but still well oriented crystals grow. It appears that the thermal gradient has an effect for a wide range of cooling rates.

Application to natural rocks

One important goal of our study was to understand the conditions in which pyroxene crystallizes in komatiites. Although this goal has been realized in a broad sense, several

important differences between the environment of crystallization in the interior of a komatiite flow and our experimental setting limit the application of our results. Our experiments have demonstrated how subtle differences in pre- or syn-crystallization conditions can significantly change the order of crystallization and the compositions of the phases that crystallize. A natural example for the unpredictability of the order of crystallization is illustrated by Figure 10. In the lower plate olivine spinifex horizon of Alexo flow one or two crystals of pyroxene take the place of olivine in a series of regularly arranged olivine plates. In the interiors of komatiite lava flows conditions were far less extreme than those in our experiments. For example, although it can be argued that some komatiites became superheated during their passage from mantle source to the surface, most komatiites contained olivine phenocrysts when they erupted which indicates that on eruption they were effectively at their liquidus. Furthermore, in the interior of a lava flow, at tens to hundreds of centimetres beneath the flow top, cooling rates are limited by conduction through the solid crust of the flow -and eventually convection in large komatiite flows- and are relatively low. At the depths of several metres below the flow top, the level at which pyroxene spinifex texture forms, cooling rates were below 1°C/h (Turner et al. 1986). The fact that we grew zoned pyroxene crystals with pigeonite cores and diopside mantles in our experiments is significant because the similarity between these crystals and those in natural komatiites indicates that we have reproduced the essential features of the natural environment. In both settings the pyroxene grains crystallize during constrained growth in a thermal gradient. The growth starts at the cool end of the experimental charge or lava flow, then proceeds downwards. However, many specific aspects of the experimental results, such as the appearance of metastable olivine, have no direct application to komatiite crystallization. In almost all natural lava flows the liquidus mineral is olivine and pyroxene spinifex forms in evolved liquids developed by extraction of olivine, usually into the cumulate base of the lava flow. Under conditions of slower cooling in systems in which olivine has crystallized in the lower part of the unit, this mineral will not grow metastably.

An area where our results may have direct application is in the interpretation of textures in chondrites, where olivine and pyroxene with skeletal and dendritic habits are found (Lofgren and Lanier 1990; Lofgren and Russell 1986; Lofgren 1989).

5. Conclusions

- Spinifex textures result from crystallization at moderate cooling rates within a thermal gradient. Analogues of komatiitic basaltic compositions crystallize zoned crystals with pigeonite cores and diopside (or augite) margins.
- Pigeonite formed at cooling rates up to 100°C/h.
- Large degrees of undercooling occur at the onset of crystallization of pyroxene crystals (both pigeonite and augite)
- Under conditions of moderate superheating, forsterite crystallizes metastably from a liquid with pigeonite at the liquidus. If the liquid is heated to high temperatures before cooling, pyroxene nucleation is promoted but it is strongly delayed. Once crystallization starts it proceeds rapidly.

References

- Baker MB, Grove TL (1985) Kinetic controls on pyroxene nucleation and metastable liquid lines of descent in a basaltic andesite. *American Mineralogist* 70(3-4):279-287
- Bouquain S, Arndt NT, Hellebrand E, Faure F (2008) Crystallochemistry and origin of pyroxenes in komatiites and lunar basalts. Submitted to *Contrib. Mineral. Petrol.*
- Donaldson CH (1976) An experimental study of olivine morphology. *Contrib. Mineral. Petrol.* 57:187-213
- Donaldson CH (1979) An experimental investigation of the delay in nucleation of olivine in mafic lavas. *Contrib. Mineral. Petrol.* 69:21-32
- Donaldson CH (1982) Spinifex-textured komatiites: A review of textures, mineral compositions, and layering. In: Arndt NT, Nisbet EG (eds) *Komatiites*, vol. George Allen and Unwin, London, pp 211-244
- Donaldson CH, Williams RJ, Lofgren G (1975) A sample holding technique for study of crystal growth in silicate melts. *American Mineralogist* 60:324-326
- Faure F, Arndt NT, Libourel G (2006) Formation of spinifex texture in komatiites: an experimental study. *J. Petrology* 47(8):1591-1610
- Faure F, Trolliard G, Nicollet C, Montel J-M (2003) A developmental model of olivine morphology as a function of the cooling rate and the degree of undercooling. *Contrib. Mineral. Petrol.* 145:251-263
- Kinzler RJ, Grove TL (1985) Crystallization and differentiation of Archean komatiite lavas from northeast Ontario: Phase equilibrium and kinetic studies. *Am. Mineralogist* 70:40-51
- Kirkpatrick RJ (1983) Theory of nucleation in silicate melts. *American Mineralogist* 68(1-2):66-77
- Lofgren G, Lanier AB (1990) Dynamic crystallization study of barred olivine chondrules. *Geochimica et Cosmochimica Acta* 54(12):3537-3551
- Lofgren G, Russell WJ (1986) Dynamic crystallization of chondrule melts of porphyritic and radial pyroxene composition. *Geochimica et Cosmochimica Acta* 50(8):1715-1726
- Lofgren GE (1983) Effect of heterogeneous nucleation on basaltic textures: a dynamic crystallization study. *J. Petrol.* 24:229-255
- Lofgren GE (1989) Dynamic crystallization of chondrule melts of porphyritic olivine composition: Textures experimental and natural. *Geochimica et Cosmochimica Acta* 53(2):461-470
- Longhi J, Boudreau AE (1980) The Orthoenstatite liquidus field in the system forsterite-diopside-silica at one atmosphere. *American Mineralogist* 65(5-6):563-573
- Parman S, Dann J, Grove TL, de Wit MJ (1997) Emplacement conditions of komatiite magmas from the 3.49 Ga Komati Formation, Barberton Greenstone Belt, South Africa. *Earth Planet. Sci. Lett.* 150:303-323
- Turner JS, Huppert HE, Sparks RSJ (1986) Komatiites II: Experimental and theoretical investigations of post-emplacement cooling and crystallization. *J. Petrol.* 27:397-437

List of Figures

- Fig. 1. Details of the four procedures of cooling used during dynamic crystallization experiments
- Fig. 2. Typical experimental charge. The charge was cut along its length, then polished and scanned. Temperatures of appearance of crystalline phases are compared to their liquidus temperature determined in isothermal experiments
- Fig. 3. Starting material compositions plotted in the forsterite (Fo) - diopside (Di) - silica (Qz) pseudo-ternary. Liquid compositions are projected from anorthite. Phase boundaries and reaction curves are also shown from Figure 4. Composition A was used in dynamic crystallization experiments
- Fig. 4. Liquidus boundaries in the system forsterite-diopside-anorthite-silica. Represented join is Fo95An05-Di95An05-SiO₂95An05: this plane is parallel to the pseudo-ternary Fo-Di-SiO₂ and contains 5% An. Squares are liquid compositions saturated with two crystalline phases (white squares) or three crystalline phases (black squares). Analysis of pyroxene crystals are also drawn. Single arrows indicate cotectic curves; double arrows indicate reaction curves
- Fig. 5. Photomicrographs showing olivine morphologies observed in dynamic crystallization experiments. Nomenclature is from Donaldson (1976) and Faure et al. (2003), respectively. a: Chain olivine / swallowtail shape (CPX02). b: Branching olivine / swallowtail shape (CPX02). c: Hopper olivine (CPX09). d: Plate olivine / swallowtail shape (CPX09). e: Detail of dendritic tail of a swallowtail olivine crystal (CPX02). f: Polyhedral olivine (CPX04)
- Fig. 6. Photomicrographs showing pyroxene morphologies observed in dynamic crystallization experiments. a: Dendritic pigeonite growing on a rounded forsterite crystal (CPX09). b: Chain diopside nucleation and growth on a plate olivine crystal. c: Plumose zoned pyroxene between platy olivine crystals (CPX09). d: Dendrites on complex pyroxene crystal (CPX14). e+f: Zoned pyroxene needles, growing downwards and parallel to each other
- Fig. 7. Textural and mineralogical data from dynamic crystallization experiments. The graphite capsules are represented in black. Minerals are in black and lie in a glass shawn in white. Grey fields are bubbles
- Fig. 8. Microfluorescence images of the experimental charge labelled CPX09. Indicated temperatures are quenched temperature
- Fig. 9. Range of crystallization temperatures of silicate phases observed in both isothermal and dynamic experiments
- Fig. 10. (a) Scanned thin section of olivine cells in Alexo komatiite. (b) Enlargement of grey zone in (a); this microscope image shows pyroxene needles between olivine plates

Table headings

Table 1. Isothermal crystallization experiments with composition A

Table 2. Dynamic crystallization experiments data

Table 3. Liquid and mineral compositions

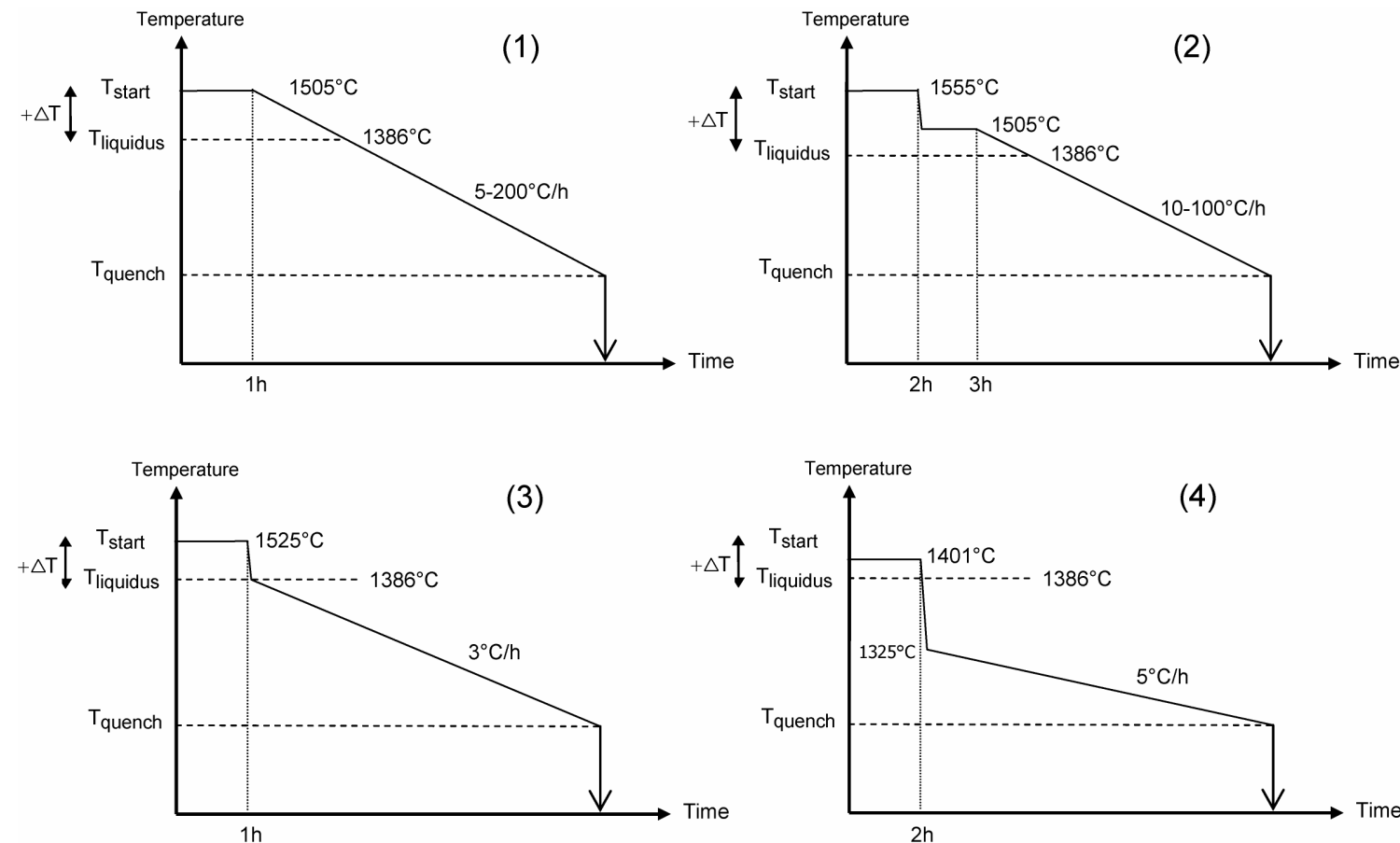


Fig. 1. Details of the four procedures of cooling used during dynamic crystallization experiments.

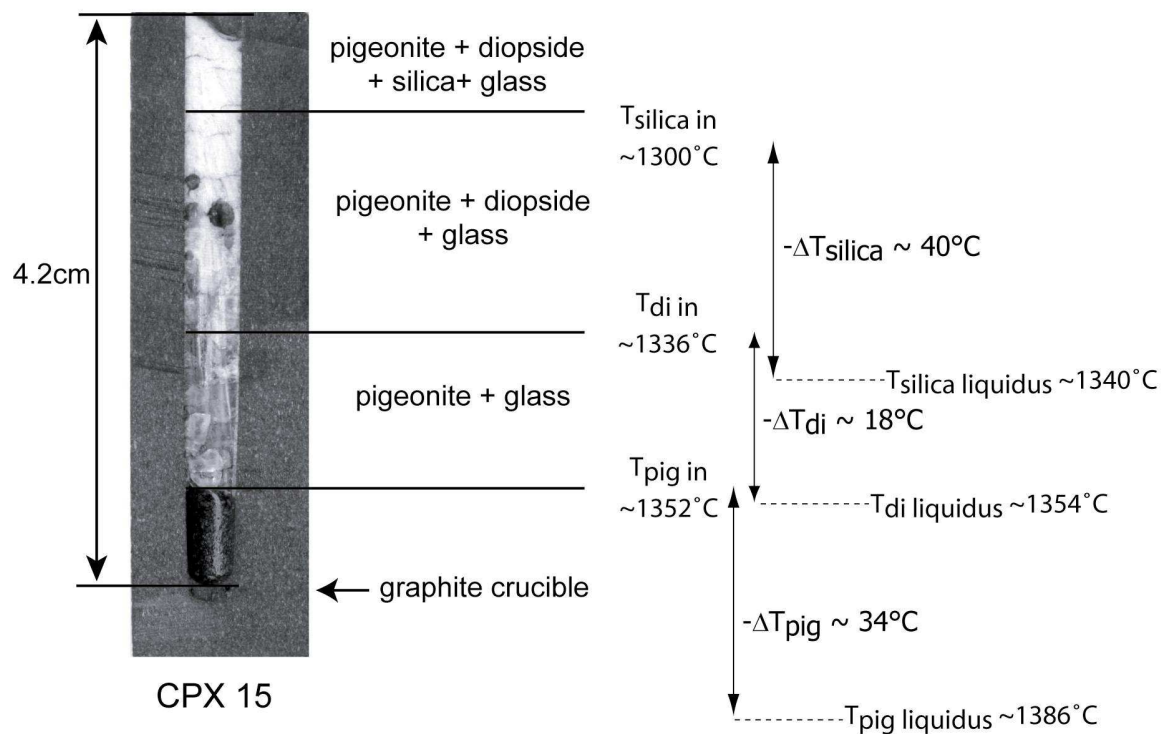


Fig. 2. Typical experimental charge. The charge was cut along its length, then polished and scanned. Temperatures of appearance of crystalline phases are compared to their liquidus temperature determined in isothermal experiments.

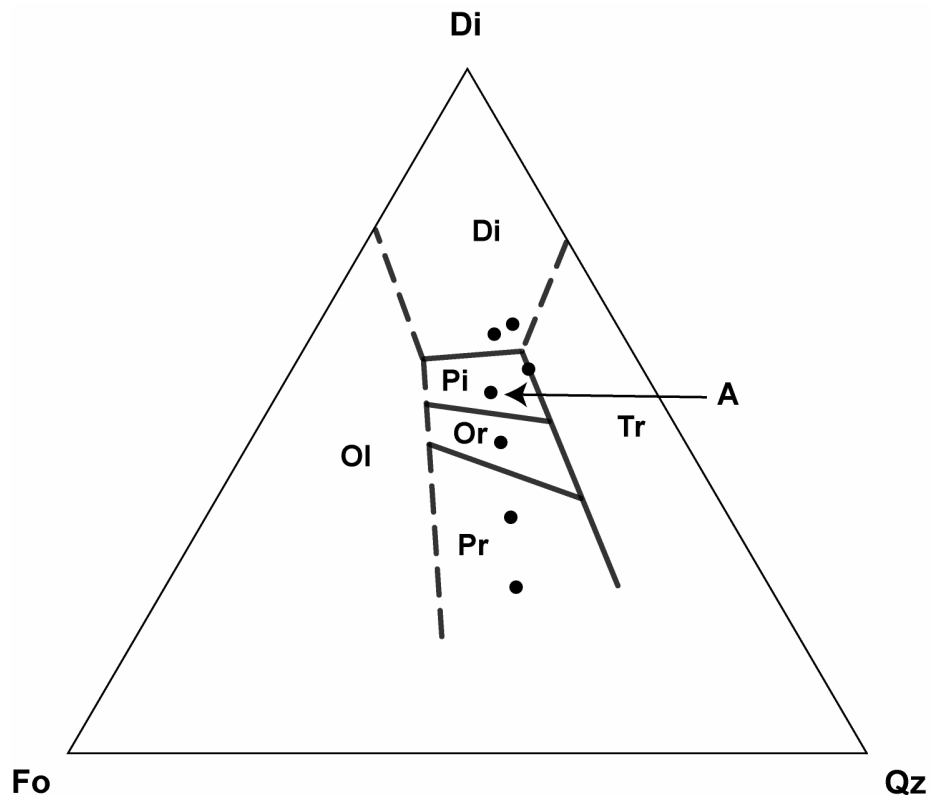


Fig. 3. Starting material compositions plotted in the forsterite (Fo) - diopside (Di) - silica (Qz) pseudo-ternary. Liquid compositions are projected from anorthite. Phase boundaries and reaction curves are also shown from Figure 4. Composition A was used in dynamic crystallization experiments.

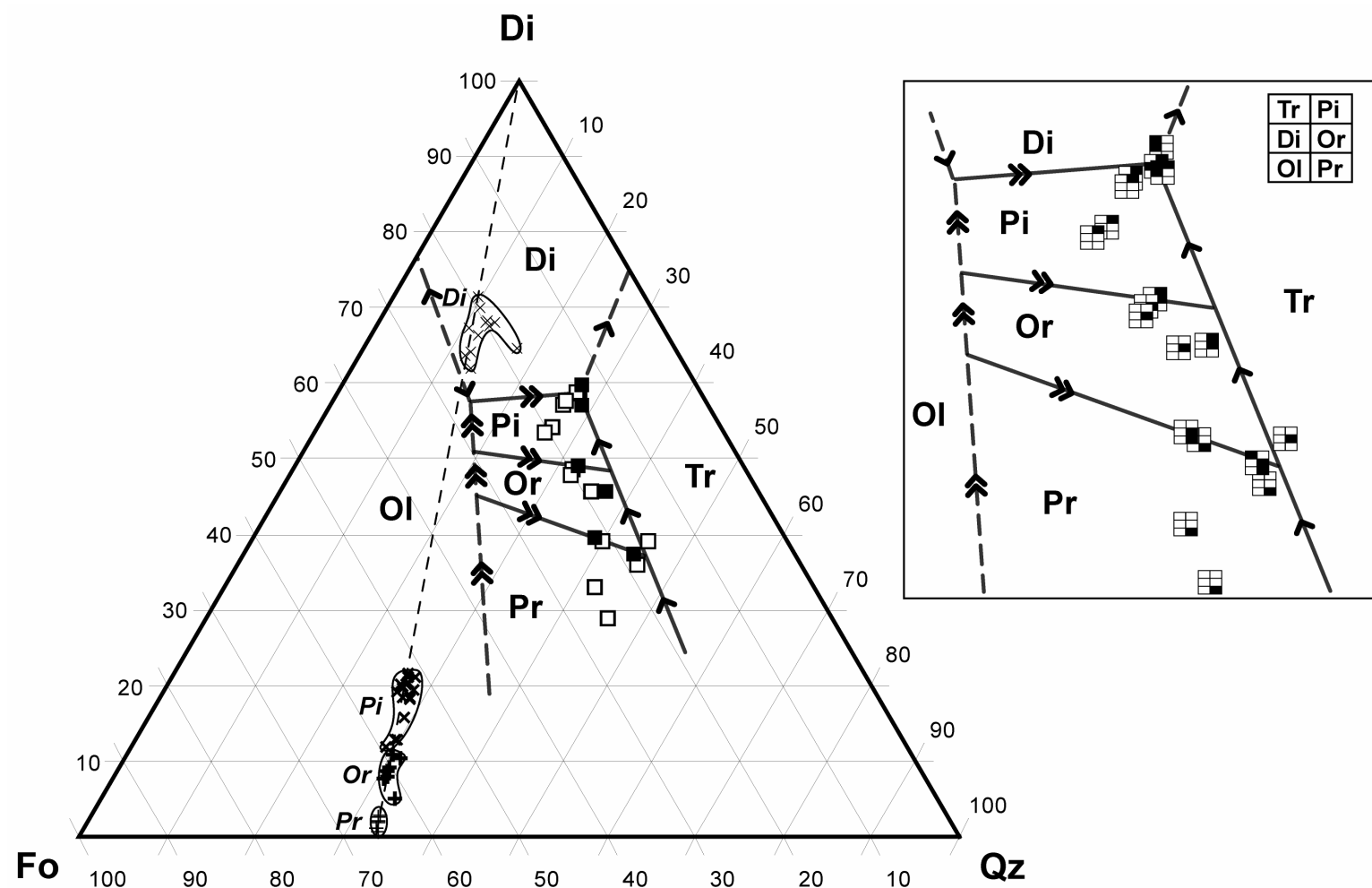


Fig. 4. Liquidus boundaries in the system forsterite-diopside-anorthite-silica. The plane shown corresponds to $\text{Fo}_{95}\text{An}_{05}\text{-Di}_{95}\text{An}_{05}\text{-SiO}_2\text{95}\text{An}_{05}$. It is parallel to the pseudo-ternary Fo-Di-SiO_2 and contains 5% An. Squares are liquid compositions saturated with two crystalline phases (white squares) or three crystalline phases (black squares). Analyses of pyroxene crystals are also drawn. Single arrows indicate cotectic curves; double arrows indicate reaction curves.

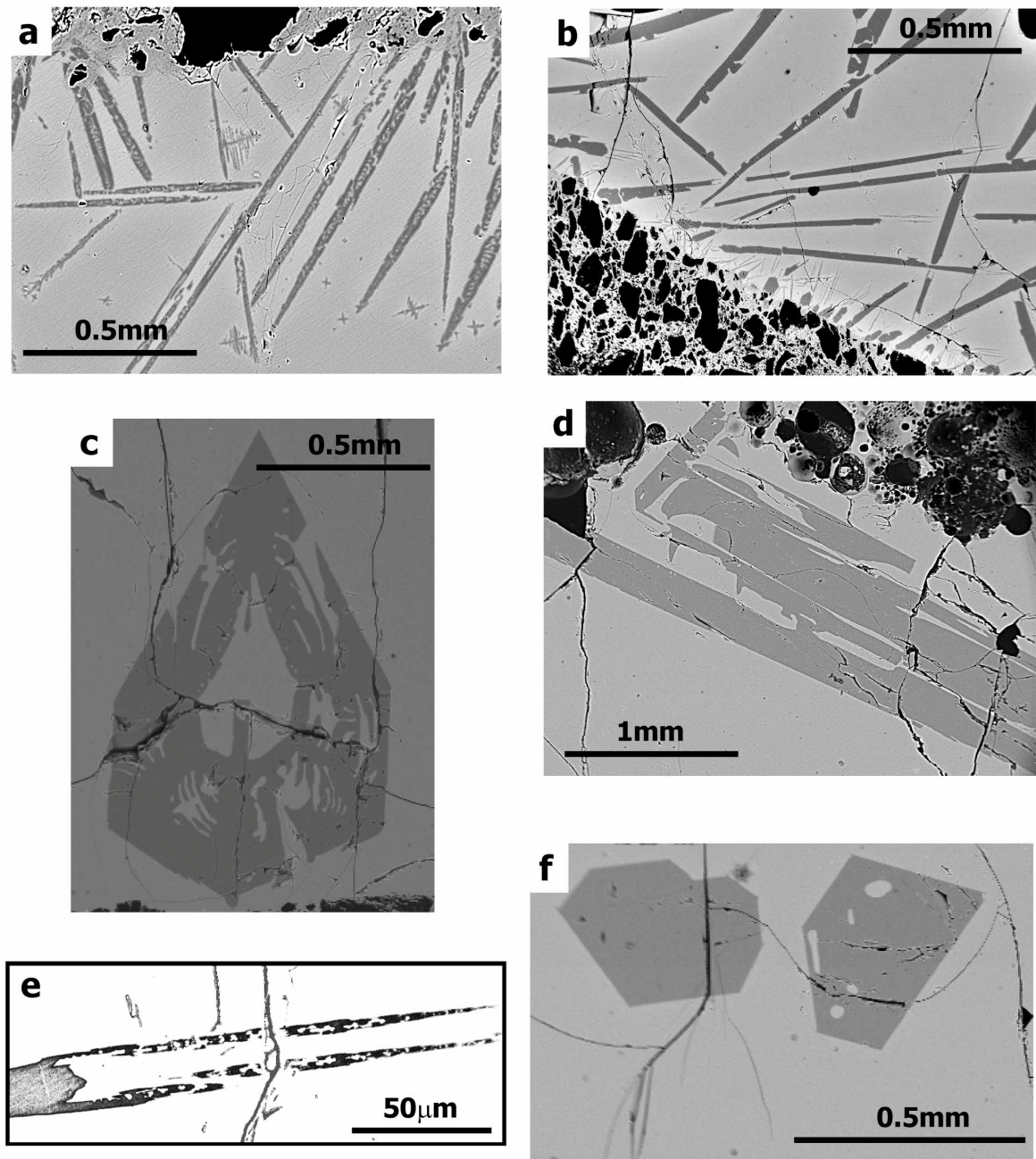


Fig. 5. Photomicrographs showing olivine morphologies observed in dynamic crystallization experiments. Nomenclature is from Donaldson (1976) and Faure et al. (2003), respectively. a: Chain olivine / swallowtail shape (CPX02). b: Branching olivine / swallowtail shape (CPX02). c: Hopper olivine (CPX09). d: Plate olivine / swallowtail shape (CPX09). e: Detail of dendritic tail of a swallowtail olivine crystal (CPX02). f: Polyhedral olivine (CPX04).

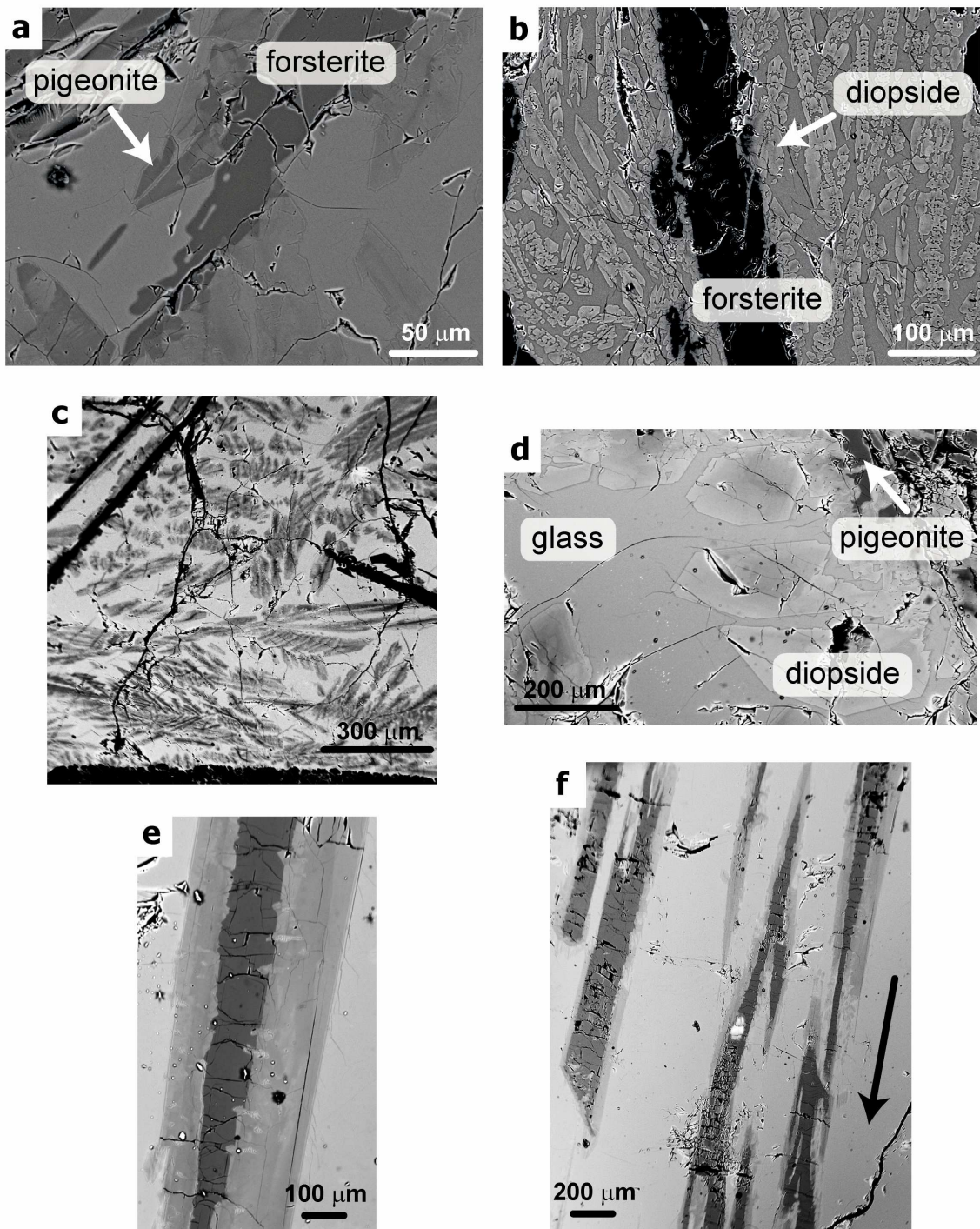


Fig. 6. Photomicrographs showing pyroxene morphologies observed in dynamic crystallization experiments. a: Dendritic pigeonite growing on a rounded forsterite crystal (CPX09). b: Chain diopside nucleation and growth on a plate olivine crystal. c: Plumose zoned pyroxene between platy olivine crystals (CPX09). d: Dendrites on complex pyroxene crystal (CPX14). e+f: Zoned pyroxene needles, growing downwards and parallel to each other.

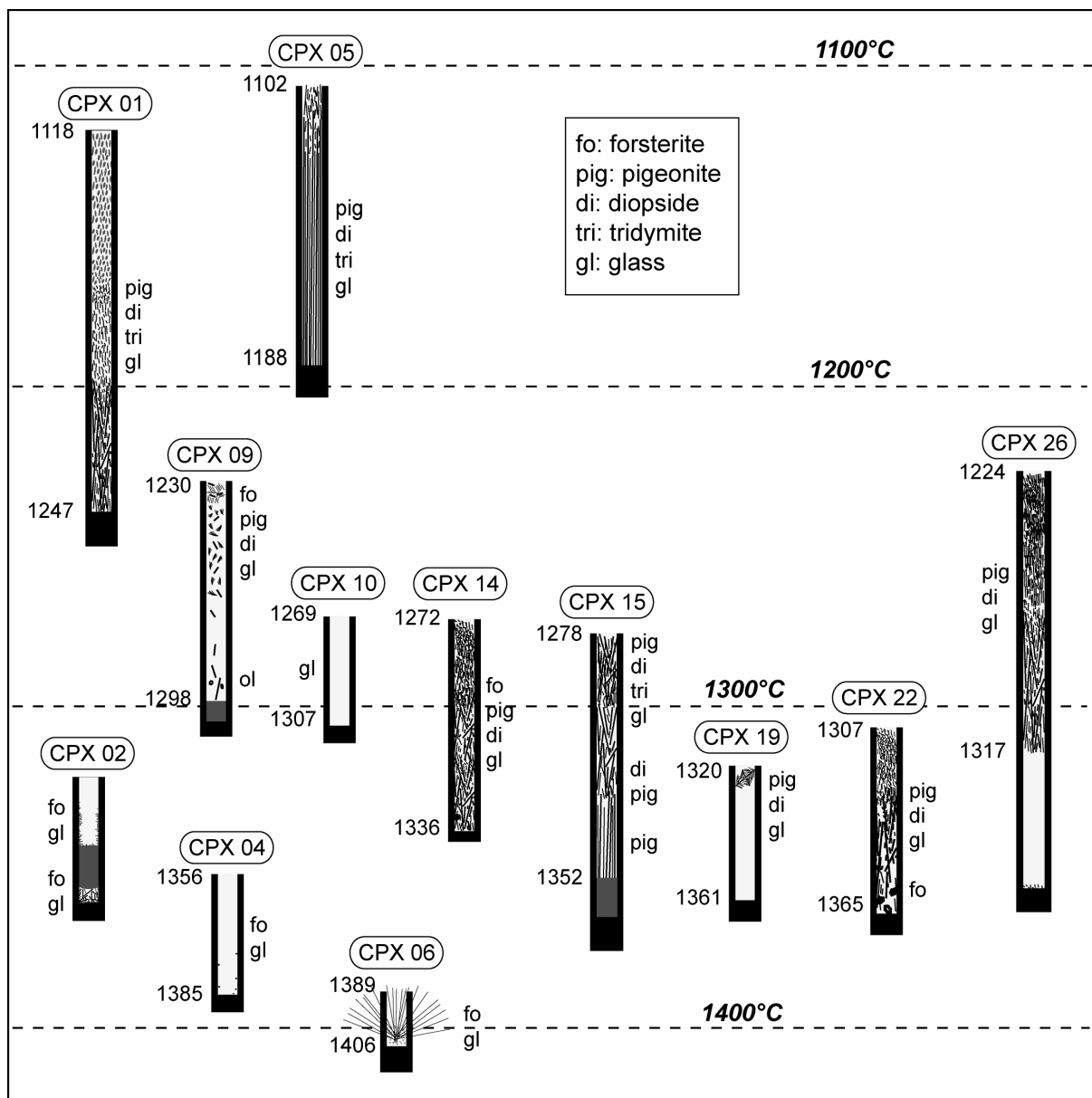


Fig. 7. Textural and mineralogical data from dynamic crystallization experiments. The graphite capsules are represented in black. Minerals are in black and lie in a glass shown in white. Grey fields are bubbles.

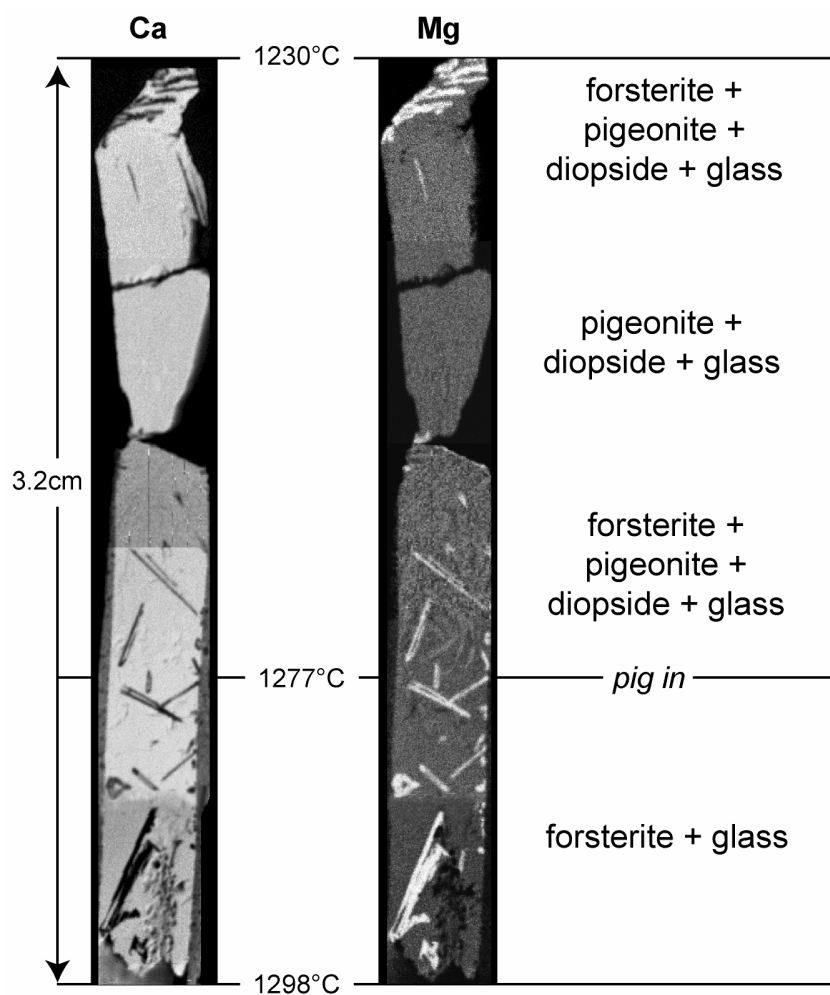


Fig. 8. Microfluorescence images of the experimental charge labelled CPX09. Indicated temperatures are quench temperatures.

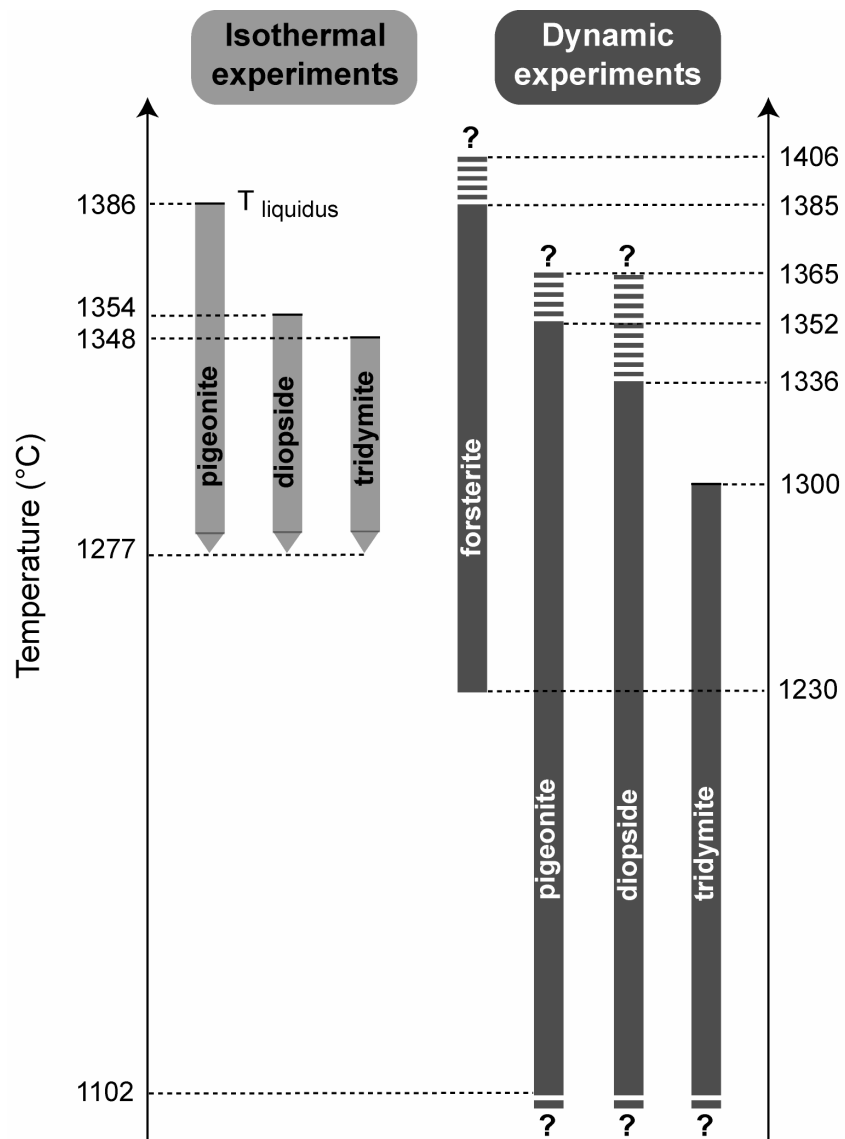


Fig. 9. Range of crystallization temperatures of silicate phases observed in both isothermal and dynamic experiments.

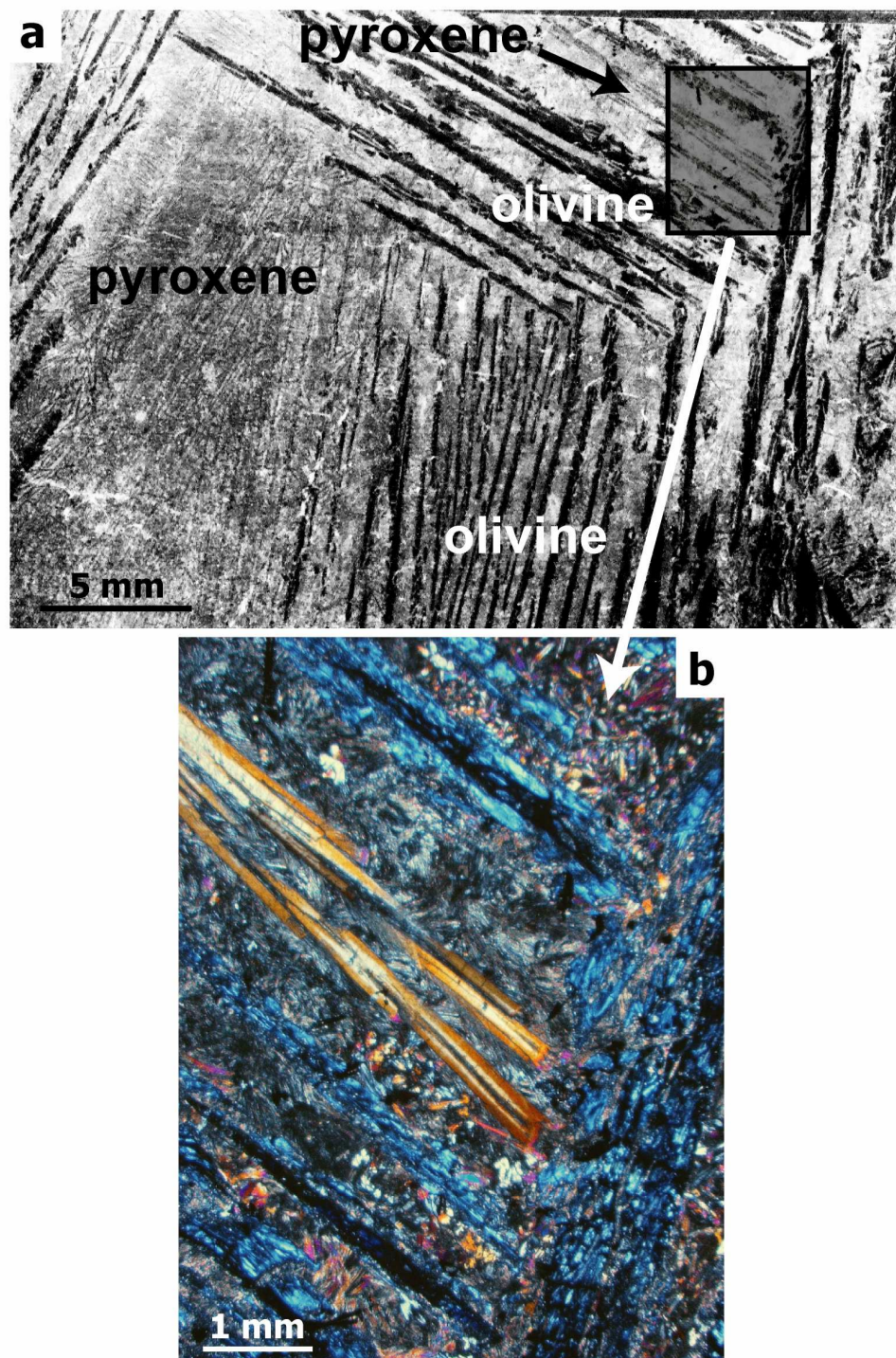


Fig. 10. (a) Scanned thin section of olivine cells in Alexo komatiite. (b) Enlargement of grey zone in (a). This microscope image shows pyroxene needles between olivine plates.

Table 1. Isothermal crystallization experiments with composition A

# Run	T (°C)	melting time (h)	Fe-free pigeonite	Ca-rich diopside	silica
SB632	1320	102	+	+	+
SB633	1340	24	+	+	+
SB618	1348	100	+	+	+
SB626	1354	15	+	+	-
SB625	1359	7	+	-	-
SB627	1364	7.5	+	-	-
SB615	1379	15.3	+	-	-
SB613	1385	11.2	+	-	-
SB623	1388	9	-	-	-
SB624	1389	14.7	-	-	-
SB622	1394	96	-	-	-
SB611	1486	1.3	-	-	-

Notes

+ = present

- = absent

Table 2. Dynamic crystallization experiments data

# Run	Cooling rate (°C/h)	Thermal gradient (°C/cm)	Starting temperature*	T _{quench} °(°C)	Total run duration (h)	Degree of superheating° (°C)	# Procedure	Forsterite	Pigeonite	Diopside	other minerals	special
CPXI 01	5	22.7	1401	1247 / 1118	18.7	15 / -94	3	-	a	a	silica	
CPXI 02	5	13.7	1488	-	?	102 / 70	1	p, ld	-	-	-	stopped before the end
CPXI 04	5	10.7	1478	1385 / 1356	20	92 / 64	1	e	-	-	-	
CPXI 05	3	21.7	1525	1188 / 1102	67.5	139 / 60	4	-	a	a	silica	
CPXI 06	5	16.8	1505	1406 / 1389	21.5	119 / 103	1	ld	-	-	-	"porcupine-like" forsterite
CPXI 09	10	21.6	1505	1298 / 1230	24.5	119 / 47	1	h, p	plu, ld	plu, ch	-	
CPXI 10	200	18.7	1505	1307 / 1269	2	119 / 83	1	-	-	-	-	glass only
CPXI 14	10	20	1505	1336 / 1272	20	119 / 57	1	h	c	c	-	
CPXI 15	10	20.7	1555	1352 / 1278	20	169 / 34	2	-	a	a	silica	
CPXI 19	100	18.5	1555	1361 / 1320	4.5	169 / 79	2	-	c	c	-	
CPXI 22	10	20	1555	1365 / 1307	17.1	169 / 64	2	h	c	c	-	
CPXI 26	100	21.0	1555	1317 / 1224	4.8	169 / 31	2	-	a	a	silica	

Notes

* at the bottom of the charge

°at the bottom / at the top of the charge

- = absent

e = euhedral

h = hopper

a = acicular

p = platy olivine

ch = chain-like

ld = linear dendrites

plu = plumose

c = complex crystals

Table 3. Liquid and mineral compositions

Starting material (composition #8)	Isothermal crystallization experiments #SB633				Dynamic crystallization experiments #CPX15			
	glass	glass	pigeonite	diopside	silica	glass	pigeonite	diopside
MgO	21,6	16,6	35,8	24,6	0,0	18,1	37,2	28,2
Al ₂ O ₃	1,6	3,6	n.d.	0,1	0,2	2,7	0,1	0,1
SiO ₂	62,3	63,8	59,9	57,3	99,4	64,4	60,9	58,3
CaO	14,7	15,4	5,7	18,7	0,1	16,3	3,9	14,9

Conclusions

To investigate the primitive Earth using small rock samples dating back several billion years: that was our challenge. Using technological advances in the analysis of chemical elements at very small scales, I was able to obtain high-quality data that improve our understanding of the conditions of crystallization of pyroxene in komatiites and lunar basalts. The samples of Archean komatiite from Alexo are relatively well preserved, and allowed a comprehensive study of compositions and textures of pyroxenes in these rocks. The lunar basalts selected from the Apollo 12 and 15 missions are exceptionally fresh.

Our understanding of the textures of olivine, pyroxene and plagioclase in mafic rocks stems mainly from the experimental studies carried out by several authors (Donaldson, 1976, 1979, 1982, Grove & Bence, 1977, 1979, Grove & Raudsepp, 1978, Kirkpatrick, 1981, 1983, Lofgren & Lanier, 1990, Lofgren & Russell, 1986, Lofgren, 1980, 1983, 1989, Lofgren & Donaldson, 1975, Lofgren et al., 1974) between 1965 and 1990. These experiments showed that the skeletal or dendritic morphologies resulted from crystallization during rapid cooling and/or at high degrees of undercooling, as is to be expected during the solidification of lavas. Faure et al. (2006) then showed that to reproduce spinifex textures in ultramafic komatiites required that the presence of a thermal gradient also be reproduced in the experimental studies. In my thesis project, I extended the study of Faure et al. (2006) by working on basaltic compositions that crystallized olivine, pigeonite and diopside.

The combined use of electron microprobe, the scanning electron microscope and the ion microprobe provided chemical profiles across pyroxene crystals from komatiites and lunar samples. The pyroxene crystals are zoned with a core of pigeonite and a border of augite. The evolution of the liquid from which the pyroxene crystallized can be followed with two indicators: the Mg/Fe ratio, expressed as $Mg / (Mg + Fe)$ and the Cr content. I successfully modeled the behavior of trace elements such as the rare earths and light elements (Li, Be, B) during the crystallization of pyroxene. This work also provided better constraints on the partition coefficients of these trace elements. In pyroxenes from the lunar basalt, the light elements are incompatible with partition coefficients similar to those of the light rare earths, and their concentrations higher in augite of the mantle than in the pigeonite core. In pyroxenes from komatiites, the levels of light elements do not vary with position in the crystal probably because these elements re-equilibrated during alteration of these samples.

In komatiite flows, pyroxene crystallizes in contrasting environments. During solidification of the upper crust, the cooling rate is very high, commonly hundreds of degrees per hour. When the interior of the flow crystallizes, however, conductive heat transfer through the crust limits the cooling rate which drops to a few degrees per hour. For a given composition of komatiitic liquid, the type of pyroxene and the crystallization sequence depends on the conditions of crystallization. Pigeonite is absent from the uppermost part of a komatiite flow, but appears deeper down in komatiite flows in slowly cooled cells enclosed by large platy olivine crystals or in the pyroxene spinifex layers of thick differentiated flows. Pigeonite is also absent from the lower cumulate portions of differentiated flows, its place being taken by orthopyroxene. Constrained growth in a thermal gradient appears to promote the crystallization of the pigeonite, which appears after olivine and before augite. When the crystallization sequence inferred from petrographic and geochemical data is compared with the results of equilibrium experimental studies, pigeonite appears sooner than it should, in liquids that crystallize olivine under equilibrium conditions. To resolve this problem, we propose that the komatiitic liquid in the crystal mush in the upper crust of the flow undergoes

Conclusions

Soret differentiation, producing a Si-rich Mg-poor liquid at the crystal front where pigeonite grows.

A comparison of the compositions of pyroxenes from komatiites from various Archean and younger localities shows that the komatiite of the 3.5 Ga Barberton greenstone belt in South Africa contains augites with peculiar combination of high wollastonite content and high Mg#. Rather than attributing the high Wo to crystallization at moderate pressure from hydrous magma, as proposed by Parman et al. (1997), we call on several factors: (1) amphibolite-facies metamorphism of Barberton komatiites may have altered the composition of the pyroxenes, (2) interaction between olivine and pyroxene in cumulate samples may have increased the Mg# of the pyroxene; (3) komatiites of Barberton have an exceptionally high CaO/Al₂O₃, compared to other komatiites and this may have led to early crystallization of pyroxene with high Mg#.

In our experimental work we were able to reproduce pyroxene crystals like those in natural lavas. When liquids with pigeonite at their liquidus are cooled in a thermal gradient, zoned acicular crystals with pigeonite cores and diopside margins commonly form. In our experiments, we were able to crystallize the pigeonite at high cooling rates, up to 100 °C/h. We were also able to measure the degree of supercooling associated with the onset of pyroxene nucleation: pigeonite nucleated at 34 to 109°C below its equilibrium liquidus and diopside at 18 to 77°C below its equilibrium liquidus. Once nucleated, pyroxene grows rapidly to produce complex dendritic crystals. In some experiments forsterite crystallized metastably under conditions that in other experiments had led to the crystallization of pigeonite with diopside. Evidence of haphazard crystallization due to the random nucleation of one phase or the other is seen in some spinifex lavas where pyroxene appears in place of olivine, or olivine appears instead of pyroxene.

To conclude, the compositions and textures of pyroxene in ultramafic and mafic lavas provide no evidence for the presence of water. Crystallization of anhydrous magma cools in a thermal gradient reproduces all the important features of these minerals. Accordingly, most komatiites are dry and hot, the fruit of the extraordinary activity of the mantle of the Archean Earth.

APPENDIX

A.	Chapitre 4: Méthodologie (in French)	112
	4.1. Etude expérimentale	
	4.2. Les techniques de caractérisation	
B.	Chapitre 5 : Pétrographie détaillée (in French)	124
	5.1. Rappel du contexte général	
	5.2. Coulée de basalte komatiitique d'Alexo	
	5.3. Coulée de komatiite d'Alexo	
C.	Tables	129

Appendix A
Chapitre 4 : Méthodologie

4.1. Etude expérimentale	113
4.1.1. Le système chimique CMAS	113
4.1.2. Les fours verticaux	114
4.1.3. Synthèse des verres : problèmes et solutions	115
4.1.4. Le diagramme de phases des pyroxènes	117
4.1.5. Mise en place et évolution du dispositif expérimental	119
4.1.6. Protocoles thermiques utilisés	120
4.2. Les techniques de caractérisation	121
4.2.1 Microscope électronique à balayage (MEB)	121
4.2.2. Microsonde électronique	122
4.2.3. Microsonde ionique	122
4.2.4. Analyses roche totale : ICP-MS et ICP-OES	122

4.1. Etude expérimentale

4.1.1. Le système chimique CMAS

Le système CMAS (pour CaO-MgO-Al₂O₃-SiO₂) est utilisé depuis un demi-siècle pour simuler les processus pétrogénétiques. Près de 90% des constituants chimiques des basaltes et des périclases sont représentés par ce système simple à quatre composantes (Biggar, 1989, Longhi & Boudreau, 1980). La relative simplicité de ce système a motivé son usage par de très nombreux pétrologues. En particulier, les acteurs de la recherche sur les pyroxènes pauvres en calcium ont été friands d'expérimentations dans le système CMAS (Biggar, 1985, 1989, Boyd & Schairer, 1964, Carlson, 1989, Gamble & Taylor, 1980, Kushiro, 1972, Lindsley & Andersen, 1983, Longhi & Boudreau, 1980, Yang, 1972, Yang & Foster, 1973).

Les compositions chimiques étudiées ont été choisies dans le champ de stabilité des pyroxènes, c'est à dire pour que le premier minéral qui cristallise soit un pyroxène. Sept compositions chimiques ont ainsi fait l'objet d'expériences de cristallisation isotherme, afin de déterminer pour chacune la température liquidus ainsi que les températures d'apparition des autres phases minérales. Ces compositions sont présentées sur le diagramme pseudo-ternaire forstérite-diopside-quartz de la Figure 4.1. En compilant toutes les données, un diagramme de phases a pu ensuite être établi (voir le paragraphe 4.1.6 de ce chapitre). La composition chimique A (avec la pigeonite au liquidus) a servi aux expériences de cristallisation dynamique. Pour obtenir cette composition chimique, nous sommes partis de compositions « extrêmes » situées dans les champs de stabilité de la protoenstatite et du diopside, que nous avons légèrement modifiées jusqu'à obtenir la composition voulue.

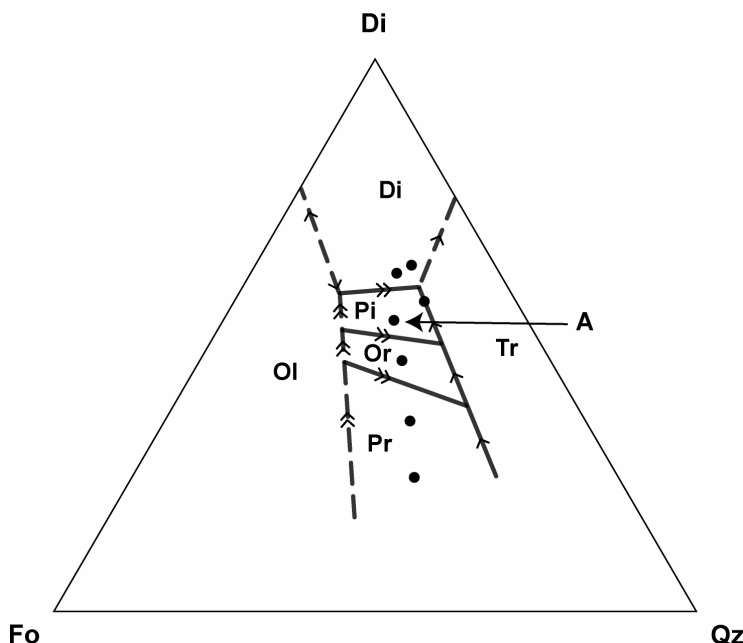


Fig. 4.1. Compositions étudiées, projetées à partir du pôle Anorthite dans le triangle Forstérite-Diopside-Quartz (diagramme « pseudo-ternaire »). Pour rappel : Forstérite Mg_2SiO_4 , Diopside $CaMgSi_2O_6$; Quartz SiO_2 . La composition A est celle qui a été choisie pour les études de cristallisation dynamique.

Fig. 4.1. Starting material compositions plotted in the forsterite (Fo) - diopside (Di) - silica (Qz) pseudo-ternary. Liquid compositions are projected from anorthite. Phase boundaries and reaction curves are also shown from Figure 4. Composition A was used in dynamic crystallization experiments.

Bien entendu, les phases étudiées ne contiennent pas de fer, puisque celui ci est absent du système CMAS. Ainsi, on trouve dans la littérature le préfixe « *iron-free* » (Yang & Foster, 1973) devant pigeonite pour désigner la pigeonite cristallisant dans le système CMAS.

4.1.2. Les fours verticaux

Les expériences de cristallisation réalisées dans le cadre de cette thèse ont toutes été faites dans le même four vertical, au CRPG à Nancy. L’élément chauffant est constitué de 6 épingle MoSi (Fig. 4.2). Les échantillons peuvent être trempés rapidement, grâce à la forme verticale du four. Un thermocouple PtRh₆-PtRh₃₀ est logé dans la canne porte-échantillons, et permet de contrôler la température à l’intérieur du four. Des calibrages du thermocouple ont été effectués à plusieurs reprises pour corriger d’éventuelles dérives. En particulier, un calibrage était systématique avant une série d’expériences. Ce calibrage est réalisé à l’aide de fils d’or et de palladium, qui ont des températures de fusion connues. En faisant fondre ces fils, on détermine alors l’écart précis entre la température réelle (donnée par la fusion du fil), et la température mesurée (température donnée par le thermocouple). La canne porte-échantillon est graduée, ce qui permet de faire un calibrage complet de la température régnant à tous les endroits du four. Cette configuration permet de choisir la zone du four où placer l’échantillon pour obtenir le gradient thermique souhaité (Fig. 4.3). L’incertitude de température est de 1.5°C. L’électronique du four permet de contrôler la vitesse de refroidissement, et plus généralement offre la possibilité de programmer le protocole souhaité. Les charges expérimentales (petites billes – se référer au paragraphe 4.1.3), sont suspendues sur un « panier » en platine par leur fil de platine. Le panier est un maillage de fils de platine,

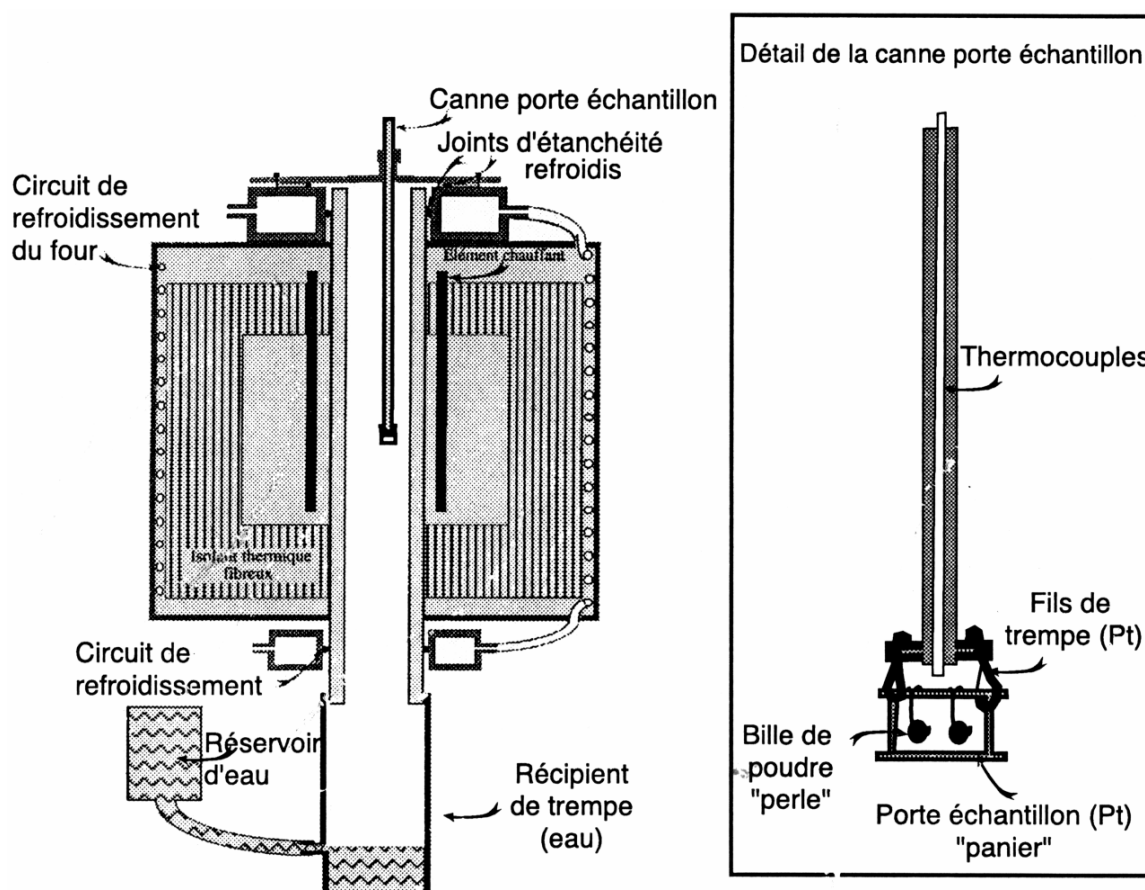


Fig. 4.2. Schéma du four vertical utilisé (d’après Faure, 2001).

Fig. 4.2. Diagram of the vertical furnace used for this study (from Faure, 2001).

conçu pour pouvoir accueillir plusieurs charges à la fois (jusqu'à 6-8 charges simultanées). Ce panier ou porte-échantillons est relié à la canne en alumine par deux fils de platine de faible section. La trempe des échantillons est obtenue en faisant fondre ces fils de platine, en envoyant une impulsion électrique qui crée un court-circuit : le panier peut alors tomber dans un bocal d'eau distillée. Les vitesses de refroidissement obtenues par un tel dispositif sont suffisamment élevées pour stopper toute réaction dans les systèmes silicatés étudiés ici (Faure, 2001) ; typiquement de l'ordre de plusieurs centaines de degrés par seconde (1000°C/s d'après Donaldson (2001)).

Le four est pourvu d'un système de contrôle d'atmosphère. Lors des expériences, il est ainsi possible d'installer des atmosphères neutre, oxydante ou réductrice, selon l'effet recherché. Les expériences à l'équilibre ont été effectuées à l'air libre, tandis que les expériences de cristallisation dynamique ont été menées en présence de flux d'argon (atmosphère réductrice).

4.1.3. Synthèse des verres : problèmes et solutions

Le but initial était d'obtenir un verre dont la composition chimique a la pigeonite au liquidus. La difficulté de trouver des expériences faites sur de telles compositions dans la littérature (Yang & Foster, 1973) a finalement conduit à tester plusieurs compositions pour choisir le meilleur candidat.

Faure (2001) a montré que la fabrication de charges expérimentales directement à partir d'oxydes entraînait de trop gros problèmes d'hétérogénéités. Nous avons donc choisi de synthétiser un verre pour avoir la meilleure homogénéisation du matériel de départ. Pour

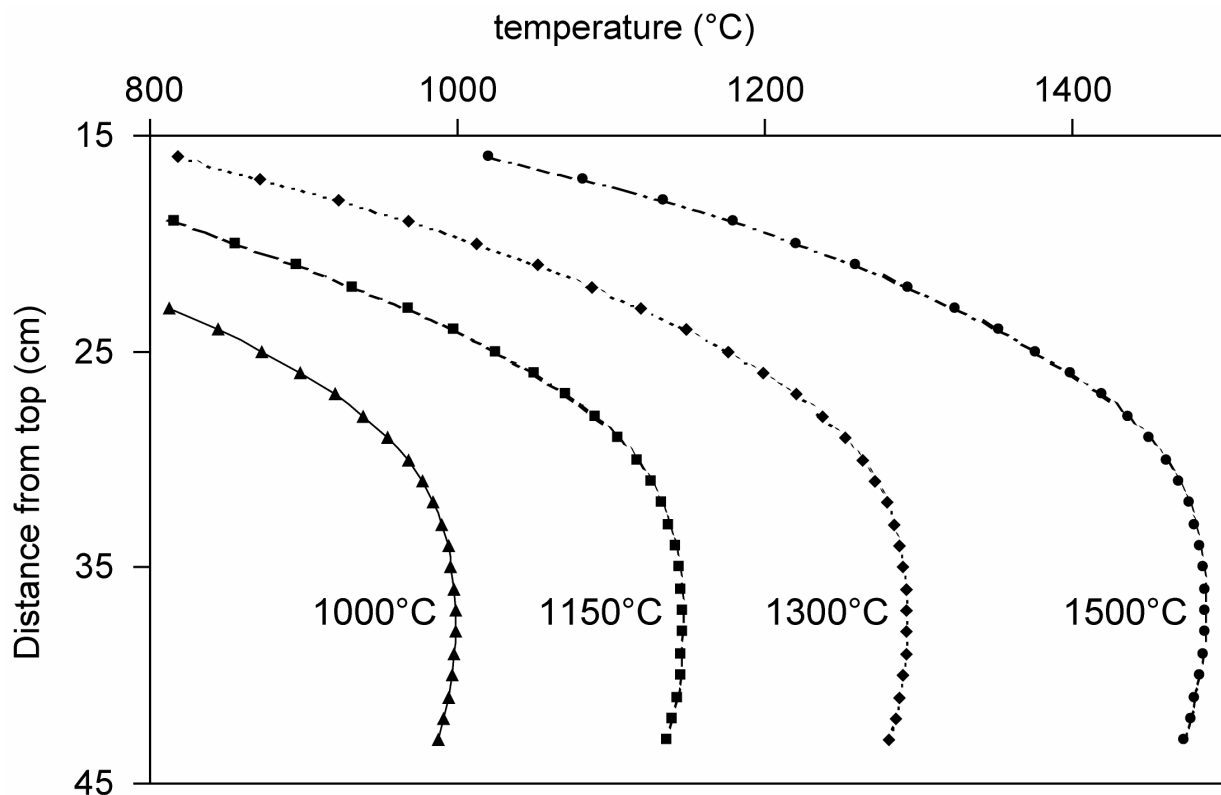


Fig. 4.3. Courbes de températures du four, pour 4 températures données. Un fort gradient thermique règne dans la partie supérieure, tandis que la partie inférieure est la plus chaude avec un gradient faible.

Fig. 4.3. Curves of temperature inside the furnace. A strong thermal gradient occurs in the upper part of the furnace, whereas the lower hotter part has a less strong thermal gradient.

synthétiser un verre, il suffit de mélanger des poudres d'oxydes ($\text{CaCO}_3\text{-MgO-Al}_2\text{O}_3\text{-SiO}_2$), de chauffer le mélange au-dessus du liquidus (très haute température dans le cas de charges très magnésiennes comme les nôtres), puis de tremper le liquide en fusion pour obtenir un verre homogène. Ce faisant, nous avons rencontré des problèmes lors de la trempe : les liquides magnésiens ne sont pas trempables facilement, si bien que la charge, d'un volume de 20 cm³ environ, cristallisait systématiquement. En réduisant le volume (donc la masse d'oxydes) de la charge trempée par quatre, nous avons pu résoudre le problème. Par contre, nous étions ainsi limités dans le nombre d'expériences possibles avec une même composition donnée. Le verre obtenu après trempe est ensuite extrait à la main de son creuset en platine, puis il est broyé dans des broyeurs à agate nettoyés soigneusement au sable, pour éviter toute contamination. Les charges expérimentales sont élaborées à partir de ce verre broyé, mélangé à de l'alcool polyvinyle qui permet d'agglomérer les poudres. La bille ainsi constituée est déposée sur un fil de platine dont une extrémité a été préalablement préparée en forme de goutte d'eau, pour mieux accueillir la bille. Selon Faure (2001), les très petites particules de platine détachées en grattant le creuset servent de site de nucléation pour les minéraux synthétisés. Ceci est nécessaire lors des expériences à l'équilibre, pour ne pas observer de retard à la nucléation du à un manque de nucléï. Nous observons donc de la nucléation de type hétérogène dans les charges expérimentales.

# Expérience	T (°C)	Durée	Pigeonite	Diopside	Silice
SB630	1277	16h40	x	x	x
SB631	1310	15h15	x	x	-
SB632	1320	102h	x	x	x
SB617	1339	12h	x	x	x
SB629	1339	269h	x	x	-
SB633	1340	24h	x	x	x
SB618	1348	100h	x	x	x
SB626	1354	15h	x	x	-
SB625	1359	7h	x	-	-
SB627	1364	7h30	x	-	-
SB614	1369	10h15	x	-	-
SB615	1379	15h20	x	-	-
SB613	1385	11h15	x	-	-
SB623	1388	9h	-	-	-
SB624	1389	14h45	-	-	-
SB621	1390	15h30	-	-	-
SB616	1394	7h20	-	-	-
SB622	1394	96h	-	-	-
SB620	1395	6h30	-	-	-
SB619	1397	17h20	-	-	-
SB612	1402	3h35	-	-	-
SB611	1486	1h15	-	-	-

Table 4.1. Série d'expériences à l'équilibre réalisées avec la composition A. Cette composition est celle qui a été utilisée pour les expériences de cristallisation dynamique. Légende : - absent ; x présent.

Table 4.1. List of isothermal experiments performed with composition A. This composition was then used in dynamic crystallization experiments. Legend: -absent; x present.

4.1.4. Le diagramme de phases des pyroxènes

Afin de réaliser le diagramme de phases, il a fallu effectuer de longues séries d'expérience à l'équilibre (de type cristallisation isotherme), pour plusieurs compositions chimiques de départ. Les charges expérimentales sont maintenues à une température fixe pendant plusieurs heures, puis trempée à l'eau, le tout à pression atmosphérique. La durée de chaque expérience varie entre 1h pour des expériences au-dessus du liquidus et plusieurs jours pour des expériences à basse température, pour diminuer le risque de ne pas atteindre l'équilibre thermodynamique. Dans le cas du pyroxène, le calcium est un bon indicateur de cet équilibre. Si la valeur de CaO du pyroxène, déterminé par analyse microsonde, montre des variations supérieures à 1% (% en poids d'oxyde), on peut considérer que l'équilibre n'a pas été atteint lors de l'expérience.

Lorsque dans une charge donnée, l'équilibre n'était pas atteint (en utilisant ce critère), une moyenne des compositions analysées a été utilisée pour dresser le diagramme de phases, mais n'est donc strictement pas valide. Les phases cristallisant à partir des différentes compositions chimiques de départ sont (entre parenthèses sont indiquées les valeurs de CaO en % de poids d'oxyde mesurées dans les pyroxènes) :

- la protoenstatite (entre 0.4 et 0.9% de CaO)
- l'orthopyroxène (entre 1.4 et 3.1% de CaO)
- la pigeonite (entre 3.2 et 6.6% de CaO)
- le diopside (entre 16.8 et 19.3% de CaO)
- la silice (vraisemblablement la tridymite qui est la phase stable dans cette gamme de pression et de températures)

Outre leurs différences de teneur en calcium, les différents minéraux sont identifiables à la sonde électronique en analysant les images d'électrons rétrodiffusés (images BSE, *Back Scattered Electrons*). La protoenstatite cristallise sous forme de gros cristaux (100-300 µm)

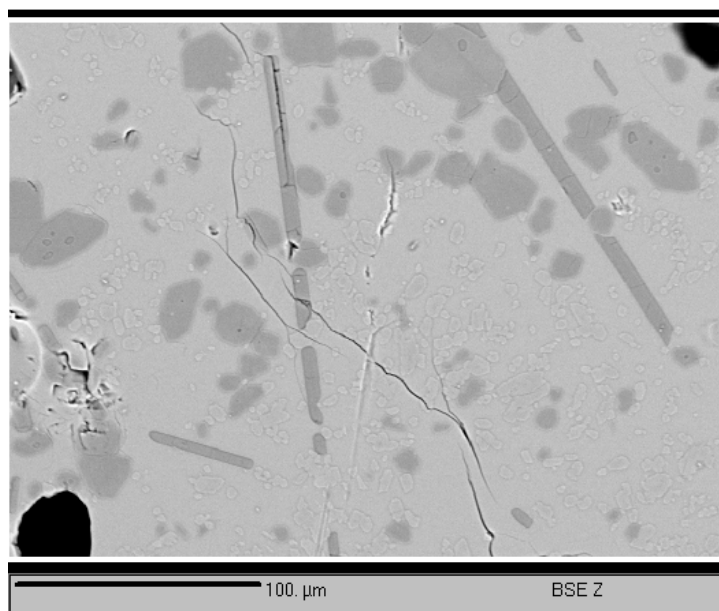


Fig. 4.4. Photo MEB (Microscope Electronique à Balayage) montrant des cristaux de pigeonite (cristaux arrondis de couleur gris clair), de diopside (petits cristaux blancs) et de tridymite (longs cristaux aciculaires gris). Echantillon SB304, 102h à 1320°C.

Fig. 4.4. SEM (Scanned Electron Microscope) image that shows crystals of pigeonite (rounded crystals in grey), diopside (smaller crystals in white) and tridymite (long acicular crystals in grey). Sample SB304, 102h, 1320°C.

équants et peu nombreux ; tandis que l'orthopyroxène et la pigeonite montrent plutôt des amas de nombreux cristaux arrondis à équants (selon la longueur des expériences) d'une taille de l'ordre de plusieurs dizaines de microns. Le diopside cristallise comme des petites billes de quelques microns de diamètre, en occupant tout le volume disponible. Nos observations montrent donc que parmi les polymorphes, plus le pyroxène est riche en calcium, plus il nucléa facilement. Enfin, la tridymite exhibe des cristaux aciculaires, dont le rapport longueur/largeur excède toujours 10. Il est donc aisément détecter dans une charge expérimentale (Fig 4.4). Pour chaque expérience, le verre résiduel est analysé à différents endroits dans la charge. Une moyenne de ces analyses est ensuite utilisée pour dresser le diagramme de phases (Fig. 4.5). Ce diagramme montre une projection du système forstérite-

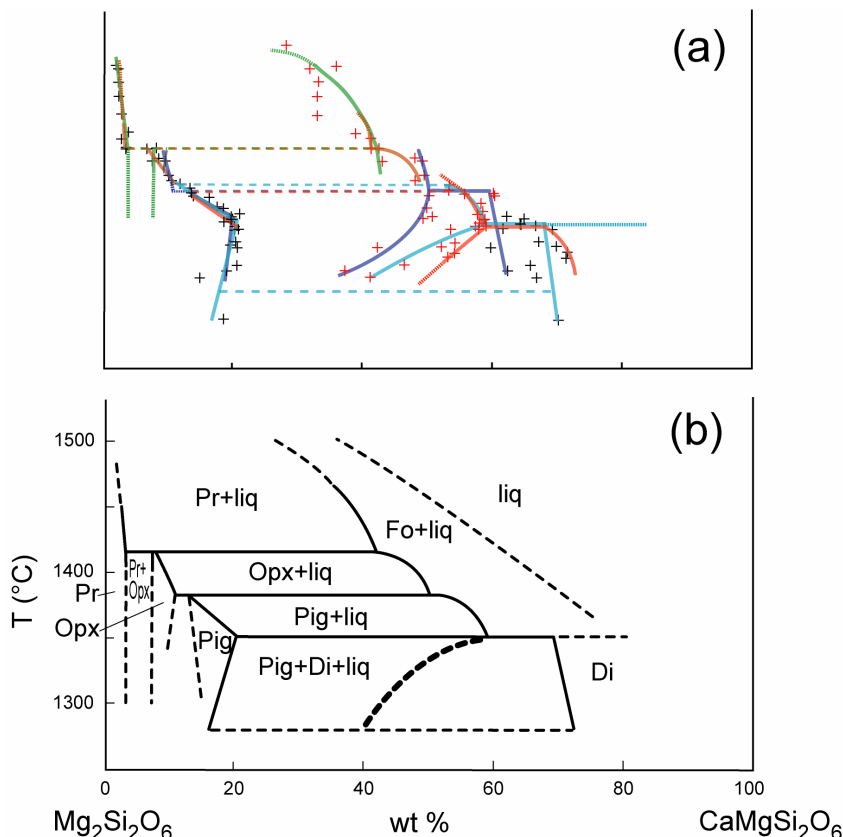


Fig. 4.5. Diagrammes de phase du système forsterite-diopside-anorthite-quartz : projection depuis le pôle anorthite sur le joint enstatite ($\text{Mg}_2\text{Si}_2\text{O}_6$)-diopside ($\text{CaMgSi}_2\text{O}_6$). (a) Compilation des données à l'équilibre de cette étude. Pour corriger les différences de températures dues aux teneurs différentes en composante anorthite de chaque composition de départ, nous avons utilisé la relation donnée dans la figure 4.6. (b) Compilation des données de cette étude et de Longhi et Boudreau (1980). Les lignes pleines sont les limites de phases dans le système Fo-Di-SiO₂. La ligne supérieure représente le liquide sur le joint En-Di. Les lignes en pointillés sont les limites de phases supposées. La ligne pointillée en gras traversant le champ Pig+Di+liq représente la pseudo-eutectique, et donc l'évolution du liquide le plus évolué avant cristallisation complète, qui s'enrichit en composante anorthite.

Fig. 4.5. Part of the system forsterite-diopside-anorthite-silica projected onto the enstatite ($\text{Mg}_2\text{Si}_2\text{O}_6$)-diopside ($\text{CaMgSi}_2\text{O}_6$) join. (a) This is a compilation of our isothermal experimental data. (b) This is a compilation of data from this study and from Longhi et Boudreau (1980). Heavy solid lines are phase boundaries in the system Fo-Di-SiO₂. Upper solid line is the liquidus of the En-Di join. Dashed lines are expected phase boundaries. Heavy dashed line in the Pig+Di+liq field should be seen as a pseudo-eutectic, and so a projection from anorthite end member. It reflects the last evolution of the liquid before complete crystallizing of the melt, which is enriched in anorthite component.

anorthite-diopside-silice sur le joint enstatite-diopside. Il s'agit d'une compilation des données de la littérature déjà compilées par Longhi et Boudreau (1980) et de celles obtenues dans cette étude. La droite pointillée entre les champs Pig+liq et Di+liq doit être vue comme une pseudo-eutectique, et reflète l'évolution d'un liquide s'enrichissant en composante anorthite, en dehors du plan $Mg_2Si_2O_6$ - $CaMgSi_2O_6$. De plus, ce type de projection qui est la plus utilisée ne montre pas clairement l'influence de la composante anorthite sur les limites de phases. Longhi et Boudreau (1980) ont précisé le champ de l'orthopyroxène dans le système Forstérite-Diopside-Silice, qui ne contient donc pas d'aluminium. La présence d'aluminium dans un liquide silicaté tel que ceux utilisés dans cette étude a pour effet d'abaisser la température liquidus et les températures des limites de phase (Fig. 4.6).

4.1.5. Mise en place et évolution du dispositif expérimental

Pour nos expériences de cristallisation dynamique, le dispositif expérimental employé est celui développé et utilisé par Faure et al. (2006) dans le cadre de son étude des textures de croissance rapide des cristaux d'olivine. Le dispositif final est le suivant : un tube en graphite est rempli par la poudre de composition choisie pour l'étude (obtenue par broyage d'un verre synthétisé à partir d'oxydes purs, voir le paragraphe 4.1.3). La poudre est ensuite tassée plusieurs fois manuellement jusqu'à obtenir une hauteur de poudre de 6cm. Un fil de platine épais transperce le haut du tube et relie celui-ci à la canne porte-échantillon, via une tige en alumine (même matériau que la canne) reposant sur une encoche pratiquée dans la canne. La hauteur de l'ensemble du dispositif est mesurée avec précision, afin de déterminer la position exacte du tube expérimental à l'intérieur du four. L'avantage de ce dispositif est de pouvoir contrôler avec précision le gradient thermique souhaité pour chaque expérience.

Les problèmes rencontrés ont été les suivants :

- Remontée du liquide à l'intérieur de la canne porte-échantillon. Ce problème a été solutionné de deux manières : 1) en rajoutant le fil de platine épais entre le tube en graphite et la canne, au lieu d'une prise directe entre les deux. Le fil de platine doit être de bonne épaisseur pour ne pas fondre lors des longues expériences. 2) en

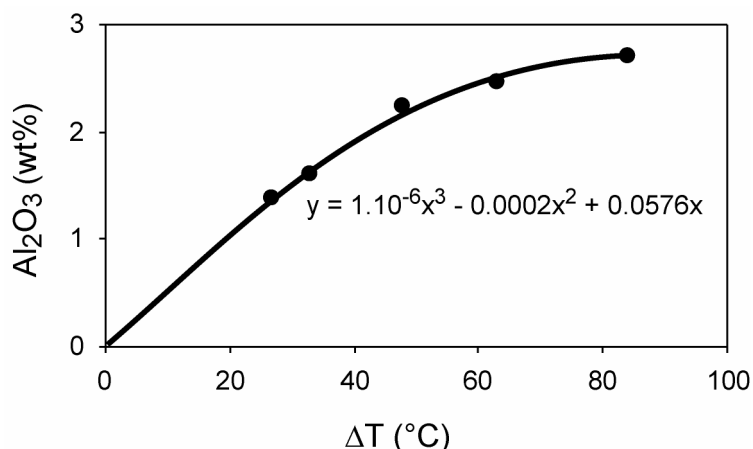


Fig. 4.6. Influence de la teneur en aluminium dans les compositions de départ sur les températures des limites de phases. Le diagramme montre la corrélation entre la teneur en aluminium dans le liquide (y) et la différence de température ΔT mesurée entre les données de Longhi et Boudreau (1980) et notre étude (x). Les données sont montrées dans les Annexes, Table 5.

Fig. 4.6. Influence of alumina content in starting materials on the phase boundary temperatures. This diagram shows the correlation between alumina content in the melt (Y axis) and ΔT , the difference of temperature between Longhi et Boudreau (1980) data and our data (X axis). Data is shown in Appendix, Table 5.

augmentant la hauteur des tubes.

- Mauvaise tenue dans le temps des tubes en graphite, malgré le flux d'argon dans le tube (pour ne pas avoir d'atmosphère oxydante). Pour palier à ce problème (pouvant entraîner des fuites sur les expériences de longue durée), nous avons opté pour des tubes de plus gros diamètre, qui résistent plus longtemps. Au final, les tubes en graphite utilisés ont les cotes suivantes : 8cm de longueur, 13mm de diamètre extérieur, 4mm de diamètre intérieur. Chaque tube est percé sur toute sa longueur moins 5mm.

4.1.6. Protocoles thermiques utilisés

La composition A (voir Fig. 4.1) a été choisie comme composition de départ pour la série de cristallisation dynamique. Au préalable, les températures liquidus et d'apparition des phases ont été déterminées par une série d'expériences à l'équilibre (Table 4.1). La température liquidus de cette composition est $1386 \pm 1^\circ\text{C}$ (see Chapter 7). Le diopside apparaît à $1356 \pm 2^\circ\text{C}$ et la silice à 1348°C . Ces incertitudes sont dues au caractère incomplet de la série d'expériences, et sont indépendantes de l'incertitude inhérente au thermocouple. Lors des expériences de cristallisation dynamique, les charges sont portées à des températures supérieures au liquidus. La différence entre cette température « de départ » et la température liquidus se définit comme le degré de surchauffe symbolisé $+\Delta T$.

Quatre cycles thermiques ont été utilisés lors des expériences de cristallisation dynamique (Fig. 4.7):

- (1) Cristallisation dynamique simple : les charges expérimentales sont maintenues à une température supérieure au liquidus pendant une heure ($+\Delta T$ variant de 13 à 119°C (de haut en bas de la charge), puis sont refroidies à vitesse constante jusqu'à une température où la cristallisation est stoppée brutalement (trempe à l'eau). Les vitesses

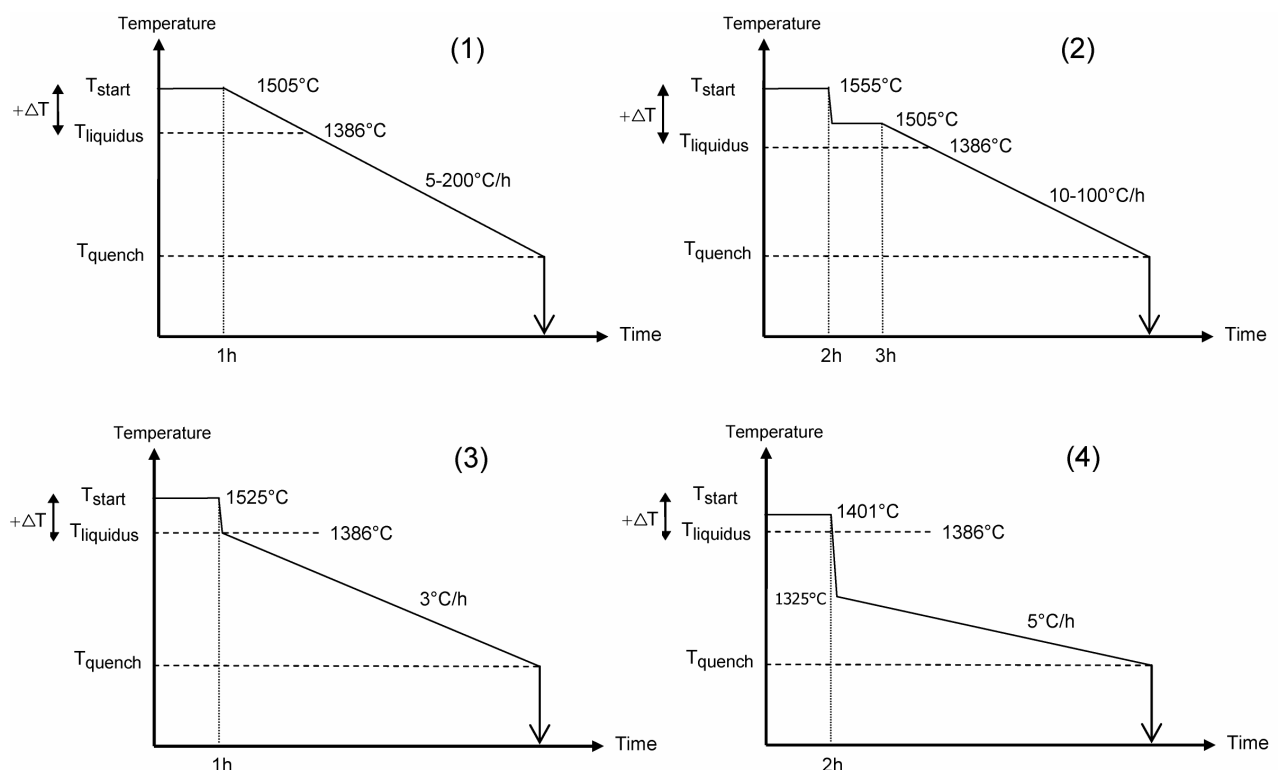


Fig. 4.7. Protocoles expérimentaux utilisés lors des expériences de cristallisation dynamique.

Fig. 4.7. Thermal protocols used during dynamic crystallization experiments.

de refroidissement sont de 5, 10 ou 200°C/h.

- (2) Cristallisation dynamique (1) précédée d'une forte surchauffe : les charges sont chauffées à très haute température ($+ΔT=170^{\circ}\text{C}$) pendant 2h, puis la température est abaissée rapidement ($1000^{\circ}\text{C}/\text{h}$) tout en restant au-dessus du liquidus ($+ΔT$ variant de 13 à 119°C de haut en bas de la charge). Le cycle se poursuit alors comme en (1). Les vitesses de refroidissement utilisées sont de 10 ou $100^{\circ}\text{C}/\text{h}$.
- (3) Cristallisation dynamique précédée d'un refroidissement rapide jusqu'à des températures sub-liquidus. La charge est maintenue à une température supérieure au liquidus ($+ΔT$ variant de 33 à 139°C de haut en bas de la charge) pendant 1h, puis la température est abaissée rapidement jusqu'à porter le bas de la charge à la température liquidus. Le haut de la charge est alors à environ 1300°C après compaction.). Le cycle se poursuit alors comme en (1) avec une vitesse de refroidissement de $3^{\circ}\text{C}/\text{h}$. Ce cycle n'a été utilisé que dans une expérience (CPX05).
- (4) Protocole similaire à (3) excepté pour les températures. La première phase de chauffe porte le bas de la charge à une température légèrement supérieure à la température liquidus (1401°C), tandis que le haut de la charge est lui chauffé à environ 1292°C . Après la baisse rapide de la température, la charge est à 1325°C dans sa partie inférieure, et 1200°C dans sa partie supérieure.). Le cycle se poursuit alors comme en (1) avec une vitesse de refroidissement de $5^{\circ}\text{C}/\text{h}$. Ce cycle n'a été utilisé que dans une expérience (CPX01).

4.2. Les techniques de caractérisation

Dans cette partie, le lecteur trouvera un aperçu des techniques analytiques employées pour caractériser l'ensemble des objets étudiés lors de la thèse : objets naturels (komatiites, basaltes lunaires) et objets synthétiques (charges expérimentales).

4.2.1 Microscope électronique à balayage (MEB)

Le MEB fournit des images à fort grossissement. Couplé à un système de microanalyse chimique appelé EDS (Energy Dispersive Spectroscopy), il permet l'association d'une image à grande résolution spatiale (de l'ordre du micron) à des informations chimiques. On a ainsi accès à une cartographie chimique de la zone étudiée. Tous les éléments majeurs sont en principe disponibles. Pour mon étude de la composition des pyroxènes des komatiites, j'ai sélectionné les éléments suivants : Si, Mg, Fe, Ca, Al, Cr et Ti. Deux types d'imageries sont utilisés :

- l'imagerie en électrons rétrodiffusés utilise la différence de numéro atomique des atomes rencontrés pour produire des images de contraste chimique (représentatives de la composition des différentes phases présentes dans la zone concernée). C'est ce mode que j'utilise pour l'étude des sections polies. Pour un gain de temps, plusieurs résolutions sont disponibles selon le travail à effectuer.
- l'imagerie en électrons secondaires permet d'obtenir très rapidement des informations sur la topographie de l'échantillon.

Le MEB du laboratoire « Magmas et Volcans » (Clermont-Ferrand) est de type JEOL JSM-5910 LV. L'EDS est constitué d'un détecteur piloté par le logiciel Spirit pour l'acquisition et le traitement des images. Les images ont été obtenues en utilisant une tension d'accélération de 20kV.

4.2.2. Microsonde électronique

Les analyses par sonde électronique ont été menées au CRPG à Nancy et à l’Institut de Géosciences de l’Université Johannes Gutenberg à Mayence (Allemagne). A Nancy, l’instrument utilisé est une sonde Cameca SX100. Les éléments Na, Mg, K, Ca, Ti, Fe, Mn, Cr, Si et Al ont été analysés sous les conditions suivantes : tension 15kV, courant échantillon 10nA, taille du faisceau environ 2µm. J’ai surtout effectué des profils au travers des cristaux de pyroxène zonés, avec un pas variant de 3µm à 15µm. La durée d’analyse pour chaque élément est d’environ 20 secondes, la limite de détection est de l’ordre de la dizaine à la centaine de ppm suivant l’élément chimique, et la précision relative de l’ordre de 1%.

A Mayence, la microsonde est de type JEOL JXA-8900 RL, à pointages préliminaires sur microscope optique. Les conditions analytiques utilisées sont : tension 20kV, courant 20nA, taille du faisceau environ 2µm. Les standards utilisés sont des verres ultrabasiques de la collection de l’Institut.

4.2.3. Microsonde ionique

La sonde ionique est un instrument d’analyse construit pour mesurer à l’échelle microscopique les concentrations et les compositions isotopiques de tous les éléments connus, même à des teneurs très faibles. Des ions sont accélérés dans la colonne primaire et focalisés sur une zone de l’échantillon. Cette zone est pulvérisée sous l’impact et émet une partie des éléments qui la constituent sous forme d’ions appelés ions secondaires. Ceux-ci sont accélérés par un champ électrique présent entre la surface de l’échantillon et la première lentille de l’optique de transfert, qui envoie le faisceau d’ions dans la partie spectromètre de la machine. Les ions secondaires passent dans le secteur électrostatique qui va les séparer en fonction de leur énergie initiale. Ensuite ils sont refocalisés par la lentille du spectromètre avant de passer dans le secteur magnétique qui va les séparer en fonction de leur masse. Les ions ainsi sélectionnés sont dirigés sur un écran fluorescent en imagerie, soit sur un système de comptage dans le cas d’une analyse. Plus de détails sur la physique de la machine peuvent être obtenus dans les notices techniques constructeur, ainsi que dans Chaussidon et Demange (1988).

Les analyses ont été effectuées à l’aide de la sonde Cameca IMS-3f du Max Planck Institut für Chemie à Mayence. Les paramètres utilisés sont les suivants : tensions d’accélération 10kV, diamètre du faisceau primaire de 20µm, courant d’arc de 50mA.

4.2.4. Analyses roche totale : ICP-MS et ICP-OES

Les éléments majeurs ont été analysés sur commande au Centre de Recherches Pétrographiques et Géochimiques (Nancy), par ICP-OES (Inductively Coupled Plasma – Optic Emission Spectrometer).

Les éléments en traces ont été dosés par ICP-MS (instrument ELAN 5000 du Laboratoire de Géodynamique des Chaînes Alpines, Grenoble). Le protocole utilisé est décrit dans IONOV et al. (2006). En voici un bref résumé :

Pour l’attaque acide : à une petite quantité de poudre (100 mg environ) pesée dans un bêcher en téflon de type savilex, ajouter un mélange d’acide nitrique (10 gouttes de HNO₃ à 14 moles/l) et d’acide fluorhydrique (9 ml de HF). L’ensemble a été mis à évaporer sur plaque chauffante de façon à obtenir un résidu sec. Ce dernier est repris par 10 ml d’acide chlorhydrique à 6 mol/l. La solution acide est ensuite versée dans un pilulier en plastique, qui sera pesé avant et après. Une petite quantité de la solution mère est mélangée avec 0,5 ml de spike (⁹Be, ⁷⁸As, ¹¹⁵In, ¹⁶⁹Tm, ²⁰⁹Bi), avant d’être mise à évaporer sur la plaque chauffante. Le résidu à sec est finalement repris avec 10 gouttes d’acide nitrique à 14 mol/l, puis transvasé dans un pilulier de 50 ml avec de l’eau distillée. Une goutte d’acide fluorhydrique est ajoutée avant de refermer le pilulier. La solution ainsi obtenue est analysée par ICP-MS, la prise en

Appendix A

compte des interférences et la calibration étant respectivement assurées par le passage de blancs et d'un géostandard (BHVO SP 26.02) spiké ou non.

Appendix B
Chapitre 5. Pétrographie détaillée

5.1. Rappel du contexte général	125
5.2. Coulée de basalte komatiitique d'Alexo	125
Ax 104	126
Ax 101-102	126
Ax103	126
5.3. Coulée de komatiite d'Alexo	127
Ax 105	127
Ax 106	127
Résumé	128

5.1. Rappel du contexte général

Les échantillons étudiés proviennent de deux coulées de laves archéennes et se situent dans la zone d'Alexo, dans le canton de Dundonald, non loin de Timmins, Ontario, dans la ceinture de roches vertes de l'Abitibi. Dans la zone d'Alexo, on rencontre plusieurs types de roches volcaniques : des coulées de komatiite et de basalte, des pillow-lavas andésitiques, ainsi qu'une vaste intrusion basique-ultrabasique : le sill de Dundonald (Arndt et al., 2004). Les échantillons de notre étude ont été prélevés dans deux coulées distinctes : une coulée de basalte komatiitique et une coulée de basalte. Ces coulées ont fait l'objet d'études préalables (Arndt, 1986, Arndt & Fleet, 1979, Barnes, 1983, Campbell & Arndt, 1982, Lahaye & Arndt, 1996).

Les échantillons Ax101-102-103-104 proviennent du sommet de la coulée de basalte komatiitique, tandis que Ax105-106 sont issus de la zone inférieure à spinifex à olivine de la coulée de komatiite (cette zone est également nommée horizon A3, voir le Chapitre 3). Ils ont la particularité d'avoir un excellent état de préservation, montrant en particulier des cristaux de pyroxène peu ou pas altérés. Les échantillons ont été préparés de manière classique pour une étude pétrographique : confection de sucres de roche, collage de lame mince et réduction à 30µm d'épaisseur.

Les caractéristiques des échantillons étudiés sont récapitulées dans la Table 5.1.

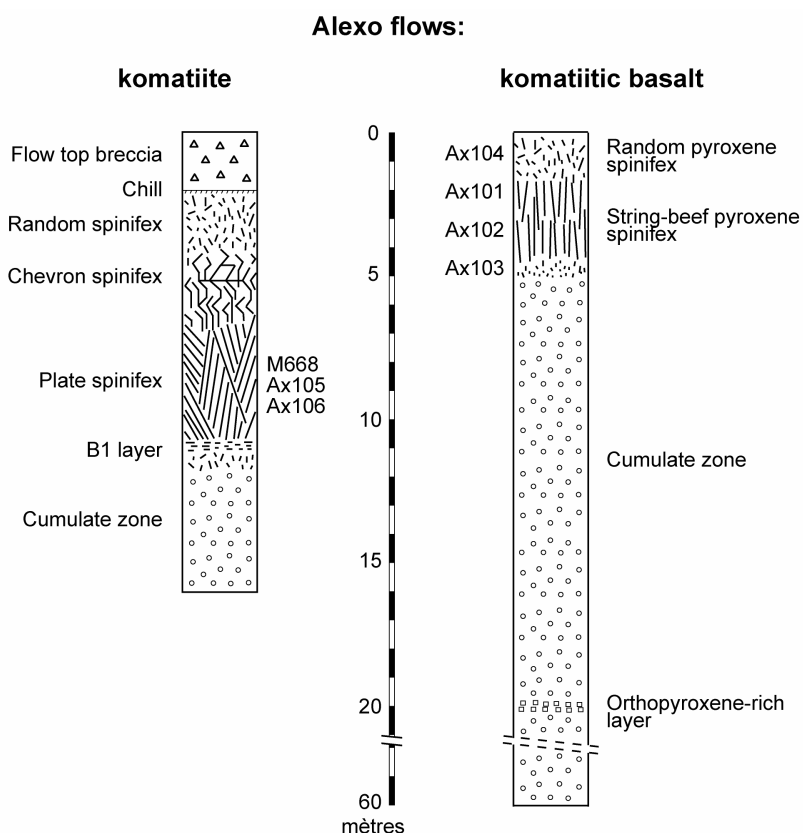


Fig. 5.1. Coupes des coulées de komatiite et basalte komatiitique d'Alexo, montrant la localisation des échantillons étudiés ainsi que les variations texturales (d'après Arndt, 1986 et Barnes, 1983).

Fig. 5.1. Sections through the Alexo flows, showing sample locations and textural variations (after Arndt, 1986 and Barnes, 1983).

5.2. Coulée de basalte komatiitique d'Alexo

Ax 104

Dans cet échantillon issu du haut de la coulée (Fig. 5.1), de gros cristaux de pyroxène trapus, zonés (œur de pigeonite, bordure d'augite), aux contours assez irréguliers, côtoient des aiguilles très fines de spinifex à pyroxène.

Les cristaux de plagioclase, de belle taille (jusqu'à 3mm de long), sont fortement altérés sur leurs bords.

Ax 101-102

40% de pyroxènes en forme d'aiguilles allongées et fortement zonés sont présents dans ces échantillons, pour 60% de matrice. Ces aiguilles présentent en leur cœur une teinte gris-beige mouchetée ; il s'agit de pigeonite complètement altérée en un minéral secondaire, la chlorite. Le pourtour (manteau) a la composition d'une augite. On définit ainsi la structure "*core and mantle*" (Fig. 5.2). Les aiguilles sont orientées perpendiculairement au toit de la coulée, avec une variation d'une vingtaine de degrés. La distribution est uniforme sur la lame. D'un diamètre compris entre 0.2 et 1.0mm, elles atteignent jusqu'à 45mm de long. Leur taille moyenne est de 25mm, pour un diamètre de 0.5mm. Ces aiguilles semblent parfois se regrouper en amas de deux ou trois aiguilles, pour former des mégacristaux. La partie centrale des grandes aiguilles (altération de la pigeonite) présente systématiquement une sorte de maclage, pas forcément symétrique par rapport au plan passant au milieu du mégacristal (Fig. 5.2). Entre ces grands mégacristaux de clinopyroxènes, la matrice se compose de trois phases :

- Des cristaux d'augite très fins (n'excédant pas 2mm) sont groupés en gerbes de « plumes d'oiseaux ». Si la base des gerbes a le plus souvent la même orientation que les mégacristaux, les cristaux sont courbes vers le sommet, et forment un angle de plus ou moins 45°. On rencontre deux cas. Soit ils poussent de la périphérie du mégacristal vers l'extérieur : les sites de nucléation se situent le long du mégacristal (Fig. 5.2) et vers la base de la coulée, soit la nucléation se fait au hasard dans la matrice et l'orientation des gerbes est alors aléatoire (Fig. 5.2).
- Les cristaux de plagioclase, fortement altérés, sont de taille inférieure à 0.4mm et sont présents dans les sites de croissance simultanée avec l'augite (*intergrowths*, Fig. 5.3). Au sein des « plumes d'oiseau », le plagioclase est en compétition directe avec le pyroxène pour arriver à croître. Le pyroxène et le plagioclase poussent alternativement en puisant l'un après l'autre dans le bain silicaté les éléments dont ils ont besoin pour croître.
- Des oxydes, de type spinelle (chromite) et ilménite se trouvent aussi bien près des gerbes de petits pyroxènes que près des grands cristaux aciculaires de pyroxène.

Ax103

Cet échantillon, situé à la base de la partie spinifex, montre des pyroxènes de morphologie différente. Contrairement à Ax101-102, le pyroxène n'est présent ici ni sous forme squelettique, ni sous forme de mégacristaux zonés. On observe ainsi des cristaux trapus, de morphologie variable, qui paraît tout de même parfois proche des mégacristaux de pyroxène en section basale. Certains individus mieux préservés montrent encore une zonation (œur de pigeonite et bordure d'augite).

5.3. Coulée de komatiite d'Alexo

Dans les deux échantillons de komatiite Ax105 et Ax106, de grandes plaques d'olivine spinifex, bien développées (plusieurs centimètres à décimètres de long), isolent des volumes (« cellules ») où se développent des fines plaques d'olivine et des cristaux aciculaires complexes de pyroxène. Entre ces grands cristaux, on trouve des gerbes de petits clinopyroxènes, ainsi que des grains fins de clinopyroxène et de plagioclase (en *intergrowths* : figures d'intercroissance), et enfin des petites chromites. Les deux échantillons décrits sont représentatifs des « cellules » de l'horizon A3 de la coulée de komatiite.

Ax 105

Les proportions de cristaux estimées sont les suivantes :

- 15% d'olivine
- 60% de pyroxène aciculaire
- 25% d'un ensemble de petits cristaux qui constituent une matrice (pyroxène + plagioclase + chromite + verre altéré)

Les olivines, presque totalement serpentiniisées, sont présentes sous formes de tablettes (ou plaques), massives (plusieurs mm à cm de long) et sous forme de mégacristaux squelettiques ou dendritiques (largeur moyenne : 0.1-0.2mm, plusieurs cm de long). Ces olivines délimitent des zones (véritables « poches »), où des spinifex à pyroxène croissent d'une manière superbement ordonnée. Leur longueur semble uniquement contrôlée par la place disponible, puisqu'on retrouve très souvent un seul et même mégacristal d'un bout à l'autre d'une poche. La figure 5.3b montre que la croissance des cristaux aciculaires de pyroxène se fait dans le moindre intervalle disponible. On distingue deux séries de cristaux de pyroxène : des grands cristaux aciculaires complexes avec des dendrites parallèles les uns aux autres, ainsi que des petits cristaux, en gerbes, coincés entre les baguettes d'olivine. L'épaisseur des aiguilles de pyroxène est proche de celui des olivines (0.1-0.2mm) et varie assez peu sur l'étendue de la lame mince. Certains pyroxènes montrent une sorte de maillage : les teintes de biréfringence au microscope polarisant varient brutalement et de manière géométrique, au sein d'un même individu (Fig. 5.3d). Ces pyroxènes sont zonés, avec un cœur de pigeonite et une bordure d'augite. La Figure 5.3c montre l'extrémité un individu complexe, zoné, avec ce que je définis sous le nom de structure en « vis ». Les extrémités du cristal sont aciculaires, tandis que le coeur est structuré en spirales, avec des zones creuses. Les structures de spirales sont orientées de manière oblique à l'axe *c* du minéral. Vues au microscope polarisant, les zones creuses cachent d'autres spirales et aiguilles de pyroxène. Entre les fines plaques d'olivine, espacés en moyenne de 0.5mm, on retrouve des pyroxènes « en plumes d'oiseau », avec un site de nucléation sur le bord de l'olivine (Fig. 5.3e).

De la famille des spinelles, les chromites $[(\text{FeMg})(\text{CrAl})_2\text{O}_4]$ sont des minéraux assez spectaculaires dans leur parure komatiitique : les cristaux sont squelettiques et souvent en forme de croix. Dans cette lame, les plus grands cristaux mesurent jusqu'à 1 mm de long, et se trouvent à proximité de la zone à olivines dendritiques. D'autres chromites, squelettiques ou sub-automorphes, bien plus petites, ont aussi poussé sur les bords des mégacristaux d'olivine (Fig. 5.3f).

Ax 106

Les mégacristaux de clinopyroxène constituent ici 70% de la roche. Entre ces grands cristaux aciculaires de pyroxène se trouve une mésostase brune, fibreuse, rappelant les gerbes de petits clinopyroxènes en forme de « plumes d'oiseau » décrits dans les lames Ax101-102-105. Les olivines sont uniquement présentes sous forme dendritique et sont totalement serpentiniisées. A proximité, on remarque la présence de chromites squelettiques cruciformes,

d'environ 0.5mm de longueur. En sections allongées, la plupart des mégacristaux squelettiques de pyroxène a une longueur dépassant celle de la lame mince ($> 3\text{cm}$) et leur diamètre varie quelque peu (0.1 à 0.4mm). Ils offrent parfois des structures très complexes ; en plus de la zonation *core and mantle* (cœur de pigeonite, bordure d'augite) et du maclage (décris également dans Ax101-102-105), les mégacristaux montrent une structure en « vis » (Fig. 5.4a, b). Cette structure, visible au microscope en lumière polarisée et en lumière naturelle, affecte l'ensemble d'un cristal de pyroxène, cœur de pigeonite et bordure d'augite. Ces cristaux en « vis » comportent plusieurs secteurs de taille variable orientés de manière oblique par rapport à l'axe *c*. Plusieurs secteurs situés côte à côte ont les mêmes propriétés optiques, avec une extinction commune lorsqu'ils sont observés au microscope en lumière analysée. Ces secteurs regroupent systématiquement la pigeonite et l'augite. Il est possible que cette structure et le maclage décrit plus haut soit un seul et même phénomène, du à des coupes particulières dans les cristaux. Les cristaux en « vis » côtoient les mégacristaux classiques. Ce phénomène n'affecte donc pas toutes les aiguilles de pyroxène. Le maclage est présent dans une partie des mégacristaux de pyroxène de cette lame (Fig. 5.4c). Entre eux, la mésostase foncée se compose de gerbes de petits pyroxènes et d'un verre altéré.

Dans une petite partie de la lame, les pyroxènes développent des cristaux extrêmement squelettiques, en forme d'échelons (Fig. 5.4). Ceux-ci ne sont pas zonés. Les petits pyroxènes de la matrice ont cristallisé dans les espaces laissés à l'intérieur des cristaux. Des minuscules pyroxènes se sont également développés à proximité immédiate des olivines dendritiques, au milieu d'autres pyroxènes en « plumes d'oiseau » (Fig. 5.4f). Leur structure est comparable à celle relevée sur des pyroxènes squelettiques qui ont, eux, poussés au milieu des autres spinifex. Ceci implique des conditions de cristallisation relativement similaires dans les deux cas.

Les olivines sont ici toutes serpentiniées et uniquement présentes sous formes dendritiques et de fines plaques (Fig. 5.4e). Les seules chromites de la lame sont situées près de ces olivines : la chromite se développe donc au contact des olivines, et jamais des pyroxènes. Elles ont une taille maximale de 0.8mm et montrent une morphologie squelettique (Fig. 5.4e).

Résumé

Dans les deux contextes : 1) sommet de la coulée de basalte komatiitique et 2) volumes limités par les grandes plaques d'olivine dans la partie inférieure de la zone à spinifex de la coulée de komatiite, on trouve des pyroxènes offrant les mêmes formes spectaculaires et complexes. Les cristaux ont des morphologies squelettique (cristaux aciculaires du basalte komatiitique et de la komatiite), dendritique (cristaux complexes de l'horizon A3 de la komatiite, cristaux « en échelons ») ou presque sphérolitique (« gerbes »). Les cristaux dendritiques complexes exhibent de longues aiguilles parallèles les unes aux autres. La plupart des cristaux de pyroxène sont zonés, avec un cœur de pigeonite et une bordure d'augite.

Table 1. Complete major and trace element data: komatiite Ax106, px 6 (see Chapter 6)

<i>mineral</i>	<i>aug</i>	<i>aug</i>	<i>aug</i>	<i>aug</i>	<i>pig</i>	<i>aug</i>	<i>aug</i>	<i>aug</i>						
SiO₂	47,63	48,99	50,81	51,58	53,01	53,80	53,93	54,20	53,63	53,21	53,14	50,59	48,77	46,16
Al₂O₃	8,88	6,93	5,02	3,85	3,00	2,71	2,68	2,45	2,84	2,80	2,96	4,69	7,08	10,30
TiO₂	0,63	0,52	0,34	0,26	0,18	0,10	0,14	0,13	0,11	0,19	0,39	0,29	0,66	0,81
Cr₂O₃	0,02	0,21	0,57	1,20	1,16	1,37	1,50	1,15	1,53	1,36	1,54	0,70	0,25	0,03
FeO	9,64	8,03	7,86	7,54	10,02	9,52	9,55	9,60	9,36	9,34	9,39	7,91	8,44	10,13
MnO	0,23	0,20	0,23	0,19	0,26	0,26	0,24	0,24	0,21	0,25	0,27	0,22	0,22	0,19
MgO	14,95	16,36	18,38	20,22	26,87	27,54	27,72	27,94	27,30	26,82	26,58	18,64	16,89	13,80
CaO	17,47	18,08	16,61	14,80	5,59	5,20	5,31	5,00	5,58	6,19	6,88	16,17	17,34	18,21
Na₂O	0,17	0,13	0,14	0,17	0,07	0,04	0,07	0,06	0,07	0,08	0,07	0,14	0,15	0,18
K₂O	0,02	0,00	0,00	0,01	0,00	0,01	0,01	0,00	0,01	0,01	0,00	0,01	0,04	0,00
Total	99,69	99,54	100,00	99,87	100,17	100,65	101,22	100,85	100,68	100,33	101,30	99,42	99,96	99,88
Mg#	0,73	0,78	0,81	0,83	0,83	0,84	0,84	0,84	0,84	0,83	0,83	0,81	0,78	0,71
En	45,41	48,31	52,92	57,62	73,59	75,20	75,13	75,67	74,66	73,46	72,24	53,71	49,54	42,36
Wo	38,15	38,38	34,38	30,32	11,01	10,21	10,35	9,74	10,97	12,19	13,44	33,50	36,57	40,19
Fs	16,43	13,31	12,70	12,06	15,40	14,59	14,52	14,59	14,37	14,36	14,32	12,79	13,89	17,45
Li		1,27		1,23		1,08		1,13		1,12			1,10	
Be		0,008		0,010		0,003		0,006		0,003			0,006	
B		0,08		0,29		0,06		0,13		0,10			0,06	
Ba		0,09		0,25		0,09		0,11		0,03			0,08	
Sr		4,29		1,01		0,63		0,62		0,53			4,02	
Zr		26,98		1,49		1,10		1,18		0,91			17,28	
Y		20,37		3,38		2,77		2,94		2,41			18,13	
La		0,28		0,03		0,01		0,01		0,01			0,17	
Ce		1,27		0,10		0,04		0,04		0,02			0,90	
Pr		0,29		0,02		0,01		0,02		0,01			0,29	
Nd		2,90		0,16		0,10		0,11		0,09			1,86	
Sm		1,60		0,13		0,07		0,10		0,08			1,08	
Eu		0,59		0,06		0,06		0,08		0,04			0,46	
Gd		2,55		0,27		0,19		0,21		0,20			1,93	
Dy		3,40		0,39		0,47		0,47		0,29			3,63	
Er		2,31		0,40		0,37		0,38		0,27			1,96	
Yb		2,21		0,53		0,50		0,48		0,50			1,93	

Note

Oxides in wt%; trace elements in ppm

Table 2. Complete major and trace element data: komatiite Ax106, px 2

<i>mineral</i>	<i>aug</i>	<i>aug</i>	<i>aug</i>	<i>aug</i>	<i>aug</i>	<i>pig</i>	<i>aug</i>	<i>aug</i>	<i>aug</i>									
SiO₂	47,38	48,06	49,75	49,71	50,44	51,24	52,45	52,86	52,86	53,48	52,90	52,72	53,27	53,04	52,91	50,27	49,29	48,71
Al₂O₃	8,41	7,33	6,32	5,44	4,82	4,03	3,06	2,92	2,89	2,47	2,70	2,78	2,44	2,54	2,03	4,95	5,97	6,98
TiO₂	0,57	0,47	0,40	0,31	0,29	0,24	0,16	0,12	0,14	0,06	0,08	0,07	0,15	0,17	0,06	0,38	0,53	0,44
Cr₂O₃	0,05	0,03	0,06	0,19	0,36	0,75	0,98	1,31	1,59	1,16	1,42	1,49	1,26	1,35	0,60	0,39	0,26	0,07
FeO	11,72	10,81	9,60	9,19	8,47	8,52	9,43	9,61	9,57	9,62	9,69	9,53	9,64	9,61	13,07	8,03	8,09	9,54
MnO	0,27	0,26	0,23	0,22	0,28	0,18	0,24	0,28	0,30	0,23	0,29	0,23	0,26	0,27	0,32	0,19	0,20	0,22
MgO	15,70	17,45	17,86	18,39	19,30	20,83	24,83	26,30	26,70	27,24	27,24	27,00	27,52	27,08	25,18	18,07	16,71	16,72
CaO	15,77	15,26	15,62	15,70	15,46	13,67	9,11	6,93	6,32	5,89	6,07	6,12	5,88	5,97	5,53	18,02	18,08	17,15
Na₂O	0,19	0,17	0,13	0,11	0,13	0,12	0,06	0,10	0,08	0,07	0,08	0,08	0,04	0,07	0,08	0,12	0,16	0,15
K₂O	0,00	0,00	0,00	0,00	0,00	0,00	0,00	0,00	0,01	0,02	0,00	0,00	0,02	0,00	0,00	0,00	0,01	0,00
Total	100,06	99,89	100,02	99,32	99,62	99,67	100,39	100,45	100,57	100,40	100,55	100,05	100,56	100,18	99,83	100,46	99,31	100,09
Mg#	0,70	0,74	0,77	0,78	0,80	0,81	0,82	0,83	0,83	0,83	0,83	0,83	0,84	0,83	0,77	0,80	0,79	0,76
En	46,71	50,60	51,80	52,79	54,88	58,78	67,71	71,71	72,92	73,87	73,54	73,47	74,06	73,66	69,00	50,86	48,79	48,60
Wo	33,73	31,81	32,57	32,40	31,61	27,73	17,86	13,59	12,41	11,48	11,78	11,97	11,38	11,67	10,90	36,46	37,95	35,84
Fs	19,57	17,59	15,63	14,80	13,52	13,49	14,43	14,70	14,67	14,64	14,68	14,55	14,56	14,67	20,10	12,68	13,26	15,56
Li										1,01							0,94	
Be										0,003							0,003	
B										0,04							0,03	
Ba										0,02							0,07	
Sr										0,50							3,07	
Zr										1,03							11,74	
Y										2,93							13,64	
La										0,01							0,12	
Ce										0,04							0,64	
Pr										0,02							0,19	
Nd										0,08							1,27	
Sm										0,09							1,03	
Eu										0,02							0,44	
Gd										0,22							1,68	
Dy										0,54							2,30	
Er										0,40							1,64	
Yb										0,48							1,43	

Note

Oxides in wt%; trace elements in ppm

Table 3. Complete major and trace element data: lunar basalt 12052,91 px8 (see Chapter 6)

mineral	pyroxfer-roite	aug	aug	aug	aug	aug	aug	pig	pig	pig	pig	pig	pig	pig	pig	pig	pig	pig
SiO₂	47,91	47,14	47,37	47,72	48,26	48,41	48,73	50,24	51,25	51,34	51,23	51,51	51,44	51,37	51,54	51,77	51,31	51,42
Al₂O₃	2,91	5,21	5,11	4,94	4,46	4,44	3,96	2,90	2,54	2,47	2,37	2,32	2,47	2,41	2,54	2,52	2,55	2,54
TiO₂	2,07	2,23	2,17	2,07	1,71	1,82	1,58	0,98	0,89	0,83	0,82	0,88	0,86	0,83	0,79	0,83	0,77	0,89
Cr₂O₃	0,38	0,73	0,84	0,93	1,27	1,30	1,25	1,14	1,16	1,22	1,16	1,18	1,23	1,21	1,25	1,30	1,24	1,27
FeO	24,64	15,46	14,62	13,86	14,32	13,71	14,04	16,76	17,64	17,36	17,42	17,72	17,49	17,47	17,33	17,20	17,22	17,40
MnO	0,47	0,29	0,34	0,23	0,32	0,27	0,27	0,31	0,31	0,29	0,33	0,31	0,37	0,31	0,31	0,33	0,35	0,34
MgO	13,40	12,54	12,85	13,43	14,40	14,73	15,64	18,61	20,36	20,48	20,96	21,38	21,81	22,12	22,25	21,78	22,26	22,21
CaO	8,41	15,89	16,40	16,34	15,44	15,67	14,27	8,86	6,83	6,37	6,20	5,88	5,53	5,31	4,89	5,09	4,86	4,94
Na₂O	0,04	0,09	0,08	0,06	0,03	0,06	0,04	0,02	0,00	0,00	0,00	0,02	0,00	0,06	0,01	0,03	0,05	0,01
K₂O	0,00	0,00	0,01	0,01	0,01	0,00	0,01	0,00	0,00	0,01	0,03	0,00	0,00	0,00	0,00	0,00	0,01	0,00
Total	100,23	99,58	99,81	99,60	100,24	100,41	99,81	99,84	100,98	100,39	100,51	101,21	101,21	101,09	100,91	100,88	100,64	101,03
Mg#	0,49	0,59	0,61	0,63	0,64	0,66	0,66	0,66	0,67	0,68	0,68	0,68	0,69	0,69	0,70	0,69	0,70	0,69
En	40,27	38,42	39,12	40,75	42,94	43,72	46,30	54,12	57,89	58,85	59,56	60,14	61,26	61,89	62,69	62,07	62,85	62,52
Wo	18,17	35,00	35,90	35,65	33,10	33,44	30,37	18,53	13,96	13,16	12,67	11,89	11,17	10,68	9,91	10,43	9,87	10,00
Fs	41,56	26,58	24,98	23,60	23,96	22,84	23,32	27,35	28,15	27,99	27,78	27,97	27,57	27,43	27,40	27,51	27,28	27,49
Li		3,48				2,70			1,95			2,03			1,78			1,83
Be		0,079				0,053			0,015			0,019			0,017			0,014
B		0,07				0,05			0,03			0,06			0,04			0,03
Ba		0,03				0,04			0,01			0,01			0,01			0,00
Sr		9,57				7,66			0,84			1,50			1,06			0,72
Zr		31,63				22,29			4,51			5,76			5,00			4,96
Y		29,14				23,88			7,62			9,00			7,40			6,84
La		0,38				0,29			0,02			0,06			0,04			0,04
Ce		2,19				1,60			0,16			0,27			0,23			0,16
Pr		0,62				0,42			0,05			0,10			0,04			0,05
Nd		3,56				2,84			0,24			0,61			0,41			0,30
Sm		2,13				1,47			0,22			0,43			0,31			0,25
Eu		0,15				0,14			0,02			0,03			0,03			0,02
Gd		3,88				2,74			0,71			0,71			0,58			0,48
Dy		5,22				4,29			1,03			1,41			1,30			0,88
Er		3,29				2,75			0,98			1,13			0,89			0,89
Yb		3,25				2,68			0,95			1,16			1,03			1,09

Note

Oxides in wt%; trace elements in ppm

<i>mineral</i>	<i>pig</i>	<i>pig</i>	<i>pig</i>	<i>pig</i>	<i>pig</i>	<i>pig</i>	<i>aug</i>	<i>pyroxfer-</i> <i>roite</i>	<i>pyroxfer-</i> <i>roite</i>	<i>pyroxfer-</i> <i>roite</i>	<i>pyroxfer-</i> <i>roite</i>						
SiO₂	51,81	51,70	51,39	51,11	51,25	50,58	49,35	47,79	48,60	48,02	47,85	47,51	46,87	49,04	47,97	46,85	46,45
Al₂O₃	2,15	2,11	2,30	2,53	2,77	3,03	4,08	4,69	4,61	5,11	5,71	6,14	6,27	1,90	1,48	1,40	1,16
TiO₂	0,84	0,82	0,79	0,89	0,81	1,07	1,69	1,74	1,77	2,06	2,35	2,48	2,56	1,56	1,31	1,24	0,85
Cr₂O₃	1,15	1,15	1,14	1,12	1,19	1,12	1,36	1,29	1,21	1,22	0,97	0,98	0,84	0,23	0,19	0,02	0,06
FeO	17,68	18,14	18,01	17,86	17,29	17,25	13,42	12,96	13,74	13,20	13,87	14,49	15,35	28,63	34,04	37,07	42,54
MnO	0,31	0,25	0,37	0,35	0,37	0,31	0,25	0,26	0,24	0,27	0,24	0,26	0,30	0,45	0,49	0,50	0,49
MgO	21,61	21,39	20,86	19,90	19,36	18,50	14,88	13,90	14,30	13,45	12,59	12,48	11,87	9,22	4,91	2,20	0,68
CaO	5,30	5,40	6,13	6,78	7,25	9,44	15,20	16,00	15,51	16,30	16,97	16,49	15,96	9,57	10,59	11,43	8,55
Na₂O	0,02	0,03	0,03	0,00	0,02	0,04	0,01	0,06	0,02	0,04	0,10	0,05	0,06	0,03	0,06	0,03	0,06
K₂O	0,01	0,01	0,01	0,00	0,01	0,01	0,01	0,00	0,01	0,01	0,01	0,01	0,02	0,13	0,02	0,00	0,01
Total	100,89	101,01	101,08	100,54	100,34	101,39	100,24	98,72	100,03	99,68	100,66	100,90	100,10	100,78	101,05	100,73	100,92
Mg#	0,69	0,68	0,67	0,67	0,67	0,66	0,66	0,66	0,65	0,64	0,62	0,61	0,58	0,36	0,20	0,10	0,03
En	61,15	60,33	58,97	57,19	56,48	52,91	44,63	42,54	43,12	41,29	38,65	38,44	37,14	28,66	15,53	7,05	2,21
Wo	10,78	10,95	12,46	14,01	15,21	19,41	32,78	35,20	33,63	35,97	37,46	36,52	35,91	21,39	24,07	26,32	20,02
Fs	28,07	28,71	28,57	28,80	28,31	27,68	22,59	22,26	23,25	22,74	23,89	25,04	26,95	49,95	60,40	66,63	77,76
Li								1,86		1,83			2,49			2,67	
Be								0,017		0,018			0,045			0,066	
B								0,04		0,07			0,06			0,06	
Ba								0,01		0,06			0,03			0,04	
Sr								0,97		0,68			7,05			8,85	
Zr								5,63		4,55			23,27			30,29	
Y								7,98		6,98			22,98			26,85	
La								0,04		0,02			0,33			0,39	
Ce								0,19		0,14			1,55			2,04	
Pr								0,05		0,05			0,44			0,51	
Nd								0,55		0,35			3,01			3,22	
Sm								0,34		0,28			1,52			2,06	
Eu								0,02		0,01			0,16			0,16	
Gd								0,55		0,57			2,66			2,99	
Dy								1,01		1,12			4,14			4,87	
Er								0,94		0,75			2,61			2,91	
Yb								0,96		1,07			2,76			3,03	

Table 4. Complete major and trace element data: lunar basalt 15597,77 px1 (see Chapter 6)

mineral	aug	aug	aug	pig	pig	pig	pig	pig	pig	pig	pig	pig	pig	pig	aug	aug	aug	aug
SiO₂	42,68	45,91	47,68	51,74	52,42	52,64	52,97	52,75	52,33	52,26	52,56	51,62	51,82	50,76	48,81	47,36	43,50	51,01
Al₂O₃	10,54	6,78	5,66	2,07	1,78	1,87	1,67	1,75	1,87	1,69	1,35	1,61	1,90	2,56	4,18	5,47	9,49	17,15
TiO₂	2,34	2,18	1,50	0,49	0,38	0,39	0,42	0,39	0,46	0,33	0,31	0,39	0,40	0,52	1,06	1,48	2,61	1,62
Cr₂O₃	0,02	0,44	1,20	1,27	1,22	1,32	1,26	1,20	1,29	1,18	1,03	1,12	1,23	1,29	1,51	1,07	0,07	0,04
FeO	30,31	16,84	15,69	18,23	16,98	16,19	15,68	16,00	16,47	17,22	17,28	17,55	17,97	18,07	15,95	15,47	21,54	18,29
MnO	0,34	0,31	0,31	0,32	0,28	0,34	0,26	0,29	0,28	0,31	0,25	0,25	0,33	0,30	0,25	0,25	0,33	0,23
MgO	4,48	9,88	12,55	21,97	24,03	24,65	25,15	24,65	24,25	23,58	23,86	22,93	22,09	19,79	15,41	12,44	7,37	0,50
CaO	9,36	16,66	15,57	4,20	3,18	2,83	2,54	2,69	3,10	3,39	3,28	3,59	4,32	6,27	12,50	15,85	14,71	9,20
Na₂O	0,08	0,05	0,07	0,05	0,02	0,00	0,00	0,00	0,01	0,01	0,01	0,03	0,03	0,06	0,06	0,07	1,03	
K₂O	0,02	0,00	0,00	0,01	0,00	0,00	0,00	0,00	0,00	0,00	0,01	0,00	0,00	0,02	0,00	0,01	0,01	0,21
Total	100,19	99,06	100,23	100,39	100,29	100,25	99,96	99,71	100,11	100,03	99,95	99,09	100,09	99,61	99,76	99,48	99,74	99,28
Mg#	0,21	0,51	0,59	0,68	0,72	0,73	0,74	0,73	0,72	0,71	0,71	0,70	0,69	0,66	0,63	0,59	0,38	0,05
En	15,88	31,56	38,56	62,38	67,04	68,91	70,30	69,31	67,89	66,09	66,43	64,85	62,61	57,47	46,21	38,26	24,54	2,89
Wo	23,85	38,26	34,39	8,57	6,38	5,69	5,10	5,44	6,24	6,83	6,57	7,30	8,80	13,09	26,95	35,05	35,21	38,06
Fs	60,28	30,18	27,05	29,05	26,58	25,40	24,60	25,25	25,87	27,08	27,00	27,85	28,58	29,44	26,84	26,70	40,25	59,05
Li						1,32642			1,39			1,76559					4,07526	
Be		0,05762				0,00839			0,010			0,0126					0,11301	
B		0,10354				0,02596			0,07			0,06855					0,03602	
Ba			2,24839			0,01265			0,01			0					0,04583	
Sr			11,7173			0,31807			0,41			0,66845					11,5006	
Zr			45,4074			3,00949			2,50			3,88225					104,271	
Y			24,8376			2,90602			3,14			4,45702					45,7293	
La		0,61887				0,00799			0,02			0,02252					1,16004	
Ce		2,99543				0,04266			0,05			0,14811					5,56661	
Pr		0,79027				0,02305			0,02			0,02993					1,33742	
Nd		4,28811				0,10333			0,14			0,31014					9,42831	
Sm		2,34845				0,06978			0,14			0,19407					4,17436	
Eu		0,24056				0,01123			0,02			0,0166					0,34442	
Gd		3,26196				0,20061			0,27			0,26843					6,0032	
Dy		5,2051				0,42287			0,35			0,7512					9,03329	
Er		2,86776				0,28346			0,31			0,42982					4,3973	
Yb		2,38814				0,47399			0,42			0,71804					3,9726	

Note

Oxides in wt%; trace elements in ppm

Table 5. Influence of alumina content in starting materials on the phase boundary temperatures. See the companion Figure 4.7. which shows the correlation between alumina content in the melt and the difference of temperature between Longhi & Boudreau (1980) data and our data.

Considered boundary	Temperature of Longhi & Boudreau, 1980 (°C)	Temperature of this study (°C)	Difference between both temperatures	Al ₂ O ₃ content of starting material (wt%)
protoenstatite / orthopyroxene	1445	1361	84	2,70
protoenstatite / orthopyroxene	1445	1382	63	2,46
orthopyroxene / pigeonite	1407	1359	48	2,23
pigeonite / diopside	1387	1354	33	1,60
pigeonite / diopside	1387	1360	27	1,37

References

- Allègre, C. J. (1982). Genesis of Archaean komatiites in a wet ultramafic subducted plate. In: Arndt, N. T. & Nisbet, E. G. (eds.) *Komatiites*. London: George Allen and Unwin, 495-500.
- Arndt, N. T. (1976). Melting relations of ultramafic lavas (komatiites) at 1 atm and high pressure. *Carnegie Institution Washington, Yearbook* 75, 555-562.
- Arndt, N. T. (1977). Thick, layered peridotite-gabbro lava flows in Munro Township, Ontario. *Can. J. Earth Sci.* 14, 2620-2637.
- Arndt, N. T. (1986). Differentiation of komatiite flows. *J. Petrol.* 27, 279-301.
- Arndt, N. T. (2003). Komatiites, kimberlites and boninites *J Geophys. Res.* 108.
- Arndt, N. T., Albarède, F., M. Cheadle, M., Ginibre, C., Herzberg, C., Jenner, G., Chauvel, C. & Lahaye, Y. (1998). Were komatiites wet? *Geology* 26, 739-742.
- Arndt, N. T., Barnes, S. T. & Lesher, C. M. (2008). *Komatiite*: Cambridge University Press.
- Arndt, N. T. & Fleet, M. E. (1979). Stable and metastable pyroxene crystallization in layered komatiite flows. *Am. Mineralogist* 64, 856-864.
- Arndt, N. T., Lesher, C. M., Houle, M. G., Lewin, E. & Lacaze, Y. (2004). Intrusion and crystallization of a spinifex-textured komatiite sill in Dundonald Township, Ontario. *J. Petrology* 45, 2555-2571.
- Arndt, N. T., Naldrett, A. J. & Pyke, D. R. (1977). Komatiitic and iron-rich tholeiitic lavas of Munro Township, northeast Ontario. *J. Petrology* 18, 319-369.
- Arndt, N. T. & Nesbitt, R. W. (1984). Magma mixing in komatiitic lavas from Munro Township, Ontario. In: Kröner, A., Hanson, G. N. & Goodwin, A. M. (eds.) *Archaean geochemistry*. Berlin: Springer-Verlag, 99-114.
- Arndt, N. T. & Nisbet, E. G. (1982). *Komatiites*. London: George Allen & Unwin.
- Barnes, R. G., Lewis, J. C. & Gee, R. D. (1973). Archean ultramafic lavas from Mount Clifford. *Geol. Survey of Western Australia Annual Report*, 59-70.
- Barnes, S.-J. (1983). A comparative study of olivine and clinopyroxene spinifex flows from Alexo, Abitibi greenstone belt, Canada. *Contrib. Mineral. Petrol.* 83, 293-308.
- Barrie, C. T., Corfu, F., Davis, P., Coutts, A. C. & MacEachern, D. (1999). Geochemistry of the Dundonald komatiite-basalt suite and genesis of Dundal Ni deposit, Abitibi subprovince, Canada. *Economic Geology and the Bulletin of the Society of Economic Geologists* 94, 845-866.
- Biggar, G. M. (1985). Calcium-poor pyroxenes: Phase relations in the system CaO-MgO-Al₂O₃-SiO₂. *Mineralogical Magazine* 49, 49-58.
- Biggar, G. M. (1989). Experimentally Determined Compositions of Protopyroxene, Orthopyroxene and Pigeonite (Including Metastable Pigeonite) with Liquids in the System CaO-MgO-Al₂O₃-SiO₂. *European Journal of Mineralogy* 1, 181-191.
- Bottinga, Y. & Weill, D. P. (1970). Densities of liquid silicate systems calculated from partial molar volumes of oxide components. *Am. J. Sci.* 269, 169-182.

References

- Boyd, F. R. & Schairer, J. F. (1964). The System MgSiO₃--CaMgSi₂O₆. *J. Petrology* 5, 275-309.
- BVSP. (1981). *Basaltic Volcanism on the Terrestrial Planets*. New York: Pergamon.
- Byerly, G. R., Kröner, A., Lowe, D. R., Todt, W. & Walsh, M. M. (1996). Prolonged magmatism and time constraints for sediment deposition in the early Archean Barberton greenstone belt: evidence from the Upper Onverwacht and Fig Tree groups. *Precamb. Geol.* 78, 125-138.
- Campbell, I. H. & Arndt, N. T. (1982). Pyroxene accumulation in spinifex-textured rocks. *Geological Magazine* 119, 605-610.
- Canup, R. M. & Asphaug, E. (2001). Origin of the Moon in a giant impact near the end of the Earth's formation. *Nature* 412, 708-712.
- Carlson, W. D. (1989). Subsolidus phase equilibria near the enstatite-diopside join in CaOMgO-Al₂O₃-SiO₂ at atmospheric pressure. *American Mineralogist* 74, 325-332.
- Chaussidon, M. & Demange, J. C. (1988). Instrumental mass fractionation in ion microprobe studies of sulphur isotopic ratios. In: Benninghoven A, H. A. M., Werner H W (ed.) *Proceedings of the Sixth International Conference on secondary Ion Mass Spectrometry (SIMS VI)*. Chichester: Wiley & sons, 937-940.
- Dann, J. C. (2000). The Komati Formation, Barberton Greenstone Belt, South Africa, part I: new map and magmatic architecture. *S. Afr. J. Earth Sci.* 6, 681-730.
- Dann, J. C., Holzheid, A. H., Grove, T. L. & McSween, H. Y. (2001). Phase equilibria of the Shergotty meteorite: Constraints on pre-eruptive water contents of martian magmas and fractional crystallization under hydrous conditions. *Meteoritics & Planetary Science* 36, 793-806.
- de Wit, M. J., Hart, R. A. & Hart, R. J. (1987). The Jamestown ophiolite complex, Barberton mountain belt: a section through 3.5 Ga oceanic crust. *J. Afr. Earth Sci.* 6, 681-730.
- Donaldson, C. H. (1976). An experimental study of olivine morphology. *Contrib. Mineral. Petrol.* 57, 187-213.
- Donaldson, C. H. (1979). An experimental investigation of the delay in nucleation of olivine in mafic lavas. *Contrib. Mineral. Petrol.* 69, 21-32.
- Donaldson, C. H. (1982). Spinifex-textured komatiites: A review of textures, mineral compositions, and layering. In: Arndt, N. T. & Nisbet, E. G. (eds.) *Komatiites*. London: George Allen and Unwin, 211-244.
- Dupré, B., Chauvel, C. & Arndt, N. T. (1984). Pb and Nd isotopic study of two Archean komatiitic flows from Alexo, Ontario. *Geochim. Cosmochim. Acta* 48, 1965-1972.
- Faure, F. (2001). Les Textures de Croissance Rapide dans Les Roches Magmatiques Basiques et Ultrabasiques : Etudes Expérimentale et Nanoscopique. Clermont-Ferrand: Université B. Pascal, 206.
- Faure, F., Arndt, N. T. & Libourel, G. (2006). Formation of spinifex texture in komatiites: an experimental study. *J. Petrology* 47, 1591-1610.
- Faure, F., Trolliard, G., Nicollet, C. & Montel, J.-M. (2003). A developmental model of olivine morphology as a function of the cooling rate and the degree of undercooling *Contrib. Mineral. Petrol.* 145, 251-263.

References

- Gamble, R. P. & Taylor, L. A. (1980). Crystal-Liquid Partitioning in Augite - Effects of Cooling Rate. *Earth and Planetary Science Letters* 47, 21-33.
- Grove, T. L. & Bence, A. E. (1977). Experimental study of pyroxene-liquid interaction in quartz-normative basalt 15597. *Proceedings of the 8th Lunar and Planetary Science Conference*, 1549-1579.
- Grove, T. L. & Bence, A. E. (1979). Crystallization kinetics in a multiply saturated basalt magma: An experimental study of Luna 24 ferrobasalt. *Proceedings of the 10th Lunar and Planetary Science Conference*, 439-478.
- Grove, T. L., de Wit, M. J. & Dann, J. (1997). Komatiites from the Komati Type Section, Barberton, South Africa. In: de Wit, M. J. & Ashwal, L. D. (eds.) *Greenstone Belts*. Oxford: Oxford Science Publications, 422-437.
- Grove, T. L., Gaetani, G. A. & M.J., d. W. (1994). Spinifex textures in 3.49 Ga Barberton Mountain Belt komatiites: evidence for crystallization of water-bearing, cool magmas in the Archean. *Eos* 75, 354.
- Grove, T. L., Gaetani, G. A., Parman, S., Dann, J. & M.J., d. W. (1996). Origin of spinifex textures in 3.49 Ga komatiite magmas from the Barberton Mountainland South Africa. *Eos* 77, 281.
- Grove, T. L., Parman, S. W. & Dann, J. C. (1999). Conditions of magma generation for Archean komatiites from the Barberton Mountainland, South Africa. In: Fei, Y., Bertka, C. M. & Mysen, B. O. (eds.) *Mantle petrology: field observations and high-pressure experimentation*. Houston: The Geochemical Society, 155-167.
- Grove, T. L. & Raudsepp, M. (1978). Effects of kinetics on the crystallization of quartz-normative basalt 15597: An experimental study. *Proceedings of the 9th Lunar and Planetary Science Conference*, 585-599.
- Hart, S. R. & Brooks, C. (1977). The geochemistry and evolution of the Early Precambrian mantle. *Contrib. Mineral. Petrol.* 61, 109-128.
- Huppert, H. E. & Sparks, R. S. J. (1985). Komatiites I: Eruption and flow. *J. Petrol.* 26, 694-725.
- Ionov, D. A., Chazot, G., Chauvel, C., Merlet, C. & Bodinier, J.-L. (2006). Trace element distribution in peridotite xenoliths from Tok, SE Siberian craton: A record of pervasive, multi-stage metasomatism in shallow refractory mantle. *Geochimica Et Cosmochimica Acta* 70, 1231-1260.
- Kinzler, R. J. & Grove, T. L. (1985). Crystallization and differentiation of Archean komatiite lavas from northeast Ontario: Phase equilibrium and kinetic studies. *Am. Mineralogist* 70, 40-51.
- Kirkpatrick, R. J. (1981). Kinetics of crystallization of igneous rocks. *Reviews in Mineralogy and Geochemistry* 8, 321-395.
- Kirkpatrick, R. J. (1983). Theory of nucleation in silicate melts. *American Mineralogist* 68, 66-77.
- Kushiro, I. (1972). Determination of liquidus relations in synthetic silicate systems with electron probe analysis: the system forsterite-diopside-silica at 1 atmosphere. *American Mineralogist* 57, 1260-1271.
- Kushiro, I. & Haramura, H. (1971). Major Element Variation and Possible Source Materials of Apollo 12 Crystalline Rocks. *Science* 171, 1235-1237.

References

- Lahaye, Y. & Arndt, N. T. (1996). Alteration of a komatiitic flow: Alexo, Ontario, Canada. *J. Petrol.* 37, 1261-1284.
- Lindsley, D. H. & Andersen, D. J. (1983). A two-pyroxene thermometer. *Journal of Geophysics Research* 88, A887-A906.
- Lofgren, G. & Lanier, A. B. (1990). Dynamic crystallization study of barred olivine chondrules. *Geochimica Et Cosmochimica Acta* 54, 3537-3551.
- Lofgren, G. & Russell, W. J. (1986). Dynamic crystallization of chondrule melts of porphyritic and radial pyroxene composition. *Geochimica Et Cosmochimica Acta* 50, 1715-1726.
- Lofgren, G. E. (1980). Experimental studies on the dynamic crystallization of silicate melts. In: Hargraves, R. B. (ed.) *Physics of magmatic processes*. Princeton: Princeton University Press, 487-552.
- Lofgren, G. E. (1983). Effect of heterogeneous nucleation on basaltic textures: a dynamic crystallization study. *J. Petrol.* 24, 229-255.
- Lofgren, G. E. (1989). Dynamic crystallization of chondrule melts of porphyritic olivine composition: Textures experimental and natural. *Geochimica Et Cosmochimica Acta* 53, 461-470.
- Lofgren, G. E. & Donaldson, C. H. (1975). Curved branching crystals and differentiation in comb-layered rocks. *Contrib. Mineral. Petrol.* 274, 243-273.
- Lofgren, G. E., Donaldson, C. H., Williams, R. J., Mullins, O. & Usselman, T. M. (1974). Experimentally reproduced textures and mineral chemistry of Apollo 15 quartz normative basalts. *Proceedings of the 5th Lunar Science Conference*, 549-568.
- Longhi, J. & Boudreau, A. E. (1980). The Orthoenstatite liquidus field in the system forsterite-diopside-silica at one atmosphere. *American Mineralogist* 65, 563-573.
- McSween, H. Y., Grove, T. L., Lentz, R. C. F., Dann, J. C., Holzheid, A. H., Riciputi, L. R. & Ryan, J. G. (2001). Geochemical evidence for magmatic water within Mars from pyroxenes in the Shergotty meteorite. *Nature* 409, 487-490.
- Morimoto, N., Fabries, J., Ferguson, A. K., Ginzburg, I. V., Ross, M., Seifert, F. A., Zussman, J., Aoki, K. & Gottardi, G. (1988). Nomenclature of pyroxenes. *American Mineralogist* 73, 1123-1133.
- Naldrett, A. J. & Gasparrini, E. L. (1971). Archean nickel sulphide deposits in Canada: Their classification, geological setting and genesis with some suggestions as to exploration. *Geol. Soc. Australia (Special Publication)* 3, 201-226.
- Naldrett, A. J. & Mason, G. D. (1968). Contrasting Archaean ultramafic igneous bodies in Dundonald and Clerque Townships, Ontario. *J. Can. Earth Sci.* 5, 111-143.
- Nesbitt, R. W. (1971). Skeletal crystal forms in the ultramafic rocks of the Yilgarn Block, Western Australia: Evidence for an Archaean ultramafic liquid. *Geol. Soc. Australia* 3, 331-347.
- Nisbet, E. G. (1982). The tectonic setting and petrogenesis of komatiites. In: Arndt, N. T. & Nisbet, E. G. (eds.) *Komatiites*. London: George Allen and Unwin, 501-520.
- Nisbet, E. G., Bickle, M. J. & Martin, A. (1977). The mafic and ultramafic lavas of the Belingwe greenstone belt, Rhodesia. *J. Petrol.* 18, 521-566.

References

- Papike, J. J., Hodges, F. N., Bence, A. E., Cameron, M. & Rhodes, J. M. (1976). Mare Basalts - Crystal-Chemistry, Mineralogy, and Petrology. *Reviews of Geophysics* 14, 475-540.
- Parman, S., Dann, J., Grove, T. L. & de Wit, M. J. (1997). Emplacement conditions of komatiite magmas from the 3.49 Ga Komati Formation, Barberton Greenstone Belt, South Africa. *Earth Planet. Sci. Lett.* 150, 303-323.
- Parman, S., Grove, T. L. & Dann, J. (2001). The production of Barberton komatiites in an Archean subduction zone. *Geophys. Res. Lett.* 28, 2513-2516.
- Parman, S., Grove, T. L., Dann, J. & de Wit, M. J. (2004). A subduction origin for komatiites and cratonic lithospheric mantle. *South African J. Geol.* 107, 107-118.
- Parman, S. W., Shimizu, N. & Grove, T. L. (2003). Constraints on the pre-metamorphic trace element composition of Barberton komatiites from ion probe analyses of preserved clinopyroxene. *Contrib. Mineral. Petrol.* 144, 383-396.
- Pyke, D. R., Naldrett, A. J. & Eckstrand, O. R. (1973). Archean ultramafic flows in Munro Township, Ontario. *Geol. Soc. Amer., Bull.* 84, 955-978.
- Renner, R. (1989). Cooling and crystallization of komatiite flows from Zimbabwe. University of Cambridge.
- Shore, M. & Fowler, A. D. (1999). The origin of spinifex texture in komatiites. *Nature* 397, 691-694.
- Stone, W. E., Jensen, L. S. & Church, W. R. (1987). Petrography and geochemistry of an unusual Fe-rich basaltic komatiite from Boston Township, northeastern Ontario. *Can. J. Earth Sci.* 24, 2537-2550.
- Viljoen, M. J. & Viljoen, R. P. (1969). The geology and geochemistry of the lower ultramafic unit of the Onverwacht Group and a proposed new class of igneous rocks. *Geol. Soc. S. Africa, Spec. Publ.* 21, 55-85.
- Williams, D. A., Kerr, R. C., Lesher, C. M. & Barnes, S. J. (2000). Analytical/numerical modeling of komatiite lava emplacement and thermal erosion at Perseverance, Western Australia.
- Wilson, A. H., Shirey, S. B. & Carlson, R. W. (2003). Archean ultra-depleted komatiites formed by hydrous melting of cratonic mantle. *Nature* 423, 858-861.
- Yang, H. (1972). Stability of iron-free pigeonite at atmospheric pressure. *American Mineralogist* 57, 1232-1241.
- Yang, H. & Foster, W. R. (1973). Crystallization of iron-free pigeonite in the system anorthite-diopside-enstatite-silica at atmospheric pressure. *American Journal of Science* 273, 488-497.

